THE UNIVERSITY OF HULL

Development of an autonomous lab-on-a-chip system with ion separation and conductivity detection for river water quality monitoring

being a Thesis submitted for the Degree of Doctor of Philosophy

in the University of Hull

by

Etienne Pierre Joly MEng (ENSIM, France)

December 2013

Abstract

This thesis discusses the development of a lab on a chip (LOC) ion separation for river water quality monitoring using a capacitively coupled conductivity detector (C^4D) with a novel baseline suppression technique.

Our first interest was to be able to integrate such a detector in a LOC. Different designs (On-capillary design and on-chip design) have been evaluated for their feasibility and their performances. The most suitable design integrated the electrode close to the channel for an enhanced coupling while having the measurement electronics as close as possible to reduce noise. The final chip design used copper tracks from a printed circuit board (PCB) as electrodes, covered by a thin Polydimethylsiloxane (PDMS) layer to act as electrical insulation. The layer containing the channel was made using casting and bonded to the PCB using oxygen plasma. Flow experiments have been conduced to test this design as a detection cell for capacitively coupled contactless conductivity detection (C^4D).

The baseline signal from the system was reduced using a novel baseline suppression technique. Decrease in the background signal increased the dynamic range of the concentration to be measured before saturation occurs. The sensitivity of the detection system was also improved when using the baseline suppression technique. Use of high excitation voltages has proven to increase the sensitivity leading to an estimated limit of detection of 0.0715 µM for NaCl (0.0041 mg/L).

The project also required the production of an autonomous system capable of operating for an extensive period of time without human intervention. Designing such a system involved the investigation of faults which can occur in autonomous system for the *in-situ* monitoring of water quality. Identification of possible faults (Bubble, pump failure, *etc.*) and detection methods have been investigated. In-depth details are given on the software and hardware architecture constituting this autonomous system and its controlling software.

Acknowledgments

I would like to thank all the persons who have contributed one way or another to this work. I would like to express my gratitude to my supervisor Dr. Ian Bell for welcoming me in his laboratory. His expertise in electronic and computer science was very valuable all along the project when developing and debugging the system. I also greatly appreciated his help and patience while reviewing my manuscript.
Prof. Gillian Greenway, my second supervisor for chairing the weekly meetings and providing support and guidance during the project.
Prof. Steve Haswell, my third supervisor for his technical and scientific help about microfluidics.
I would like to acknowledge the rest of the persons involved in the LIMPIDS project at the University of Reading Prof. Richard Skeffington, Dr Andrew Wade and Dr Sarah Halliday. Members of the Centre for Ecology and Hydrology are also acknowledged and Matt Loewenthal from the Environment Agency.

I would also like to thank all my past and present colleagues from the engineering group especially Sunny, Nasr, Richard and my colleagues from chemistry, Ahmed, Ryan, David, Fernando and Jerry to name a few.

I would like to especially thank my family for their support and encouragement in the course of this thesis.

Last but not least, I want to thank Dr Cédric Floquet for getting me into the microfluidics world and giving me a foretaste about research during my internship at the NOC. Special thanks to Dr Tom Myers for the useful discussions about microfluidic and electronics. Finally, thanks to Dr Yuehua Dou and Professor John Greenman for providing the information regarding the use of the conductivity detection for biological analysis.

The EPSCR is acknowledged for providing financial support (EP/G014221/1)

Table of contents

Abstract I
Acknowledgments II
Table of contents III
Table of figures VIII
List of acronyms XIII

Chapter 1 : Introduction 1
1.1. Water quality monitoring 1
1.1.1. Current practice versus high frequency monitoring 3
1.1.2. Potential of LOC based measurement 4
1.1.3. Motivation for improved water quality monitoring 5
1.2. Presentation of the LIMPIDS project 6
1.2.1. LIMPIDS project requirements 8
1.3. Outline of the thesis 9
1.4. Posters and publications 10
1.4.1. Posters 10
1.4.2. Publications 10
Chapter 2 : Background in Lab-on-Chip 12
2.1. Outline of the chapter 12
2.2. What is a Lab-on-chip? 12
2.3. Microfluidic principles 13
2.3.1. Pumping 13
2.3.2. Flow switching 16
2.3.3. Mixing 17
2.4. Manufacturing techniques 18
2.4.1. Micro patterning techniques 19
2.4.2. Bonding techniques 24
2.5. A lab-on-a-chip for environmental monitoring 26

2.5.1. Assessment of LOC techniques for use in *in-situ* environmental monitoring 26
2.5.2. Review of existing LOC systems for environmental monitoring 27
2.6. Summary of the chapter 28
Chapter 3 : Background to separation and C^4D 29
3.1. Outline of the chapter 29
3.2. Ion separation 29
3.2.1. Monolithic column for ion chromatography 30
3.2.2. Capillary electrophoresis 33
3.3. Introduction on conductivity detection 37
3.4. Electrode models for C^4D 38
3.4.1. Electrode / Electrolyte coupling and stray capacitance 38
3.4.2. Electrolyte conductivity 42
3.5. Introduction of additional complex element in the model 44
3.6. Electrode design 47
3.6.1. On-capillary configuration 48
3.6.2. On-Chip configuration 51
3.6.3. On-capillary / On-chip comparison 58
3.7. Measurement electronics 59
3.7.1. Signal generation 59
3.7.2. Current to voltage conversion 60
3.7.3. AC to DC conversion and noise filtering 62
3.7.4. Baseline suppression 66
3.7.5. Signal Noise Ratio considerations 67
3.8. Detection of inorganic ions 68
3.9. Future of the C^4D 71
3.10. Summary of the chapter 72
Chapter 4 : Design of a Lab-on-chip for IC for water quality monitoring 73
4.1. Outline of the chapter 73
4.2. Block diagram 73
4.3. Implementation of the electrodes 74
4.3.1. Capillary cell 75
4.3.2. Off-chip cell 81
4.3.3. On-chip cell 85

4.3.4. Summary of the chapter 94
Chapter 5 : Design of a conductivity detector with baseline suppression 96
5.1. Outline of the chapter 96
5.2. Structure of the measurement electronics 96
5.2.1. Overview 96
5.2.2. Baseline suppression principle 98
5.2.3. Signal generator 99
5.2.4. Transimpedance amplifier 101
5.2.5. Baseline suppression system 103
5.2.6. Synchronous detection 108
5.2.7. Implementation of the baseline suppression automation 110
5.3. Conductivity detection in continuous flow 117
5.3.1. Contact mode 117
5.3.2. Contactless mode 119
5.4. Separation of inorganic ions with conductivity detection 125
5.4.1. Experimental setup 125
5.4.2. Preliminary electrophoresis results 127
5.5. Summary of the chapter 129
Chapter 6 : Self-testing, fault detection and autonomous operation 130
6.1. Outline of the chapter 130
6.2. Self-testing 131
6.3. Fault and methods of detection 131
6.3.1. Bubble fault 131
6.3.2. Electrophoresis current fault 133
6.3.3. Pump fault 134
6.4. Field testing of LOC with real samples 136
6.5. Summary of the chapter 137
Chapter 7 : System integration 139
7.1. Outline of the chapter 139
7.2. Contributing developers 139
7.3. Overview 140
7.4. User roles 142
7.4.1. Hydrologist 142
7.4.2. Lab Analyst 142

7.4.3. Routine maintenance operative 143
7.4.4. Repair and maintenance operative 143
7.4.5. Developer mode 143
7.5. Software architecture 144
7.5.1. Overview 144
7.5.2. Instrument manager architecture 145
7.5.3. Graphic User Interface (GUI) architecture 147
7.5.4. Embedded software architecture 153
7.6. Instrument manager to user interface interaction 154
7.7. PC to instrument interaction 155
7.7.1. Instrument commands 157
7.7.2. Data Packet Structure 158
7.7.3. Data streaming 160
7.8. Embedded hardware architecture 162
7.8.1. Overview 162
7.8.2. Embedded hardware description 163
7.8.3. Embedded hardware configuration 164
7.8.4. Electrophoresis operation 166
7.8.5. Data converters control for C^4D measurement 167
7.8.6. Baseline suppression automation 168
7.9. Summary of the chapter 169
Chapter 8 : Conclusion 171
8.1. Development of a Lab-on-chip for IC 171
8.2. Design of a conductivity detector with baseline suppression 172
8.3. Self-testing, fault detection and autonomous operation 173
8.4. System integration 174
8.5. Further work 174
8.5.1. Future development 175
8.5.2. Monitoring of clotting process using conductivity detection 177

Bibliography 180
Appendix 192
Monitoring Site Description 192
COMSOL 197
Numerical method 198
PCB CAD 199
LT Spice 206
Pictures 207
Experimental method 209
MATLAB 216
LIMPIDS Software documentation 218

Table of figures

Figure 1.1: Electrical conductivity measured monthly, weekly, daily, and hourly, with hourly pH and discharge, at Hore stream, Plynlimon, Wales from [4] 2
Figure 1.2: Example of shed housing instruments at the river Cut [16] 5
Figure 2.1: Example of microfluidic chip with a diffusive mixer 13
Figure 2.2: Electroosmotic flow principle 14
Figure 3.1: SEM of a PDMS channel (100x100 µm) filled with photoinitiated polymer monolith from [105] 32
Figure 3.2: Principle of Capillary Zone Electrophoresis (CZE) 33
Figure 3.3: Hydrodynamic (A) and Electrokinetic (B) injection and separation (C) .. 34
Figure 3.4: Electropherogram of cationic species from [78] – Lower curve is a 125 µM standard of K^+, Na^+, Li^+ - Upper curve is a 1:10 diluted milk sample spiked with 4.4 mM of Ca^{2+} 35
Figure 3.5: Typical MCE designs (Straight and offset injection channels variance) .. 36
Figure 3.6: Typical axial capillary arrangement with two electrodes and shield plane 38
Figure 3.7: Equivalent circuit of the cell 39
Figure 3.8: Bode plot of the cell without stray capacitance 40
Figure 3.9: Bode plot of the cell with stray capacitance Cs=0.212 pF 41
Figure 3.10: Sensitivity analysis of the cell impedance versus the stray capacitance . 41
Figure 3.11: Bode plot of the cell with stray capacitance Cs=0.212 pF at various concentration 43
Figure 3.12: Plot of the cell behaviour with stray capacitance Cs=0.212 pF at various frequencies 44
Figure 3.13: New shielding arrangement from [130] 45
Figure 3.14: Electrode model with external coil and new shielding arrangement from [130] 45
Figure 3.15: Layout of the CE chip and overview of the C^4D cell from [142] 48
Figure 3.16: Simulation of the coupling difference in case of capillary displacement [131] 49
Figure 3.17: Implementation of the C^4D module in a capillary cartridge [155] 50

Figure 3.18: Structure of the movable mini C^4D from [143].....51
Figure 3.19: Typical microchip arrangement with two electrodes 52
Figure 3.20: Two-dimensional numerical simulations of the electric field intensity for dual top–bottom compared with top–top electrode geometry using FlexPDE 5 2D [69] 54
Figure 3.21: Fabrication process of the cell from [167]. (A) Insulation of the electrode, (B) Patterned photoresist, (C) Reflowed photoresist to form semicircular sacrificial core, (D) Oxide covering of the wafer, (E) Channel creation by salvation of the photoresist 55
Figure 3.22: CE chip with four buried electrodes from [173] 57
Figure 3.23: SEM of the hybrid chip using DFR and the two protocols used to create integrated devices and hybrid devices respectively, from [61].....58
Figure 3.24: Typical electronic schematic of a C^4D 59
Figure 3.25: Block diagram of the synchronous detection circuitry.....62
Figure 3.26: Matlab simulation of the FFT and the output signal of the multiplication of two AC signals at 500kHz 63
Figure 3.27: Schematic of the orthogonal vector lock-in amplifier.....65
Figure 3.28: Block diagram of the detection electronics with offset voltage cancellation 67
Figure 4.1: Block diagram of the system 74
Figure 4.2: Polyimide coated fused-silica capillary with stainless steel electrode cell75
Figure 4.3: Calibration curve for the Stainless Steel electrode design 76
Figure 4.4: Wire wrapping electrode cell 78
Figure 4.5: Circuit board with the SMD feedback resistor, transimpedance amplifier (A), dephaser (B) and amplifying stage (C).....78
Figure 4.6: Calibration curve of the system with wire wrapping electrode.....79
Figure 4.7: Calibration curve of the most recent system with wire wrapping electrode 80
Figure 4.8: Picture of the epoxy potted C4D 81
Figure 4.9: SolidWorks model of the plugs 82
Figure 4.10: 3D printed plugs after washing off.....82
Figure 4.11: Picture of the 2 electrodes plug 82
Figure 4.12: 3D view of the glass chip 82
Figure 4.13: Schematic of the experiment in continuous flow 83

Figure 4.14: Successive injection of NaCl at 100µL/min 84
Figure 4.15: Calibration curve of the Plug Electrode system 84
Figure 4.16: Calibration curve of the PCB/Double sided tape/PMMA system 86
Figure 4.17: Surface profile after PDMS coating 87
Figure 4.18: PCB after PDMS coating with tape to cover connection holes 88
Figure 4.19: Surface profile of a Cu pad before coating 88
Figure 4.20: Surface profile of a Cu pad after coating 89
Figure 4.21: Channel profile of the SU-8 mould 89
Figure 4.22: Channel profile of the casted PDMS 90
Figure 4.23: PDMS Cell with Upchurch nanoports 91
Figure 4.24: Calibration curve of the PCB/PDMS system 92
Figure 4.25: Experimental behaviour of a cell for low concentrations 93
Figure 4.26: Experimental behaviour of a cell for high concentrations 94
Figure 5.1: Detection system overview 97
Figure 5.2: Baseline current suppression principale diagram 98
Figure 5.3: Block diagram of a basic DDS system 99
Figure 5.4: Diagram of the amplitude control of the DDS 101
Figure 5.5: Block diagram of the baseline suppression 103
Figure 5.6: Block diagram of the amplitude control 104
Figure 5.7: Block diagram of the voltage to current conversion for the cancelation current 106
Figure 5.8: CAD design of the voltage-current converter 106
Figure 5.9: Block diagram of the digitally controlled suppression voltage generator 107
Figure 5.10: Example of multiplication of one cosine signals with one shifted by 90° 109
Figure 5.11: Schematic of the DC current balancing of the Source/Sink branch 110
Figure 5.12: Step 2 of the automated baseline suppression 111
Figure 5.13: Reference signal phase versus frequency 112
Figure 5.14: Experimental filtered synchronous detection output while sweeping φ_{90} 113
Figure 5.15: Filtered synchronous detection output while sweeping φ_{90} 114
Figure 5.16: Step 3 of the automated baseline suppression 114

Figure 5.17: Filtered synchronous detection output of the cancelled signal while sweeping φ_C 115
Figure 5.18: Implementation of the quadrature lock-in amplifier 116
Figure 5.19: Output signal in contact mode without current baseline suppression ... 118
Figure 5.20: Output signal in contact mode with current baseline suppression 118
Figure 5.21: Calibration curve comparison without and with current baseline suppression..... 119
Figure 5.22: Output signal in contactless mode without current baseline suppression 120
Figure 5.23: Output signal in contactless mode with current baseline suppression . 120
Figure 5.24: Calibration curve comparison without and with current baseline suppression..... 121
Figure 5.25: Output signal without current baseline suppression and moderate excitation voltage 122
Figure 5.26: Output signal with current baseline suppression and high excitation voltage..... 122
Figure 5.27: Calibration curve comparison 123
Figure 5.28: Phase output of the transimpedance amplifier during plug injection.... 124
Figure 5.29: Electropherogram of two anions Cl^- and SO_4^{2-} 128
Figure 5.30: Electropherogram of two anions Cl^- and PO_4^{3-} 128
Figure 6.1: Detection of bubble injected in the system 132
Figure 6.2: Comparison of normal and faulty current profile during separation..... 133
Figure 6.3: Baseline signal and associated spectrum..... 134
Figure 6.4: Linear fitting of the extracted pump noise frequency versus pump supply voltage..... 135
Figure 6.5: Detection of peak broadening due to pump failure 136
Figure 6.6: LOC channel showing blockage deposits from river water 137
Figure 7.1: Possible system arrangement on a riverbank 140
Figure 7.2: User roles and system structure..... 141
Figure 7.3: Block diagram of the Instrument manager..... 145
Figure 7.4: Architecture of the PC software 145
Figure 7.5: System Setup tab of the UOHC4D software GUI..... 147

Figure 7.6: Customized section created by the GUI in function of the available data channels....148
Figure 7.7: “Live” charting of the DataTable object....149
Figure 7.8: Baseline tab of the UOHC4D software GUI....150
Figure 7.9: General tab of the UOHC4D software GUI....150
Figure 7.10: Sampling tab of the UOHC4D software GUI....151
Figure 7.11: Logging tab of the UOHC4D software GUI....152
Figure 7.12: Built-in console of the UOHC4D software GUI....152
Figure 7.13: Overview of the embedded software architecture....153
Figure 7.14: System communication overview....156
Figure 7.15: Packet structure....158
Figure 7.16: Packet structure for data streaming....160
Figure 7.17: Block diagram of the embedded hardware....162
Figure 7.18: Embedded software interrupts....165
Figure 7.19: GUI for the control of the electrophoresis experiment....167
Figure 8.1: Evolution of the impedance of the coagulating blood and blank cell culture media....179

List of acronyms

ADC:	Analog to Digital Converter
BGE:	Background Electrolyte
C^4D:	Capacitively Coupled Conductivity Detector
CE:	Capillary Electrophoresis
CEC:	Capillary Electrochromatography
COC:	Cyclic Olefin Copolymer
DAC:	Digital to Analog Converter
DDAB:	Didodecyldimethylammonium Bromide
DDS:	Direct Digital Synthesis
DOC:	Dissolved Oxygen Concentration
DSP:	Digital Signal Processing
EEPROM:	Electrically Erasable Programmable Read-Only Memory
EOF:	Electroosmotic Flow
FDA:	Fully Differential Amplifier
FPBW:	Full Power Bandwidth
FPGA:	Field-Programmable Gate Array
GPIO:	General Purpose Input Output
HDF:	Hydrodynamic Flow
HIS:	Histidine
HPLC:	High Performance Liquid Chromatography
I2C:	Inter Integrated Circuit Bus
IC:	Ion Chromatography
ICP-MS:	Inductively Coupled Plasma – Mass Spectrometry
ICP-OES:	Inductively Coupled Plasma – Optical Emission Spectrometry
LIMPIDS:	Linking Improved Modelling of Pollution to Innovative Development of Sensors
LOC:	Lab-on-a-Chip
LOD:	Limit Of Detection
MCE:	Microchip Capillary Electrophoresis
MCU:	Microcontroller
MEMS:	Microelectromechanical Systems

MES:	2-Morpholinoethansulfonic acid
MQW:	Milli-Q Water
PCB:	Printed Circuit Board
PDMS:	Polydimethylsiloxane
PECVD:	Plasma-Enhanced Chemical Vapour Deposition
PGA:	Programmable Gain Amplifier
PMMA:	Poly(methyl methacrylate)
PP:	Polypropylene
PTFE:	Polytetrafluoroethylene (Also known as Teflon®)
uTAS:	Miniaturized Total Chemical-Analysis Systems
RMS:	Root Mean Square
RTC:	Real Time Clock
SNR:	Signal-Noise Ratio
SPI:	Serial Peripheral Interface
T_g:	Glass Transition Temperature
TIA:	Transimpedance Amplifier
TOC:	Total Organic Carbon
TRP:	Total Reactive Phosphorus
VCP:	Virtual COM Port

Chapter 1 : Introduction

1.1. Water quality monitoring

With the worldwide increases in population leading to higher water demand, concern about the quality of the surface water is growing. The European Union's Water Framework Directive (WFD) entered into force in December 2000, one of its objectives is to achieve a good water quality monitoring programme by 2015. It will allow the assessment of the chemical status of the freshwater in European countries by comparing the measured level of the chemical species with the environmental quality standard. This directive is a real challenge for environmental organisations and analytical chemistry science.

Simulation models can be used to predict and help the management strategies of freshwater resources. Water quality is affected by numerous factors (Water demand, water treatment, climate, land management), therefore, development of new models capable of giving accurate predictions, taking into account a multitude of parameters, is needed. The effects of climate and land use on water quality are highly complex and models are often over-parameterized which lead to similar results with different parameters [1]. These problems highlight the fact that hydrologic systems are still not fully understood and the design of new field experiments and observations are needed to replace the current linear, additive "blackbox" models with non-linear, non-additive ones capable of fitting the calibration data while being "parametrically efficient" [2].

The development of new methods of high frequency water measurement has been identified as likely to lead to conceptual and practical advances in the hydrological and biochemical science since the need for sub-daily measurements of water quality has been established, not only for nutrients, but also for many other chemicals [3, 4]. These methods will help to provide a better understanding of the contribution of chemicals to the river network, not only during storm events but also between storm events. Kirchner shows [4] (Figure 1.1) that it is during just such periods that

interesting biogeochemical signals may emerge, precisely because they are not obscured by large hydrological fluctuations.

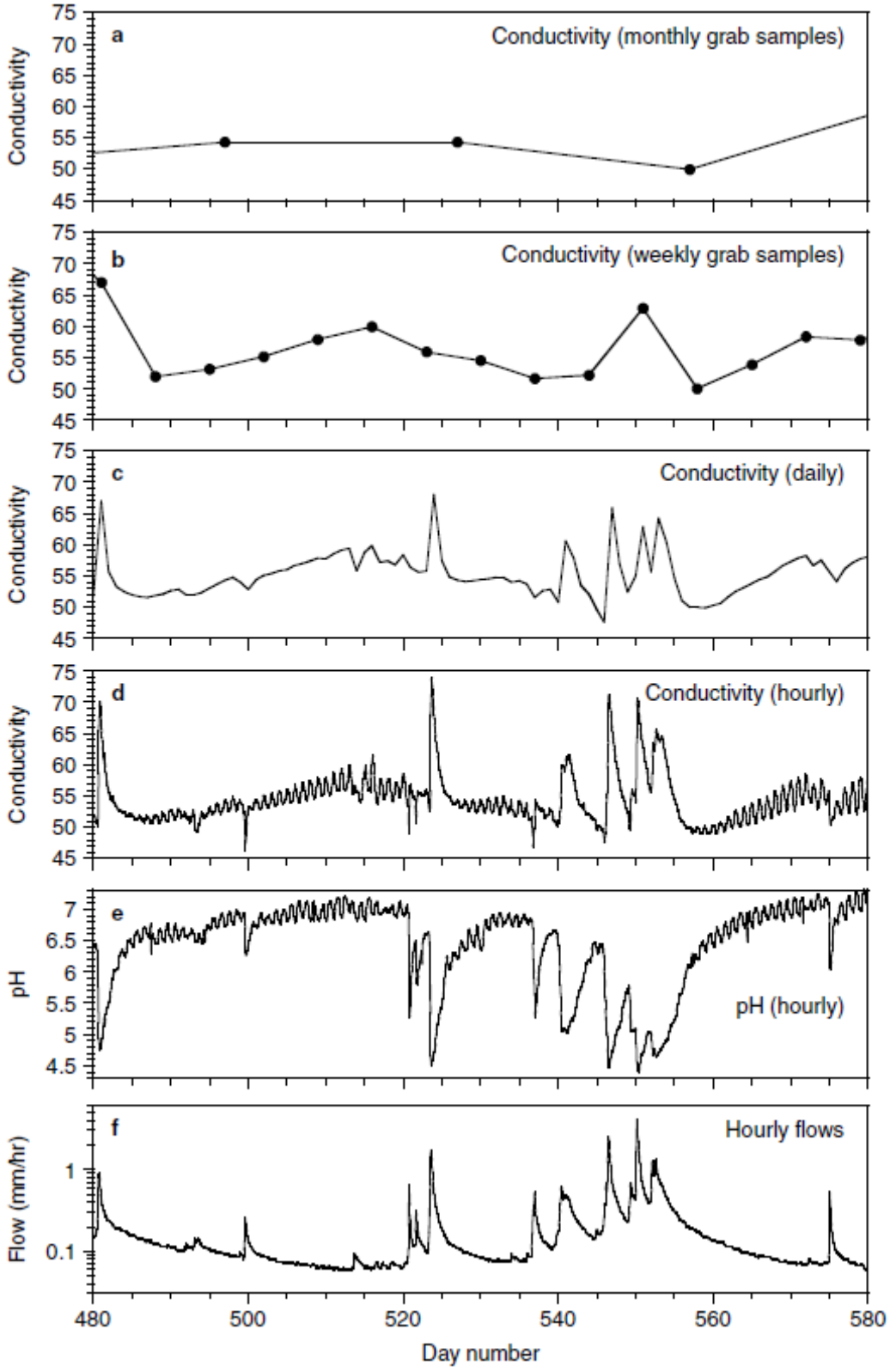

Figure 1.1: Electrical conductivity measured monthly, weekly, daily, and hourly, with hourly pH and discharge, at Hore stream, Plynlimon, Wales from [4]

This example demonstrates the need for hourly records of catchment hydrochemistry measurements instead of the monthly grab samples. This applies to not only conductivity and pH as further understanding would result from the monitoring of additional chemical species which have differing flow responses [5]. “If we want to understand the full symphony of catchment hydrochemical behaviour, then we need to be able to hear every note” [4].

1.1.1. Current practice versus high frequency monitoring

Currently, monitoring techniques are still mainly based on sample grab prior to laboratory analysis [6, 7]. For example, [8] describes an eighteen month of 7-hourly analyses of rainfall and stream water chemistry have been done using different sample collecting system prior to analysis in laboratory. The analysis was exhaustive, Inductively Coupled Plasma – Mass Spectrometry (ICP-MS) (Al, Sb, As, Ba, Be, Cd, Cs, Ce, Cr, Co, Cu, Fe, La, Pb, Li, Mn, Mo, Ni, Pr, Rb, Sc, Se, Sr, Sn, Ti, W, U, V, Zn), Inductively Coupled Plasma – Optical Emission Spectrometry (ICP-OES) (B, Ca, Mg, K, Si, Na, S), Ion Chromatography (IC) (Br, Cl, F, NO_3, NO_2, SO_4), Auto-Titrator (I, Gran alkalinity), colorimetric analyser (NH_4), conductivity meter, TOC analyser (DOC) and pH meter were the instruments used.

The authors declare that this study represents, the practical limit that the current monitoring approach can reach due to the large amount of resources required (Field, laboratory, *etc.*). The method used has many disadvantages compared to a more automated on-site analysis. As demonstrated, it is time consuming and the delay between the grab and the analysis may lead to a change in the sample [7, 9]. Neal [8] also states that the 7-hourly sampling frequency is not enough to capture water quality dynamics and there is still an increasing interest in sub-daily measurement of water quality, which could lead to a better understanding of river hydrochemical dynamics.

Neal concludes by highlighting the fact that the analysis must be accurate and precise so the difference between consecutive samples can be detected [8]. With the uses of high resolution time series, new tools could be used like spectral analysis, wavelet techniques, and cross-spectral and cross-correlation analysis [4]. Such high frequency

measurements are not feasible without an on-site measurement system and hydrometric data can probably give a first indication of the necessary measurement frequency. Kirchner stated that additional pH and conductivity measurements at Plynlimon became redundant at about the same sampling frequency as additional discharge measurements do. This implies that the necessary measurement frequency is likely to be higher in smaller catchments [4] as the hydrologic response to a change in the water stream chemistry is in the matter of minutes. Moreover, if parallel measurements (Simultaneous measurements) in the same area are the only way to achieve high frequency, it supports the idea of using small and autonomous measurement systems to achieve effective monitoring strategies in small catchments.

1.1.2. Potential of LOC based measurement

The use of Lab-on-a-chip (LOC) based measurement is of interest in environmental water monitoring as it has the potential to answer most of the problems people are currently facing. Reviews of the existing microfluidic techniques (Sample preparation, fluid handling, detection, *etc.*) applied to environmental analysis have been published [6, 10-12]. Systems capable of fast and accurate *in-situ* real time monitoring which can be robust and confined in a small package, with the possibility of wireless communication, will solve most of the issues hydrology research groups are dealing with. Some commercial system already exists like the GuardianBlue (Hach HST) which can measure several parameters used to characterise the water quality (pH, Conductivity, Turbidity, TOC and Chlorine concentration). However, they are cumbersome, limited to a certain range of species and expensive to deploy in the field (Main power, large reagent consumption, waste, *etc.*).

A few studies on nutrients like phosphorus (P) [13, 14] or dissolved oxygen [15] have been recently published using data collected by the deployment of in-field analytical equipment (Figure 1.2) but their number remains low [16]. These alternative methods provide on-site measurement abilities but still have numerous disadvantages in comparison with LOC [16]. The installation and maintenance of such sites is difficult as they need housing to protect the instrument from the outside environment, mains electricity due to the high power consumption of some instrument while still having

easy access to the water stream. In the case of the study of TRP (*i.e.* unfiltered molybdate reactive phosphorus) [13], hourly *in-situ* measurement of water quality was recorded from January 2004 to November 2006. The measurement instruments were housed in a kiosk on the river bank and were composed of a Nutrient Probe Analyser (NPA, Systea, Italy) and an YSI6600 multiparameter probe (Dissolved oxygen, pH, water temperature, conductivity, turbidity and chlorophyll). While the multiparameter probe can operate without reagent, the NPA uses a colorimetric method based on phosphomolybdenum blue complexation which needs reagent filling and recalibration every 3 weeks. Each week, manual water samples were also collected for ground truthing of the TRP data.

Figure 1.2: Example of shed housing instruments at the river Cut [16]

1.1.3. Motivation for improved water quality monitoring

The preceding discussion highlights the need for improving both understanding and monitoring of water resources as global pressures lead increase stresses. There is potential to take advantage of recent developments in LOC-based analytical science to develop a system for making high-frequency chemical measurements in lakes and rivers which will be cheaper, more reliable under field conditions, and have low power and reagent consumption. The requirements (Main power, space, maintenance, *etc.*) for such LOC-based system being less constraining, more system could be implemented. This should make it possible to collect much more detailed data, which can then be used to develop improved predictive models, potentially facilitating

improved land and water management and strengthening enforcement of pollution legislation through more accurate and trustworthy evidence.

1.2. Presentation of the LIMPIDS project

The LIMPIDS project (Linking Improved Modelling of Pollution to Innovative Development of Sensors) is an interdisciplinary project involving chemists, engineers and environmental modellers from the Universities of Reading and Hull, the Centre for Ecology and Hydrology and the Environment Agency. It was funded by EPSRC grants EP/G019967/1 (Reading) and EP/G014221/1 (Hull). The aims of the LIMPIDS project is to evaluate the use of high frequency water monitoring to improve hydrological models (Reading) and to develop a novel, high-resolution, multi-parameter water quality measuring system using an innovative miniaturised chemical sensing device (Hull). Ideally the system will be tested and validated in the field, and the data obtained will be used to advance the science of hydrochemistry and initiate development of a new generation of catchment pollutant transport models to address pressing environmental questions. Given the expect development time of the LOC-based monitoring system, high frequency data on a number of parameters (Phosphorous, Sulphate, Nitrate, *etc.*) will be collected by the University of Reading using convention equipments such as the ones depicted in Figure 1.2 (See appendix A and B for description of the monitoring site set up by the CEH and the Environmental Agency). This will also help provide a point of comparison between the capabilities and constraints of the two monitoring approaches.

The role of the University of Hull in the LIMPIDS project is to focus on the design of the microfluidic system with a chemistry part which deals with microfluidic sample handling, extraction and analytical separation process required to measure multiple dissolved species. The engineering part, which was undertaken by the author, deals with the detection and control electronics in order to have an autonomous system which can be used in the laboratory but also in the field for *in-situ* monitoring. This involves the creation of hardware and software which can be used to control and communicate with the monitoring system. The feasibility of an LOC module tailored for this system will also be evaluated by the author in term of ease of manufacturing, analytical performance and compatibility with the extraction and separation methods.

The aim of the University of Hull in the LIMPIDS project is to develop a novel, high-resolution, multi-parameter water quality measuring system using an innovative miniaturised chemical sensing device. The specific objectives related to this work are listed below:

1. Development and evaluation of a detection / signal processing system for miniature / LOC separation-based chemical analysis (*e.g.* Electrophoresis and ion chromatography), which is usable in the field, and has a good limit of detection whist minimising the number and volume of chemical reagents required.
2. Development and evaluation of analytical LOC device and electrode design(s) (Structures) which have low manufacturing costs and increased robustness to facilitate long term use in the field.
3. Development of a self contained system for field deployment of the analytical LOC device(s) for water quality monitoring, integrating power management, control, signal processing, communications and data logging.
4. Development of a software in order to provide the user with a friendly interface to control the analytical system for real-time laboratory use and autonomous *in-situ* operation.
5. Given the expectation of temporary extreme conditions and limited expected operating life of LOC devices, the system should provide self-test capabilities to facilitate identification of rogue data, overall data robustness, and alert users of actual or pending failures.
6. Development and evaluation of a robust and reproducible inorganic ions extraction method, intended for sample introduction and preconcentration from water sample prior analytical separation (Chemistry part).
7. Development and evaluation of a fast analytical separation method for inorganic ions in LOC system with small reagent consumption and high separation efficiency (Chemistry part).

1.2.1. LIMPIDS project requirements

The system to be developed needs to be able to replace or augment the existing system that the Environment Agency (EA) and the Centre for Ecology and Hydrology (CEH) are already using on the field. The specification of the system was decided during the research proposal development and is listed below:

- Detection of Na^{+}, K^{+}, Ca^{2+}, Mg^{2+} and NH_4^{+}, NO_3^{-}, NO_2^{-}, SO_4^{2-}, Cl^{-} down to 0.01 mg/L
- Detection of PO_4^{3-} down to 0.001 mg/L and preferably the same for Br^{2+} and I^{-}
- Possibility of measuring trace elements such as B, Li, Al, Fe and Mn down to 0.001 mg/L
- Operating temperature of 0 to +35°C
- Housed in a secure unit
- Self calibrating with the option of weekly/monthly field visits
- Running cost should be less than £2k/year and preferably less than £1k/year
- Option for automatic cleaning
- Possibility of use without mains power *i.e.* Batteries
- Possibility of monitoring rainfall
- Monitoring frequency should preferably be down to 15 minutes without loss of accuracy

In June 2012, the small business research initiative (SBRI) and the environment agency have opened a competition on a project named “Innovative Environmental Sensors” [17]. The main objective of this project is to develop a flexible system, suitable for on-field use which can measure a wide range of nutrients (Orthophosphate, nitrogen, ammoniacal nitrogen, nitrite, nitrate, chloride) in freshwater. To be used in the field, the device should preferably be small and lightweight with its own power and the ability to communicate with the user. These requirements highlight a growing demand for such monitoring devices. The LIMPIDS (Linking Improved Modelling of Pollution to Innovative Development of Sensors) project may help to move forward in the field of *in-situ* monitoring by using microfluidic principles and electronics.

1.3. Outline of the thesis

Chapter 2 will give a background on microfluidics principles and present various manufacturing techniques used to produce Lab-on-a-chip (LOC) systems. Understand these principles and manufacturing techniques can be the key to design future water quality monitoring platforms. These manufacturing techniques can also be used to manufacture the detection cell for the capacitively coupled contactless conductivity detection (C^4D) described in the next chapter. An example of existing monitoring platform is also given.

Chapter 3 will focus on the presentation of the most commonly used separation techniques for inorganic ions and their use in LOC. The method of detection for LOC system, the conductivity detection (C^4D) technique, will also be presented. Starting with a brief introduction, this part will provide useful information on the detection principle from the cell electrical model and design to the measurement electronic involved.

Chapter 4 will present different cell designs for C^4D application using fused silica capillary and microfluidic chip which have been developed to be used with the detection system. The manufacturing process and performance of the different cells is discussed. These cells should be ideally compatible with the separation and detection (C^4D) methods used for the LIMPIDS project.

Chapter 5 will describe the use of a novel electronic baseline suppression system for the C^4D detection of inorganic ions. The different elements constituting this system will be presented and the operating principle explained. Experimental results using this detection system will also be presented.

Chapter 6 will demonstrate the detection of faults which can occur in microfluidic system due to bubble, pump failure or blockage.

Chapter 7 will give details about the system integration, describing the software architecture (PC and embedded) and hardware architecture.

Chapter 8 will conclude this thesis by giving an overview of the progress made on the LIMPIDS project. This chapter will also talk about further work which can be done.

1.4. Posters and publications

The following public outputs have arisen from the work described in this thesis.

1.4.1. Posters

Joly, E., Bell, I.M., Webster, A., Greenway, G.M., Haswell, S.J., "Capacitively coupled conductivity detection (C^4D) for a miniaturised separation system for in situ water monitoring" poster presented at The 14th Biennial Challenger Conference for Marine Science "Microfluidics and Sensor Technology for Oceanographic and Environmental Science Applications", Southampton, 10th September 2010.

Joly, E., Esfahani, N., Bell, I.M., Greenway, G.M., Haswell, S.J., "Development of a Lab-on-a-chip miniaturised extraction and separation system for automated in-situ river water monitoring with capacitively coupled conductivity detection (C^4D)" poster presented at Monitoring the Aquatic Environment using Sensor Technologies, London, 19th October 2011

Joly, E., Bell, I.M., Fallatah, A., Greenway, G.M., Haswell., "Overcoming sample introduction issues for Lab-on-Chip environmental analysis" poster presented at Lab-on-chip European congress, Edinburgh, 28-29th March 2012.

1.4.2. Publications

Wade, A.J., Palmer-Felgate, E.J., Halliday, S.J., Skeffington, R.A., Lowenthal, M., Jarvie, H.P., Bowes, M. J., Greenway, G.M., Haswell, S.J., Bell, I.M., Joly, E., Fallatah, A., Neal, C., Williams, R.J., Gozzard, E. and Newman, J.R., From existing in situ, high-resolution measurement technologies to lab-on-a-chip – the future of water quality monitoring? Hydrology and Earth System Sciences Discussions, 2012. 9: p. 6457-6506.

Joly, E., Bell, I.M., Fallatah, A., Greenway, G.M., Haswell., S.J., Wade, A.J., Skeffington, R.A., Design and Test Issues for Lab-on-Chip Ion Separation for In-Situ Water Quality Monitoring. in the 18th International Mixed-Signals, Sensors and Systems Test Workshop (IMS3TW), 2012.

Chapter 2 : Background in Lab-on-Chip

2.1. Outline of the chapter

In the early 1990s, Manz *et al.*[18] described the Miniaturized Total Chemical-Analysis Systems (uTAS). This is now often referred to as Lab-on-a-Chip Systems (LOC) as uses extend beyond analysis. They proposed a system which takes advantage of microfluidics (Small channel dimensions) in order to achieve low sample and reagent consumption, faster analysis time and higher throughput compared to bench top equipment found in laboratories. This chapter will describe the microfluidic principles used in Lab-on-a-Chip devices (Section 2.3) and give an overview of the available techniques for the construction of LOC devices (Section 2.4) which hold the promise for creating miniaturised analytical systems. The use of LOC for environmental monitoring will also be discussed in this chapter.

2.2. What is a Lab-on-chip?

These Lab-on-a-chip devices are composed of microchannels with micrometric size (10-400 µm in cross section and volumes of pico to nanoliter) which can be created in hard (*e.g.* Glass, PMMA, PC) (See Figure 2.1) or soft (PDMS) materials using different manufacturing techniques. The reduction in scale induces many advantages over conventional systems. First of all, smaller volume will lead to smaller reagent consumption and waste. Secondly, microfluidic devices benefit from a large surface to volume ratio; useful in cases of liquid/surface interaction. This large surface to volume ratio also contributes to a high thermal diffusivity, which makes the heating and cooling of the device or liquid faster and more homogeneous making the use of these devices of interest for chemical reactions (*e.g.* Polymerase chain reaction). Thirdly, laminar flow (Low Reynolds number) is prevalent in microfluidic channels, and this phenomenon is exploited for various applications. Depending on the channel designs, chemical gradient generation [19, 20], *in-situ* micro fabrication [21], flow focusing or passive mixing [22] can be achieved.

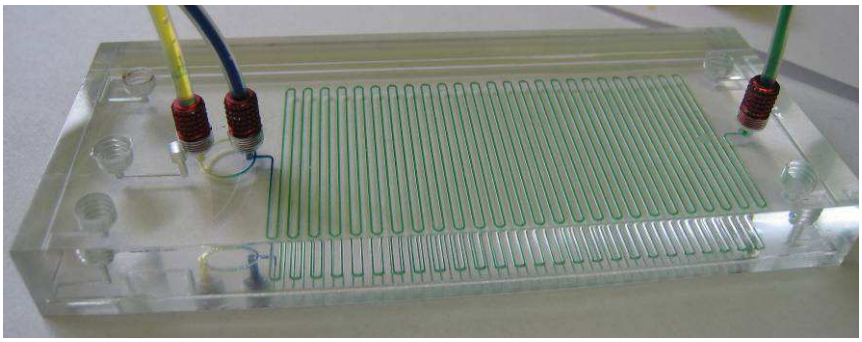

Figure 2.1: Example of microfluidic chip with a diffusive mixer

The multidisciplinary field of LOC research has received much attention over the past twenty years and many of these benefits have been demonstrated. Review articles summarizing work performed in the area of microfluidic chips have been published [23, 24].

2.3. Microfluidic principles

Since Manz *et al.* introduced the concept of the uTAS [18], researchers have tried to apply miniaturisation to the standard techniques used in chemical analysis. The principal constituting stages of a LOC are a sample introduction stage (Solid phase extraction, filtering, electrodialisys, *etc.*), sample treatment stage (Reagent mixing, separation, *etc.*) and a detection stage (Spectrophotometric, electrochemical, *etc.*).
Theses stages can be built using microfluidic features such as micro-reservoirs (Reagent and waste storage), inlet/outlet (Fluidic interface to the outside world), electrodes (EOF, electrophoresis, *etc.*), micro channels (Fluid transport, mixing, reaction with surface coating, *etc.*), micro-valves (Flow switching and pumping, *etc.*). Some of these microfluidic functions will be presented in more detail in the following sections.

2.3.1. Pumping

Microfluidics generally involves the use of one or more liquid phases (Reagents, wash buffer, sample, *etc.*) which need to be transported through the microfluidic system

from the inlet to the outlet. Two mains flow movement techniques are used for such purpose, electroosmotic flow (EOF) and hydrodynamic flow (HDF).

2.3.1.1. Electroosmotic flow

Electroosmotic flow (EOF) is an electrokinetic effect which can be used to move liquid without the need of moving parts like pumps, but by using an electric field. This phenomenon can be observed in systems when an electric field is applied to the liquid which is in contact with a charged surface (Fused silica, Oxidized PDMS, *etc.*). An area called the double layer exists at the interface between the boundaries of two phases and can be described by Stern's model. This double layer is composed of a rigid layer and a diffuse layer which will move toward the electrode of opposite charge, inducing a bulk flow. In the case of fused silica, the surface will be composed of silanol groups (Si-OH) which are negatively charged and the counterions from the water of the solution contained inside are positively charged. Ultimately, this diffusive layer will migrate toward the negative electrode (Cathode) dragging the main flow with it (Figure 2.2).

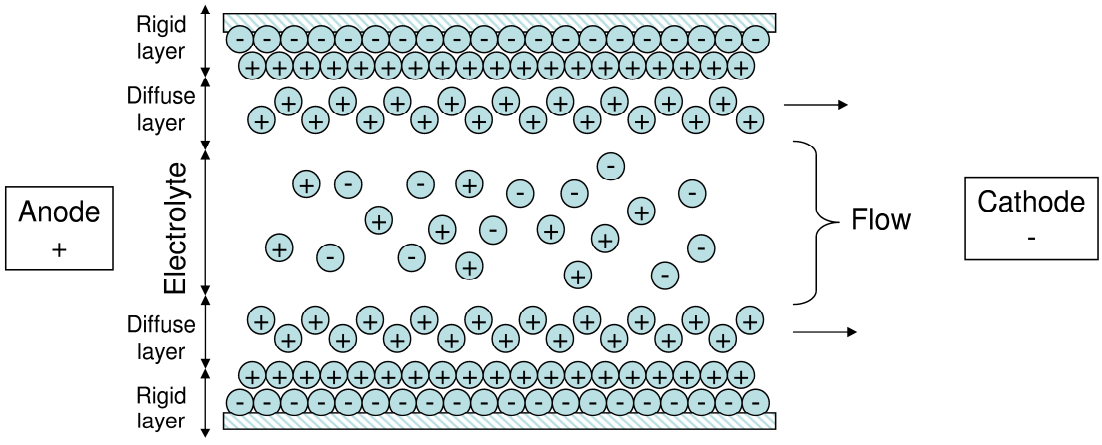

Figure 2.2: Electroosmotic flow principle

The electroosmotic mobility (Constant linking the electroosmotic velocity to the electric field strength) depends on numerous factors (Ionic strength, pH, viscosity, permittivity of the medium, surface characteristics, *etc.*) which can be changed in order to manipulate the EOF. Using surface modification (Coating, *etc.*) or an electrolyte additive (Cationic surfactants, *etc.*) EOF mobility can be increased,

decreased or even reversed. When using these modifications, particular attention must be given to stability and reproducibility as the resulting EOF may vary with time (*e.g.* Useful lifetime of 3h for oxidized PDMS [25]). Competitive hydrodynamic flow (Actions from external pressure exerted to the liquid) should also be avoided as it has the potential to counteract the EOF. This can be done by making sure that all inlets / outlets are at an even pressure.

2.3.1.2. Hydrodynamic flow

In hydrodynamic flow, a difference in pressure between two points (Inlet and outlet) is used. This difference of pressure can be created by numerous means, from the low hydrostatic pressure (When the liquid is at rest, generally with a height difference between the inlet and outlet) to the high pressure difference possible with an HPLC pump (Used for flow experiments in Section 5.3).

Between these two extremes (Pumpless and bulky bench equipment), lie micropumps which can be external modules but can also be integrated directly inside the microfluidic chip. Small external pumps are often membranes driven with piezoelectric actuation. They can achieve good flow rate but are limited by the usable back pressure. Bartels mikrotechnik, Tagasako or Kikuchi metal Micro Pump (MMP) are examples of the manufacturers of such micropumps.

Different designs of integrated micropumps (Active pumping) exist and they use different means of actuation. Some integrated designs use a combination of piezoelectrically actuated membrane and check valve [26], like the commercially available ones, or mimic the principle of the peristaltic pumps where the successive closure of valves creates peristalsis.

Passive pumping also exists, no moving parts or external actuator are needed and it relies mainly on capillary forces. This type of pumping is useful for single use, low cost point-of-care products. For example, electrochemical detection of bio molecules with the use of few electronics components (OEM potentiostat, UART-USB interface) and a mobile phone (To provide power and GUI) has been presented as a possible diagnostic platform [27].

2.3.1.3. Comparison between Electroosmotic and Hydrodynamic flow

The main advantages of using electroosmotic as opposed to hydrodynamic pumping are the absence of pulsation and backpressure which normally occur when using a mechanical pump. The flow profile is also different compared to using hydrodynamic flow, which has a parabolic shape (Maximum speed in the centre, null at the channel wall) whereas EOF has a fairly flat profile across the whole channel, ideal for forming narrow peaks in electrophoresis.

2.3.2. Flow switching

Flow switching is the action of controlling the path of the fluid flow using valves. These valves can be actuated in different manners: mechanically by the use of solenoids [28] which is not generally suitable for miniaturisation; Pneumatically, often referred as Quake valves [29], use a flexible membrane which can deflect under pressure and thus block the channel they are on top (or bottom) of. Other valve designs exist, using the same principle.

Another type of actuation is phase change actuation which uses hydrogel [30, 31] or paraffin. The shrinking or swelling of the hydrogel in a microfluidic channel can be controlled by a wide range of stimulus (Temperature, pH change, electromagnetic wave, *etc.*). However their response time is slow compared to the other valves, hence the use of such valves in system where the switching delay is not critical. Paraffin wax (and other wax) valves will respond to temperature stimulus and have a faster response time than hydrogel ones. As demonstrated in a Lab-on-a-disc experiment, in which a laser irradiation can be use to close or open ferrowax valves [32].

Flow deflection is also a way of switching the flow in microfluidics, and can be done using different technique. Bifucation, Lateral displacement, Repulsion array to name a few, have been reviewed by Pamme [33].

In electrophoresis, the sample injection step can be considered as an electrokinetic flow switching [34], the sample plug is created by combinations of voltage changes at the different reservoir to switch part of the sample to the separation channel while the rest is going to a waste reservoir.

2.3.3. Mixing

Due to the laminar flow usually present in the microfluidic channels, mixing of different species along a channel is a slow (Diffusive) process in comparison with turbulent flow. Therefore mixing techniques adapted to microfluidics have been developed and can be classified as either passive or active.

2.3.3.1. Passive mixing

In the passive technique, the main principles used are molecular diffusion and chaotic advection. Using the molecular diffusion technique, the mixing is enhanced by maximising the contact area between the species. This contact area can be increase by using a multitude of channels and reassociating them together to create multiple streams (Also called multi-laminating flow). This process has been demonstrated by Bessoth *et al.* where 95% of the mixing was done after 15ms [35] using 2x16 streams. The Split-and-Recombine flow technique (SAR) is similar to multi-laminating flow but only uses two channels to split and recombine the flow to create the multi-lamination [36].

Chaotic advection, on the other hand, tends to favour recirculation and turbulent like behaviour. It is implemented by creating different features of various complexities (Groove, pillars, 3-D serpentine, *etc.*) inside the channel. For example, Beebe's group created a 3D serpentine mixer which they compared against a 2D serpentine mixer and a straight channel. At a Reynolds number of 70, they announced a mixing difference between the straight channel and the 3D serpentine of 16 times. The difference between the 3D and 2D serpentine was however only 1.6 times [37]. The usage of this mixer is therefore restricted to $Re > 50$ in order to increase the complexity of the flow and it efficiency. Another common feature is the staggered herringbone mixer (SHM) developed by Stroock *et al.*[38] who created microstructures at the bottom of the channel. Compared to a straight channel at low Reynolds number ($Re < 1$), the SHM can achieve the same mixing while decreasing the channel length needed by a factor 100.

A particular passive mixer has also been simulated to work with EOF using heterogeneous surface charges to create recirculation. In addition, the heterogeneous

surfaces were placed on blocks inside the channel to improve the mixing. The heterogeneous blocks with a zeta potential of +75mV were able to improve the mixing from 41% to 91% [39].

2.3.3.2. Active mixing

Active mixer uses external energy to stir and mix the fluid (Acoustic waves, piezoelectric membranes, electrokinetic instability, pulsed flow, *etc.*). Liu *et al.* [40] developed a bubble-induced acoustic mixer which uses air pockets to create circulatory flow in the presence of sound wave. They were able to micromachine the chamber in such a way that they have the desired bubble distribution and size, which is critical in the mixing efficiency, by avoiding fluid stagnation. Comparison in efficiency of capturing E.Colli K12 bacteria against standard centrifuge mixing and diffusion showed a 73% capture rate for the active mixing while standard mixing achieved 91% and diffusion only 2% during the same period of time (30 min). Furthermore, acoustic mixing didn't cause cell lysis nor sample heating, which is ideal for biological analysis. Similar method have been used in channel by Ahmed *et al.* [41] where bubbles trapped in the sidewall groove excited at their resonance frequency achieved recirculation by the same acoustic streaming phenomenon.
Mixers using fluctuating electric fields for mixing have also been investigated intensively (Electrokinetic instability [42], electrohydrodynamic mixing [43], *etc.*). AC and DC electric fields applied to various electrode patterns (Simple electrode, array, asymmetric serpentine, *etc.*) can be used to stretch then fold the liquid to achieve rapid mixing.

2.4. Manufacturing techniques

The manufacturing techniques used in the field of microfluidics originated from microelectronics and MEMS manufacture where they are commonly used for the micromachining of silicon wafers. Micromachining methods are substrate dependent. In the case of glass like materials (Pyrex glass, fused silica, *etc.*), the common technique used to create micro channel uses the following steps.

First, the substrate is spin coated with a photoresist resin (Negative or positive) prior to UV exposure, generally at a wavelength of around 365 nm (I-line) generated by a mercury lamp. The UV radiation passes through a photolithographic mask, ideally placed as close as possible to the photoresist, which contains the desired pattern. Then the exposed photoresist is baked then developed, which will dissolve part of the photoresist (The exposed one for a positive photoresist, the non exposed one for a negative photoresist). Commonly the substrate is wet etched with hydrofluoric acid (HF). Some additives can be used to enhance the etching rate and selectivity (HNO_3, NH_4F, *etc.*). The composition of the etching bath, the temperature and the material determine the etching rate. This technique is normally used for shallow etching, less than 50 µm. Deeper glass etching is possible but requires more cumbersome methods like Deep reactive-ion etching (DRIE). The technique previously described is called photolithography. Finally, access holes can be created using diamond–bit drilling or CO_2 laser drilling, then the substrate can be thermally bonded in order to close the created micro channel.

The following part will concentrate on polymeric chips and thus give a more detailed description of the employed micromachining techniques. These techniques usually use a master or mould which can be created using the photolithography technique described previously.

2.4.1. Micro patterning techniques

2.4.1.1. Elastomer casting

The casting of elastomers for the fabrication of microchips is now a widespread technique in academia as it does not require complicated manufacturing processes, is low cost and may be applied to materials with desirable properties. Elastomer casting for prototyping of microfluidic devices for capillary electrophoresis was first introduce by Effenhauser *et al.* [44] and Duffy *et al.* [25].

The most used elastomer for casting is PDMS sometimes referred to as Sylgard® 184 which is the commercial name of the PDMS from Dow Corning®. PDMS is sold as two separate components, the base elastomer and the curing agents. The two

components are mixed with ratio of 10:1, this ratio is recommended by the manufacturer but the curing agent can be increased to obtain a harder material after curing due to a more cross-linked material (also a function of the curing temperature). After mixing, it is also recommended to degas the mixture prior to casting as air bubbles are easily trapped and will create unwanted cavities. The container with the mixed PDMS can be put under vacuum for 10 minutes to achieve a bubble free elastomer. The mixture is then poured onto the master, which will define the pattern. The overall chip thickness is mainly dependant on the volume of PDMS and the volume of the container holding the master. The curing can take place at room temperature or when faster curing time is required, a hotplate or oven can be used. After curing, the cast elastomer can be peeled off from the master, which can be eased by the use of releasing agents. For example, the surface of a silicon mould can be made more hydrophobic by salanizing the surface to help with the removal of the elastomer. The access holes for microfluidic connections and reservoirs can be punched into the cured material due to its relative low elastic modulus.

Elastomer casting is an appropriate technique when the long process time is not a problem and throughput is small. This technique provide good mould lifetime, for example a silicon mould with Teflon coated protective layer showed not visible degradation after ~100 castings [45]. Other mould materials can be used, like silicon-photoresist master (SPM) [46], polymeric master (PM) [47] or aluminium master.

Other casting materials can be use with this technique, RTV 615 from Momentive Performance Materials (formerly GE Silicones) is a silicon rubber similar from PDMS, but requires higher curing temperature and is less chemically inert. Two-part polyurethane plastic has also been used, and has the advantage of not needing the silanization of the mould surface when used with a silicone one [47]. UV-curable materials have also been used. NOA 81 from Norland, a photopolymer, have been cast in a PDMS mould [48]. Other thiol-enes based UV curable polymers have been proposed for casting, featuring off-stoichiometry ratios (Initial reagent remaining at the end of the chemical reaction) which confer on this material the ability of easy surface modification, bonding and mechanical property modification. Such features make off-stoichiometry thiol-enes polymers (OSTEmers) a very good candidate for the replacement of the PDMS for microchip prototyping [49].

The equipment needed to produce a chip from OSTEmer is minimal as it involves only a UV lamp (Preferably collimated). A hotplate also can be used to facilitate the demoulding of the casted polymer by decreasing the elastic modulus and Butyle acetate can be used to wash away the uncured OSTEmer. Carlborg's group further improved the bonding strength of the OSTEmer by adding epoxy monomers (Denomination of the new material is OSTE+) [50]. In this new material, the curing of the material is made by UV as the previous OSTEmer and can be use as such. If further bonding strength is needed, the reaction of the epoxy group and the remaining thiol with the surface to bond to can be initiated by a temperature of 70°C and 1,5-diazabicyclo[4.3.0]non-5-ene (DBN) previously added to the OSTE+ mixture [50].

2.4.1.2. Hot embossing

Hot embossing, also called compression moulding, is a fabrication method for polymer based microfluidic devices and is suitable to use when a small to medium quantity of microchips is needed. In this process, a thin polymer substrate is first heated above the materials glass transition temperature (T_g), generally between 100-175°C. A heated mould (Silicon, Electroplated silicon, PDMS, *etc.*) with the inverse of the desired feature pattern (*e.g.* Ridges and posts where channels and wells are desired in the final part) is pressed into the part, and the pressure (0.5 kN-2 kN per cm^2 [51]) is maintained over sufficient time for the material to deform around and replicate the mould features. The embossing pressure is maintained while the part and mould are cooled to the demoulding temperature, whereupon the part is separated from the mould.

The main advantage of the hot embossing technique is the relatively low cost of the tool and the fact that nearly perfect replication can be achieve with the optimisation of the embossing parameters [52]. The main parameters influencing the reproduction accuracy are the embossing temperature, pressure and hold time and are all correlated. For example, a shorter holding time can lead to improper replication as the cavities doesn't have time to be filled by the plastic, however an increase of temperature can decrease the holding time needed to obtained good replication but may yield other problems (Bubble formation, demoulding problem, *etc.*).

The choice of thermoplastics suitable for hot embossing is large, the most commonly used are PMMA and PC but other plastic have been used like cyclic-olefin copolymers (COC), cyclic-olefin polymers (COP), polystyrene (PS) and poly(ethylene terephthalate) (PET), to name a few.

Material such as photoresist can also be embossed. In this case the layer of photoresist is shaped with the help of a mould instead of been chemically altered by radiation. This process is called Nano-imprint Lithography (NIL) and have been proposed by Chou *et al.*[53] in 1996. This process is able to reach very fine resolution (25nm) and the author is confident that sub-10-nanometer resolution can be achieve with further improvement to the technique.

2.4.1.3. Injection moulding

Injection moulding is a very well established fabrication technique in the plastics industry for macroscopic objects. The injection moulding machine has three basic components: the injection unit, the mould, and the clamping system. The injection unit, also called the plasticator, prepares the plastic melt (Conversion of the plastic pellets in a melting plastic). Via the injection port, the melt is transferred into the next component that is the mould. Typical temperatures for the molten plastic range from 200°C for PMMA, 280°C for PC to 350°C for PEEK [51]. The molten plastic is injected under high pressure (60-100 MPa) into the mould, which is ideally kept under vacuum to allow for a good filling of the mould. When the moulded part is sufficiently rigid, the clamping system opens the mould and the part is ejected. As the cycle is finished, the mould is closed, ready to start another cycle.

When using injection moulding for the fabrication of microstructures, the mould is heated closer to the melting point of the polymer material to allow the plastic to fill all the small cavities before being cooled down. This extra step has the consequence of increasing the cycle time compared to the process used for large macro scale structures. Due to the phase transition of the plastic (Liquid to solid) and the large temperature difference between injection and ejection, the mould needs to be designed to take into account the effects of temperature (Shrinking of the melt, *etc.*). An extensive review has been done on micro-injection molding for microfluidic application by Attia *et al.* [54].

Applications of this technique include the fabrication of chips for use in electrophoretic separation of DNA, made out of acrylic resin [55] and for gel capillary electrophoresis chips for the separation of protein made in PMMA [56].

2.4.1.4. Milling and laser micromachining

In contrast to the replication method, milling and laser micromachining are direct machining methods which don't require any mould. For micromilling, the excess material is removed using small cutting and drilling tools (Down to 50 µm). The sizes of these tools limit the range of applications where micromilling can be used, as small complex features cannot be resolved fully with this technique. Depending on the feed rate and material to machine, high throughput can be obtained by milling. Hard materials with good thermal conductivity like aluminium, can be milled faster than polymer where heating of the plastic can lead to tool breakage. Thus lower feed rates and multiple passes are needed, increasing the machining time. Removal of the plastic can lead to an increase of surface roughness [57] which might interfere with the optical transmission or fluid flow.

Laser micromachining also called photoablation, may be used to remove polymer material by decomposition. The two mains decomposition processes occurring are photo degradation and thermal degradation [58]. In photo degradation, which occurs for UV wavelength, the polymer chains absorb enough energy to break their bonds, resulting in a smaller chain (More volatile with lower melting point). Thermal degradation is seen for every wavelength; the induced heat will melt the polymer but can also eject the polymers particles outside the targeted area thus leaving a void.

The polymer subtract can be either photoablated by moving a focused laser beam across it (Direct writing) or by a beam projected through a mask. In direct writing, the reproduction accuracy and resolution of the pattern are respectively dependant on the reproducibility of the laser positioning system and the optical system (Relative aperture, focal length, wavelength). As the intensity and number of passes can be controlled, different depths can be obtained for the same substrate. When a higher throughput is needed, the use of a mask is necessary. The feature sizes will then depend mainly of the mask quality instead of the optical system.

In laser micromachining, the source can be pulsed, especially for exciplex lasers (ArF, KrF, XeCl, *etc.*) or continuous (CO_2, *etc.*) [59]. Surface roughness of photoablated channels is higher than other methods, partly due to use of pulsed lasers which can leave a certain rippled appearance on the substrate [58], plus the addition of possible resolidified protusions from the ablated polymer.

2.4.2. Bonding techniques

After patterning of the feature onto the polymeric layer, the channels need to be enclosed by a second layer acting as a lid which may also contain features (Channel, access holes, electrodes, *etc.*). The bonding of this extra layer can be done by multiple processes which need to be chosen according to the tools available, the bond strength required, the optical properties, the size of the features and the future application of the chip were the bonding chemicals can interfere (*e.g.* Clinical applications).

The simplest sealing technique can be the use of nuts and bolts but it is inelegant and prone to leakage. Another technique is the use of adhesive between the two layers. The adhesive can be a single or double sided tape [32] which might need to be laser ablated or cut to permit access for channel or holes. The adhesive layer can also be applied by the use of a laminator. The lamination process uses a heated roller to activate the thermo-sensitive adhesive contained on the film, this process as been used in some C^4D microchips [60, 61]. Direct dispensing of glue at the interface between the two layers may lead to channel clogging thus the need for alternative glue application techniques like screen-printing [62].
The direct bonding of two thermoplastics can be done by the use of a heated press. The same principle as for hot embossing is used as the polymer is heated above it glass transition temperature (T_g) and pressed together. Careful control of the pressure needs to be maintained as channels and features can be crushed. This problem can be overcome if only one layer contains the channels. In this case, the thermoplastic used for the lid can have a lower T_g, and thus only the lid will be soften, leaving the features of the other layer intact [63]. Strong bonding strength can be obtained by this technique for temperatures lower than the glass transition with the use of surface modifications described below.

Some processes use surface modification to enhance the bonding of the two layers. One of them is the solvent bonding technique where a solvent is used to “melt” the surface of the polymer and bond the two layers irreversibly with a heated press. In the case of PMMA, ethanol [59], chloroform [57], acetonitrile or methanol form a non exhaustive list of solvents that have been used. The solvent can be applied to the surface of the thermoplastic by dipping, stamping [56] or vapour exposure [57]. This method can help reduce the surface roughness of the feature in case of micromachining with milling tools [57]. This technique is however unusable when the depth of the feature are small as a sacrificial depth is needed, it is possible to spatially restrict the solvent exposure but leaking can occurs at the unexposed areas.

UV/ozone surface treatments coupled with a hot press permit low temperature bonding (temperature lower than the T_g of the material) with bonds strength close to the ones obtained when using a press temperature above the glass transition point of the polymer tested (PMMA and COC) [64]. Corona discharge treatment is also known to improve the adhesion of polymers to other surfaces in the same way as plasma treatment does. These techniques can be, for example, coupled with the use of silane agents (APTES and GPTMS) to achieve robust and irreversible bond stronger than the techniques using only O_2 plasma or APTES [65].

The use of mechanical or electromagnetic waves to induce localised heating are referred to as welding techniques. Ultrasonic welding uses ultrasonic vibration to generate heat by friction at the interface of the two substrates. In order to obtain uniform bonding over a large surface, one of the substrates is equipped with energy directors which concentrate the ultrasonic energy, melting in seconds and thus creating the bond. Control on the molten polymer is important as it can clog the small structures present in the microfluidic chip. Only a few groups have used this technique but convincing examples of its efficiency have been published, such as a deformation free micromixer [66] or the bonding of multi layer microchip from 4 up to 12 layers [67].

The uses of electromagnetic radiation such as microwave and infrared lasers for the bonding of polymeric microfluidic chip have been achieved. However, these techniques make the fabrication of the microchip more cumbersome as microwave welding requires the deposition of metal strips and laser welding requires materials with different absorption characteristics.

2.5. A lab-on-a-chip for environmental monitoring

2.5.1. Assessment of LOC techniques for use in *in-situ* environmental monitoring

As stated in Chapter 1, a lab-on-a-chip platform for environmental monitoring has many advantages over a sample grab technique or the use of on-site monitoring with laboratory equipment.

The LOC devices are commonly made of hot-embossed poly(methyl methacrylate) (PMMA) [68-73] but other material like glass [74-76] , PDMS [61, 77], COC [78] and more recently with multiple layers of low-temperature cofired ceramics (LTCC) [79, 80] can be used. For the development of the system for laboratory testing and field test, a PDMS cast microfluidic device is the most suitable. As previously stated, microfluidic chips can be easily produced by PDMS casting with the use of a mould, and can be bonded to PDMS or glass without the use of glue or tape but with oxygen plasma. They also have the advantage of being chemically inert and also have the benefit of nonbiofouling techniques [81] useful when dealing with large surface to volume ratio and repeated environmental samples.

For small series, soft lithography is a more appropriate solution and a thermoplastic such as PMMA with a good transmission spectrum is a candidate if future implementation of optical detection is needed. COC can also be considered for soft lithography due to its high optical transparency, high chemical resistance and low water absorption. CNC milling can also be considered if the width of the channels and pattern are big enough compared to the milling cutter diameter. In the case of microchip capillary electrophoresis (MCE), the surface roughness achieved by milling may lead to erratic current or non-uniform sample flow however no significant loss in performance have been observed compared to other fabrication processes [82, 83]. If high manufacturing throughput is needed, injection moulding is the method of choice due to the fast process time. The accuracy and the finish of the plastic chip will depend mainly from the quality of the master and the setting of the injection moulding process. Injection moulded plastic chips have been used for analytical analysis of food samples [78].

Pumps and valves might be of interest when using a LOC for analytical chemistry since sample injection, buffer wash or renewal are steps which may be needed. These actuators can be external to the system using off the shelf equipment but ideally embedding these functions inside the chip will help reduce the size of the whole system. It will also help to reduce dead volume which can be problematic for microfluidic systems where the volume at play is in the range of µL or less. Integration of such features can render the manufacturing process more cumbersome and thus make more difficult the manufacturing in larger number. Associated with a mixer, valves and pump can be used to prepare solutions of know concentration which can be used as self-calibration solution in autonomous system.

In this work, elastomer casting and micromachining with CNC milling tools have been used for microfluidic prototyping (Section 4.3.3). These techniques provide an excellent repeatability between each parts and do not require extensive set up time or optimisation. Oxygen plasma as a bonding method for sealing PDMS chip is used by several research groups [41, 65, 84, 85]. This same method was used to bond a PDMS coated PCB containing the electrodes to a PDMS microfluidic chip containing the microfluidic channel with a watertight and durable bond.

2.5.2. Review of existing LOC systems for environmental monitoring

Recently, a microfluidic system for the *in-situ* monitoring of nitrite (NO_2^-) concentration within sea water using a PMMA microchip, external valves and pumps with a optical detection has been demonstrated [86]. The microchip was produced using a CNC milling machine then solvent bonded with the optical detection (LED, photodiode) attached using UV curing glue [87]. The valves and the syringe pump where located directly on top of the chip, thus minimising the dead volume which can be introduced by the use of extra fluidic tubing. Such assembly minimises the complexity of the microchip manufacturing process while keeping the footprint of the system fairly small. The housing of the system was done in a PMMA tube (160 mm OD x 300 mm) which accommodated 4x500 mL bottles (Griess Reagent, blank, standards and waste) and the control electronics and the batteries. The authors claim that this system could be improved for energy efficiency, size but also the number of

species monitored (*e.g.* Iron or pH [88]) and the monitoring frequency with the possible addition of parallel optical measurement cells. The group from the National Oceanographic Centre (NOCS) did redeploy a revised version which also included nitrate (NO_3^-) measurements in addition to the nitrite measurements [89]. They were able to collect 1872 points over 26 days, involving also the measurements of 1872 blanks and 1872 standards which is an average of 6 measurements per hour.

This microfluidic system is a great example of the possibility to monitor a chemical species autonomously and *in-situ*. Even if it is limited to only two species, it has the potential to be transposed to other colorimetric assay. Being developed for oceanic monitoring, access to the system while in operation is more restricted than for river monitoring. This could influence the design toward robustness at the expense of resolution or functionalities.

2.6. Summary of the chapter

This chapter introduced the background about microfluidics (principles and manufacture techniques). It also described an existing system used for environmental monitoring, more precisely for measuring the concentration of nitrite in sea water.

Numerous manufacturing techniques have been presented, and one method of choice for rapidly produce microchannel is elastomer casting. This will be one of the methods used by some of the papers presented in the next chapter focusing on various separation techniques and C^4D detection. This manufacturing method will also be used in Chapter 4 for one of the designs presented.

Chapter 3 : Background to separation and C^4D

3.1. Outline of the chapter

The monitoring system to be developed for the LIMPIDS project will need to separate and detect the analyte of interest; therefore background on separation and C^4D will be presented. Section 3.2 will be about the separation techniques of inorganic ions which can be used with the C^4D (Ion chromatography and electrophoresis). The next sub-chapters (3.3, 3.4 and 3.5) will give a deeper understanding of C^4D detection, starting with a brief introduction and an overview of the electrical model of the system. This complex system responds differently depending on the frequency used, the conductivity of the electrolyte inside the capillary and the electrode configuration. Having a model can help us understand the experimental results we obtain with different frequencies and electrolyte concentrations. Next, in Section 3.6, descriptions of the different electrode designs will underline the difficulties in integrating such detection and the problems encountered for the two main designs (On-capillary and on-chip) considered in this work. The measurement electronics is also an important part of the system and details will be given in Section 3.7. The final sub sections (3.8 and 3.9) will present the past and future applications using this detection technique for inorganic ions. Tables comparing the different separation systems provide an overview of the evolution in the number of species detected and their limit of detection (LOD).

3.2. Ion separation

The system developed by the University of Hull needs to be able to extract the species of interest but must also separate them in order to know the variation of the concentration of the different species. Initially the method of separation chosen for the project was based on porous monolithic silica columns. More details can be found in

the next section which will explain why the change toward capillary electrophoresis has been made.

3.2.1. Monolithic column for ion chromatography

3.2.1.1. Principles

Monolithic column are continuous porous separation media generally made either of organic polymer or silica and used for liquid chromatography. These monoliths can be prepared for different types of separation principle (reverse-phase [90], ion exchange [91-94]) using surface modifications. The major advantages of monolithic silica columns, as compared to particle - packed columns used in a microscale system, are the fast separation, short analysis time, and the low column pressure drop [95]. Inorganic porous materials also exhibit advantages over polymeric substitutes: higher mechanical strength, higher thermal stability and higher chemical durability [90]. Such monolithic columns already exist as a commercial product from Merck (Chromolith®) and Phenomenex (Onyx™). Concerning the pH stability of monolith columns, silica-based ones cannot be used over a pH range as extended as the organic monolith [96, 97], especially in the basic region (over pH 8) where the silica dissolves due to silica backbone hydrolysis [92]. However organic monolith can still shrink or swell due to pH changes [95].

In ion exchange columns, electrostatic interactions between the analyte and the ion-exchange group bonded to the stationary monolithic phase of opposite charge cause the analyte to adsorb onto the stationary phase. When the ion-exchange group carries a negative charge, the stationary phase is classified as a cation-exchange material. Reciprocally, the stationary phase is classified as an anion-exchange material when it has a positively charged ion-exchange group. Anion separation can be achieved by the use of surface modification of the stationary phase with cationic surfactants such as DDAB [92], long chained zwitterionic carboxybetaine-type surfactants [93], lysine [94] or latex particles [91]. Separation of cations from rainwater has been achieved by coating lithium dodecylsulfate to an octadecyl-boned silica monolith [98].

To be used as a flow through column, the separation media must be encased using a process called cladding. This ensures that the mobile phase does not flow around the stationary phase but through. PTFE heat shrink or PEEK resin can be used for the cladding [99]. *In-situ* preparation can also be used which negates the additional cladding step and is of interest when the monolithic column needs to be implemented in a LOC.

3.2.1.2. Implementation in microchip

The main preparation methods of monolith systems are the sol-gel or particles fixed techniques [100]. However, not all monolith preparation techniques are compatible with microchip implementation, especially in polymer microchips. The heat treatment step in some sol-gel techniques require high temperatures [90, 101] and will not be compatible with polymer chips, the porogenic mixture also needs to be compatible with the channel material. Polymer based monoliths have the advantage of polymerising at lower temperatures [102] or using a photoinitiator for the polymerisation which permits spatial control of the monoliths. Some techniques involve the grafting of the monolith to the polymeric microchip walls, *e.g.* COC [103, 104], PDMS [104, 105] (Figure 3.1) and polymeric tubing *e.g.* PP [103]. Direct grafting of the stationary phase has an advantage over the more conventional column design where the beads packed against a retaining frit can create bubbles or cracks under high pressure [106]. It is also important to note that the gas permeability of the material where the *in-situ* monolith is prepared needs to be low. This is due to the chemical reactions involved in both wall functionalisation and monolith polymerization being sensitive to the presence of oxygen which can inhibit these reactions [107]. Glass can also be an issue due to the exposed silanol group on the wall surface which can produce ion-exchange absorption. Such interaction may produce tailing and broadening of the analyte plug [108].

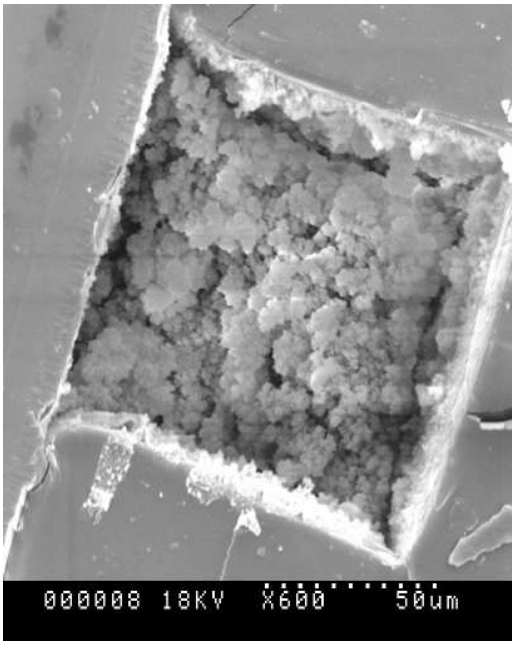

Figure 3.1: SEM of a PDMS channel (100x100 µm) filled with photoinitiated polymer monolith from [105]

3.2.1.3. Inconvenience of ion chromatography in lab-on-chip for environmental monitoring

Even though IC is still one of the methods of choice when it comes to the monitoring of inorganic ions in water, especially anions [8], some issues using a pressure driven column may arise. A pump will be required to cause the sample to flow through the column to overcome the back pressure due to the column. The use of a morphology in the monolith (large macropore) will result in a lower back pressure compared to a more packed column but may be enough to increase the risk of leakage or column damage if an excessive flow rate is used to obtain a faster cycle time. It can also be noted that contaminants may block the column more easily due to the porous structure and thus increase the back pressure.

An alternative to pressure driven flow would be to use EOF instead (Section 2.3.1.1). This alternative separation technique is called electrochromatography (CEC) [109]. The use of an electric field to drive the mobile phase results in no back pressure even with small particles, it also reduces the waste normally produced by a constant mobile phase flow. The flow profile is also advantageous with EOF compared to pressure driven, where its parabolic shape increases band broadening [109]. One of the drawbacks in using a current running through the channel is the ohmic heating (Joule

heating) produced, which requires using smaller channel to increase the surface to volume ratio and thus the heat dissipation.

The next technique presented, named capillary electrophoresis, is similar to CEC, but the difference is that no stationary phase is used. This technique can be used for fast separation of anions and cations will very high separation efficiency.

3.2.2. Capillary electrophoresis

3.2.2.1. Principles

The purpose of capillary electrophoresis (CE) is to separate analyte ions present in a mixture, to identify the different analytes, and to quantify their amount (Related as a concentration). The CE-separation mode described hereafter and illustrated in Figure 3.2 is called capillary zone electrophoresis (CZE). Other CE-separation modes exist, namely isotachophoresis (ITP), isoelectric focussing (IEF), micellar electrokinetic chromatography (MEKC) [110].

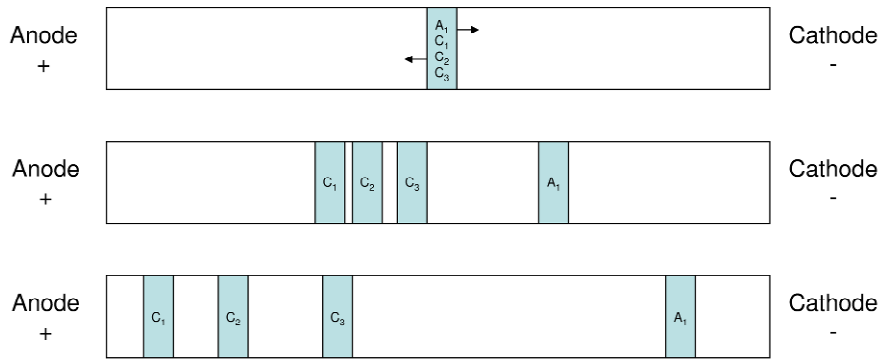

Figure 3.2: Principle of Capillary Zone Electrophoresis (CZE)

In CZE, the separation column is typically a fused silica capillary of usually ≤ 200 µm inner diameter and 375 µm outer diameter [111]. The separation capillary is filled with a carrier / background electrolyte which conducts the electric current and provides the buffering capacity. Then the sample is injected in the separation channel. To do so, sample injection can be done by either electrokinetic injection or hydrodynamic injection. For the hydrodynamic injection, the sample is moved in the

capillary by a pressure difference, using a syringe pump or different liquid level in the vials (S and B), for example (Figure 3.3A).

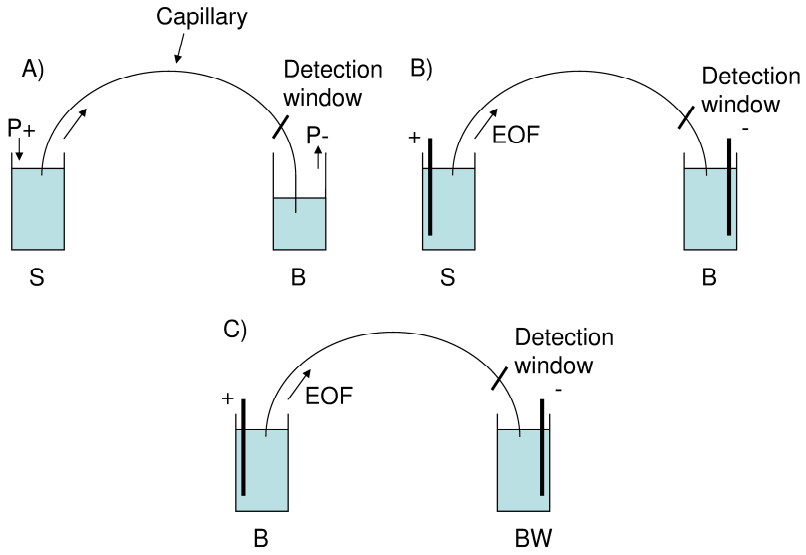

Figure 3.3: Hydrodynamic (A) and Electrokinetic (B) injection and separation (C)

In electrokinetic injection (Figure 3.3B), a potential-difference of several kV (field strength up to 500 V/cm) is applied for a short time between the sample vial (S) and the buffer / waste reservoir (B). Under the influence of the applied voltage, the analytes migrate towards the buffer reservoir due to electrophoretic and electroosmotic (EOF) movement.

The same principle as the electrokinectic injection is used for the separation (Figure 3.3C). Under the voltage applied from the buffer reservoir (B) and the buffer waste reservoir (BW), separated zones will form, each containing only one single type of analyte having the same mobility (Electrophoretic mobility). At the end of the separation capillary, a detection window measures the amount of analytes and peaks in the detection signal are observed (See Figure 3.4). The amplitude and / or area of each peak are linked to the concentration of analytes. The time at which the peak occurs is linked to the mobility of the analyte and thus its identity.

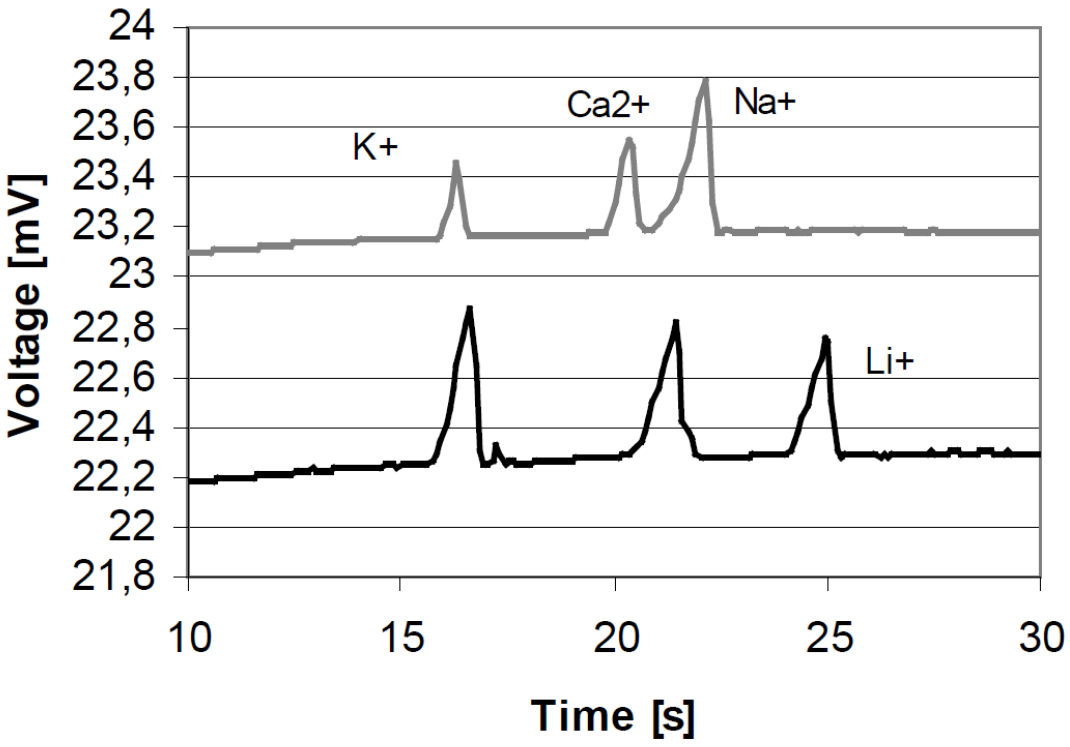

Figure 3.4: Electropherogram of cationic species from [78] – Lower curve is a 125 µM standard of K^+, Na^+, Li^+ - Upper curve is a 1:10 diluted milk sample spiked with 4.4 mM of Ca^{2+}

Different detection techniques exist (Absorbance, fluorescence, electrochemical, *etc.*) and have been used for capillary electrophoresis in accordance with the sensitivity toward the species of interest. The most commonly used ones are UV absorbance (Direct or indirect) which is the method of choice for most species. The laser-induced fluorescence (LIF) is the preferred detection technique when it comes to biomolecules. A review grouping most of the detection techniques has been done by Swinney and Bornhop [112].

3.2.2.2. Implementation in a microchip

A typical implementation of microchip capillary electrophoresis will now be described with reference to Figure 3.5. The long channel on Figure 3.5 (Named Separation channel) has two reservoirs called the “Buffer reservoir” (BR) and the “Buffer waste reservoir” (BWR). The other channel also has two reservoirs which are the “Sample reservoir” (SR) and the “Sample waste reservoir” (SWR). The traditional design of a microchip capillary electrophoresis (MCE) device consists of these channels forming a cross with a “T” junction. The main channel is used for the

separation (From BR to BWR) and the smaller intersecting one (From SR to SWR) is used to inject the sample into the separation channel. An offset between the two branches of the injection channel is used in some designs to allow a bigger sample plug to be introduced.

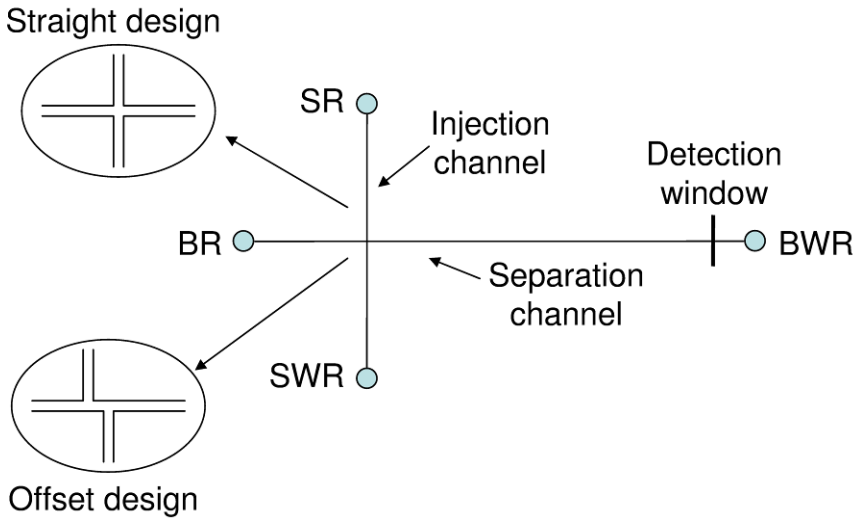

Figure 3.5: Typical MCE designs (Straight and offset injection channels variance)

The procedure for MCE is similar to than for CZE. The chip is filled with the buffer, then the sample is introduced in the associated reservoir (SR). The injection can then take place in a hydrodynamic or electrokinetic manner. Once the injection has been done, the separation can take place and the plugs of analyte can be detected through the detector's window placed at the end of the channel near the waste reservoir, giving the electropherogram. Figure 3.4 is an example of an electropherogram for cationic species obtained with a microfluidic ChipShop GmbH electrophoresis chip (03-0110-0082-01). This chip has a straight injection channel design with a channel width and depth of 50 µm and an effective separation length of 75 mm (From intersection to detection windows). The contactless conductivity detection is done with two thin gold electrodes made by sputtering and separate from the channel by a 60 µm sealing layer. The upper curve on Figure 3.4 shows the separation of 1:10 diluted milk while the lower curve is a Lithium, Sodium and Potassium standard with a concentration of 125 µM [78].

3.3. Introduction on conductivity detection

Of the available techniques, ion chromatography and electrophoresis with conductivity detection are appropriate techniques to analyse the concentration of the different species in a sample of water. Conductivity detection exists in two forms, in direct contact (also called galvanic contact) and contactless, or capacitively coupled. This review will be about the latter.

This detection method is a valid option for the detection of inorganic cations and anions, compared with well-established detection options like fluorometry or mass-spectrometry. This method is non ion-selective and can by applied to numerous designs. Furthermore, it permits development of portable instrumentation with good sensitivity and a reasonable cost [78, 113-115]. This detection technique has also been used with ion chromatography [116], which was one of the separation techniques to be considered and integrated in our device. Details of this detection technique can be found in a number of reviews and is regarded as being very important in this last decade [117-122].

Capacitively coupled contactless conductivity detection, also called CCCCD or C^4D, was originally developed for detection in isotachophoresis in 1980 [123]. The use of this technique in capillary electrophoresis (CE) was first introduced by two research groups, Fracassi da Silva and do Lago [124] from the University of São Paulo and Zemann *et al.* [125] from the University of Innsbruck. These groups were working without knowledge of each other and both published in 1998 with a quasi similar setup. Both approaches used two electrodes, one (Actuator) connected to a signal generator in order to feed the signal, by capacitive coupling, to the liquid through the fused silicate with polyimide coating capillary wall. The second electrode (Pick up) is used to retrieve the resulting current; a function of the total impedance of the system. The electronic circuits used were inexpensive, which provided a low cost measurement system.

3.4. Electrode models for C^4D

C^4D detection uses conductive electrodes around the channel where the species of interest flow. This arrangement is often called conductivity cell, detection cell or measurement cell. The electrical model of the cell will be first used to describe a system formed using two electrodes. By the nature of the model, its behaviour will vary with frequency and physical and chemical parameters (Value of the stray capacitance, electrolyte concentration, *etc.*). To finish, an existing method to overcome some of the typical system limitations will be explained in more detail.

3.4.1. Electrode / Electrolyte coupling and stray capacitance

A typical cell design contains two electrodes as show in Figure 3.6.

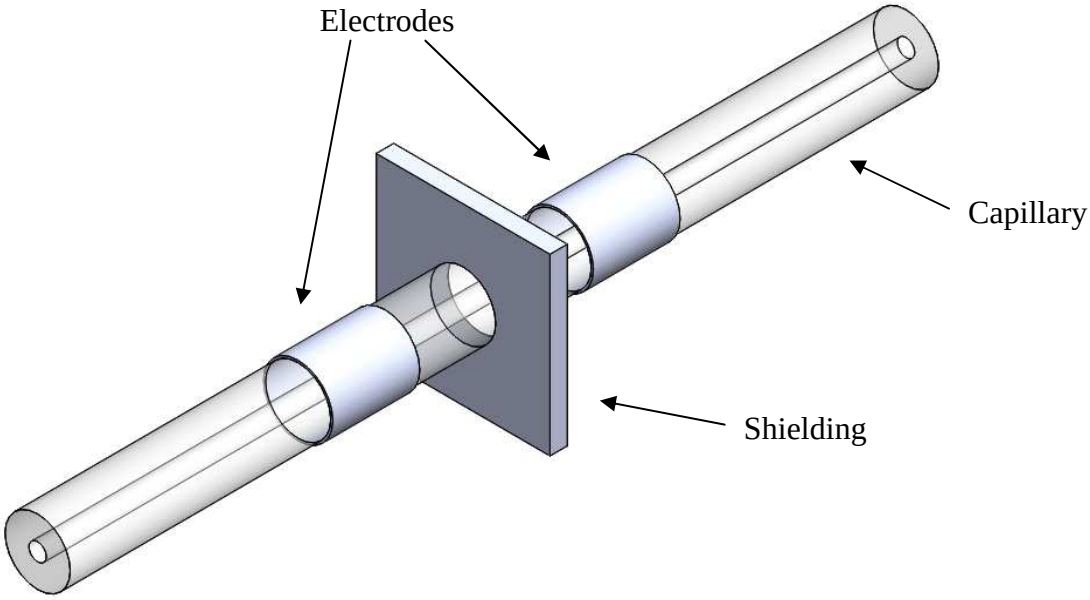

Figure 3.6: Typical axial capillary arrangement with two electrodes and shield plane

The term capacitive in C^4D refers to the link between the electrode and the solution through the wall of the channel. One of the most widely used electrical models to describe and simulate this cell is composed of two capacitors (C_W and C_S) and a resistor (R), as shown in Figure 3.7. This model was first proposed by da Silva and do Lago [124] along with another detailed model taking into account the polyimide coating, the resistance of the capillary and the double-layer capacitance. Other

detailed models also exist and introduce the shielding and improved spatial resolution along the capillary [126-128] or the capacitance of the bulk solution [129].

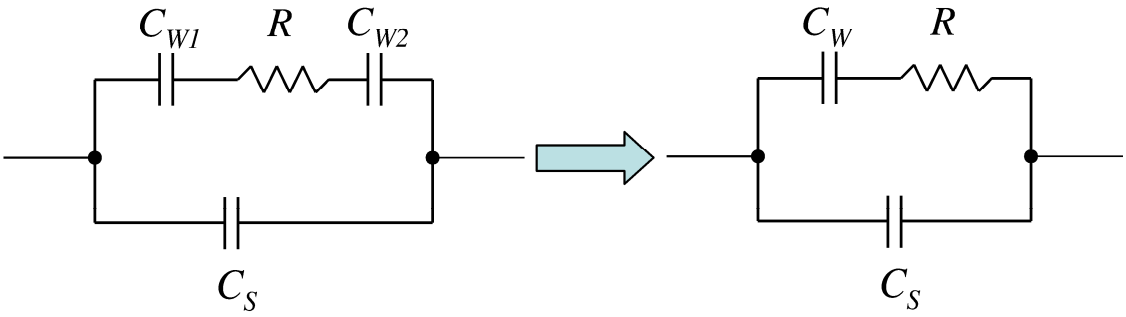

Figure 3.7: Equivalent circuit of the cell

The capacitor C_W is the total capacitance of the capacitive contact between the electrodes and the solution (which resistance R). The parasitic capacitor C_S is the leakage capacitance which can exist between the two electrodes, also called stray capacitance. Some equivalent circuits do not include C_S due to the introduction of a ground plane (Faraday shield) between the two electrodes [130]. Nonetheless, Brito-Neto *et al.* [131] pointed out that the introduction of the ground plane still creates a stray capacitance, along with two stray capacitances to the ground. These capacitances to ground can be problematic in the case of the sensing electrode, because a small part of the current to be measured will leak to ground and not be converted into voltage.

This link between the electrode and the solution through the wall of the channel can be modelled as a capacitor, which in the case of a capillary is a cylindrical capacitor. The cell capacitance can be in this case theoretically estimated by the known formula of a cylindrical capacitor [132]:

$$C = \frac{2\pi.\varepsilon_0.\varepsilon_r.l}{\ln\left(\frac{D}{r}\right)} \tag{3.1}$$

Where C is the cell capacitance in Farads, ε_0 is the relative permittivity of vacuum ($8.854187.10^{-12}$ $F.m^{-1}$), ε_r is the relative permittivity of the capillary wall, *l* is the length of the electrode in meters, *D* is the outer diameter of the capillary in meters and

r the inner diameter in meters. For example, a fused silica capillary (ε_r = 3.75) of 1000 µm O.D. (Outer diameter) and 500 µm I.D. (Inner diameter) with 10mm long electrode have a capacitance of 3.01 pF.

The equivalent circuit of the cell in Figure 3.8 has the frequency response of a high pass filter without the stray capacitance (C_s). The modulus of the cell impedance is:

$$\frac{V_{IN}}{i} = |Z_{CELL}| = \left| \frac{1 + j\omega.C_W.R}{j\omega.C_W} \right| \tag{3.2}$$

The corresponding bode plot is shown is Figure 3.8 with V_{IN}=5 V, C_W=1.505 pF (C_{W1} and C_{W2} in series give C_W) and R=3 MΩ:

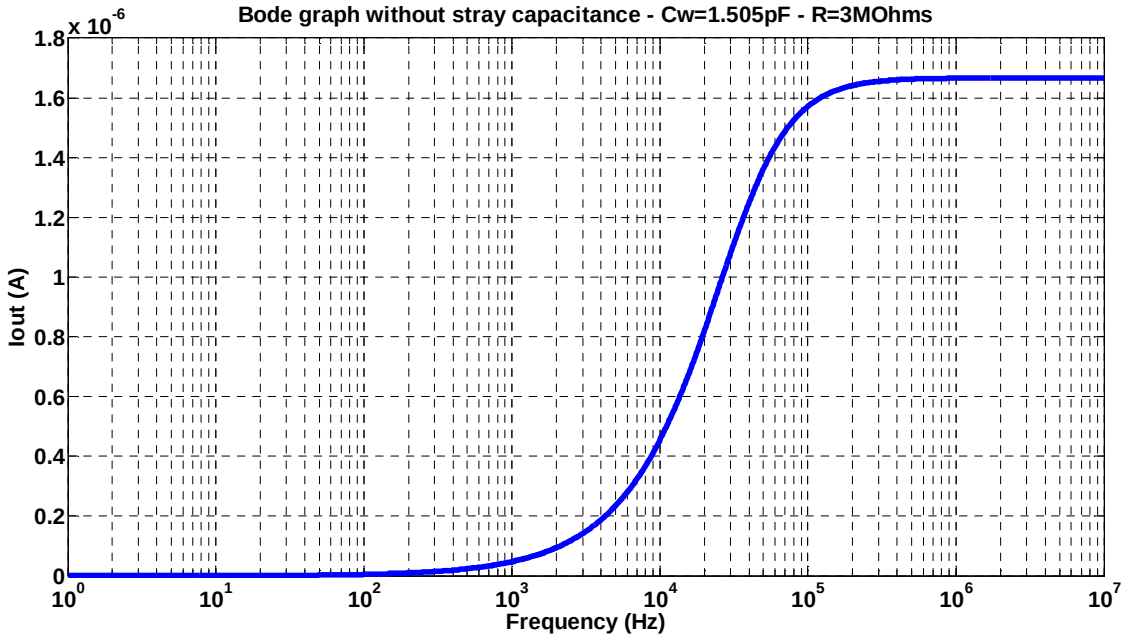

Figure 3.8: Bode plot of the cell without stray capacitance

With the introduction of the stray capacitance, the response and the modulus of the impedance changes:

$$|Z_{CELL+Cs}| = \left| \frac{1 + j\omega.C_W.R}{j\omega.C_W + j\omega.C_S - \omega^2.C_W.C_S.R} \right| \tag{3.3}$$

The corresponding Bode plot with C_S=0.212 pF (Derived from COMSOL simulation with an electrode gap of 1mm – See appendix C and D) is shown in Figure 3.9:

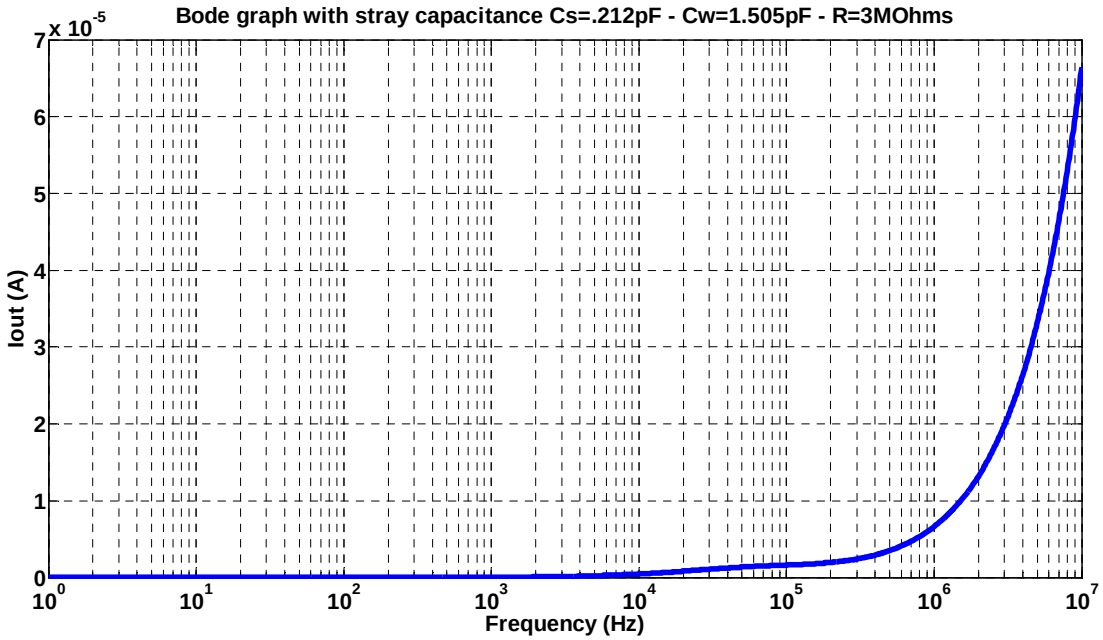

Figure 3.9: Bode plot of the cell with stray capacitance Cs=0.212 pF

A sensitivity analysis of the bode plot regarding the stray capacitance (C_S) can be useful to see the contribution of this parameter as a function of the frequency.

$$S_{Cs}^{Ycell} = \frac{Cs}{Ycell}\frac{\partial Ycell}{\partial Cs} \tag{3.4}$$

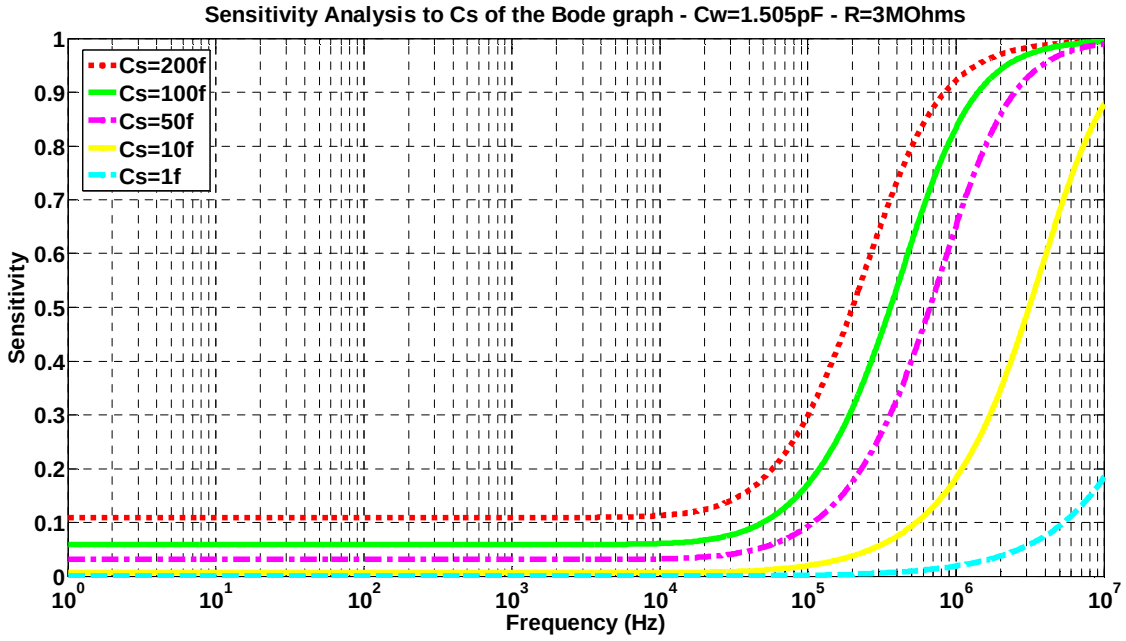

Figure 3.10: Sensitivity analysis of the cell impedance versus the stray capacitance

The plot of Eq. 3.4 (Figure 3.10) shows that the stray capacitance does not have significant influence on the impedance of the system until 100 kHz. Above this frequency, the stray capacitance creates a decrease of the impedance (Causing an increase in current (Iout)). Ideally the measurement must be done in the bandwidth of the plateau seen on Figure 3.9 (8.10^4 to 3.10^5 Hz). Over this optimum range, the impedance of the coupling between the electrode and the liquid is negligible compared to the impedance of the liquid, thus a fairly constant impedance occurs in this frequency region. The frequency is high enough to allow the current to flow through the cell, but not high enough to flow through the stray capacitance. Then at higher frequencies, the stray capacitance takes over and the total impedance becomes gradually a function of the stray capacitance.

The stray capacitance must be relatively small in order to have this plateau in the response plot (Figure 3.9), in case of a large stray capacitance; the plot would follow an exponential function. For this reason it is important to characterise the cell by doing a plot of the cell response versus the frequency to find the best operating frequency before commencing quantitative measurements. At lower frequencies, the coupling with the liquid will not be enough to have a good sensitivity. But at higher frequencies, stray capacitance will bypass more current, again reducing sensitivity.

3.4.2. Electrolyte conductivity

The conductivity of the electrolyte is also an important factor as the behaviour of the cell is different between the low and high conductivities (Figure 3.11).

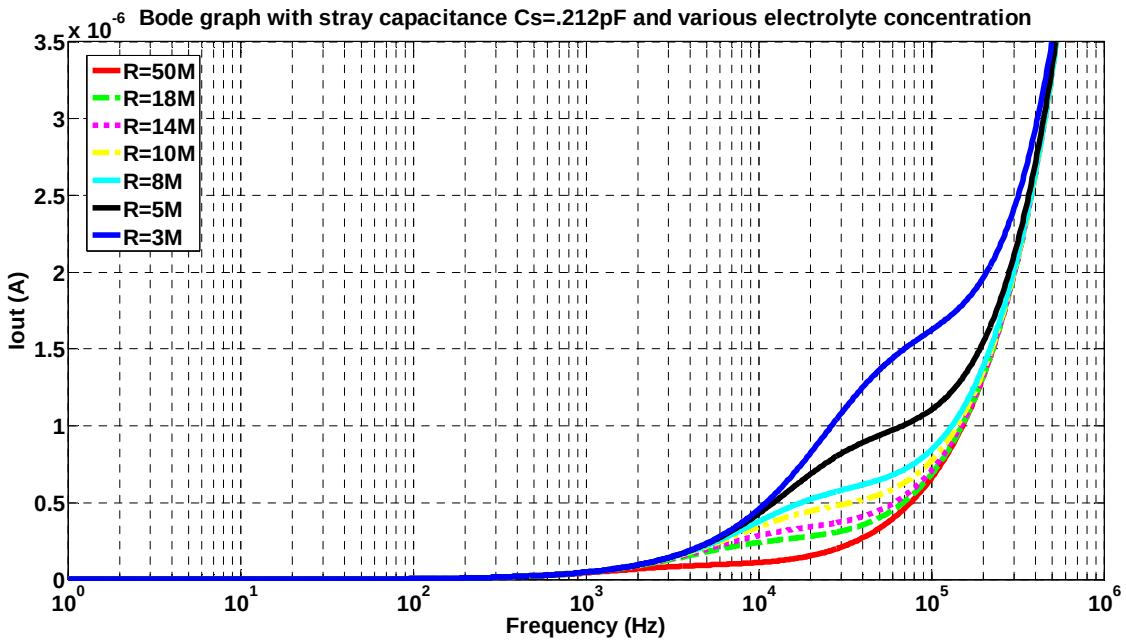

Figure 3.11: Bode plot of the cell with stray capacitance Cs=0.212 pF at various concentration

In this plot we can see that for higher conductivity electrolyte, the plateau becomes smaller and is shifted towards higher frequencies. This phenomenon can be explained by the fact that at a given frequency, the coupling capacitor C_W is less negligible for high concentration electrolytes (Higher conductivity / low resistance). Higher frequencies are required to achieve a coupling impedance significantly smaller than the electrolyte impedance. The same phenomenon is easier to spot in Figure 3.12 which plots the evolution of the current in function of the equivalent liquid conductance ($3.3.10^{-7}$S - 7.10^{-6} S equivalent to 150 kΩ - 3 MΩ) at various frequencies (50, 100, 200, 250 kHz). It can be observed that with an increase in conductance (decrease in resistance), the signal tends to reach an asymptote which is inherent in the cell. The frequency also has an effect on this asymptote, where higher frequencies tend toward an asymptote for higher conductance.

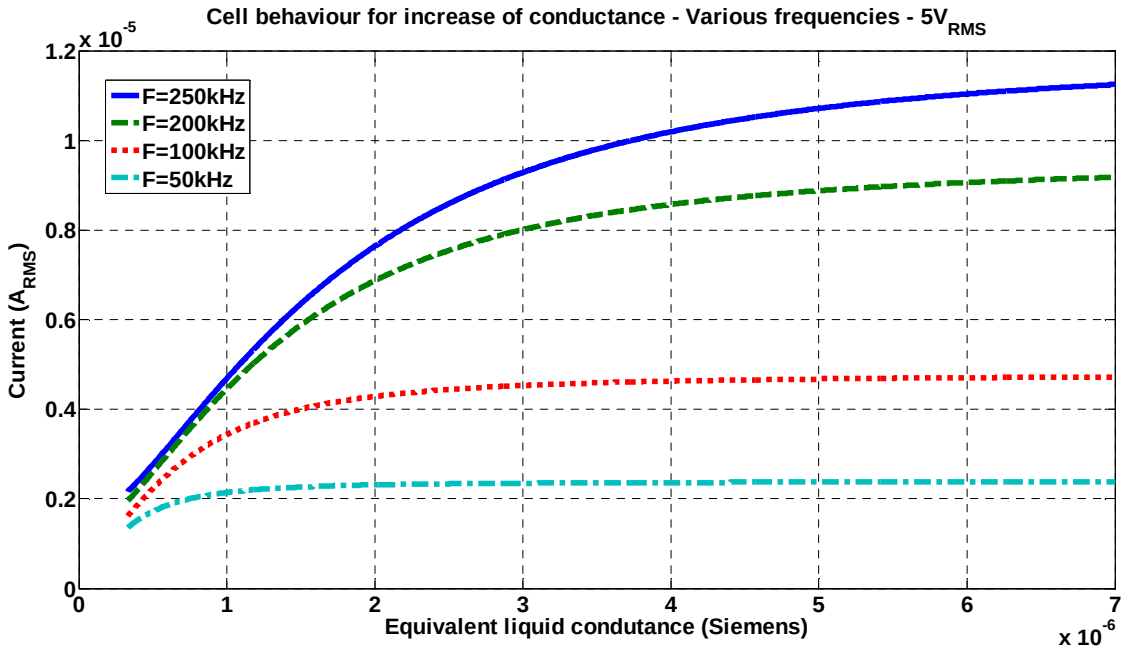

Figure 3.12: Plot of the cell behaviour with stray capacitance Cs=0.212 pF at various frequencies

3.5. Introduction of additional complex element in the model

The sensitivity of the cell to electrolyte conductance may be improved by adding a positive reactance in the system [130, 133-136]. In the case of Shih *et al.* [134], they added an inductance in parallel with the system. The difficulty was that the resonance frequency was difficult to calculate and dependant on the conductivity of the solution. The group of Huang *et al.* [130] added an inductance in series with a larger system (3.2 mm O.D. and 1.8 mm I.D.) which gave them a resonance frequency only dependant of the inductance and the capacitance of the electrode. In this system, the stray capacitance is neglected due to the addition of a new shield configuration on each electrode (Figure 3.13 and Figure 3.14).

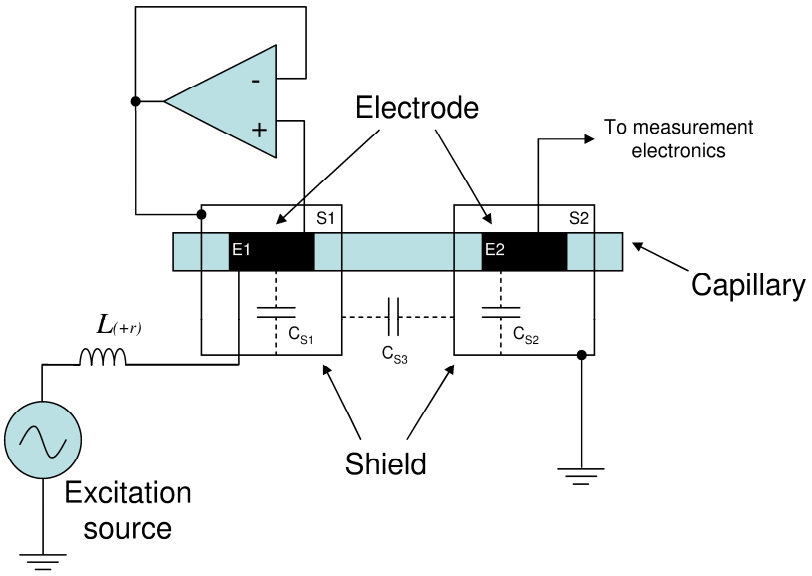

Figure 3.13: New shielding arrangement from [130]

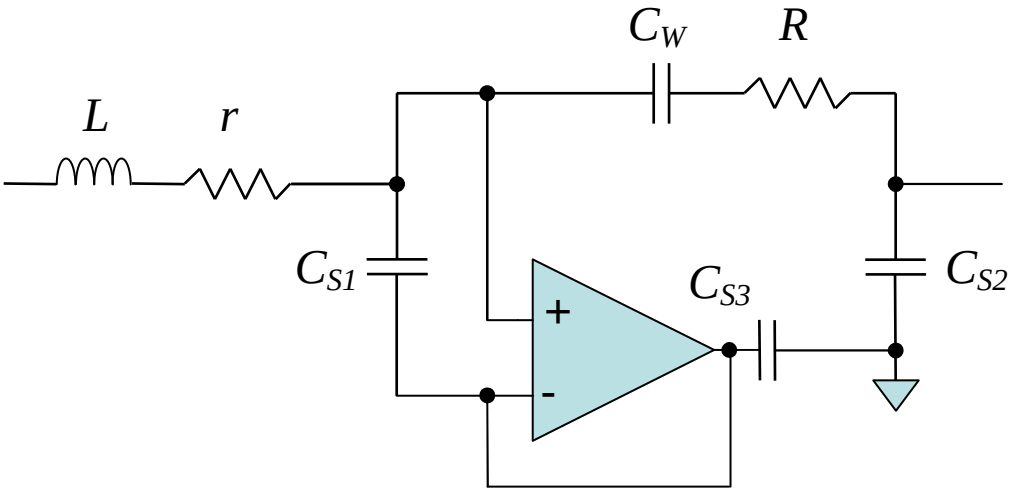

Figure 3.14: Electrode model with external coil and new shielding arrangement from [130]

The inductance is represented by *L* and *r*, the capacitive coupling between the electrode and the shield is represented by the capacitor C_{S1} and C_{S2}, coupling between the two shields is represented by C_{S3}. As stated in their paper, C_{S1}, C_{S2} and C_{S3} can be neglected in the model as they are not contributing to the detection path. The introduction of a voltage follower between the shielding *S1* and the electrode *E1* avoid the coupling between *E1* and *S1* (C_{S1}) as they are at the same potential. The coupling between *S1* and *S2* (C_{S3}) does not influence the conductivity detection as it is not in the path of the current picked up by the electrode *E2*. They also state that the coupling between the electrode *E2* and the shield *S2* (C_{S2}) does not influence the conductivity

detection as it is coupling the inverting input of the operational amplifier which is at a virtual ground state to the real ground.

The total impedance of the circuit can be described by Eq. (3.5)

$$Z = (j\omega L) + r + \left(\frac{1}{j\omega C_w}\right) + R = (R + r) + j\left(\omega L - \frac{1}{\omega C_w}\right) \tag{3.5}$$

Thus if the frequency is set for the resonance, only the non complex terms remains and the total impedance is a function of the electrolyte conductivity if the internal resistance of the inductor *r* is assumed to be negligible.

They found that the detection range is greatly expanded at higher concentrations and also achieved a lower limit of detection (LOD), with similar sensitivity compared to Gillespie's work [137] and a commercial detector (TraceDec C^4D). This system was then later used to identify the flow pattern of five Gas-Liquid two-phase flow (Stratified, wavy, bubbly, slug and annular) using a support vector machine (SVM) for the identification [138]. The glass tube used had an inner and outer diameter of respectively 2.8 mm and 5.0 mm. Identification accuracy between 88.5 % and 92.9 % has been reported for the different flow patterns. In their latest paper, they succeeded in implementing the conductivity measurement for a larger capillary of 7.8mm I.D and 10.0 mm O.D [136].

The group of Kang *et al.* [133] proposed a low-impedance capacitively coupled contactless conductivity detector (LIC^4D) which is a C^4D with a piezoelectric quartz crystal (PQC) in series. The PQC can reduce the total impedance of the cell when operated between its series and parallel resonance frequencies. They obtained a good SNR compared to existing systems. However, the generation of operating frequency must be very stable. The authors state that the frequency should deviate from less than 1 ppm due to the PQC behaviour at this frequency (Rapid rise of the reactance). Later, the same group used this system with a capillary for the detection of inorganic cations after separation with a monolithic column [135].

3.6. Electrode design

Generally, there are two types of cell design. The classical one introduced by da Silva and do Lago [124] and Zemann *et al.* [125], is on-capillary, with an axial arrangement as shown in Figure 3.6 and is still used. More recent designs are related to microfluidic chips and have a different design of the detector. Due to the chip configuration, the electrodes must be planar instead of cylindrical. Tuma *et al.* [139, 140] were the first to state that the electrodes don't have to be cylindrical. With a semi-tubular electrode configuration, they have seen no significant change in the detector behaviour and its parameters. It was not long until other groups started thinking about using this contactless detection on-chip and considering new designs.

Transferring the original design to lab on-chip format was a difficult task, but Guijt *et al.* developed a design with planar electrodes buried across each side of the channel [141]. This was a direct coupled system but was the prequel of a similar design by Lichtenberg *et al.* [142] which used the channel width as the detection volume because the electrodes were within and parallel to the channel (Figure 3.15). This produces a great dependency between the sensitivity and the channel dimension, which requires advanced micro-fabrication technique to control on such a scale (50 µm channel width and 10 µm glass insulating wall). This design was a first step to the design which appears later in the paper of Pumera *et al.* [70] and Wang *et al.* [71]. This design is now commonly used in C^4D.

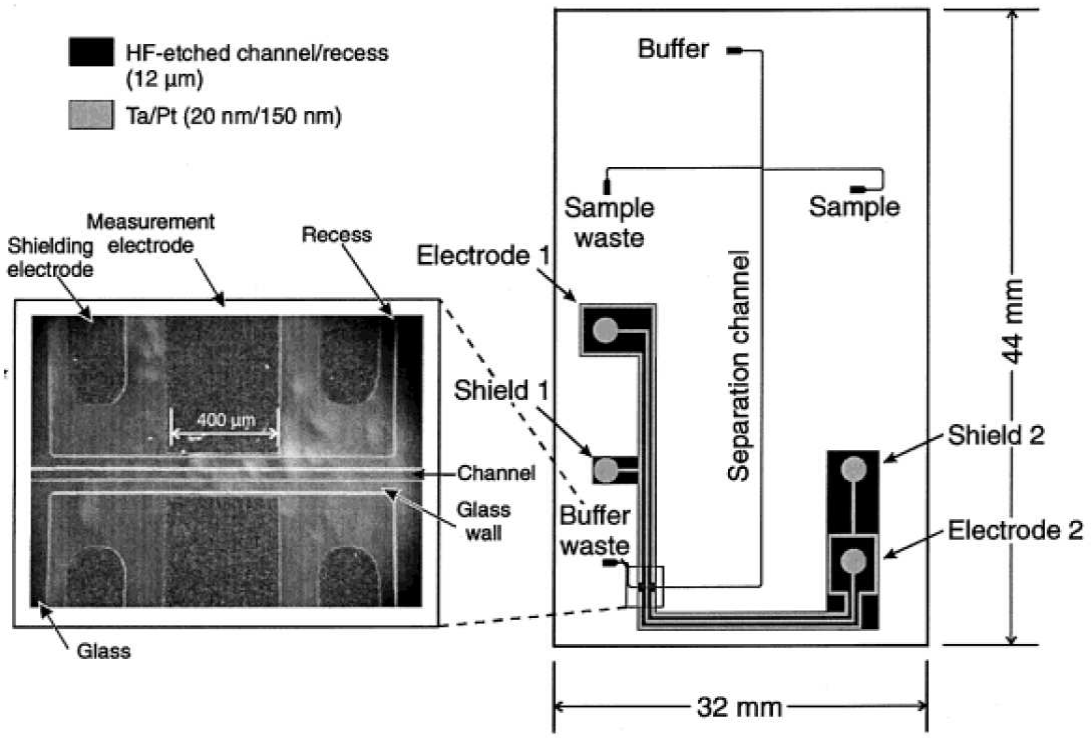

Figure 3.15: Layout of the CE chip and overview of the C^4D cell from [142]

3.6.1. On-capillary configuration

For the on-capillary designs, there are several variations that can be considered in the design of a C^4D detector.

First, the cell can include a shielding electrode between the two main electrodes [70, 116, 124, 127, 137, 143, 144] or not [125, 139, 145, 146]. Second, the electrodes can be made using silver varnish to paint electrodes directly on the capillary outer surface [124], or metal tubular electrodes made from hypodermic needles or ferrule [116, 125], or by an uninsulated metal wire coiled around the capillary and electrically linked by soldering or silver painting [145, 146]. A detailed study about electrode geometry on capillary has been published [147], comparing planar, semi-tubular and tubular electrodes. They found that the differences in analytical performance were insignificant for practical analytical use. In other words, the choice of the electrode design should be related to other requirements of the application. For example, if we want to use an optical detection at the same place as the C^4D, the best choice is semi-tubular electrode in one side of the capillary [148] in order to collect as much as light emitted from the source.

Kuban and Hauser [149, 150] also state that a tight fit (Small difference in diameter between the outer diameter of the capillary and the inner diameter of the electrode) of the electrodes onto the capillary is not important if the frequency is optimized. The existence of an air gap between the electrode inner surface and the capillary adds a new capacitor in series with the one composed of the fused-silica wall [145]. This new capacitor can cause problem due to the lower permittivity of air compared to fused-silica, which means the total capacitance decreases. Figure 3.16 shows that the coupling between the capillary (360 µm O.D.) and the electrode (600 µm O.D.) is the smallest when surrounded by air. Brito-Neto *et al.* also warned against this loose coupling which can add noise and thus decrease the SNR [131, 151] . This noise has a mechanical origin, as the capillary randomly moves inside the electrode, the capacitive coupling changes, thus affecting the measured signal. In their example, between a fully centred capillary and a right justified one, the capacitance change was as high as 50%. So tightly coupling of the electrodes to the outer wall of the capillary is needed [152].

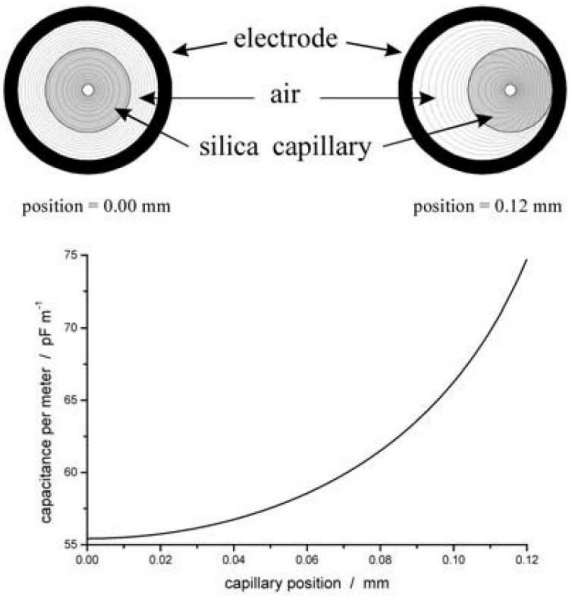

Figure 3.16: Simulation of the coupling difference in case of capillary displacement [131]

Third, the gap between the electrodes is usually between 1 mm and 5 mm [124, 125, 127, 144, 153] but smaller gaps have been also used successfully [143, 145, 146]. The length of the gap must be balanced between separation efficiency and the increase of

the stray capacitance which occurs at smaller gaps. This gap determines the detection volume and can also be used to add an optical detection [148, 154]. Some designs can include UV detection and the C^4D in the same system by putting the C^4D inside the capillary cartridge [146, 155] (Figure 3.17).

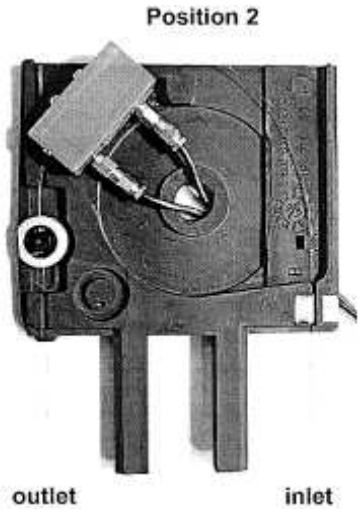

Figure 3.17: Implementation of the C^4D module in a capillary cartridge [155]

Commonly a capillary outer diameter of 360 µm is used, but Gillespie *et al.* [137] used a 1.6 mm O.D HPLC tubing and micro-bore columns. They compared the system to a TraceDec [156] and after optimizing the system using bode plot, they found that the behaviour of the cell is close to than for smaller designs. They obtained sensitivity as good as other workers. Their setup allowed the movement of the capillary which can help in the analysis of the packing homogeneity of the stationary phase but also help in the separation speed by decreasing the effective length.

Movable detection cells have been used in capillary electrophoresis (CE) by Macka *et al.* [143] who proposed a small C^4D cell trapped in epoxy resin (Figure 3.18). It was small enough to fit into the capillary cassette of their Agilent CE. They were able to simultaneously detect cations and anions with the C^4D and the built-in photometric detection. Movable detection systems on capillaries for simultaneous separation of anions and cations by dual opposite injection have also been developed [157, 158].

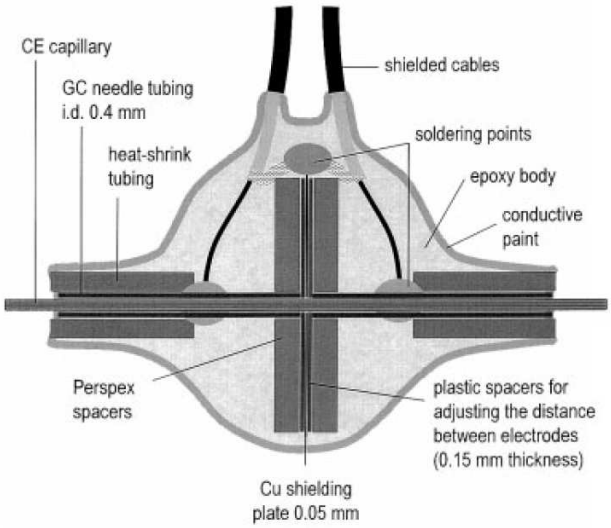

Figure 3.18: Structure of the movable mini C^4D from [143]

A "microfab-less" modular system using only 50 µm I.D. silica capillary tubing, a interconnecting cross, PMMA pieces as reservoir and a C^4D detector (Called openC^4D based on [113]) as been proposed [159]. It was then possible to reproduce a cross design with the injection branch and the separation branch made of silica capillary tubing.

A review of four systems using on-capillary configuration have been made by Kuban *et al.* [160], miniaturized cell as presented in [143], high voltage detector using mains power or battery as supplies [153] and a commercial detector from TraceDec. They have compared their SNR and LOD for low, medium and high conductivity in the separation of cations and anions. The separation efficiency and repeatability was independent of the detector design but the cell with built-in amplifier had less noise, which is expected when the electronics is closer to the cell.

3.6.2. On-Chip configuration

The alternative type of design is related to microchip devices which have a microchannel [68-72, 75, 79, 80, 142, 161] instead of a capillary. The principles stay the same but the different types of geometries lead to different problems.

There are three main schemes of C^4D on microchip, the "on top of lid" design, the "in-plane electrode" design and the "buried electrode" design. [119]

3.6.2.1. On top of lid design

The top of lid approach was proposed by Pumera *et al.* [70] and Wang *et al.* [71]. Figure 3.19 gives a view of a typical microchip with just a set of electrodes at the end of the channel.

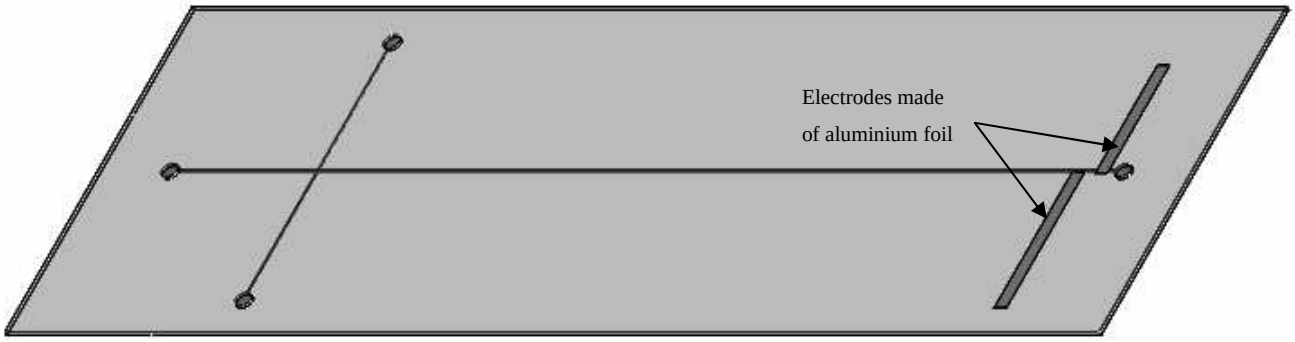

Figure 3.19: Typical microchip arrangement with two electrodes

Their microchip had the electrode made of aluminium foil strips glued with a common epoxy. They were placed along the channel in an anti-parallel configuration to minimize the stray capacitance between them. Insulation from the solution was provided by the cover lid of the microchip (125 µm). It is best to use a thin lid in order to have the highest possible coupling capacitance. Tanyanyiwa *et al.* [75] performed some experiments on lids with and without wells and found an increase of sensitivity for closer distance between the electrode and the solution. Kuban and Hauser [73] found the same effect of lid thickness and gave other recommendations about electrode dimensions (Length, width, spacing, *etc.*) to obtain the best SNR.

Commercially available polymer chips with non-contact electrode for electrophoresis are produced by the company microfluidic ChipShop (Germany). These chips feature a square channel of 50 µm or 100 µm made by injection moulding from PMMA or COP. The electrodes are composed of 10 nm titanium as adhesion layer and a 200 nm gold one with the pattern of the electrode. They have already been used for the

separation of small ions (Li^+, Na^+, K^+) [78] but also for heavy metals (Pb^{2+}, Mn^{2+}, Cd^{2+}, Cu^{2+} and Co^{2+}) [77].

Some designs do not include the electrodes on the chip but on a fixed holder [72, 74] or on a part which slides along the chip [162-165] and thus the channel. This configuration has the advantage that the chip can be easy replaced by another one without having to build new electrodes on it. The first design of this type was a sliding detector in 2003 by Wang *et al.* [162]. The point of interest in that paper was not the sensitivity of the system but the study of the separation process.

By moving the detector, they were able to create a three-dimensional plot of the resolution as a function of the channel length and the separation voltage. This was an interesting study, which indicated that the best resolution is not always obtained with a longer channel. They were also able to detect the totality of the ions by placing the detector at the beginning (Unresolved peak) and individual ions (Resolved peaks). Thus, for a known separation, the duration of the separation can be shortened by choosing the appropriate channel length before or even during the separation. A limiting factor may be the reproducibility of the detector placement but, according to the author, this is very good.

This design finally broadens the field of C^4D after Paull *et al.* [163, 165] named this technique the scanning capacitively coupled contactless conductivity detection (sC^4D). This new application shows its efficacy for measuring the physical structure of embedded columns (Packing density, porosity of monolith columns, *etc.*) and predicting the efficiency of future separation. Ion exchange monoliths in microchip channels may also be analysed in a non-invasive manner by this method. Similar work have been carried out on the chemical properties (Wall coating, *etc.*) of capillaries by Gillespie who was looking at the conductivity of covalently bound boronic acid groups at different pH [166].

The commonly used design (On top of lid) was improved a little when Mahabadi *et al.* [68, 69], implemented another set of electrodes on the bottom side of the chip with a shielded chip holder. They modelled this structure with FLEX PDE 5 2D to show that only a part of the electric field line was collected by the pick-up electrode with the top-top electrode design (Figure 3.20). But by the addition of another set of electrodes on the bottom side, the electric field lines were concentrated inside the

detection volume. The addition of these electrodes also decreases the reactance of the cell and thus the total impedance, which they reported, could lead to an increase of the signal by 100%. They observed a plateau occurring at lower frequencies with this new design, which confirmed the smaller reactance. However they also noted that at higher excitation voltages, an increase in concentration of the analyte did not give such a linear response as lower voltages did. This may be caused by saturation of the transimpedance amplifier as the signal is close to the 5 V supply. It is also most certainly due to the high conductivity affecting the plateau, shifting it toward higher frequency which can be seen on Figure 3.11. This particular design is called “the dual top bottom cell”.

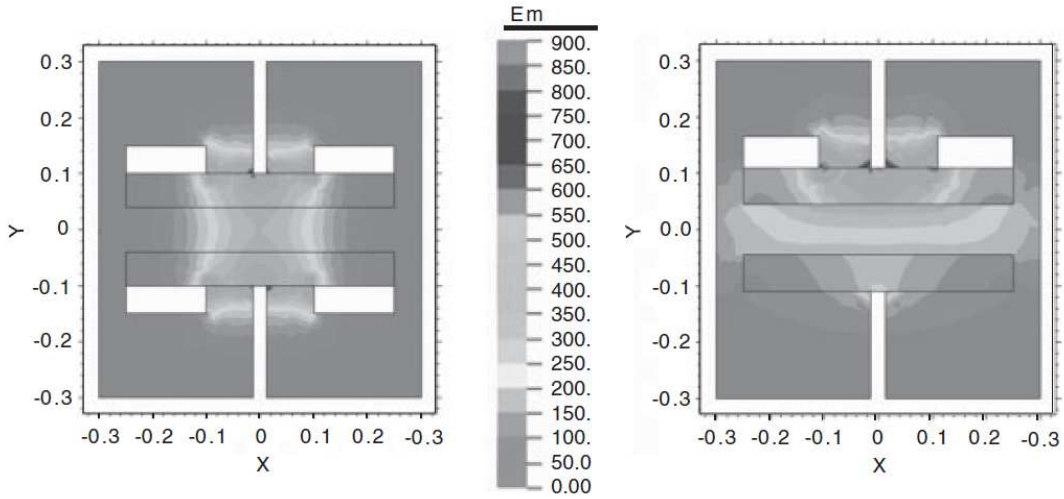

Figure 3.20: Two-dimensional numerical simulations of the electric field intensity for dual top–bottom compared with top–top electrode geometry using FlexPDE 5 2D [69]

3.6.2.2. In-plane design

Another design, which has the electrodes integrated along the channel on the same plane (In-plane electrode design) was proposed by Lichtenberg *et al.* [142]. Although this design provided a smaller distance between the electrodes and the solution (See Figure 3.15 in Section 3.6), the sensitivity was comparable to the on-lid electrodes due to the much lower detection volume. They also implemented some shielding with two shield electrodes on both sides of each signal electrode. The choice of using a recess to accommodate the electrode is due to the need of a total planarity of the bonding surface when using glass to glass bonding. This kind of design requires the

use of micro fabrication techniques (PolySi and Pt deposition, reactive ion etching, hydrofluoric acid etching, *etc.*).

A nearly similar design using a glass wafer as substrate has been published [167] with the use of chrome electrodes (200 nm) covered with 100 µm of SiO_2. The channel was created by using a particular heating method to form a semicircular sacrificial core made of photoresist (Black solid in Figure 3.21) with silicon dioxide grown on top of it by PECVD (3 µm). After the photoresist is dissolved, a hollow channel 14 mm long was obtained with 4mm long double-T injector having a 50 µm offset. No information about the electrode spacing, channel height or width is given.

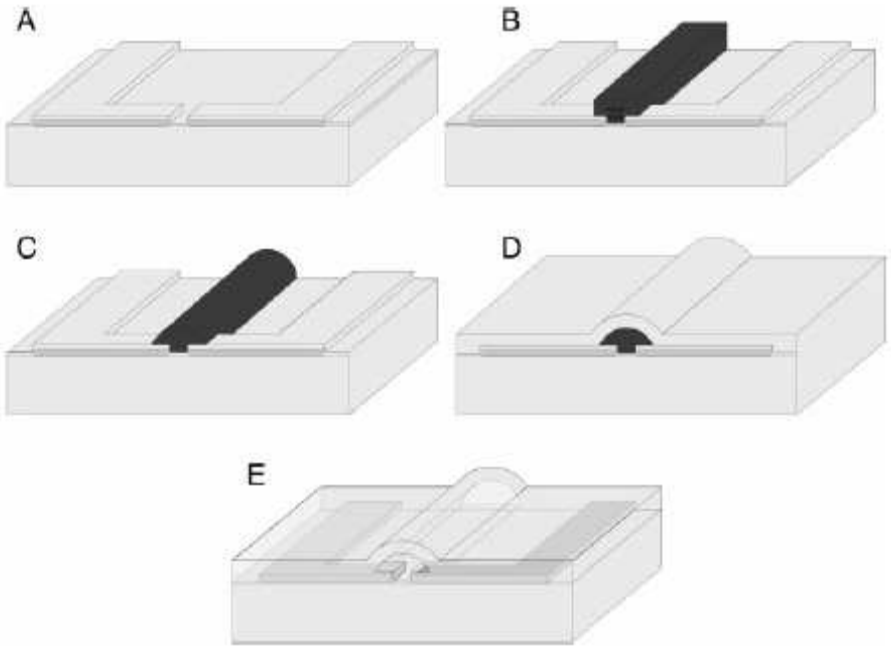

Figure 3.21: Fabrication process of the cell from [167]. (A) Insulation of the electrode, (B) Patterned photoresist, (C) Reflowed photoresist to form semicircular sacrificial core, (D) Oxide covering of the wafer, (E) Channel creation by salvation of the photoresist

Another design using sidewall electrodes has been presented by Xu *et al.* [168]. The chip was composed of boron doped sidewall electrodes (550x15 µm) isolated from the channel by a 1 µm SiO_2-polysilicon-SiO_2 layer. The separation was performed by a low-voltage driven electrophoresis due to the fragility of the insulating layer.

PDMS microchips with “Injected” in-plane metal (Molten gallium) electrodes have also been presented recently [169]. Liquid gallium was injected in two electrode

channels (100x40 µm) separated from the separation channel by a 75 µm thick PDMS wall. Two other channels (200x40 µm), used as ground electrode located 50 µm from the separation channel, were injected with the molten gallium which was then solidified. Separation of Sodium, Potassium and Lithium was achieved with the smallest LOD being 6.1 µM for Li^+. Analytical characteristics might have been improved with a higher excitation voltage as their system reached saturation when using more than 5.5 Vpp. This design is very simple as it only requires the injection of the liquid gallium on top of the usual PDMS casting and bonding. A similar design using cast metal (Tin / Lead / Cadmium / Bismuth alloy) and a hot embossed PMMA chip were proposed the same year [170]. The width of the electrode in this case was 1000 µm with an effective electrode gap of 1031 µm and a distance of 100 µm between the electrode and separation channel. The alloy pellets were introduced into the reservoirs of the electrode channels (100x50 µm) and melted at 80°C with an oven. The width of the channel was set to the minimum while allowing nearly 100% filling success of the viscous molten alloy, while a width of 50 µm only yielded a 50% success ratio. Separation of Ammonium, Sodium and Lithium was achieve with the smallest LOD being 85.5 µM for NH_4^+, it can be noted that the LOD of Li^+ was 326.1 µM

3.6.2.3. Buried design

The third on-chip design is the one from Guijt *et al.* [171] with 4 electrodes buried in the channel and protected from the solution by 30 nm of silicon carbide. This thin wall does not allow a large separation voltage, which increases the separation and analysis time. The group of Guijt continued to improve their design [172, 173], but no other groups have tried this design, probably due to the difficulty of obtaining four small electrodes in the channel width (Figure 3.22). However a group have published an electrical model of this four electrode system using VHDL-AMS [174].

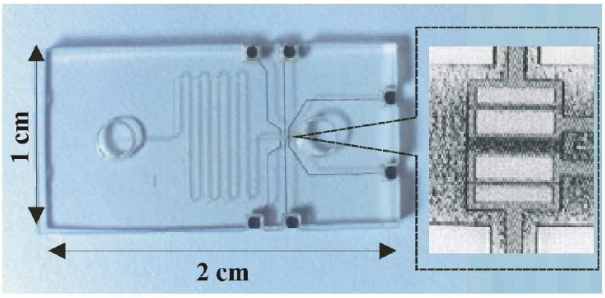

Figure 3.22: CE chip with four buried electrodes from [173]

Recently, the "buried electrode" design regained popularity. Liu *et al.* [175] proposed a three-layer PMMA microchip with Pt electrodes. Even if the manufacture process is not cumbersome, the electrode deposition phase has a large impact on the final price of the device. The same year, another group proposed a design with gold electrodes on a glass substrate with a spin coated PDMS insulating layer (100 µm [176] then 50 µm [177] thickness) and PDMS lid containing the microfluidic channels. The LOD of the system was very good (NH_4^+ 0.14 µM, Na^+ 0.39 µM, Li^+ 1.01 µM, K^+ 0.16 µM and Mg^{2+} 0.20 µM) and competes with the high excitation voltage design [75] and the top-bottom design [69].

Later Liu's group investigated using a PDMS insulating layer instead of PMMA and created a very thin coating (0.6 µm) by adding toluene to the PDMS and using higher spin-coating speeds. This thickness permitted them to reach the lowest LOD for Na^+ currently achieved with a microchip design (0.07 µM) [85]. This design still used Pt electrodes fabricated by lift-off processes, which is not low cost, but necessary for such low insulating layer thickness. This is why the design from Guijt *et al.* and Coltro *et al.* uses printed circuit board (PCB) to create the surface with the electrode. In order to insulate the electrode, they used either a poly(ethylene terephthalate) (PET) film [60] or a dry film photoresist (DFR) [61] that they laminate to the surface (Figure 3.23 shows the different processes involved for the DFR insulated chip). A PDMS chip is used to create the electrophoresis microchannels and sealed to the detector.

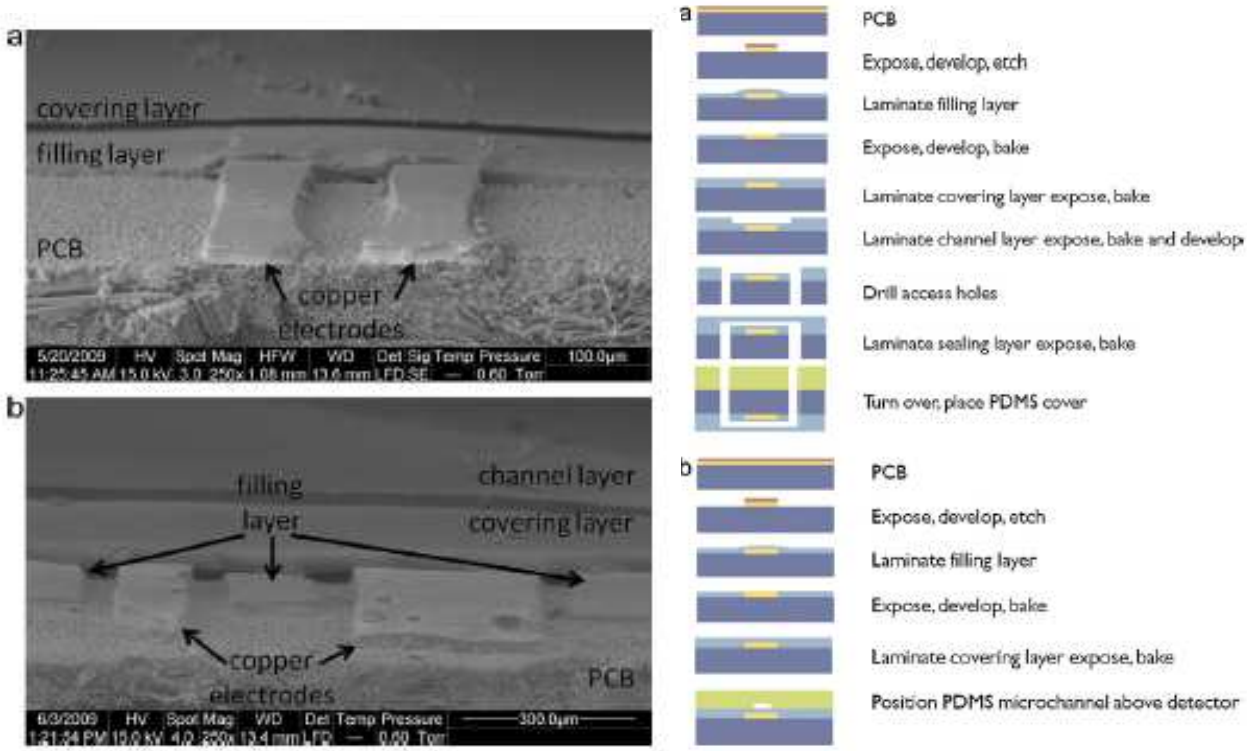

Figure 3.23: SEM of the hybrid chip using DFR and the two protocols used to create integrated devices and hybrid devices respectively, from [61]

Another solution, which has been applied to buried designs, but can also be applied to others, is doping of the dielectric layer. Lima *et al.* [178] used TiO_2 nanoparticles (NP-TiO_2) in order to increase the dielectric constant of the PDMS insulating layer and therefore the sensitivity. The sensitivity was increased proportionately to the dielectric constant, however, the limit of detection (LOD) was decreased more rapidly. Careful attention is required when doping dielectric material because conservation of insulation properties is critical for electrophoresis applications. Further investigation needs to be done as the range of possible doping materials is large and the balance between ease of manufacture, price and performance is always a challenge.

3.6.3. On-capillary / On-chip comparison

Due to its ease of adaptation to existing commercial chromatographic systems, and its being the first design to be developed, the on-capillary electrodes were initially the most extensively used. However, with the increase in new fabrication machines and techniques, more elaborate designs integrating the separation microchannel and

electrodes have been proposed. With the increasing number of designs, a portfolio of on-chip configurations is slowly building, allowing a faster implementation with any lab-on-chip (Owing to the compatibility with the manufacturing technique available).

3.7. Measurement electronics

The principle of C^4D is based on capacitive measurement of the conductivity of a solution inside a capillary / channel. One electrode is connected to a frequency generator with typical signal parameters of 20 Vpp amplitude sine wave and a frequency range from 20 kHz to 1 MHz. The other electrode picks-up the resulting current, which is a function of the total impedance of the system. A typical setup is show in Figure 3.24.

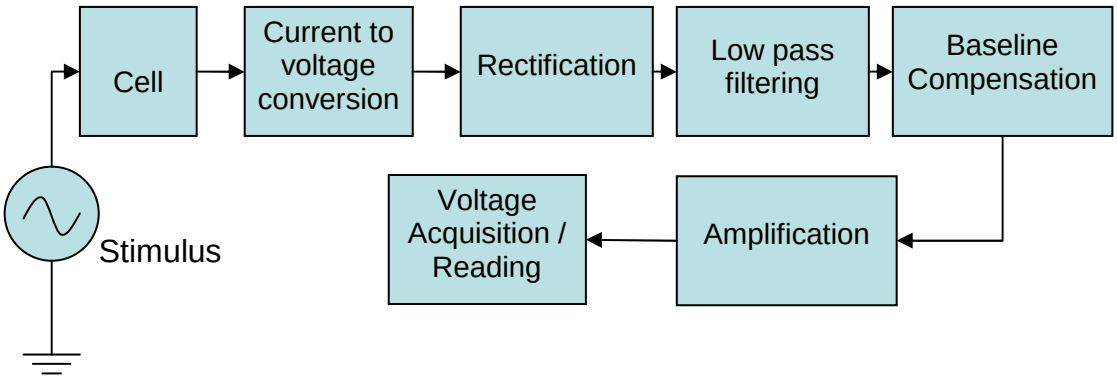

Figure 3.24: Typical electronic schematic of a C^4D

3.7.1. Signal generation

A sine wave has been identified as the preferable excitation signal as better signal to noise ratio has been obtained by Wang *et al.* [71] when comparing to square wave and triangular wave. Chen *et al.*[74] found that square waves induced more peak broadening and a larger noise to the electropherogram. Triangular waves had a smaller noise but also a smaller sensitivity compared with measurement made using sine waves. A sine wave is also a monotone signal which simplifies the signal processing and analysis. It can be sourced by a signal generator or an oscillator and a further amplification stage can be used if high excitation voltages are needed [75,

153]. Most of the groups use off-the-shelf function generator but custom printed circuit boards have been made in some cases [113, 177]. Modulated excitation signal have been used by Opekar *et al.*[179] coupled with an AM receiver circuit, the system had a narrower dynamic range, a smaller SNR and thus a higher LOD. They also stated that unmodulated excitation signal is preferable as it yield better sensitivity and easier signal processing.

3.7.2. Current to voltage conversion

The first stage of the signal conditioning is to convert the cell current into voltage before rectification and low pass filtering, often followed by an amplification stage. An easy way to convert the current into a voltage is to use a resistor tied to ground, thus the voltage drop across the resistor is proportional to the current passing through it:

$$V_{DROP} = R.i \tag{3.6}$$

This current to voltage conversion technique was done by Zemann *et al.* [125] which used the drop across a 10 kΩ resistor to measure the current. However, this simple solution has imperfections. First, the resistor which fixes the gain, will also consume a small part of the current (Responsible of the V_{DROP}) and therefore affect the total resistance of the system. Secondly, the measurement electronics will also affect the results if the input impedance of the measurement system is not infinite.

The most common way to convert this current into voltage is to use an active design composed of an operational amplifier in transimpedance configuration. This circuit is commonly used in relation to photodiodes which convert photons into current. For their setup, da Silva *et al.* [124] used an active current-to-voltage converter. Their circuit was based on an OPA606 in transimpedance configuration with a 1 MΩ feedback resistor.

The input current flows through the feedback resistor (R_f) and the output voltage is proportional to the current by the equation 3.7. Ideally, no current flows into the amplifier due to its infinite input impedance. The gain is fixed by the value of the feedback resistor, which needs to have a low tolerance (Below 1%) and a low thermal

drift (Below 50 ppm/ºC). The negative input is maintained at zero volts by virtue of the operational amplifier feedback. This point is commonly referred as a virtual ground as its electrical behaviour is similar to that of a true ground.

$$V_{OUT} = -R_f .i \tag{3.7}$$

Preferably a low bias current and low current noise density operational amplifier should be used due to the feedback resistor converting these unwanted current into unwanted output voltage. For normal temperature range, a FET amplifier is suitable as it has low bias current. However, if high temperatures are expected, the choice of a bipolar amplifier is necessary because FET amplifiers exhibit a larger bias current above 80ºC. It is also important to consider that if we choose to halve the feedback resistor, the signal will be decrease by 2 but the noise due to the resistor will decrease only by $\sqrt{2}$ due to the Johnson-Nyquist noise formula [180]:

$$v_{NOISE} = \sqrt{4 \cdot k \cdot T \cdot R \cdot \Delta f} \tag{3.8}$$

Particular attention is also needed to avoid any current leaking paths which will lead to additional error. Leakage can occur between the track linked to the current source and the surrounding environment. As the inverting input of the operational amplifier is at a virtual ground, any positive or negative voltage across this track can create leakage. This is why tracks need to be kept as short as possible and the printed circuit board needs to be cleaned from any residues of chemical which can favour this leakage. Guarding techniques can be used to create a conductive barrier which can considerably reduce the leakage by intercepting the parasitic current flow. The barrier is biased to the same potential as the protected node in order to avoid any additional leakage between the two. In the case of the current-to-voltage configuration, it is possible to use the non-inverting track as guard because it is close to the inverting track and at the potential of the circuit ground.

3.7.3. AC to DC conversion and noise filtering

Rectification is conversion of an AC signal to DC and is performed to facilitate measurement of the signal amplitude. The rectification has been done by half-wave rectification [124, 145], full-wave rectification [113, 127, 130] or synchronous detection using integrated circuit, AD630 [142, 153], MPY634 [176, 177] or MLT04 [164, 181]. The filtering is usually a passive first-order low pass filter, but 8th-order switched capacitor filters were used in [181]. Commercial Lock-in amplifiers have has also been used [126, 171, 172] (Stanford Research) [182] (Perkin Elmer).

The main advantage of synchronous detection (Figure 3.25) over classic rectification is its ability to reject noise (Unwanted frequencies and dephased signals). It is mainly used to recover small signal from larger amplitude noise by looking at only one frequency *i.e.* the reference. Therefore, the output is only a function of the amplitude of the component of the input at the defined frequency and the same phase. A more detailed explanation follows.

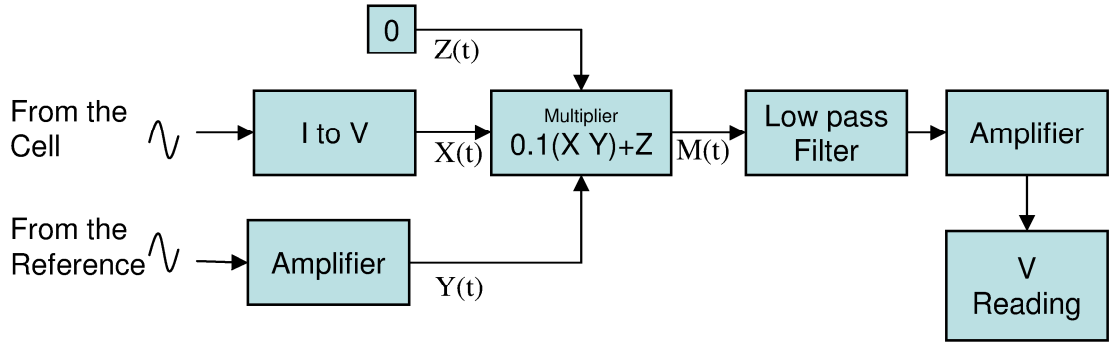

Figure 3.25: Block diagram of the synchronous detection circuitry

If we consider the signal from the cell after current to voltage conversion as X(t):

$$X(t) = TE\cos(2\pi ft + \varphi_1) + N(t) \tag{3.9}$$

With T the transfer function characteristic of the electrodes and the conductivity of the analyte at a fixed frequency and transimpedance gain, E the amplitude of the signal at the actuating electrode and N(t) the existing noise.

The signal from the generator Y(t) is assumed to be a perfect cosine without noise:

$$Y(t) = E\cos(2\pi ft + \varphi_2) \tag{3.10}$$

The integrated circuit multiplier (AD633) function is given at Eq. (3.11):

$$M(t)=\left(\frac{Y(t)\times X(t)}{10}\right)+Z(t) \tag{3.11}$$

The Z(t) function is an additional input where an external signal can be applied. In this application, the input is tied to zero, thus the resulting signal is as Eq. (3.12):

$$M(t)=\frac{E}{10}\cos(2\pi ft+\varphi_2)[TE\cos(2\pi ft+\varphi_1)+N(t)]$$
$$=\frac{TE^2}{20}(\cos(\varphi_1-\varphi_2)+\cos(4\pi ft+\varphi_1+\varphi_2))+\frac{E}{10}\cos(2\pi ft+\varphi_2).N(t) \tag{3.12}$$

This signal is made of 2 cosine signals and a dc term, which is a function of the phase difference. Only the signals which are functions of the pick-up electrode signal are of interest. Two signals have this characteristic, the dc term and the sinusoid with a frequency of two times the frequency of the signal we want to extract. This is illustrated in Figure 3.26, where we see the result of the multiplication of two signals at 500 kHz. The two highest peaks are at 0 Hz (DC) and 1 MHz (1 MHz sine wave) because the 500 kHz centred signal was shifted by the frequency of the other one (500 kHz). The sinusoid being exempt of harmonics, no secondary peaks are visible on the FFT spectrum.

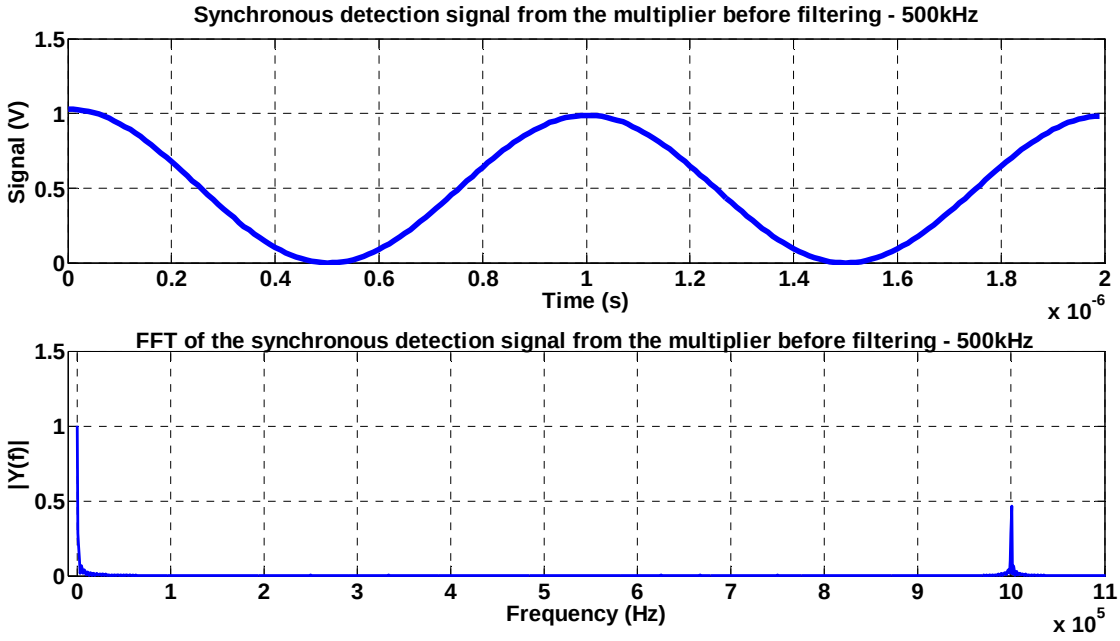

Figure 3.26: Matlab simulation of the FFT and the output signal of the multiplication of two AC signals at 500kHz

A low pass filter can be used to recover the DC value of the signal in Eq. (3.12), as given in Eq. (3.13).

$$\frac{TE^2}{20}\left(\cos(\varphi_1-\varphi_2)+\cos(2\omega t+2\varphi)\right)+\frac{E}{10}\cos(\omega t+\varphi).N(t) \quad (3.13)$$

The DC term is:

$$\frac{TE^2}{20}\left(\cos(\varphi_1-\varphi_2)\right) \quad (3.14)$$

This continuous term is maximum if the value of the phase difference is zero *i.e.* the phase of the signal from the pick up electrode and the signal generator are the same $\varphi_1=\varphi_2$. Then we have:

$$\frac{TE^2}{20} \quad (3.15)$$

Obtaining zero phase difference may be difficult due to the unknown phase shift introduced by the driver electronics and the cell. Orthogonal vector lock-in amplifiers have been investigated for use with conductivity detection [183]. The main advantage is that the input signal from the cell doesn't have to be in phase with the reference signal. It uses two multipliers which are fed with a reference signal "phase shifted" by $\pi/2$ radians. These multipliers are followed by low-pass filters to remove the AC component. However, an arithmetic unit is necessary to process the output of the multipliers to obtain the measurement. The schematic of the system is presented in Figure 3.27.

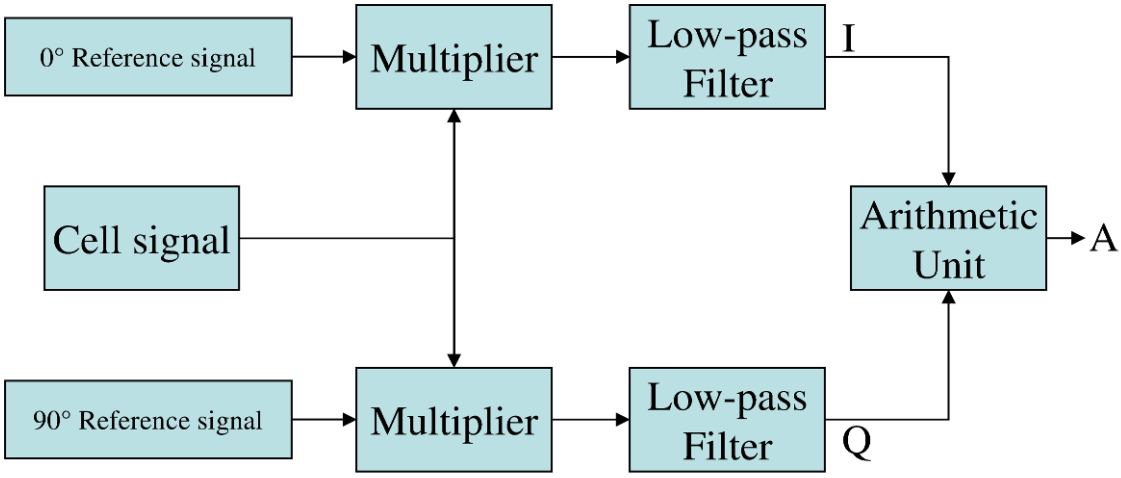

Figure 3.27: Schematic of the orthogonal vector lock-in amplifier

The signal from the first multiplier after filtering will be:

$$I = \frac{AB}{2}\cos(\varphi 1 - \varphi 2) \tag{3.16}$$

Where *A* is the amplitude of the signal from the cell and *B* is the amplitude of the signal from the reference.

And from the second:

$$Q = \frac{AB}{2}\cos\left[(\varphi 1 - \varphi 2) - \frac{\pi}{2}\right] = \frac{AB}{2}\sin(\varphi 1 - \varphi 2) \tag{3.17}$$

The amplitude of interest is *A*, as *B* is the known amplitude of the reference. In order to determine the amplitude of signal *A* we use *I* and *Q* as follow.

We know that $\cos^2(x) + \sin^2(x) = 1$.

We can write the cosines and sines from 3.14 and 3.15 as:

$$\cos^2(\varphi 1 - \varphi 2) = \frac{4I^2}{A^2B^2} \tag{3.18}$$

$$\sin^2(\varphi 1 - \varphi 2) = \frac{4Q^2}{A^2B^2} \tag{3.19}$$

And if we substitute these into the trigonometric identity:

$$\frac{4I^2}{A^2B^2} + \frac{4Q^2}{A^2B^2} = \frac{4}{A^2B^2}\left[I^2 + Q^2\right] = 1 \tag{3.20}$$

Because we want A, the next equation is used:

$$A = \sqrt{\frac{4}{B^2}\left[I^2 + Q^2\right]} = \frac{2}{B}\sqrt{I^2 + Q^2} \tag{3.21}$$

The phase difference between φ_1 and φ_2 can also be extracted from the value of *I* and *Q*. Normally, only the amplitude variation of the signal is measured but as Liao *et al.* [183] said phase difference measurement should be considered for the explanation of possible nonlinear behaviours. Their study did not include the realisation of a system, but a simulation made using VHDL-AMS language gave promising results.

3.7.4. Baseline suppression

The aim of the baseline suppression is to cancel the signal measured when no species are been detected, usually when the system is at rest, before a measurement run. Systems which operate before the detection can be named baseline suppression whereas any systems which operate after can be named baseline compensation.

In a conventional chromatographic machine, the baseline suppression is done with the help of a suppressor column. It is a particular column which is normally placed after the ion-exchange column which does the separation but before the conductivity cell. Its purpose is to interact with the ions of the running buffer. Consequently, the background is a weak electrolyte in which the separated species can be detected more easily [184]. A software auto-zero of the Y-scale can also be used in parallel for ease of reading of the chromatograph. In electrophoresis, C^4D is the most common conductivity detection used and it is this latest technique which will be discussed for baseline suppression.

In C^4D, the baseline is not only caused by the running buffer but also by the parasitic capacitance which can bypass the detection cell [149]. It has been seen that optimisation in the cell design needs to be done (Anti-parallel disposition, ground electrode, *etc.*), in order to reduce this parasitic capacitance.

Some C^4D papers use baseline compensation [69, 133, 176] which is done by offsetting the signal with a subtraction structure or an instrumentation amplifier after the rectification stage and often followed by an amplification (See Figure 3.28). This technique can be useful in order to use the full range of the acquisition electronics thus increasing sensitivity. The data acquisition is usually done with 16-bit data acquisition system plugged into a computer [69, 115, 176]. But more autonomous systems have been created, using analog to digital converter integrated circuits [113, 164]. In the compact version made by Francisco and doLago [113], baseline compensation is not directly implemented. They claim that the compensation will be done by software as the effective resolution of the 21-bit ADC (22-bit ADC used in unipolar mode) and the use of good filtering techniques is enough to see the difference between the fairly stable baseline and a separation peak.

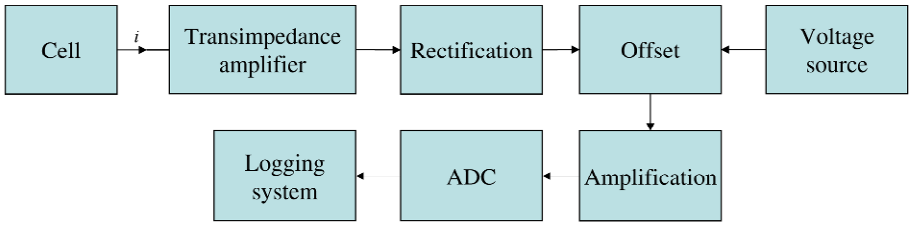

Figure 3.28: Block diagram of the detection electronics with offset voltage cancellation

However the transimpedance amplifier will be subject to saturation if the input current is too high in comparison to the gain (Feedback resistor). In this case, the baseline suppression techniques described above will not be able to overcome the loss in sensitivity and linearity associated with this unwanted phenomena. A novel baseline suppression approach using current instead of voltage and located before the transimpedance amplifier will be evaluated in this work.

3.7.5. Signal Noise Ratio considerations

In their first paper, Zemann *et al* .[125] state that they can improve the Signal Noise Ratio (SNR) if they increase the frequency of the excitation signal, but due to limited electronics they did not optimized their frequency as da Silva and do Lago did [124]. Later some authors like Gas *et al.* [127] published work about frequency optimisation

for an axial cell using a more extensive cell model. Work about frequency effects in planar interdigitated cells has also been published by Timmer *et al.* [185].

Another method to improve the SNR had been tested by Tanyanyiwa *et al.* [72, 75, 153, 186], which involves increasing the excitation voltage to several hundred volts (250 Vpp [153], 450 Vpp [186] and 500 Vpp [72, 75]). This can be done by the use of a high voltage, high speed power amplifier. Thanks to the increase of the SNR they have obtained a limit of detection for small inorganic ions of 0.5 µM. The high excitation voltage requires, besides a high speed power amplifier and high voltage supply, a good shield because a large capacitive coupling can occur between the electrodes. This coupling leads to an undesirable high background signal which reduces the SNR.

3.8. Detection of inorganic ions

In general, in the separation of inorganic ions, the cations and the anions are not separated simultaneously in capillary electrophoresis. However, the dual opposite end injection technique (The sample is injected on both ends of the capillary) performed by Kuban *et al.* [9, 157] and Unterholzner *et al.* [158] permits simultaneous separation of anions and cations in capillary. In both papers they separated at least 11 inorganic ions respectively in rain or surface and mineral water [157, 158]. Wang *et al.* [162] also performed the simultaneous separation of 3 anions and 3 cations using this dual-opposite injection technique on a microchip design.

More recently portable instruments have appeared. One is dedicated to the analysis of inorganic ions of post-blast residues of homemade explosive [114]. They used a commercial C^4D system from TraceDec mounted on a portable electrophoresis device (CE-P2) from CE Resources [187]. The device used by Kuban *et al.* [115] is mostly homemade. They evaluated their device by measuring the inorganic cation and anion levels in lake water. A newer version of the portable C^4D system has been developed recently by the same group [188]. This new system, even if the authors claim using the same design, has a higher LOD than the former one. However, the new one features fully automated operation and a robust injection system. The group of do Lago also produced a mobile robot to measure volatile compound in air samples, few

anions have been separated by capillary electrophoresis [189] while testing the device for the detection of chemical warfare agents.

The tables 3.1 and 3.2 list most of the different C^4D systems used respectively in both ion chromatography systems and capillary electrophoresis for the detection of inorganic ions. Designs have changed during the last decade from the ones developed in 1998 by Zemann *et al.* [125] or da Silva and do Lago [124] using off the shelf equipment, to the most recent system from the same group [113] using an integrated circuit to create a miniaturized C^4D system with improved limit of detection. Few groups have implemented C^4D in commercial ion chromatography systems [116] or homemade ones [135, 190] and are listed in Table 3.1. The most recent C^4D systems used for electrophoresis are listed in Table 3.2.

References	Excitation parameters	Cell characteristics	Mobile phase	Cations	LOD (µM)	Anions	LOD (µM)
[135]	1 MHz	Fused-silica capillary	10 mM MSA	NH^{4+}	5.544		
2011	1-10 Vpp	320 µm I.D.		K^+	4.092		
		560 µm O.D.		Na^+	3.262		
		500 µm Electrodes gap		Mg^{2+}	0.35		
		28 cm column		Li^+	4.466		
[190]	TraceDec	Fused-silica capillary	1mM MSA	NH^{4+}	0.998		
2012		320 µm I.D.	0.1 mM 15-crown-5	K^+	2.276		
		10 cm column	8:2 Methanol-Water	Na^+	0.783		
				Mg^{2+}	1.687		
				Ca^{2+}	3.094		
[116]		Fused-silica capillary	1 mM Tartaric acid	Non-suppressed (No suppression column)			
2004	150 kHz	Polyimide coating	185 µM Pyridine-	K^+	0.568	F^-	8.422
	50 Vpp	150 µm I.D.	2,6-dicarboxylic acid	Na^+	0.304	Cl^-	3.103
		375 µm O.D.		Li^+	0.418	NO_3^-	4.032
		1 mm Electrodes gap		Suppressed (With suppression column)			
	25 kHz					F^-	0.079
	70 Vpp					Cl^-	0.056
						NO_3^-	0.081
						SO_4^{2-}	0.042

Table 3.1: Existing C^4D used with ion chromatography

References	Excitation parameters	Cell characteristics	BGE	Cations	LOD (µM)	Anions	LOD (µM)
[69]	300 kHz	PMMA Microchip	30 mM Mes/His	NH^{4+}	0.3	Cl^-	0.15
2010	70 Vpp	50x50 µm Channel	2 mM 18-crown-6	K^+	0.56	NO_3^-	0.15
		75/125 µm Insulation Layer		Ca^{2+}	0.3	SO_4^{2-}	0.15
		500 µm Electrodes gap		Na^+	0.3	F^-	0.15
		1 mm Electrode		Mg^{2+}	0.35		
				Li^+	0.25		
[77]	50 kHz	PDMS Microchip	20 mM Mes/His	NH^{4+}	0.14		
2012	20 Vpp	Glass substrate		K^+	0.16		
		50 µm Insulation Layer		Na^+	0.39		
		1000 µm Electrodes gap		Mg^{2+}	2		
		750 µm Electrode		Li^+	1.01		
[113]	1.1 MHz	Fused-silica capillary	10 mM Mes/His	K^+	0.6		
2009	4 Vpp	Polyimide coating		Ca^{2+}	0.3		
		75 µm I.D 375µm O.D.		Na^+	0.5		
		510 µm Electrodes gap		Mg^{2+}	0.6		
		2 mm Electrodes		Li^+	0.8		
				Ba^+	0.4		
[153]	190 kHz	Fused-silica capillary	10 mM Mes/Hi	K^+	0.12	Cl^-	0.21
2002	200 Vpp	75 µm I.D 375µm O.D.		Na^+	0.2	NO_3^-	0.1
		1 mm Electrodes gap		Mg^{2+}	0.14	SO_4^{2-}	0.089
				Li^+	0.27	Br^-	0.15
						$C_2C_4^{2-}$	0.15
[61]	530 kHz	PDMS Chip	10 mM Mes/His	Li^+	8		
2011	20 Vpp	50x30 µm Channel	50 mM Acetic acid				
		30 µm Insulation layer (DFR Film)					
		400 µm Electrodes gap					
[191]	120 kHz	Fused-silica capillary	15 mM L-Arginine	NH^{4+}	0.5		
2011	300 Vpp	50 µm I.D. 375µm O.D.	3 mM 18-crown-6	K^+	0.66		
		2 mm Electrodes gap	12.5 mM Maleic	Ca^{2+}	2		
			acid	Mg^{2+}	1		
[133]	1 MHz	Glass substrate	20 mM Mes/His	K^+	0.2		
2008	10 Vpp	200 µm glass lid		Na^+	0.95		
		70x20 µm Channel		Li^+	1.4		
		250 µm Electrodes gap					
[125]	40 kHz	Fused-silica capillary	20 mM Mes/His	Na^+	8.7	Cl^-	5.641
1998	8 Vpp	Polyimide coating					
		50 µm I.D. 375µm O.D.					
		2 mm Electrodes gap					
[124]	600 kHz	Fused-silica capillary	10 mM Mes/His	K^+	1.1		
1998	20 Vpp	Polyimide coating		Na^+	1.6		
		50 µm I.D. 360µm O.D.		Mg^{2+}	1.2		
		550 µm Electrodes gap		Ca^{2+}	1.4		
				Ba^{2+}	1.2		
[115]	190 kHz	Fused-silica capillary	11 mM His	NH^{4+}	0.3	Cl^-	0.15
2007	20 Vpp	Polyimide coating	50 mM Acetic acid	K^+	0.2	NO_3^-	0.15
		50 µm I.D. 360µm O.D.	1.5 mM 18-crow-6	Ca^{2+}	0.2	SO_4^{2-}	0.1
			100 µM Citric acid	Mg^{2+}	0.4	ClO_4^-	0.15
				Na^+	0.3	NO_2^-	0.15

Table 3.2: Existing C^4D used for electrophoresis

3.9. Future of the C^4D

The rate of development and use of the C^4D by numerous research groups during this last decade proves that the C^4D technique has all the qualities necessary to become a significant solution for the sensing of inorganic ions. High sensitivity, low cost and the possibility of miniaturisation are the requirements of a good technique. Looking at the increase in publications around this detection technique, improvement and new applications will be expected in the future. Elbashir published a review of the numerous applications of C^4D for capillary electrophoresis in pharmaceutical and biological analysis [192]. Some groups are already specialized in this technique like da Silva and do Lago [60, 113, 124, 131, 145, 151, 189, 193], Kuban and Hauser [72, 73, 75, 115, 116, 149, 150, 153, 157, 186, 194] which provided several review in the last decade [117, 118, 195, 196] and Zemann [120, 125, 144, 158].

Recently, the applications of the C^4D became broader with the use of this technique for the non invasive characterisation of the packing quality of column [163], the identification of Gas-Liquid two phases flow-patterns [138], and as a biosensor for the detection of tumours with the use of folic acid as bioreceptor [197]. This may lead to an increase in the usage of the C^4D technique for non inorganic ions.

A current challenge for C^4D is the integration of the electrode and the electronics in an integrated and small package. Over the years, designs have evolved from the circular electrode for electrophoresis / ion chromatography to planar on-chip one. Several designs using different manufacturing technique have been tested (PCB, Chip holder, *etc.*). This is a good step toward low cost, ease of fabrication for commercial use and versatility in comparison with older techniques. However, only few of the groups managed to miniaturise the instrumentation and automation equipment for portable applications which enable use on the field [115, 188, 189].

3.10. Summary of the chapter

This chapter gave an overview of the separation techniques which can be used for the separation of inorganic ions. These techniques can be coupled to C^4D for the detection of inorganic ions. The theory of C^4D has been presented and existing C^4D detection cells have been reviewed to show the numerous designs which have been created using various manufacturing techniques. These designs have mainly been used in addition to separation method such as the one presented in this chapter (Separation column and electrophoresis) but some designs have been used for other purposes such as flow pattern characterisation or biosensing (Section 3.9). These published designs have inspired the detection cells presented in the next chapter. The state of the art of the electronics behind C^4D has also been presented (Section 3.7) and an improved C^4D system with baseline suppression will be detailed in Chapter 5. As seen in this chapter, most of the electronics is based on bench top equipment for laboratory usage. This new C^4D electronics is focussed on system integration and the enhancement of limit of detection (LOD) through higher excitation voltage and baseline suppression.

Chapter 4 : Design of a Lab-on-chip for IC for water quality monitoring

4.1. Outline of the chapter

This chapter will present the different Lab-on-chip design, especially the detection cells which have been tested during the course of this PhD. The first designs of cell based on capillaries are similar to the ones developed for the first C^4D cells [124, 125]. These cells however cannot be integrated into LOC devices thus the need to move toward new designs. A plug design was developed for the intended purpose of fitting various designs. This design however has some drawback such as leaking and cumbersome manufacture process. A more integrated design using printed circuit board to act as a substrate for the electrodes and the LOC device itself has also being developed. This design used manufacturing techniques described previously in Section 2.4. Experimental results collected with these cells will also be compared with the theory from the model presented in Section 3.4.

4.2. Block diagram

The block diagram in Figure 4.1 provides a rapid overview of the system which could be used for the monitoring of water quality. The main system can be split in four parts, the sample introduction which extracts the species of interest from the water pumped from the source (River, lake, *etc.*). This is followed by the separation system, its role is to separate the species prior to their entry into the detection cell. The detector, which is coupled to the baseline suppression system, will give a measurement of the current conductivity of the cell and provide the results which will be used to trigger action or be stored for later use. Electronics is also needed to control any fluidic related actuators (Pump, valves) and the detection system (Baseline suppression, measurements). The system could also be used as a bench equipment thus the possibility to use a personal computer to communicate with the system.

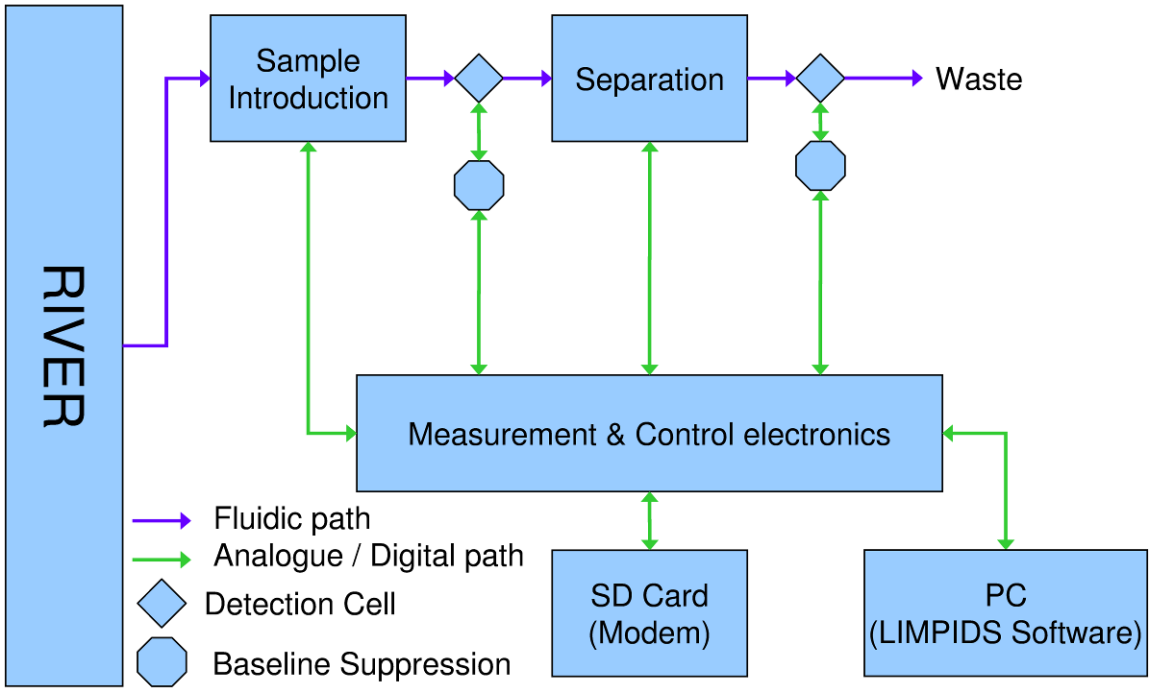

Figure 4.1: Block diagram of the system

4.3. Implementation of the electrodes

Implementing the electrodes in the system in order to create the detection cell was a real challenge. Even if lots of designs now exist, each of them is unique as they were developed to fit closely the design and the manufacture processes of particular systems based on facilities which the research group has access to. The next section will give an overview of the different cell designs used and evaluated during this project and the problems encountered, which pushed us to create a series of new designs ranging from a capillary cell to one embedded in a microfluidic chip. The reagent used for the first experiments was Potassium Chloride (KCl), the next experiments it as been changed to Sodium Chloride (NaCl), allowing us to prepare the solution from analytical grade reagent salt which were more pure than the Potassium Chloride (KCl) used previously. Measurements have been done in the laboratory which was at room temperature, the results were not subject to any extreme change of temperature, an ambient temperature of 24 °C is to consider when observing the data.

4.3.1. Capillary cell

4.3.1.1. On-capillary with needle electrodes

The first design (Figure 4.2) was based on the one created by Zemann *et al.* [125]. It was composed of a standard fused silica capillary (100 µm I.D. / 360 µm O.D.) with a polyimide coating (Polymicro) and the electrodes were made from 22 gauge needles (Hamilton) cut to a smaller length of about 13 mm. The link to the electronic circuitry was done by wire glued to the stainless steel electrode by means of conductive epoxy (Circuitworks).

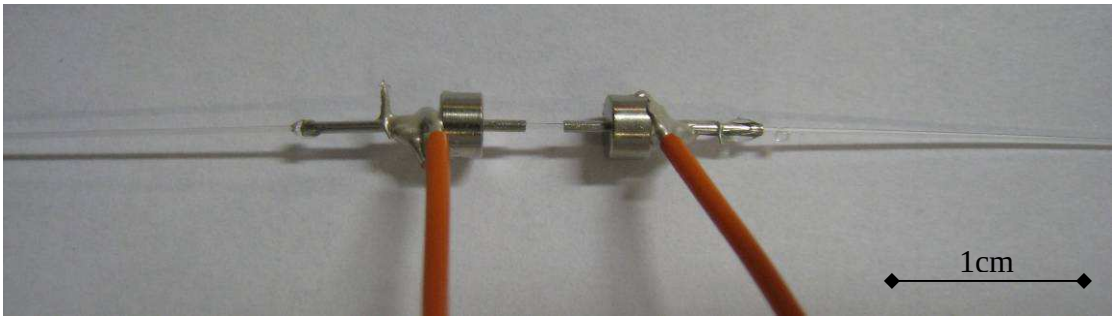

Figure 4.2: Polyimide coated fused-silica capillary with stainless steel electrode cell

The results obtained with this configuration with a 1 MΩ feedback resistor for the current to voltage converter an excitation signal of 2Vpp are represented in Figure 4.3. The transimpedance amplifier used was an OPA380 from Texas Instrument, followed by a multiplier AD633 and an amplifier with a fixed gain of 2 (Figure 4.3).

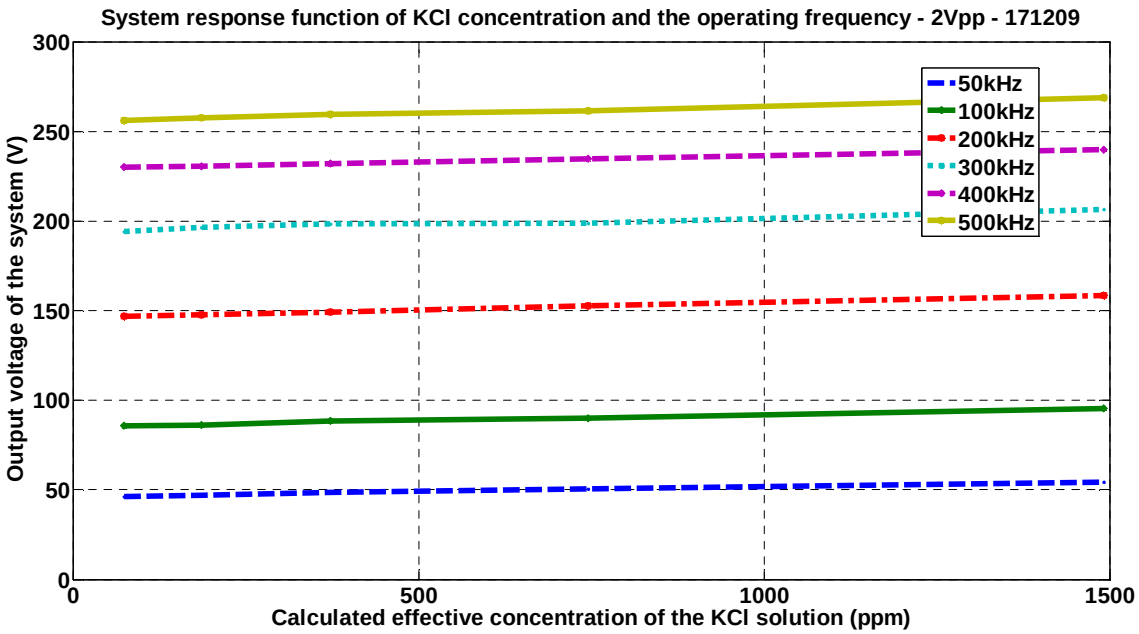

Figure 4.3: Calibration curve for the Stainless Steel electrode design

The measured response has a very low sensitivity (12.3 µV/ppm at 500 kHz) considering the concentration used (74.5ppm, 186.4ppm, 372.7ppm, 745.5ppm, 1491ppm). This poor sensitivity is mainly due to the stray capacitance in the system due to the leads which connect the electrodes to the circuitry but also the overall circuitry which was built on a breadboard which is not well suited for high frequencies. During the experiments, a great dependence between the response and the environment surrounding the system was observed. The highest dependence was seen for higher frequencies; strengthening the hypothesis that stray capacitance bypasses the system. There is also the fact that the concentrations of sodium chloride (KCl) injected to do the calibration curve were relatively large, which makes the solution very conductive. If we recall the cell simplified electrical model (Section 3.4), with the resistance of the solution being very low, the system will be sensitive to the coupling capacitor instead, as they become non negligible in comparison to the electrolyte.

Despite this lack of sensitivity at high concentration, the sensing ability of the system has been verified but the study of other design with lower stray capacitance is necessary to improve the system. We can also discuss the practicality of such design for a field instrument. The coupling of the needle to the capillary may lead to mechanical noise [131] as air gap may be present between the two if the outer

diameter of the capillary does not match closely the inner diameter of the needle. The fact the contacts are glued may lead to fault due to vibrations and is not scaled for an easy manufacture.

4.3.1.2. On-capillary with wire wrapping electrodes

This second design is inspired by the design of da Silva *et al.* [145], which uses wire wrapped over the capillary instead of the needles (Figure 4.4). It is an inexpensive way to create electrodes around the capillary but not suited to mass production. However, it reduces the risk of air gap between the electrode and the capillary due to the fact that the liquid solder tends to fill the gap when creating the electrode, which also avoids any inductive behaviour. Another advantage is that it is easier to implement these electrodes on a PCB using the copper tracks to solder the electrodes of the cell directly to the circuitry which make the link shorter and less sensitive to noise. One of the disadvantages is that this wrapping is carefully done by hand which means that each electrode is unique. This detail will make each cell different and a direct swap from a cell to another may need some adjustments to have the same response.

The polyimide coated fused silica capillary from the previous design was replaced by a high quality round capillary tubing from VitroCom (CV3040S). It was chosen in order to improve the capacitive coupling between the electrodes and the liquid due to its thin capillary wall (50 µm). The capillary length was 100 mm with an outer diameter of 400 µm and an inner diameter of 300 µm±10%.

Figure 4.4: Wire wrapping electrode cell

Figure 4.6 shows the system response for different concentrations of KCl. The actuating signal has an amplitude of 4 Vpp, a frequency of 1 MHz and the feedback resistor of the current to voltage converter is a surface mount device of 1 MΩ and tolerance of ±0.1 %, which reduces possible parasitic effects compared to a through hole component [131].

A picture of the circuit is provided in Figure 4.5 where the transimpedance amplifier (A), the dephaser (B) and the amplifying stage (C) can be seen.

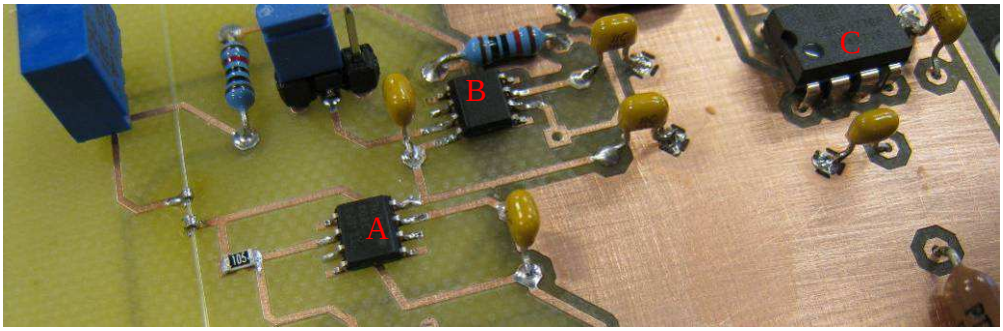

Figure 4.5: Circuit board with the SMD feedback resistor, transimpedance amplifier (A), dephaser (B) and amplifying stage (C)

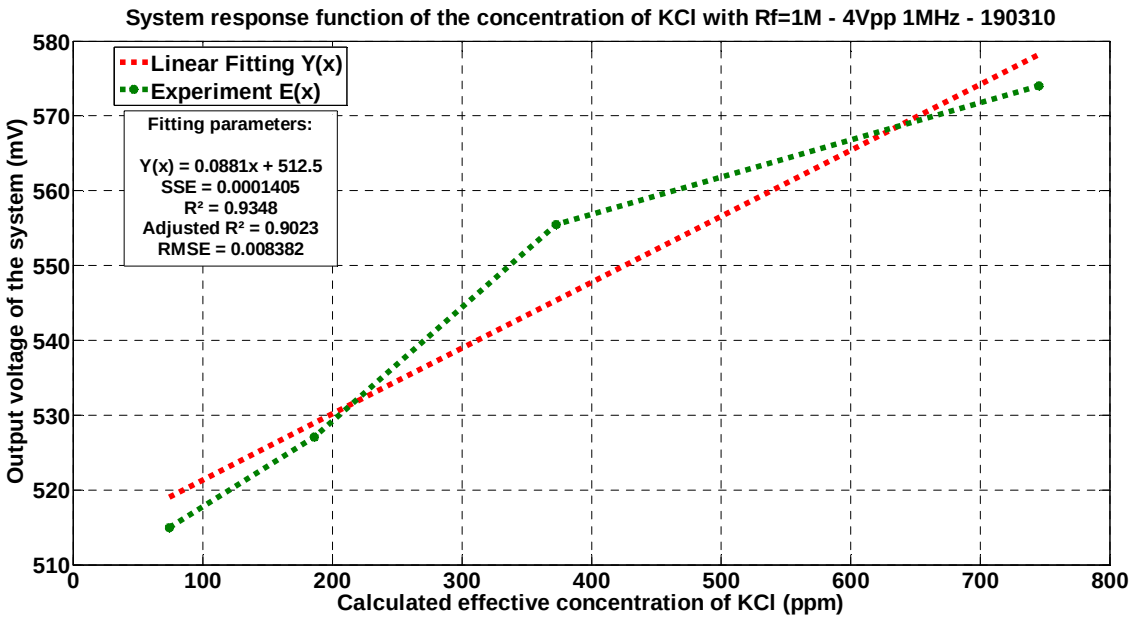

Figure 4.6: Calibration curve of the system with wire wrapping electrode

If we consider the part of the curve from 74.5ppm (1 mM) to 745.5ppm (10 mM) as linear, the resulting calculated sensitivity is 88 µV/ppm. With this configuration, the sensitivity is improved by more than a factor 7 compared to the previous system.

After the development of this design, the decision to create another design capable of being interfaced with microchip manufactured in The Chemistry Department at Hull was made, thus resulting in the creation of an on-chip cell design. However improvement of the existing design using the capillary has also been done as a point of comparison.

One of the improved designs was still using the wire wrapping technique but the goal was to make it stronger and able to be connected at the end of a commercial monolithic column. The capillary was then replaced by one which fits into the standard Fingertight fitting from Upchurch Scientific normally used with 1/16 in O.D. tubing. These capillaries (Blaubrand) are normally used for disposable micropipettes and have a thicker wall than the capillary used previously (1.6 mm O.D. and ≈ 481 µm thick wall). The resulting calibration curve can be found in Figure 4.7. A photo of the system is shown in Figure 4.8.

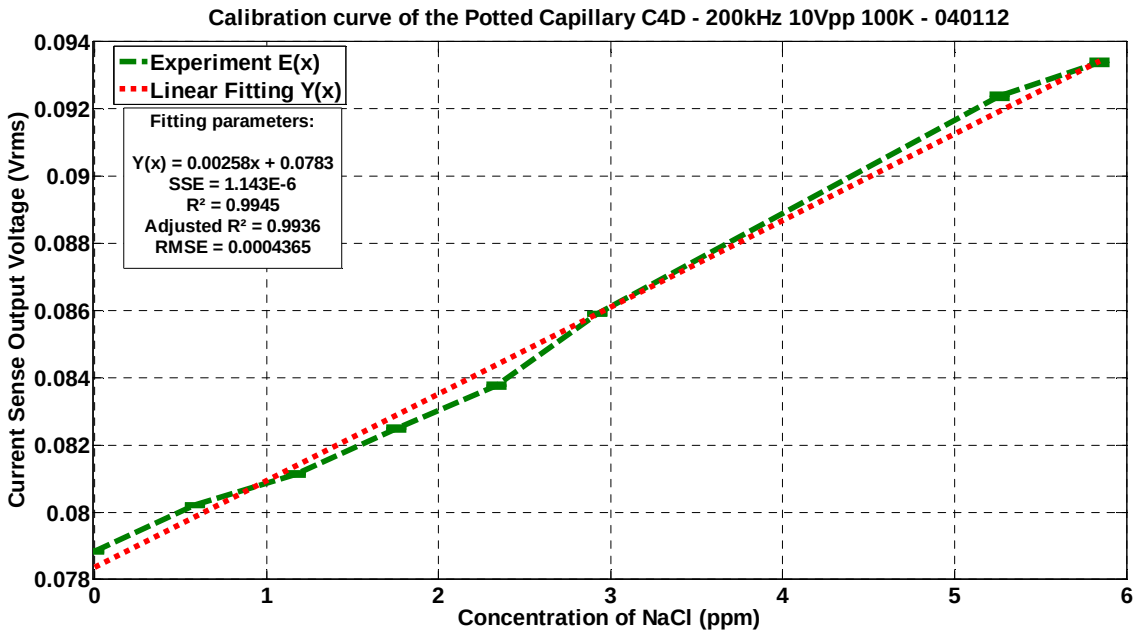

Figure 4.7: Calibration curve of the most recent system with wire wrapping electrode

The excitation voltage had a frequency of 200 kHz and an amplitude of 10 Vpp with a feedback resistor of the transimpedance amplifier of 100 kΩ. The slope of the calibration is 2.6 mV/ppm which is an improvement over the previous capillary system. The LOD can also be estimated by looking at the first experimental point's standard deviation given for the blank sample [198] (See appendix E), which is 0.3 µM for NaCl (3σ).

This improvement in sensitivity over the previous capillary system is due to the layout of the board, which allows even closer distance between the electrodes and the pick-up amplifier and also the use of a higher stimulus voltage. The previous transimpedance amplifier was an OPA657 (Texas Instrument) whereas the one used in the experiment was an OPA827. The latter has higher current noise density (2.2 fA/√Hz), a lower slew rate (28 V/µs) but a lower input bias current (±500 pA). Its wide output swing voltage increases the dynamic range and sensitivity of the system in conjunction with the correct feedback resistor and excitation voltage compared to the OPA657.

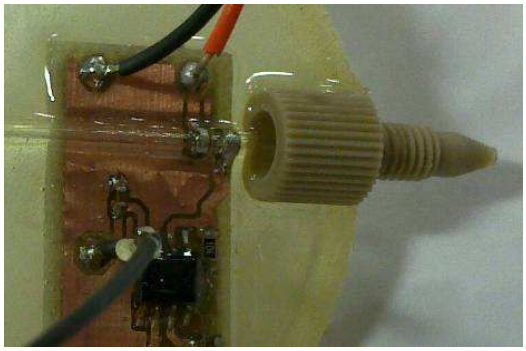

Figure 4.8: Picture of the epoxy potted C4D

4.3.2. Off-chip cell

4.3.2.1. Plug electrodes

The “Plug electrode” design was the first attempt to embed the detection cell in the microchip. In this case, the electrodes were part of the plug and a hole was made in order to give access to the channel to the plug.

The plug body is made of a special acrylic based photopolymer with the help of a 3D printer (EDEN500V) from Objet. The printed prototype has been designed using Solidworks and contained several plugs of different dimensions in order to have some spare plugs and obtain a good quantity/price ratio (Figure 4.9 and Figure 4.10). Each plug has two holes where 26AWG tinned cooper wires can be introduced in order to link the electrode to the PCB. The electrodes are made of conductive silver paint separated from each other by a gap of 1 mm. The insulation is made with a polyurethane insulating varnish (MR8008), both from Electrolube. The varnish is painted on the plug until there is no measurable real impedance (purely resistive) between the two electrodes when the plug is in contact with water. A picture of the two electrode plug is show in Figure 4.11 where the wires are easily identifiable. With the time the electrodes made of silver paint can take a golden tint but no quantifiable change in performance has been detected.

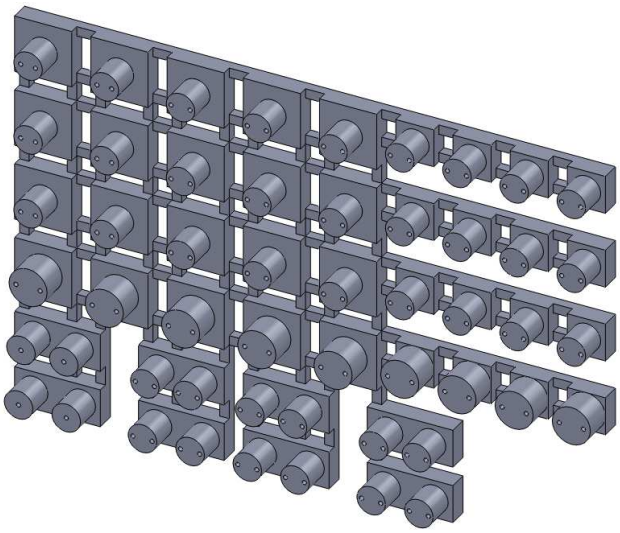

Figure 4.9: SolidWorks model of the plugs

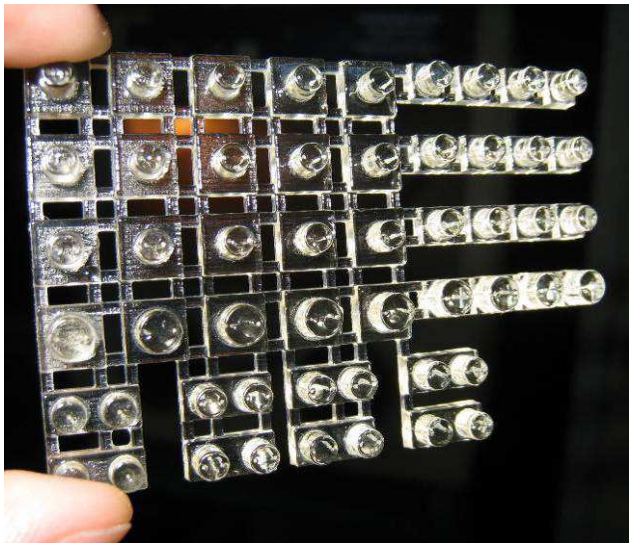

Figure 4.10: 3D printed plugs after washing off

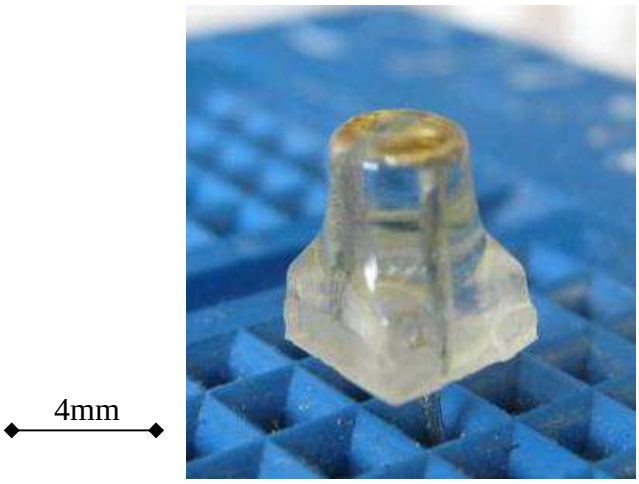

Figure 4.11: Picture of the 2 electrodes plug

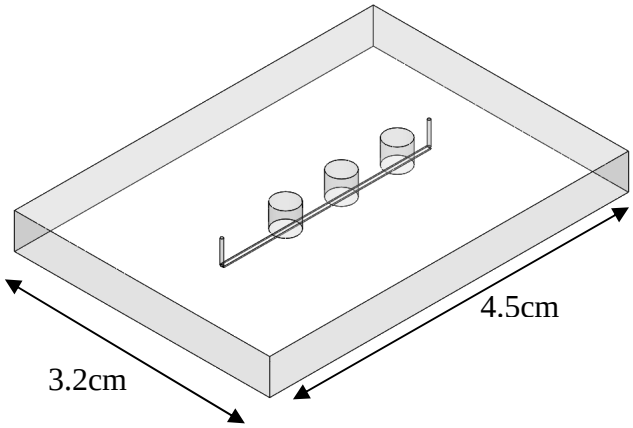

Figure 4.12: 3D view of the glass chip

During the experiments, the plug is inserted in the sensing hole of the glass microchip (Figure 4.12). Some PTFE thread seal tape can be wrapped around the plug to limit the leaking which can occur. The excitation voltage used for the calibration curve was 300 kHz and the amplitude was 4 Vpp with a feedback resistor of the transimpedance amplifier of 1 MΩ. Measurements with static fluid and different flows (20, 50, 100 µL/min) have been done. The schematic on Figure 4.13 shows the setup with the plug inserted in the microchip. During the switch between the different syringes, the record is stopped and restarted when the next syringe is in place and running. This manipulation causes a jump in the signal at each concentration. An example of successive injections of different concentration of NaCl with a syringe pump

(Babybee MD-1001 Syringe pump unit) with a fixed flow rate of 20 µL/min (Babybee MD-1000 Controller) is presented on Figure 4.13. The measurements are taken by a digital multimeter (Keithley 2700) in datalogger mode during the injection of the sample in the microchip for about 5 minutes. This permits us to see the transition between the different concentrations and the signal reaching a stationary value.

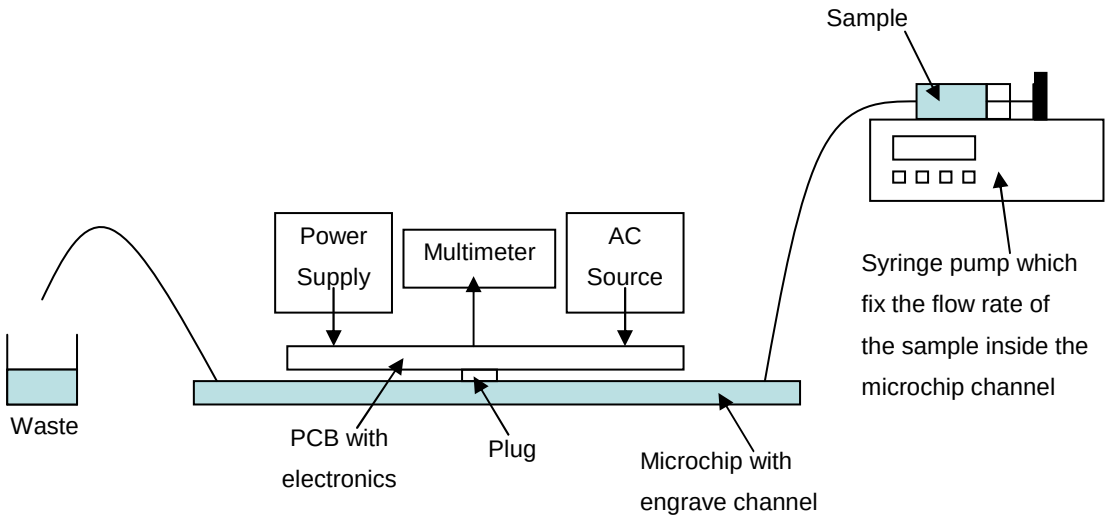

Figure 4.13: Schematic of the experiment in continuous flow

In fact without flow, a drift starts to occur and leads to a slow increase of the signal. This may be due to the heating of the solution which leads to an increase of its conductivity. Figure 4.14 shows the result of such an experiment. It is easy to see the difference between the successive concentrations of NaCl injected in the microchip. It has to be noted that the electronics used at this time included an OPA657 operational amplifier which has a maximum supply voltage of ±5 V. This is why there was a risk of saturation when dealing with concentrations higher than 7 ppm (≈ 120 µM) as it was causing the transimpedance voltage to go near is maximum output swing voltage with the 1 MΩ feedback resistor. The maximum output swing voltage of the OPA657 is ±3.9 V, the signal from the transimpedance pass through a multiplier having a built-in attenuation of 10 then an amplification stage of 2. With a reference signal of 4 Vpp, the maximum output of the amplification stage would be a sinewave with an amplitude of 1.56 V. If the sinewave is low pass filtered, the mean value is 0.78 V.

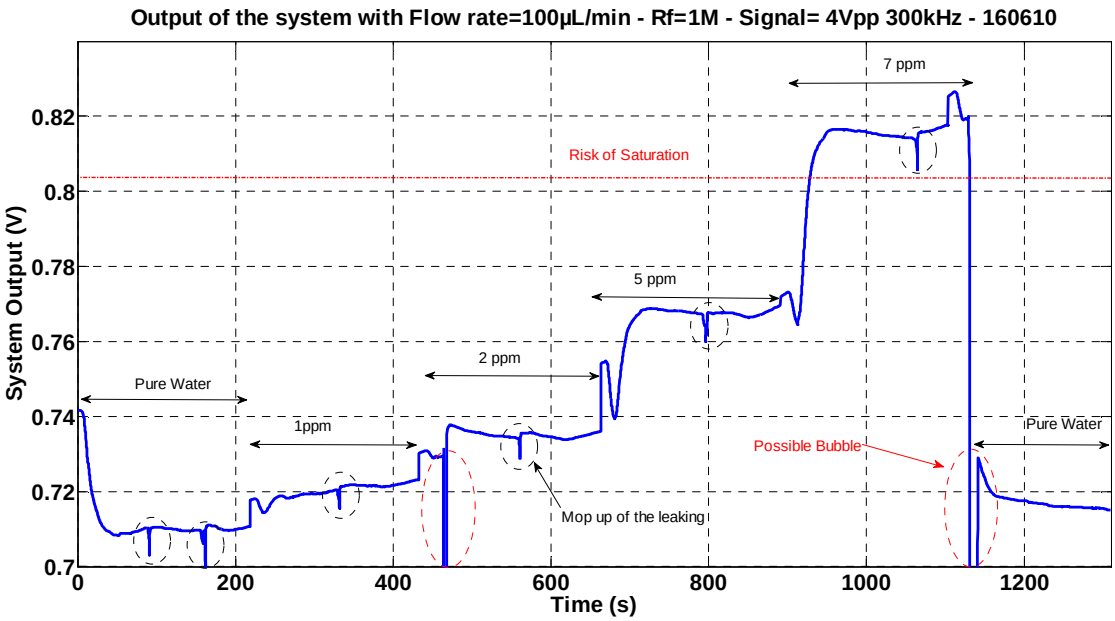

Figure 4.14: Successive injection of NaCl at 100µL/min

Experiments in static flow have also been conduced in order to give a good calibration curve (Figure 4.15).

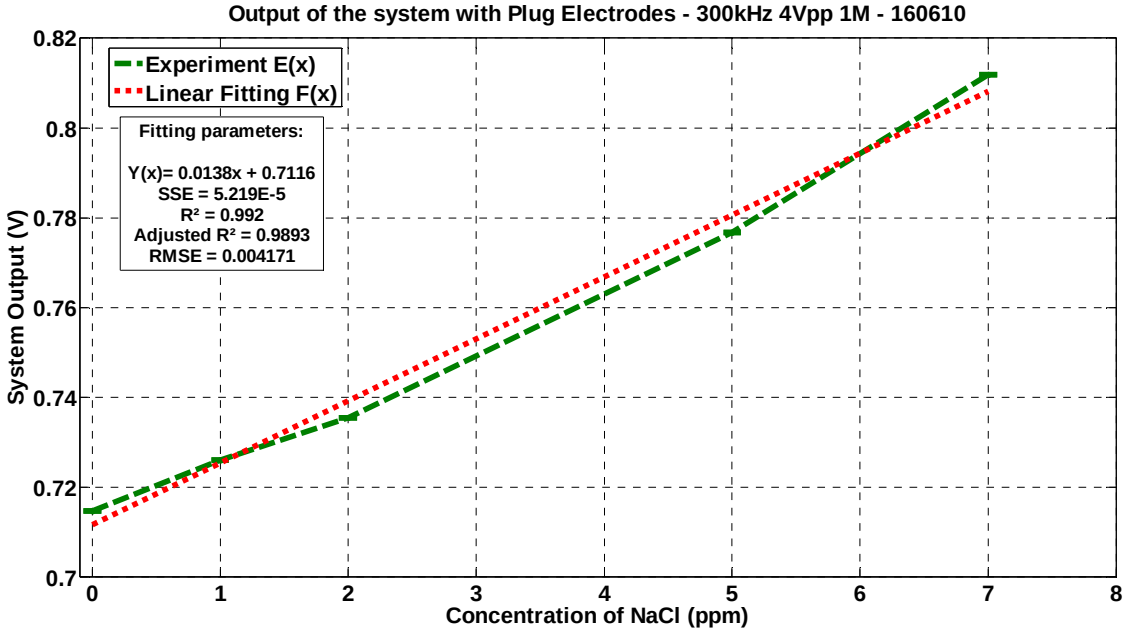

Figure 4.15: Calibration curve of the Plug Electrode system

The slope of the calibration represents a sensitivity of 13.8 mV/ppm by linear fitting. The LOD can also be estimated by looking at the standard deviation of the analyte of

null concentration (Milli-Q Water 18 MΩ.cm^{-1} at 25degC) and the sensitivity of the system, which gives us a LOD of 0.186 µM for NaCl (3σ).

This system had a high sensitivity, albeit with a few problems. The main problem was the principle of the plugs which were inserted in access holes drilled into the microfluidic chip. It was very difficult to prevent the system from leaking, sealing tape made of PTFE was applied to reduce it to some extent. On top of this problem, the possibility of a small dead volume at the plug head will be problematic for its application for separation. Another problem was the fact that only the plug body was made by an industrial process. The electrode painting, wiring and insulation were still done manually, which makes the reproducibility of the cell very difficult and limits the ability to downsize the cell.

4.3.3. On-chip cell

4.3.3.1. PCB/Double sided tape/PMMA microchip

This design used buried electrode made on a printed circuit board (PCB) to allow closer proximity between the electrode and the sensing electronics. The microfluidic chip was made in PMMA and channel was made by milling the sheet with a CNC machine (Datron M7) which allows precision down to the micrometric scale. The insulating layer was a double sided adhesive tape (Sellotape) and thus also bonds the two layers together. The electrodes for this design were separated by a 752 µm gap and the microfluidic channel's width and height were 1 mm. The calibration curve of the system with sodium chloride ranging from 0 to 3 ppm is shown in Figure 4.16:

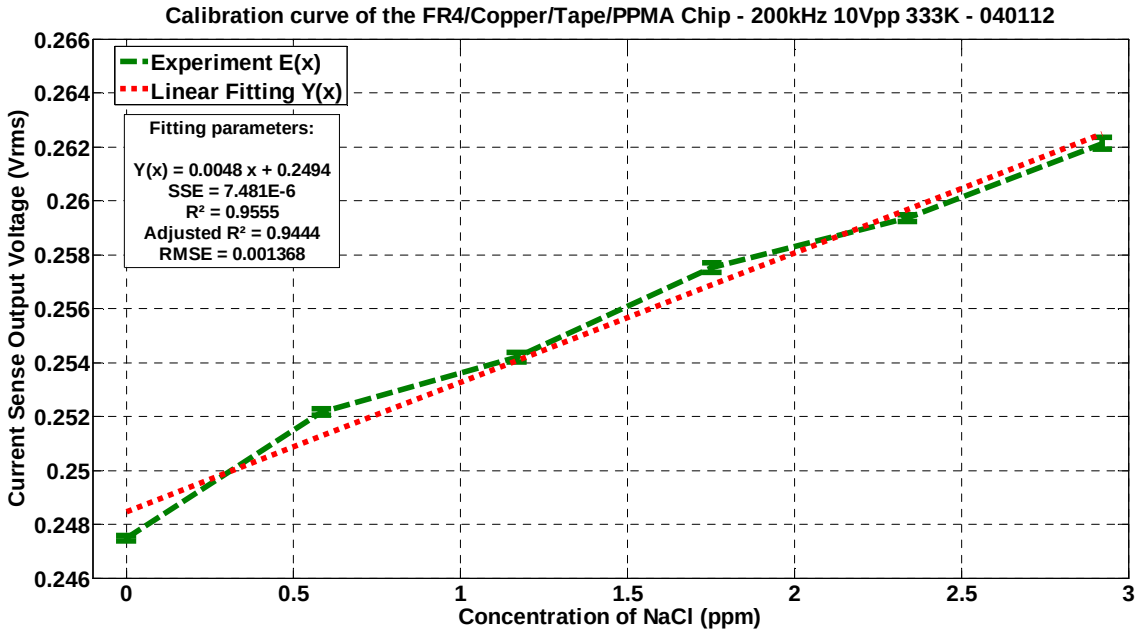

Figure 4.16: Calibration curve of the PCB/Double sided tape/PMMA system

The sensitivity of this system according to the calibration curve is 4.8 mV/pp. This sensitivity is better than for the potted capillary C^4D system but the higher standard deviation degrades the limit of detection to 1.09 µM for NaCl. This higher standard deviation is due to a drift in the measurement values. This drift could be due to the temperature of the channel slowly equilibrating with the temperature of the injected solution but the surface / volume ratio of the 1x1 mm cross section channel is not optimal, hence the slow thermal exchange. It could also be from the double sided tape used as insulating layer which can affect the capacitive coupling with the solution and thus the impedance of the overall detection cell.

4.3.3.2. PCB/PDMS microchip

In this new design, the base of the microchip is composed of a milled PCB which is composed of a layer of fibreglass epoxy commonly called FR4 and a layer of copper of 35 µm thickness (1 ounce per square foot). This PCB features the electrodes, and the interconnections for the electronic components (Resistors, operational amplifier, *etc.*). In the following protocol, the PCB will be referred to as the substrate.

The first stage consists of covering the substrate with a thin layer of PDMS. The PDMS (Sylgard 184, Dow Corning) is first prepared by adding the elastomer and the

curing agent with a ratio of 10:1 in a beaker. The mixture is stirred and degassed for 20 min in order to obtain a better finish. Adding toluene to the mix (25 %) will lower the viscosity allowing a thinner coating to be obtained. A spin coating of the PDMS onto the PCB is done by a Spincoater Model P6700 series (Specialty coating system Inc.), the substrate is fixed to the central chunk by suction. The chuck runs for 7 s at 500 RPM is then ramped up to 1000 RPM for 30 s. Higher RPM can be used for a thinner coating. Once finished, the substrate is cured in an oven for 30 min at 90 °C. The curing can also be done via a hot plate if no oven is available. The coating thickness was measured using a surface profiler (Dektak XT from Brucker) by looking at the surface where the coating has been stripped with a scalpel. Figure 4.17 shows surface profiling results. The coating thickness is estimated at 8 µm. A photo of the PDMS coated PCB is show in Figure 4.18, most of the PCB is covered except the right part which is covered by an adhesive tape to protect the interconnections which will be soldered later.

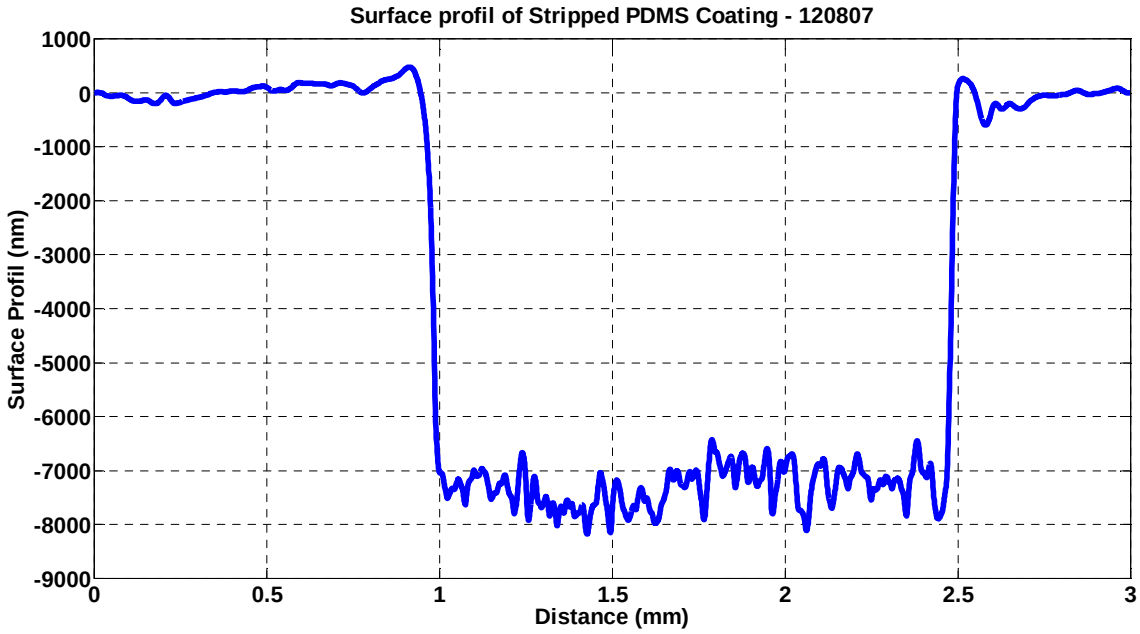

Figure 4.17: Surface profile after PDMS coating

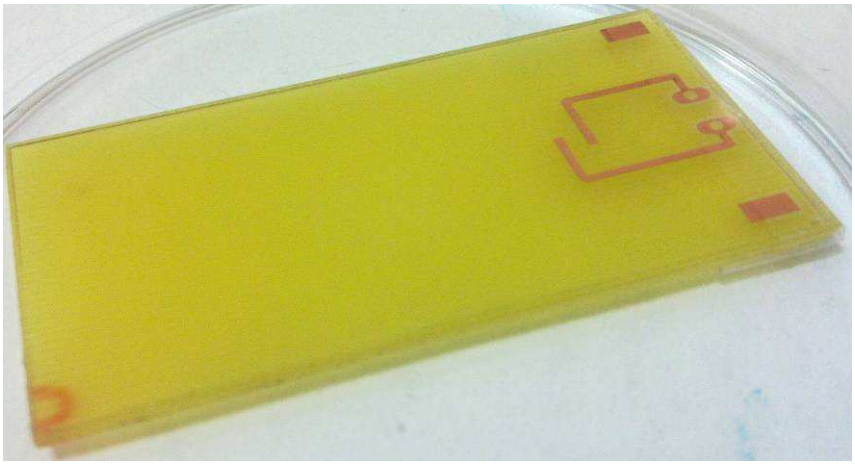

Figure 4.18: PCB after PDMS coating with tape to cover connection holes

The surface profiler can also provide an idea of the coating finish. For example on Figure 4.19, the copper pad has very sharp edge. It can also be seen that the copper which was covered by the photoresist have been partially etched, resulting in a thickness of 24 µm. After coating of the pad, PDMS tend to stack up on the sides which results in a profile of the form shown in Figure 4.20.

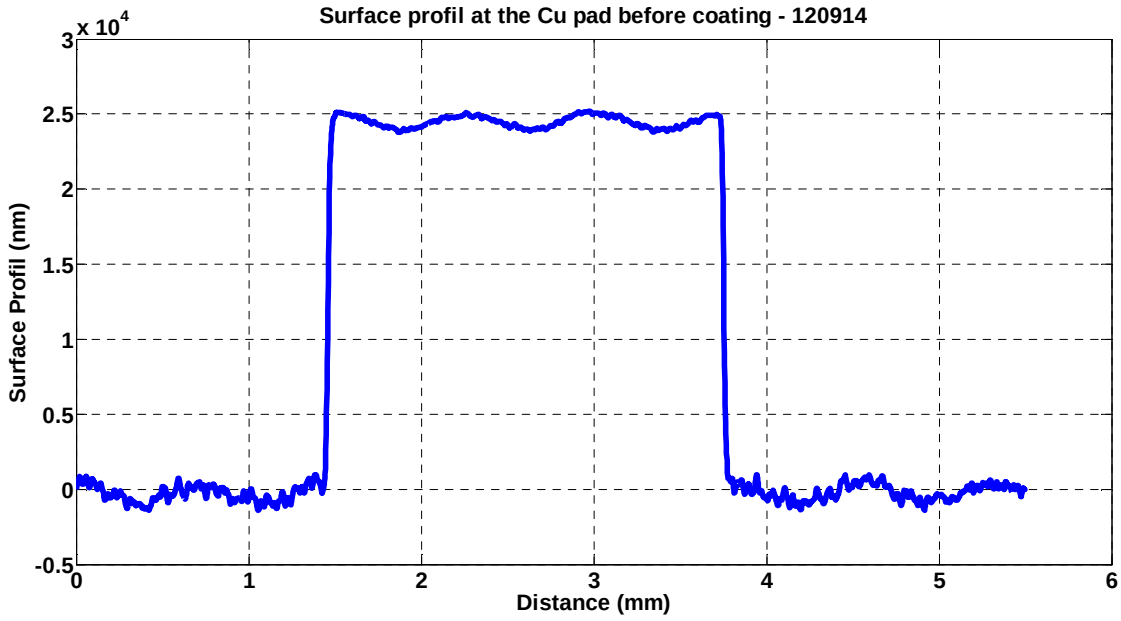

Figure 4.19: Surface profile of a Cu pad before coating

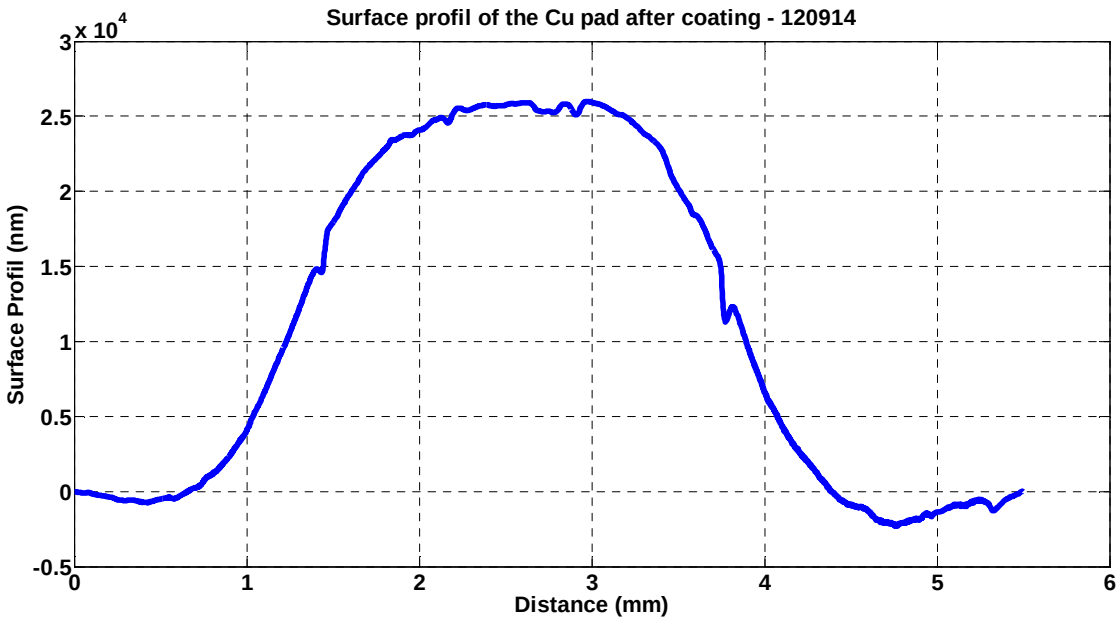

Figure 4.20: Surface profile of a Cu pad after coating

To create the top part, containing the microfluidic channel, a master mould was made using an SU-8 coated silicon wafer for the casting. An aluminium mould can be used for this purpose too if the features are big enough for a CNC machine to reproduce. Figure 4.21 shows the surface profile of the mould used for elastomer casting.

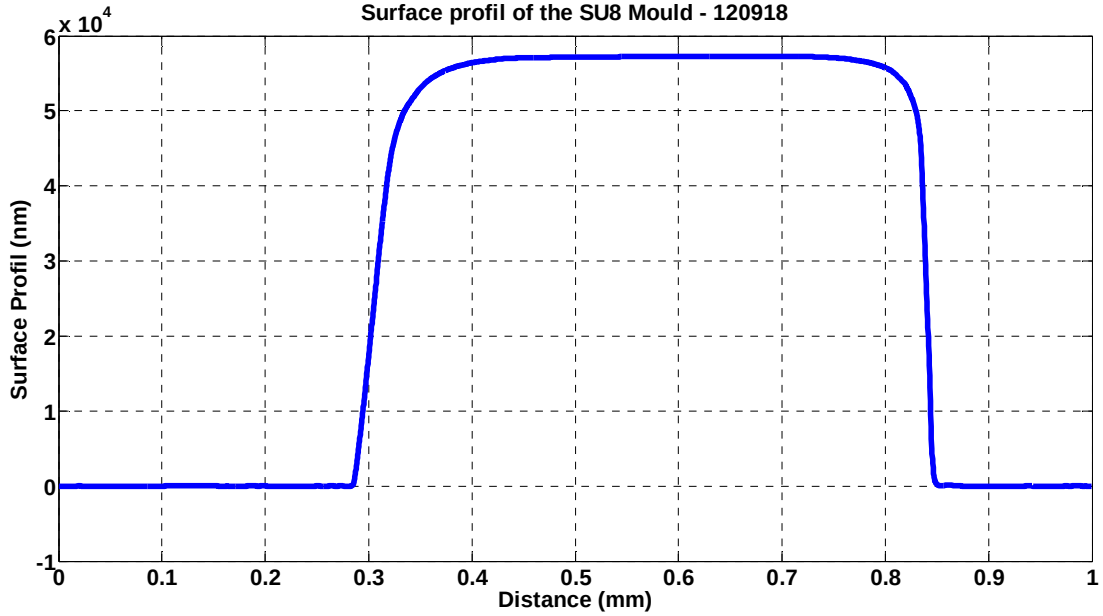

Figure 4.21: Channel profile of the SU-8 mould

The liquid PDMS elastomer was poured into the SU-8 mould and left for curing in an oven for a defined time (45min at 90°C). After curing, the chip is removed from the mould by cutting the wanted shape and pealing it off. The resulting microfluidic channel is an exact copy (Figure 4.22) of the mould which indicates that PDMS is a good material for reproducing micrometric features.

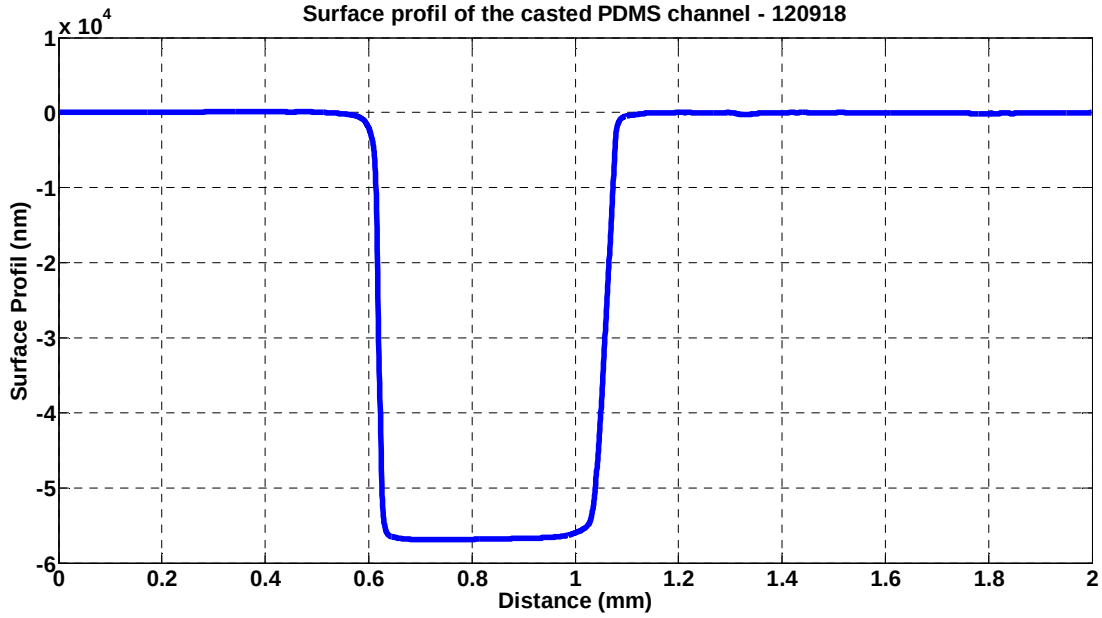

Figure 4.22: Channel profile of the casted PDMS

Once the microfluidic chip is cured, the access holes for the inlet and outlet tubing (Commonly Ø1.6 mm) were punched. Then, the part was cleaned by 5 min sonication in an Isopropanol bath followed by 5 min sonication in a deionised water bath. The chip was dried by blowing compressed air or nitrogen gas. The surface must be as clean as possible prior to the next stage, which is plasma bonding.

For the bonding, both parts are placed in the chamber of the oxygen plasma etcher with their faces to be bonded facing up. The air is slowly replaced by pure oxygen via successive pump out. Then the plasma is created with a chamber pressure of 600 mTorr and a current of 20 mA for 45 s. Usually a voltage between 300-400 V (read on the auxiliary power supply controller) is needed, depending on the oxygen concentration inside the chamber. Higher voltages may cause damage to the surface of the PDMS chip. After plasma treatment, both parts are immediately aligned and put in contact to seal then together. Care must be taken to ensure that no air is trapped between the 2 layers as it can lead to cavities, which weakens the bond. The assembly

is kept at 90 °C for 45 min in order to enhance the bonding strength. Fluidic connections (Raw tubing, Upchurch Nanoports, *etc.*) can then be glued at the access holes prior the use of the chip (Figure 4.23).

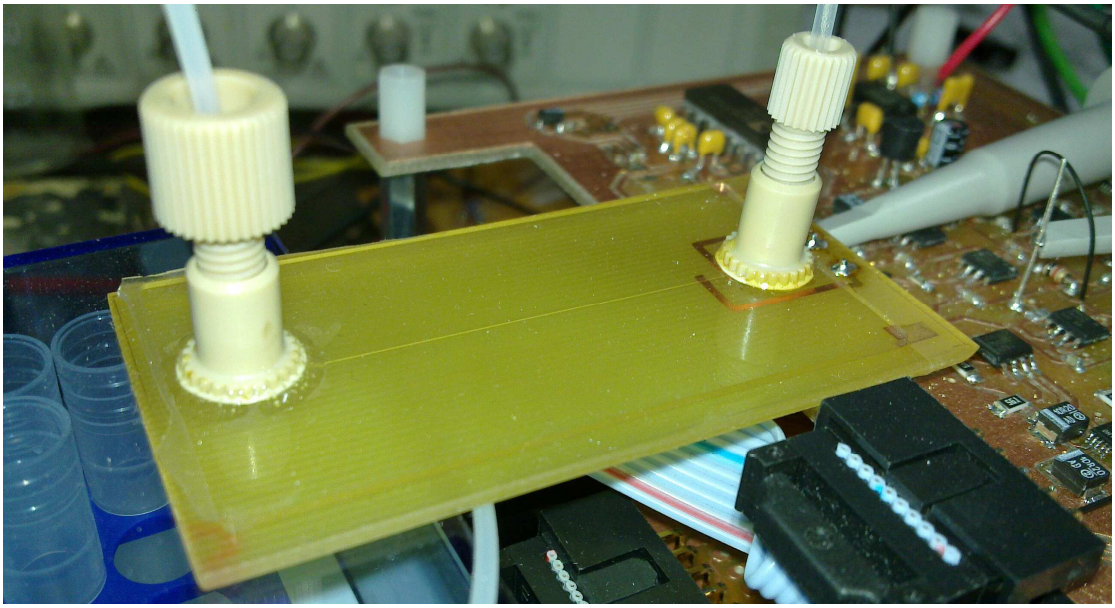

Figure 4.23: PDMS Cell with Upchurch nanoports

The following plot (Figure 4.24) is the calibration curve of such a design with an electrode spacing of 2mm and a channel cross section of 540x60 µm. The frequency used is 300 kHz, the excitation voltage is 20 Vpp and the feedback resistor is 1 MΩ. The sensitivity for NaCl is 10.8 mV/ppm and the limit of detection is 1.265 µM (3σ).

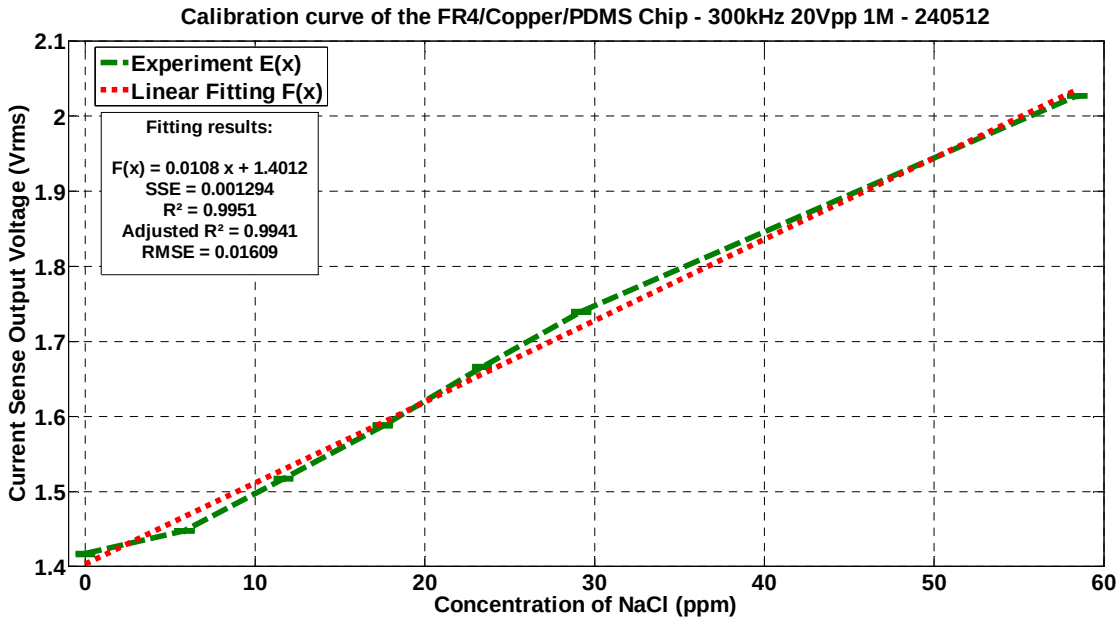

Figure 4.24: Calibration curve of the PCB/PDMS system

4.3.3.2.1. Experimental behaviour of the PCB/PDMS cell for low concentration

Experimentally, the link between the frequency of the excitation voltage, the contactless nature of the cell and the conductivity of the electrolyte can be demonstrated by doing a comparison between different frequencies. For low conductivity electrolyte, the channel conductivity will be low due to the low number of ions. If we consider the liquid electrolyte as a purely resistive element, a low conductivity channel will keep its low conductivity even at high frequency, favouring the stray capacitance at higher excitation frequencies.

Figure 4.25 shows a calibration curve of a low conductivity electrolyte (0 – 1.75 ppm) for frequencies from 30 kHz to 300 kHz. This shows that as excitation frequency increases, the sensitivity of the cell is decreases, leading to the conclusion that the current is more and more bypassed by the stray capacitance.

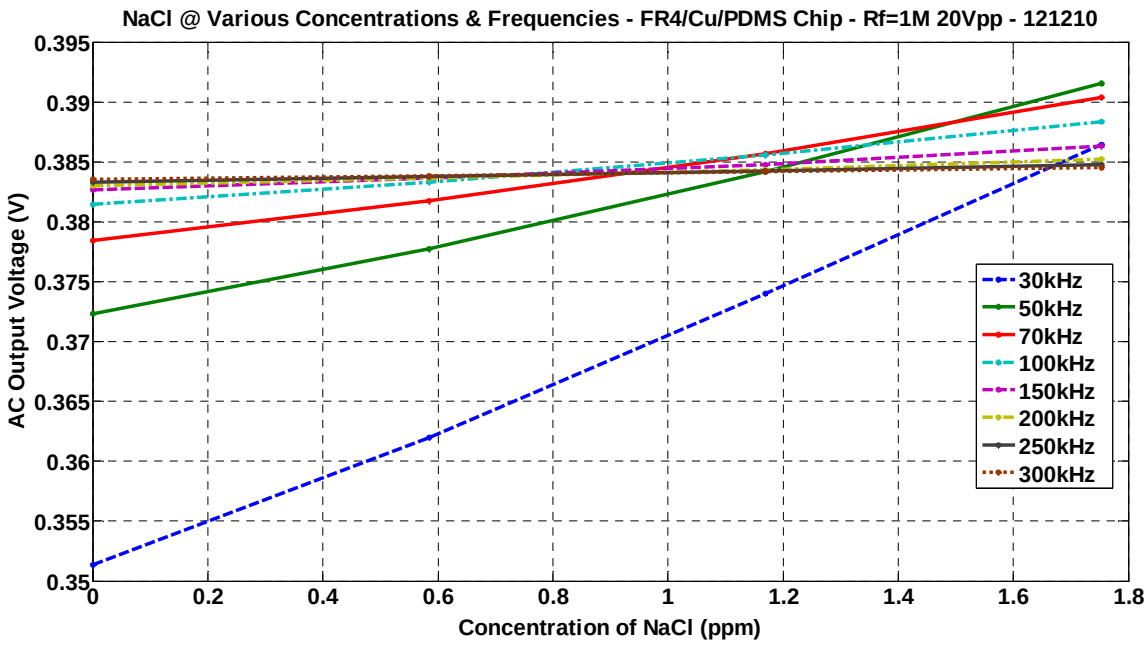

Figure 4.25: Experimental behaviour of a cell for low concentrations

4.3.3.2.2. Experimental behaviour of the PCB/PDMS cell for high concentration

In comparison, Figure 4.26 demonstrates the behaviour of the cell for a highly conductive electrolyte. The low resistance of the cell limits the effect of the stray capacitance C_S. On the other hand, the relative impedance of the capacitive coupling C_W may become non negligible, leading to a plateau for the most concentrated solutions. Increasing the excitation frequency will lower the impedance of C_W, allowing the dynamic range of the system to be extended to higher concentrations. This behaviour highlights the importance of a good capacitive coupling between the electrodes and the electrolyte as lower frequencies can be used. Lower frequency will help limiting the current bypassed by the stray capacitance C_S while keeping the dynamic range reasonably high.

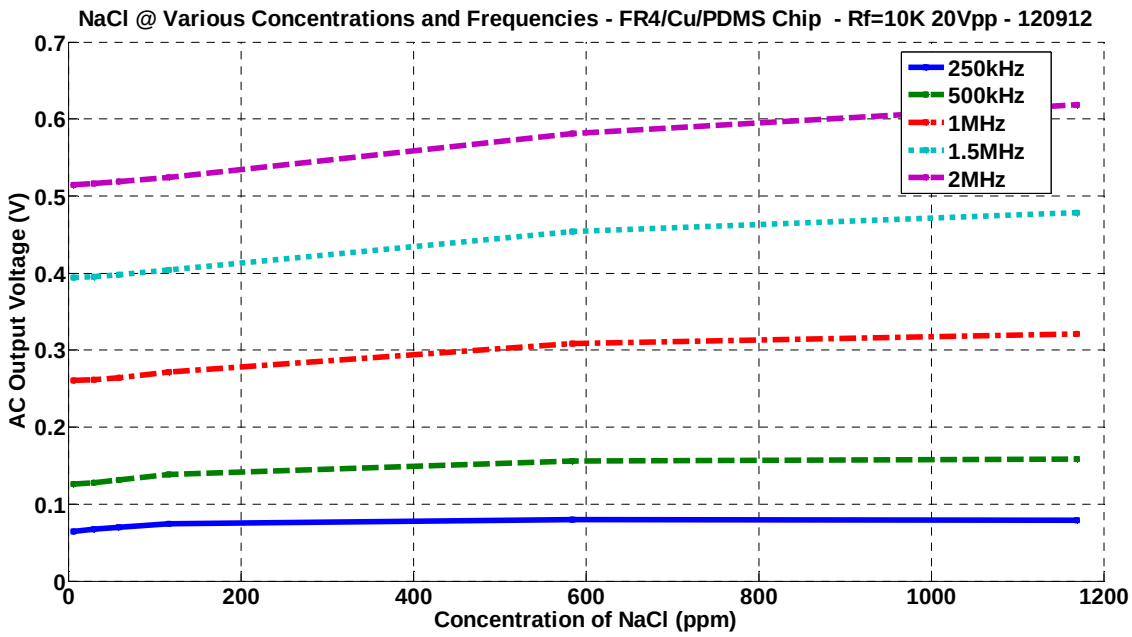

Figure 4.26: Experimental behaviour of a cell for high concentrations

4.3.4. Summary of the chapter

Different designs have been tested for C^4D detection, from the capillary based design to the microchip design. Each electrode implementation has its own advantages and disadvantages. Capillary designs are great for use with existing benchtop systems, and can have very good coupling with the solution due to the large surface area they can have with the electrolyte. They are however not compatible with integration on microfluidic chip. The current technique using syringe needles or wire wrapping are also not optimised for ease of production. Electrode parameter (Pattern, size, spacing, *etc.*) consistency is more feasible when using a technique relying on a mask. Patterned electrodes made from printed circuit boards [60, 61], metal evaporation [78] or sputtering [199] will be similar to one another and are more likely to be compatible with small and medium scale manufacture. Thin electrodes made from metal evaporation are needed for creation of thin insulation layers (to limit stack up effect near the edge of the electrode when using spin coating) but may be problematic when it comes to connecting it to the sensing electronics. Indeed, bonding wires may damage the layer; spring contact pins may be a solution if vibration of the system is avoided. Possible misalignment between the microfluidic channel and the electrode

arrangement is negligible regarding the scale of most channels and the current accuracy of XYZ stages (< 200 nm). However an off-chip detector like the plug design in 4.3.2 may lead to changes in cell characteristic if not secured correctly, similar to the mechanical noise observed in capillary designs [151] (Section 3.6.1).

A system which integrates a microchip holder is a good solution when a definitive microfluidic design is found. It permits a fast and easy replacement of the microfluidic chip in case of failure, ideally the fluidic and electrical connection should also be integrated within the holder. Designing a holder for a capillary design is more challenging and may integrate only the detection cell like the commercial detector from eDAQ [200].

Using an electrode design compatible with a microchip may benefit from the manufacturing techniques and microfluidic concepts discussed in Chapter 2 (Mixing, pumping, flow switching, *etc.*). Furthermore, various materials can be used and it is possible to have channel geometry different to what a manufacturer of fused silica capillary could achieve (Inner diameter, channel shape, *etc.*).

The performances of the different designs will also be depend of the electronics setup used thus the latest designs benefiting from better LOD than older ones. The next chapter will present the electronics used in the detection in greater details but also present the baseline suppression which is an additional function designed into the system in order to enhance the LOD.

Chapter 5 : Design of a conductivity detector with baseline suppression

5.1. Outline of the chapter

Conductivity detection is an universal technique based on the detection of charged species and thus is also sensitive to the background electrolyte. The described system was designed to integrate all the electronics needed for autonomous measurement without the need of bench top equipment (Signal generator, *etc.*). A baseline suppression circuit is integrated into the system to reduce the influence of the background electrolyte over the measurement. Such a circuit is shown to enhance the dynamic range and sensitivity of the system. The principles and the difficulties related to creating this new integrated detection system are discussed (Amplitude accuracy, phase accuracy, *etc.*). Experimental results involving the measurement of different concentration demonstrate the ability of the system in sensing low concentration analytes by monitoring not only impedance change but also phase change of the signal. Automation of the baseline suppression is possible and two automation circuits will be presented. An electrophoresis run done using a homemade setup and a C^4D without baseline suppression is also demonstrated.

5.2. Structure of the measurement electronics

5.2.1. Overview

Figure 5.1 gives an overview of the capacitively coupled contactless conductivity detection (C^4D) system developed in this work. This system has 2 electrodes, one connected to a signal generator which is the “Actuating electrode”. The second electrode is the “Sensing electrode” which is connected to the rest of the detector electronics. The transimpedance amplifier is the core of the detection which has the baseline suppression system connected to its input and thus the electrode. Baseline suppression techniques described in the literature are located after the transimpedance

amplifier as described in Section 3.3.4. But as previously stated, a baseline suppression based on current and located before the transimpedance amplifier is needed to limit the saturation which can occur at higher gain and with higher conductivity electrolytes (Figure 5.2).

This is why a different approach has been proposed in this thesis which is based on baseline current suppression before the transimpedance stage and therefore the rectification stage. With this technique, it is possible to use a high value feedback resistor in the transimpedance amplifier without regard for the baseline current.

The current I_c from the cell is cancelled by the current I_s from the baseline system which gives the current I_m flowing in the transimpedance amplifier. The output voltage V_{out} of the amplifier is given by:

$$V_{out} = -(I_c - I_s) \times R_f = -I_m \times R_f \tag{5.1}$$

After the transimpedance amplifier, the measurement electronics can be composed of noise filtering like a synchronous detection and optionally of additional amplification before the conversion by the ADC. Each stage will be described in more depth in the following parts.

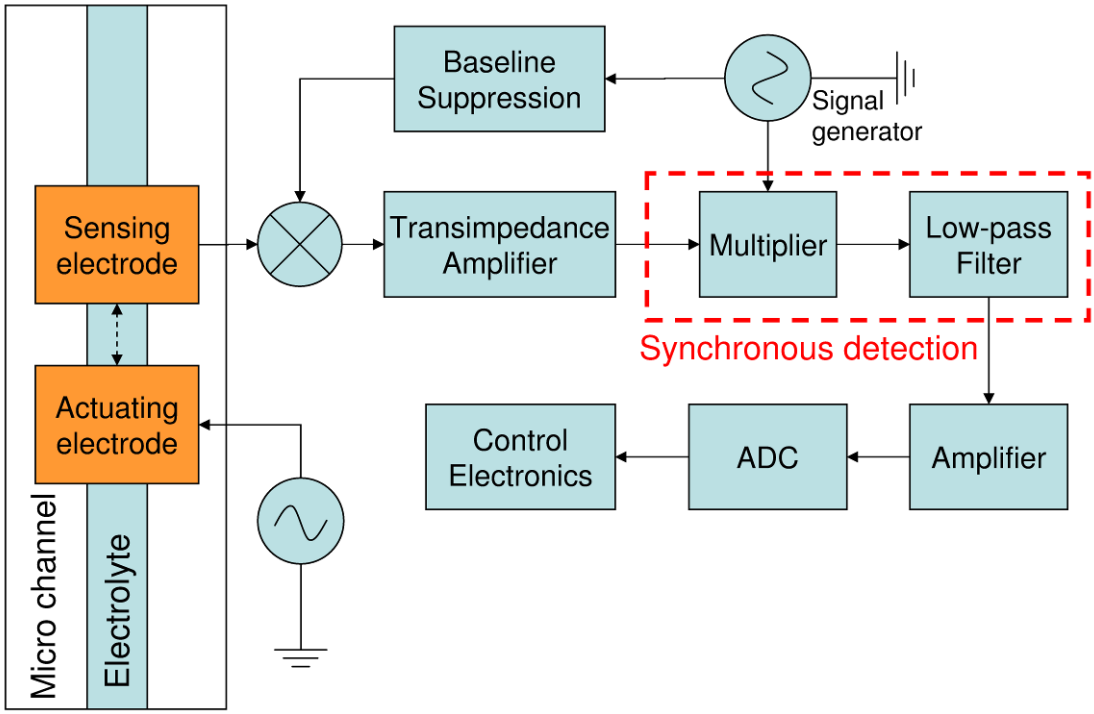

Figure 5.1: Detection system overview

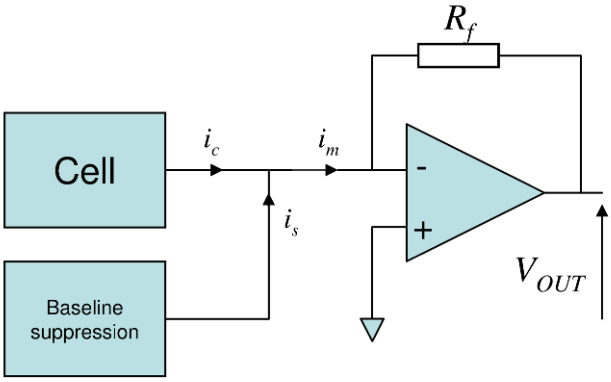

Figure 5.2: Baseline current suppression principale diagram

5.2.2. Baseline suppression principle

The principal difficulty with the proposed baseline suppression technique is the generation of the suppression current I_s. This current needs to have the same characteristics (Shape, Amplitude, Phase) as the current we want to suppress. The signal fed to the cell is a cosine but the amplitude and phase of the baseline suppression signal must change in accordance with the cell impedance and the frequency used. If we consider the current signal of amplitude A and frequency f as:

$$A\cos(2\pi ft) \tag{5.2}$$

And the "counter" signal of amplitude B, frequency f and phase φ as:

$$B\cos(2\pi ft+\varphi) \tag{5.3}$$

The subtraction of the two gives:

$$A\cos(2\pi ft)-B\cos(2\pi ft+\varphi) \tag{5.4}$$

In the case that only the amplitudes are correct (B=A) the resulting signal will be:

$$\begin{aligned} &A\cos(2\pi ft)-A\cos(2\pi ft+\varphi)=A[\cos(2\pi ft)-\cos(2\pi ft+\varphi)] \\ &=-2A\left[\sin\left(2\pi ft+\frac{\varphi}{2}\right).\sin\left(\frac{-\varphi}{2}\right)\right]=2A\left[\sin\left(2\pi ft+\frac{\varphi}{2}\right).\sin\left(\frac{\varphi}{2}\right)\right] \end{aligned} \tag{5.5}$$

The resulting signal is still sinusoidal with a frequency f, a phase φ/2 and an amplitude which is function of 2A and the phase φ.

In the case where only the phase matches (φ =0):

$$A\cos(2\pi ft) - B\cos(2\pi ft) = \cos(2\pi ft)[A - B] \tag{5.6}$$

The resulting signal is a cosine of frequency f and with an amplitude dependent on A and B. This is why correct suppression current, matching both phase and amplitude, needs to be applied, in order to cancel the current from the cell.

5.2.3. Signal generator

As the system needs to be as autonomous as possible and operate in remote sites, off the shelf laboratory signal generators are not suitable. They are an effective solution for bench experiments due to their wide bandwidth and voltage output, but here, it is more appropriate to use an integrated circuit dedicated to waveform generation. These commercial integrated circuits are called direct digital synthesis (DDS) devices and are able to synthesise sinusoidal, square and triangular waves at various frequencies and be controlled by digital commands. There is no need for external components for frequency setting like on the MAX038 as used in [115, 142, 164]. A microcontroller using a R-2R ladder could be used to generate sinewave, however kHz frequency signal will require a high cycle per seconds microcontroller. The generation process of a sinusoidal wave can be explained by the block diagram shown in Figure 5.3:

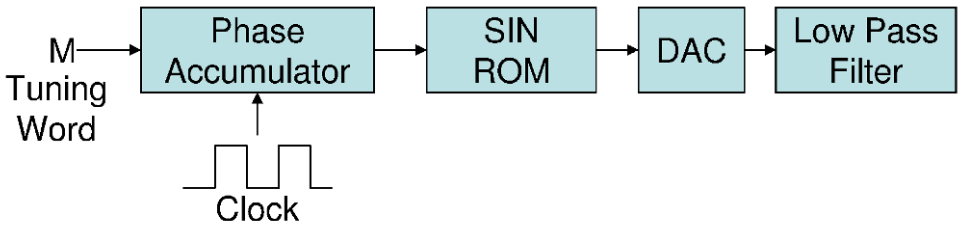

Figure 5.3: Block diagram of a basic DDS system

In order to build an analogue sine wave, a clock is fed into the phase accumulator, which is basically a counter. The content of the phase accumulator is successively

incremented by the value M, called the tuning word. The tuning word determines the jump size in the table (SIN ROM) containing the amplitude for the DAC to be read. The phase accumulator needs to be big enough (Ranging from 24 to 48-bit wide) in order to produce the smallest frequency resolution while coupled with a high frequency clock. However the SIN ROM address range is smaller than the phase accumulator word, and this aspect requires the phase word to be truncated to the SIN ROM address size. There is also commonly a size difference between the DAC resolution and the amplitude read from the SIN ROM, which therefore needs to be truncated for a second time. Spurs in the output signal spectrum from successive truncations exist but are negligible compared to the quantization noise of the DAC [201].

Filtering should be placed at the output of the DDS for antialiasing purposes. A low pass filter with a bandwidth of a third of the clock or lower is recommended for Analog Device DDS components [202, 203].

The amplitude of the DAC of the DDS is fixed by its internal reference but some DDS devices have the possibility to be connected to external analogue signal (typically from a DAC) for control of the full scale output voltage. It is this latest feature which will be used in the baseline suppression system to control the amplitude of the cancelation current (A = B), along with extra external programmable gain amplifiers (PGAs) to provide accurate fixed gain to the signal (Figure 5.4). The DDS, scale control DAC and PGA are set up using a microcontroller (µC or MCU). The DDS used (AD9834), if used in conjunction with a 75 MHz oscillator (C Grade), has a maximum frequency output of 37.5 MHz. This frequency can be tuned with 0.28 Hz steps (less if a lower frequency oscillator is used) due to the 28-bit phase accumulator. The phase is set by a 12-bit register which gives a phase step of (Eq. 5.7):

$$\Delta\varphi = \frac{2\pi}{2^{12}} = \frac{2\pi}{4096} \approx 0.00153 radians \qquad (5.7)$$

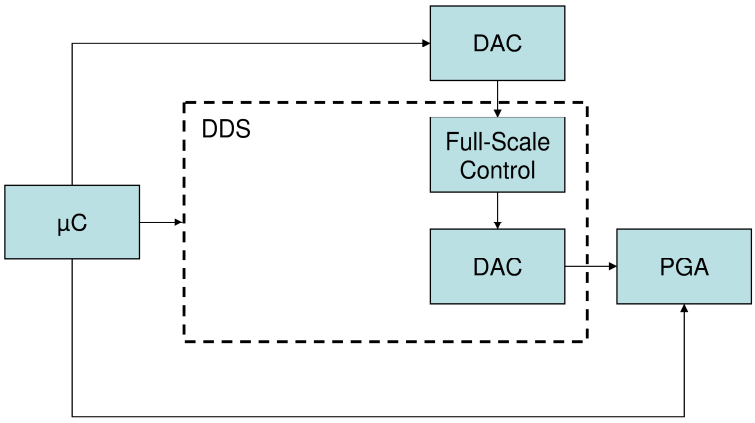

Figure 5.4: Diagram of the amplitude control of the DDS

5.2.4. Transimpedance amplifier

The transimpedance amplifier (TIA) is the main component of the detection; it converts the current into a voltage so it can be measured without disturbing the cell. In order to the detection circuit to have a large dynamic range, an amplifier with a wide output swing voltage is preferable. This allows the use of a large feedback resistor for high gain / sensitivity or a large dynamic range with a lower feedback resistor. The baseline suppression system acts before the amplifier to extend the effective dynamic range of a high gain amplifier by dynamically suppressing the current fed to the amplifier. The subtracting current need to be gradually increased in case of saturation (output from the transimpedance amplifier is clipping) so the output returns to the normal operating window of the component.

Using LT Spice we can simulate the transimpedance stage and assess the behaviour of the output signal when varying parameters of the cell or the transimpedance amplifier itself. Doing so might help to choose the amplifier suitable for the system (Slew rate, input bias current, *etc.*). For example we can model the cell followed by different transimpedance amplifiers and observe the output of the amplifier. In the case of the LT1169 which is a low noise, picoampere bias current, JFET input amplifier, the problem is the typical slew rate of 4.8 V/us. Using an excitation frequency of 250 kHz with an amplifier having an output swing voltage of 25 Vpp is thus not possible without great distortion of the signal.

The LT118A is however a high speed operational amplifier with a minimum and typical slew rate of respectively 50 V/us and 70 V/us. Such characteristic avoid the distortion of the signal but a small voltage offset can be seen comparing to the LT1028 which is a low noise, high speed, precision amplifier. This error may be due to the input bias current which is amplifier by the large feedback resistor As the baseline suppression is located before the TIA, it may be possible to correct the offset voltage produced by the current flowing to the negative input.

The operational amplifier used for the measurement characterising the detection cells described in Chapter 4 were OPA380 and the OPA657 from Texas Instrument. Both amplifiers have a high gain bandwidth, low voltage noise and current noise. Thus a high value of feedback resistor can be used for current to voltage conversion without having problem with current input noise as the JFET input stage has current noise in the order of fA/√Hz. The OPA827 is used in the baseline suppression system as it provides similar characteristic to the OPA657 with the advantage of larger output swing voltage due to the supply rail accepting voltages up to ±15 V. Its typical slew rate is 28 V/us which give a FPBW of 372 kHz for a 24 Vpp output swing voltage (V_s –3 V).

5.2.5. Baseline suppression system

A schematic of the proposed suppression system is shown in Figure 5.5:

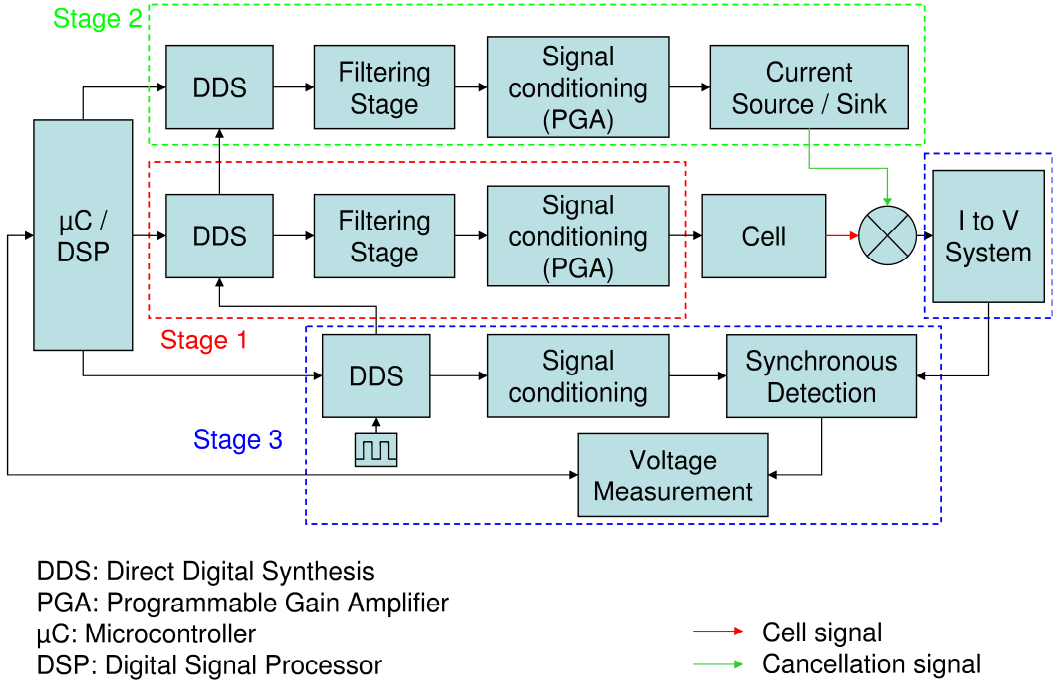

Figure 5.5: Block diagram of the baseline suppression

To achieve the required frequency and phase, the suppression signal is created by another DDS (Stage 2 in Figure 5.5) of the same type as the cell stimulus generator (Stage 1 in Figure 5.5) where both are synchronize by having the same clock source and release from reset at the same time. Moreover, having the same length of track on the circuit board for the clock signal for both DDS chips ensure that there will not be any phase difference in the shared clock signal. Even simple DDS systems have the ability of frequency modulation (FSK) or phase modulation (PSK) therefore we use the latter to accurately control the phase difference between the two DDS. The models (AD9834) used have a phase register of 12-bit which sets the accuracy of the phase. According to (5.7) the smallest phase change possible is 0.00153 radians or 0.088 °. This accuracy is enough for a good phase matching because according to equation (5.5), the error will be 0.076 % of the cancellation voltage amplitude.

The other critical point is the amplitude matching of the suppressing signal. The signal from the DDS is generated from an internal DAC which has a fixed or variable

full-scale. In the case of fixed full-scale, an additional gain or attenuation stage which can be digitally controlled is needed to create the required amplitude.

One of the solutions evaluated was to use an inverting and non-inverting operational amplifier topology with a digital potentiometer used as a rheostat (AD5293) and analogue multiplexer (ADG1408) linked to a resistor bank (Figure 5.6).

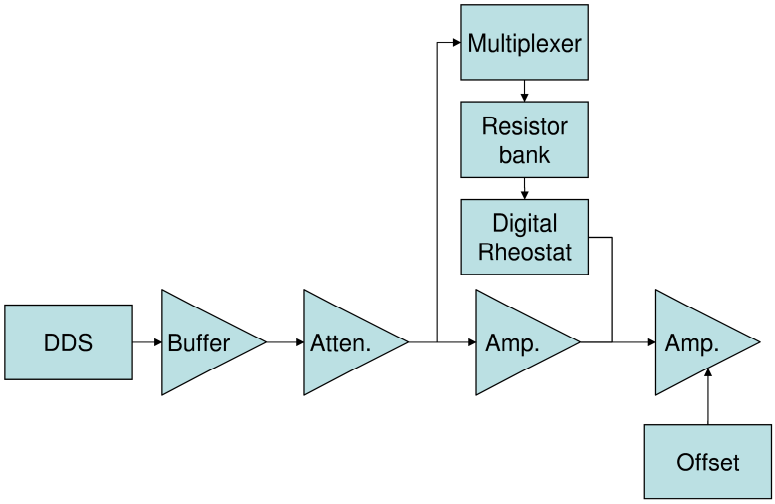

Figure 5.6: Block diagram of the amplitude control

The analogue multiplexer (IC12) (See appendix F) was used for coarse gain change by switching a resistor array of 10 kΩ increment (From 0 Ω to 40 kΩ). The fine gain tuning was done by a 20 kΩ digital potentiometer in rheostat mode (A and W pins connected together) with 10-bit resolution, which provides a theoretical increment of approximately 19.5 Ω (±1%). This provides a gain step of 0.00195 if associated with a 10 kΩ input resistor (R4). It permits a good accuracy for the suppression signal amplitude. However, at frequency above 100 kHz, problems can arise with this system.

The potentiometer‘s architecture comprises of resistors and switches. The resistance of the resistors in the signal path of a particular code (digital code for the desired resistance value), combined with the switch parasitics, pin, and board capacitances, creates a RC low-pass filter, which determines the maximum AC frequency that can be passed through the potentiometer. Lower value potentiometer settings have higher bandwidth due to the lower value of their resistor segments.

According to the datasheet, the AD5293 has a -3 dB bandwidth of 520 kHz for its 20 kΩ version. It is also possible that a high frequency, AC signals may cause

variation in the internal switch on-resistance (R_{on}), leading to some nonsymmetrical attenuation and, therefore, signal distortion. Choosing a higher end-to-end resistor option reduces the contribution of the switches' internal resistance to the total resistance, leading to better THD (Total harmonic distortion) performance but a lower bandwidth.

The analogue multiplexer used (ADG1408) can also induce problems when introduced in an amplification circuit. The MOSFET switches used in the device have a resistance which varies as a function of the applied analogue signal. This difference is referred to as "On-resistance flatness" (ΔR_{on}) in the datasheet. This variation will create DC errors and distortion when coupled with AC signals. In order to minimize the effect in amplification circuits, we can choose a higher value resistor to make the ΔR_{on} negligible with respect to other resistors, but this may lower the bandwidth and make the circuit more sensitive to leakage and bias current. We can also introduce the switches in both the input node and the feedback loop. As the switches are normally matched, they will vary by the same magnitude at both nodes (only if the input resistor and feedback resistor values are in the same order of magnitude).

It is important to know how much parasitic capacitance has been added to the amplifier input as a result of adding a multiplexer, because any capacitance added to that node introduces phase shift to the amplifier closed loop response. If the capacitance is too large, the amplifier may become unstable and oscillate. A small capacitance across the feedback resistor may be required to stabilize the circuit. This type of compensation is called "Feedback Zero Compensation" or "Phase lead Compensation".

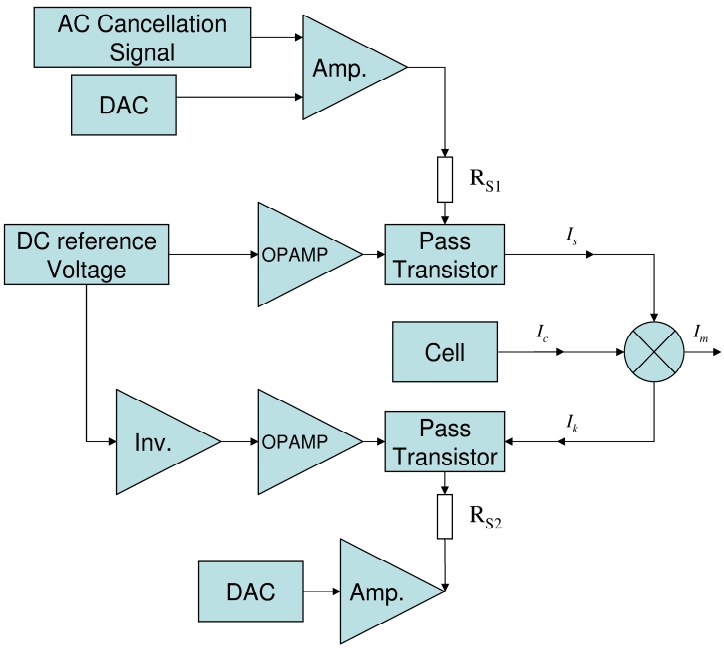

Figure 5.7: Block diagram of the voltage to current conversion for the cancelation current

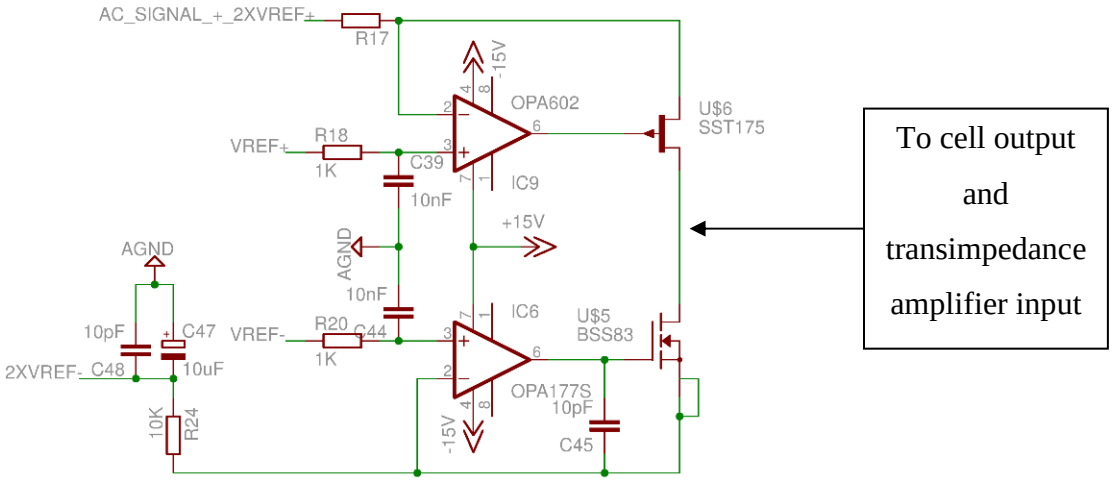

Figure 5.8: CAD design of the voltage-current converter

The amplitude of the current between the two transistors is a function of the transfer function of the voltage to current converter (Figure 5.7 and Figure 5.8 – Appendix G), which is fixed at 100 µA/V with a 10 kΩ resistor (R_{S1} and R_{S2} – R17 and R24). This voltage to current converter uses two voltage to current converters (OPAMP + Pass transistor), which are connected in series with each others and the node between the two being connected to the cell output / transimpedance input.

The top branch of the arrangement is for sourcing the current with a bias set to 300 µA (Function of the reference voltage). This bias is due to the bottom of the sense resistor (R17, R_{S1}) being clamped at a reference voltage of +3 V_{DC} by the operational amplifier and a voltage of +6 V_{DC} applied at the top of the resistor.

The bottom branch is however used to create a sinking current which is set at -300 µA. The addition of the two sources is therefore null in theory. The system can be balanced when no AC cancelation signal is applied at the top of the resistor R_{S1} ($I_s = I_k$) by the means of the top or bottom DAC (Figure 5.7). However, when a signal is applied at the top branch, the current become unbalanced and is function of the voltage applied and the value of R_{S1}, thus the need for an accurate control of the AC cancelation voltage in order to generate an accurate cancellation current.

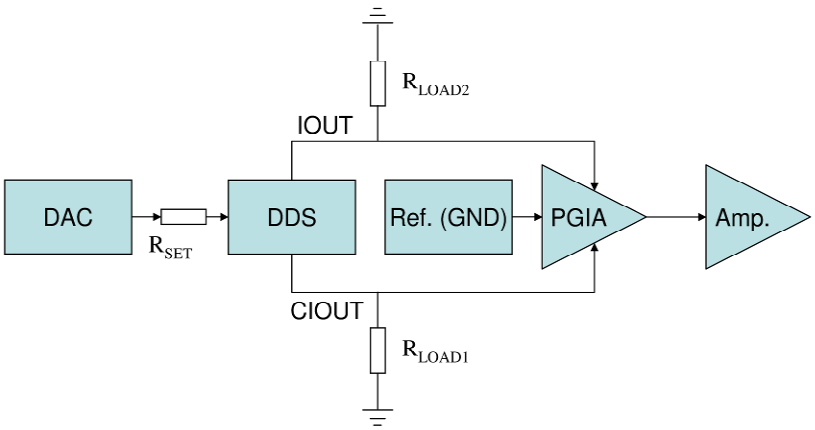

Figure 5.9: Block diagram of the digitally controlled suppression voltage generator

In the next design version, the voltage from the suppression signal generator circuit is controlled digitally by two components (Figure 5.9 – Appendix H). The first component is a 16-bit DAC with an internal reference which can supply up to 3V (AD5663R). It is connected to the FS Adjust pin (Full scale) of the DDS (IC4 AD9834 – See appendix H) which includes an amplitude modulation capability (ASK) through this pin. The current output of the DDS is then a function of the voltage applied by the DAC (V_{DAC}), the load resistors (R_{LOAD}), an external resistor (R_{SET}) and a voltage reference (V_{REF}) as given by (5.8).

$$V_{OUT} = I_{OUT} \times R_{LOAD} = \frac{18 \times (V_{REF} - V_{DAC}) \times R_{LOAD}}{R_{SET}} \tag{5.8}$$

The AD9834 features a complimentary output (IOUT and IOUTB) which is connected to an instrumentation amplifier (AD8250) which has a digitally controlled gain of 1, 2, 5 or 10 (PGIA). Therefore, the sinusoidal signal can be accurately controlled over a wide range of voltage and frequency without suffering instabilities and attenuations. Further amplification is provided by a fixed gain voltage amplifier (IC8 OPA602) which has a better slew rate than the instrumentation amplifier, its full power bandwidth (20 Vpp) is given for 570 kHz.

5.2.6. Synchronous detection

As seen in the previous chapter, synchronous detection can be used for the rectification and filtering of the signal from the transimpedance amplifier. The output signal of the synchronous detector is only a function of the component of the measured signal which has the same frequency as the reference signal fed to the multiplier. The phase difference between the two input signals is important, and must be zero ($\cos(\varphi_1-\varphi_2) = \cos(0) = 1$) for maximum response. To generate the reference signal we can use another DDS using the same clock as the others.

Experimentally, the adjustment of the phase shift is achieve by changing the phase word of the chip register in order to obtain maximum amplitude at the output of the multiplier, or by monitoring the phase shift with an oscilloscope (Tektronix TDS 3014B) between the output of the current to voltage converter and the second input signal of the multiplier. The amplitude of the reference input signal is also important because the output is directly proportional to it. The reference signal from the DDS is therefore amplified to increase the output amplitude of the multiplier.

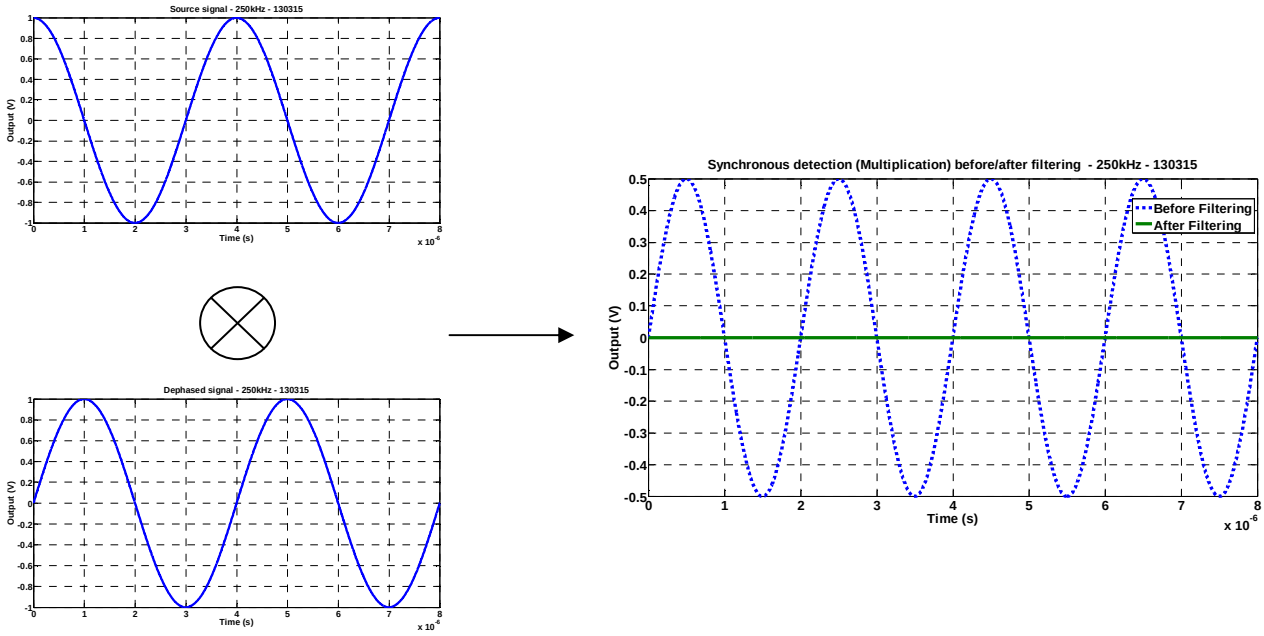

Figure 5.10: Example of multiplication of one cosine signals with one shifted by 90°

For an automated system, the phase can be found by detecting the zero crossing point, after low pass filtering of the multiplier output. Which means that the signals are dephased by 90° in regard of each other ($\cos(\varphi_1-\varphi_2) = \cos(90) = 0$) (Figure 5.10). With the output of the synchronous detection coupled with a zero crossing comparator, it is possible to sweep the phase until a sign change of the filtered multiplier output signal is detected. This feature can also be used for baseline suppression phase matching, once the corresponding perpendicular phase is known, the DDS for the baseline suppression signal can be set according to (5.9):

$$\varphi_{BASELINE} = \varphi_{90} - 90° \tag{5.9}$$

It is also possible to put both signals in anti-phase configuration which just changes the sign of the resulting signal ($\cos(180) = -1$), this is useful if an inverting amplifier follows the synchronous detection.

5.2.7. Implementation of the baseline suppression automation

5.2.7.1. Use of one multiplier

For the baseline to be used with an autonomous system, a procedure to automatically suppress the baseline is required. To do so, the cell current I_c needs to be in anti-phase with the current from the baseline suppression I_s and of similar magnitude. To achieve this, a series of steps are undertaken, which are controlled by the microcontroller (µC or MCU).

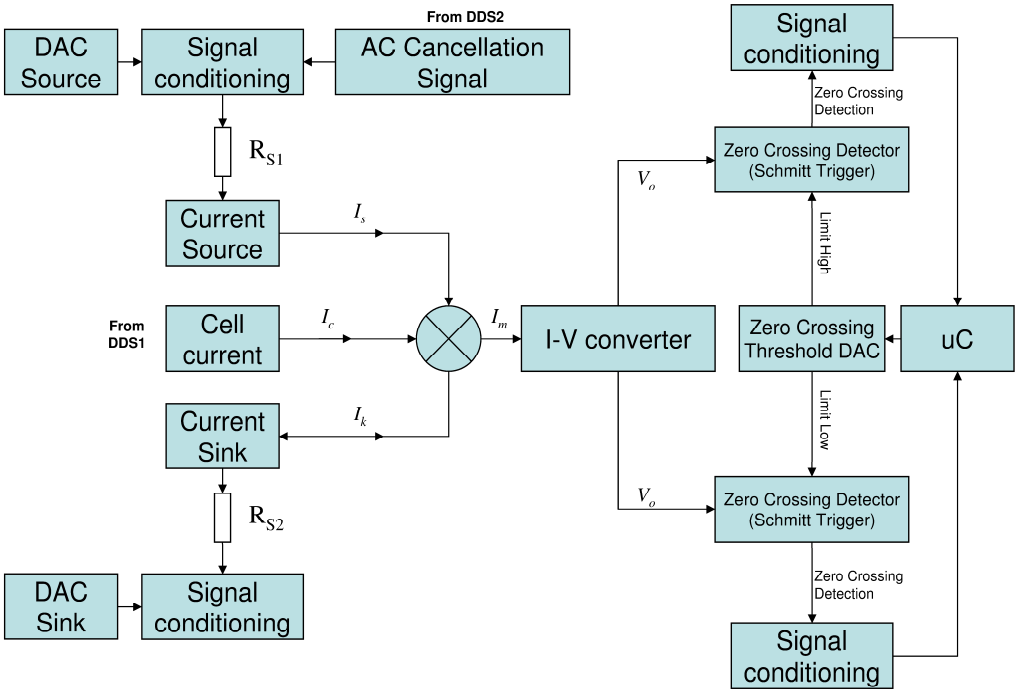

Figure 5.11: Schematic of the DC current balancing of the Source/Sink branch

The first step, called “balancing”, is DC only (Signal from the transimpedance amplifier is low pass filtered), its role is to equalize the source and sink currents (I_s and I_k) from the baseline suppression stage (See Figure 5.11). The source DAC output which fixes the voltage across the top sense resistor (R_{S1}), and thus the current, is swept until it triggers the zero crossing detector (If the Schmitt trigger threshold is

zero, other values could be set by a DAC). Two variable triggering points can be created around zero by the use of a second Schmitt trigger and a DAC (DAC Threshold), such a configuration can help track the baseline drift by creating a window around zero.

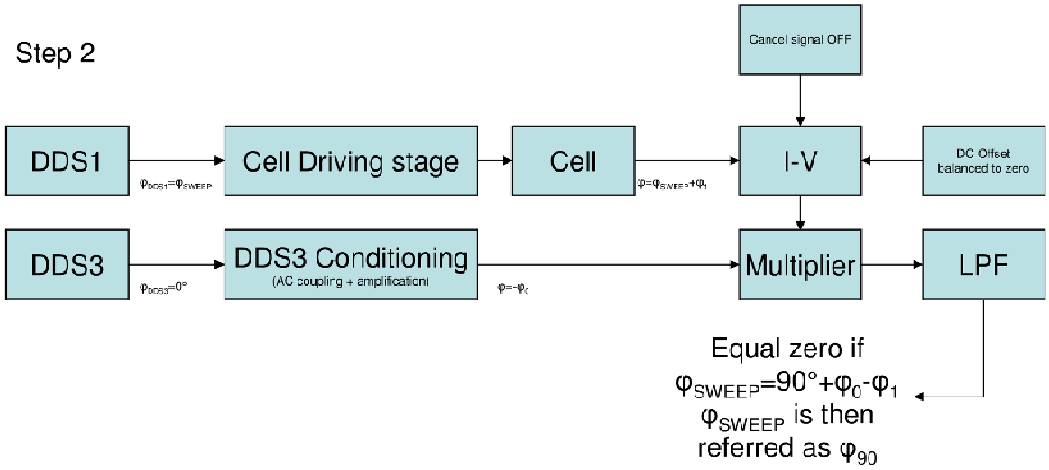

Figure 5.12: Step 2 of the automated baseline suppression

The second step (Figure 5.12) is to use the multiplier from the synchronous detection to synchronise in quadrature the reference signal with the signal from the cell in order to determine its phase in relation with the reference signal (The filtered synchronous detection output is equal to zero when this condition is achieved). The reference signal is generated by a third DDS (Stage 3 DDS in Figure 5.5) which is AC coupled then amplified before the multiplication. This particular signal conditioning creates an unknown phase shift φ_0 which can be approximated by simulation with LT Spice by looking at the frequency of a buffered AC signal, capacitively coupled to an amplifier through a capacitor (See Figure 5.13).

The experimental results differ from the simulated one for frequencies higher than 20 kHz. The experimental results were obtained by subtracting 90° from the phase needed to achieve the quadrature between the reference and the cell signals (See Figure 5.14) which gives the results in regards to DDS1 as the reference (A positive phase shift is a signal delay on the output of DDS3). At higher frequencies, the cell produces a dephasing, which explains the difference.

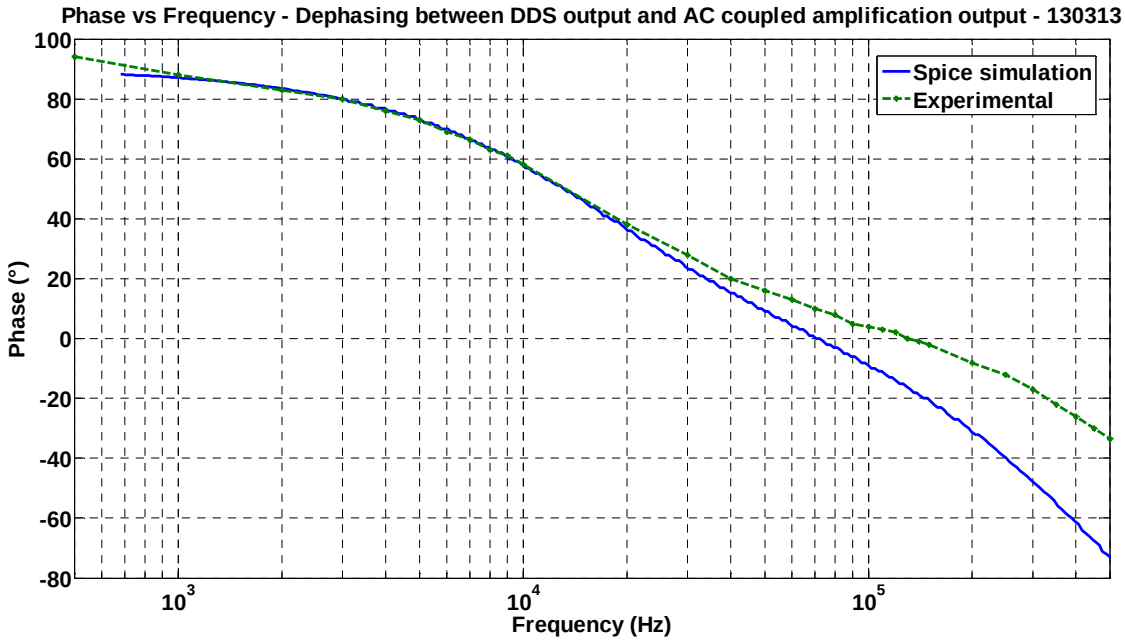

Figure 5.13: Reference signal phase versus frequency

The final quadrature phase value (φ_{90}) in reference of DDS1 will be a function of this unknown signal conditioning phase shift (φ_0) and the phase shift due to the cell and the cell driving stage (φ_1):

$$\varphi_{90(DDS1)} = 90° + \varphi_0 - \varphi_1 \tag{5.10}$$

$$\varphi_{90(DDS3)} = -90° - \varphi_0 + \varphi_1 \tag{5.11}$$

Figure 5.14 shows the experimental results of the output of the filtered synchronous detection while sweeping the phase at different frequencies. The phase value of the zero crossing (φ_{90}) from the previous plot can be extracted from this graphic. It can be noted that the amplitude of the output signal is linked to the amplitude of the input signals which is frequency dependant due to the AC coupling of the signal from DDS3.

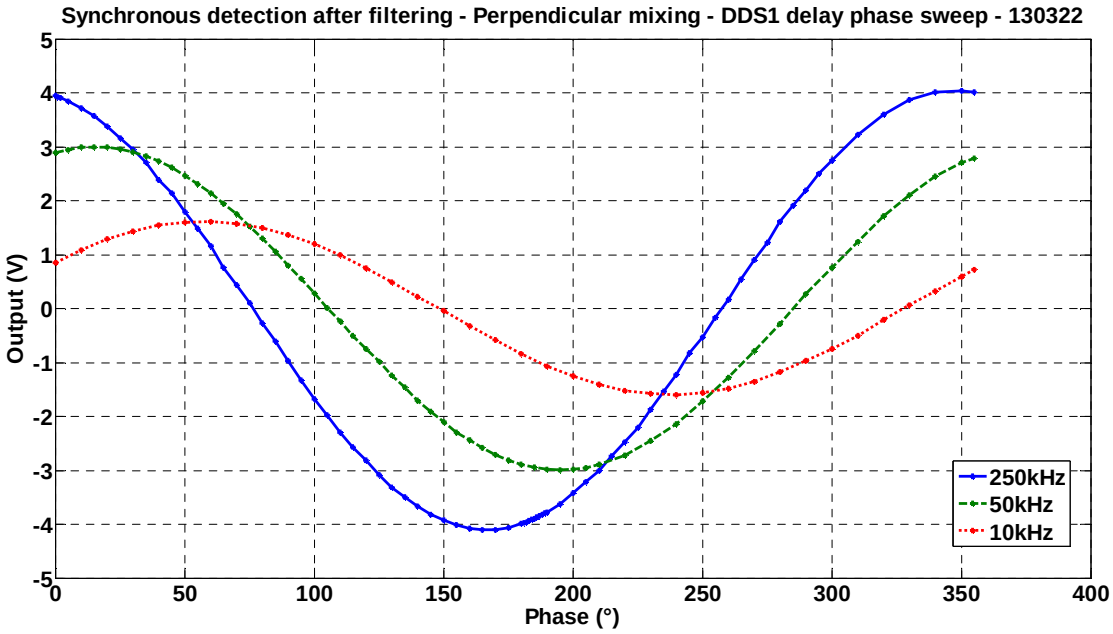

Figure 5.14: Experimental filtered synchronous detection output while sweeping φ_{90}

Figure 5.15 shows a simulation of the output of the synchronous detection after filtering for various conditioning phase (phase induced by the AC coupling and amplification of DDS3) (φ_0) and a 10° cell phase (φ_1). If we consider the signal from DDS3 to be the reference, increasing the phase accumulator of DDS1 will create a phase lag ($-\varphi_{SWEEP}$). The signal from the reference (DDS3) and the transimpedance amplifier will respectively be:

$$S_{REF(DDS3)} = \cos(2\pi ft) \tag{5.12}$$

$$S_{CELL(DDS3)} = \cos(2\pi ft - \varphi_{SWEEP} - \varphi_0 + \varphi_1) \tag{5.13}$$

The phase shift between the two signals is swept and the filtered multiplier output changes sign when the phase offset (φ_{SWEEP}) applied to DDS1 is equal to $\varphi_{90(DDS3)}$.

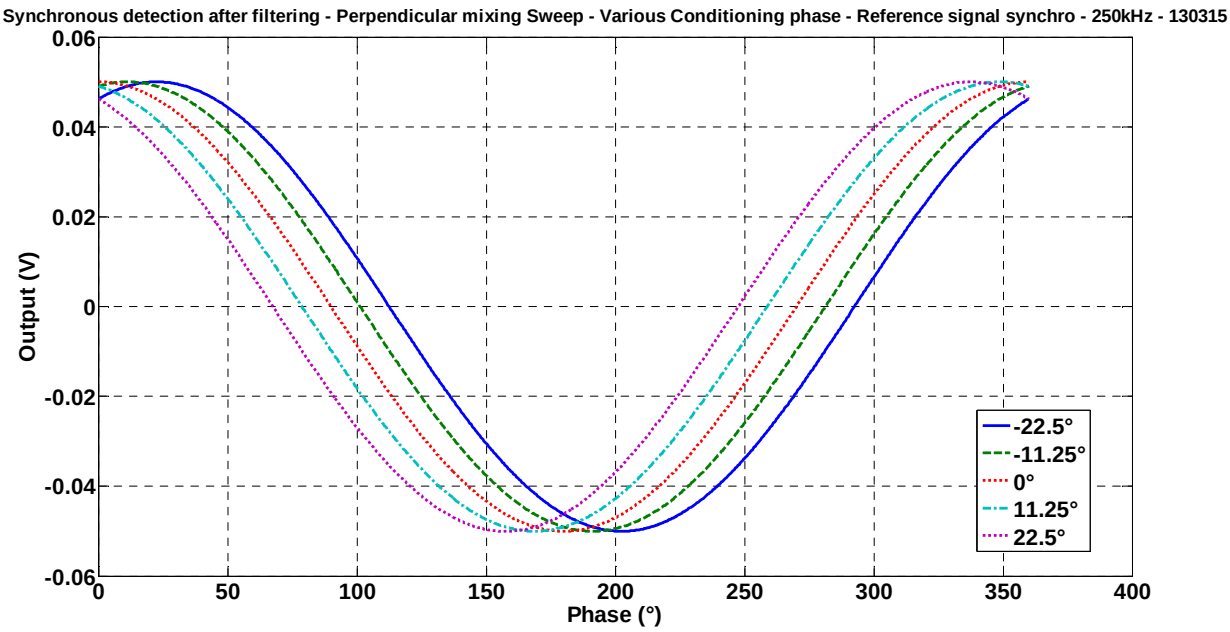

Figure 5.15: Filtered synchronous detection output while sweeping φ_{90}

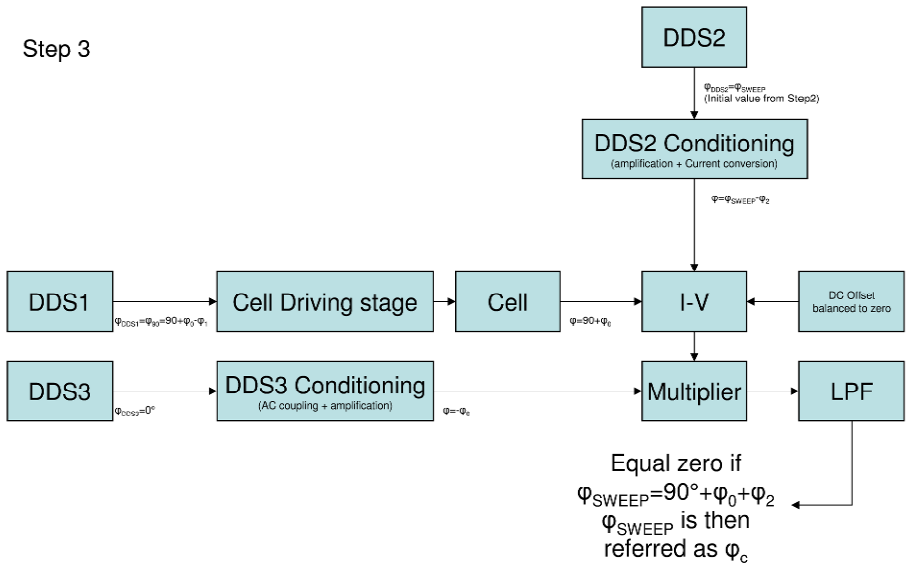

Figure 5.16: Step 3 of the automated baseline suppression

The following step (Figure 5.16) is to synchronise the subtracting signal with the signal from the cell. Ideally the cancellation signal is in phase with the cell signal, but in the real system the cancellation circuit (Circuitry between the DDS and the current summing junction) can induce an unknown phase difference (φ_2) which has to match the phase of the cell (φ_1). To do so, the cancelation DDS dephasing is set to the previously found φ_{90}, in regard to the reference DDS (Cell DDS is still dephased by φ_{90}). The phase of the cancellation signal (φ_C) is then swept until it reaches the zero

crossing point. Figure 5.17 represent the output of the filtered synchronous detection while sweeping the phase φ_C (φ_C is offset by φ_{90} for ease of reading) for various unknown cancellation phase.

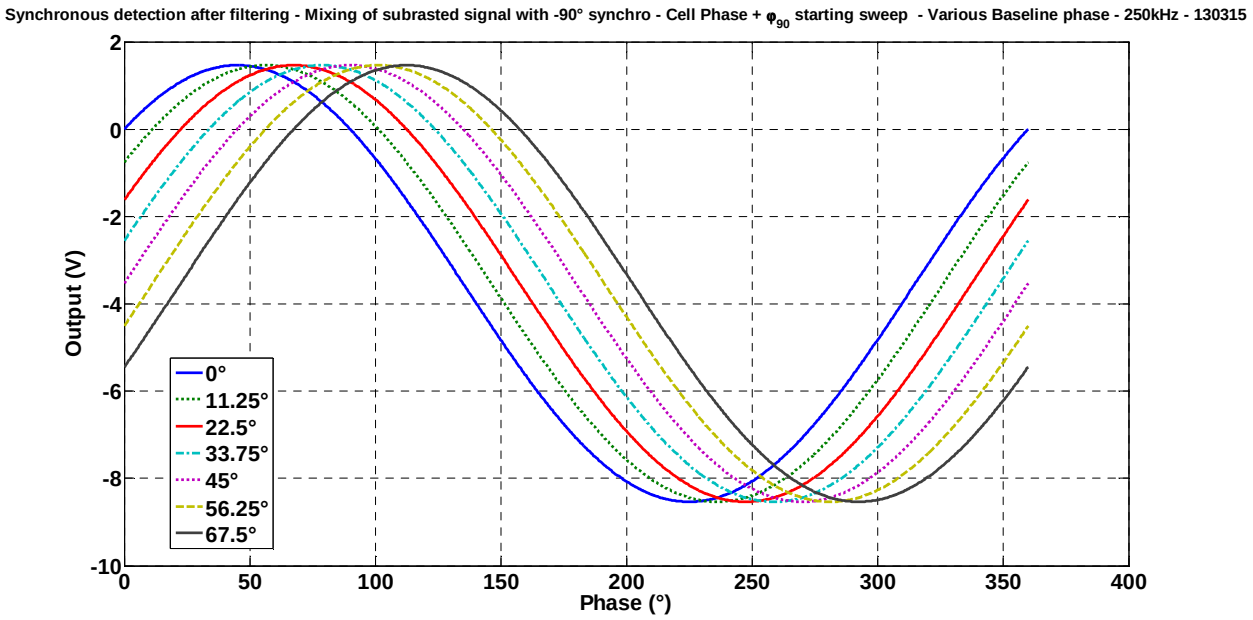

Figure 5.17: Filtered synchronous detection output of the cancelled signal while sweeping φ_C

The final phase φ_C found is then equal to:

$$\varphi_C = \varphi_{90} + \varphi_2 \tag{5.14}$$

And as the cell DDS (DDS in stage 2) is already shifted by φ_{90}, the cancellation signal is in phase with the cell signal it has to cancel. The amplitude of the cancellation current which was previously set to a nominal value of 42.43 μA_{RMS} (Full-scale DDS signal, instrumentation gain set to 1), can then be increased to a certain threshold defined by the user to match the current from the cell.

5.2.7.2. Use of a quadrature lock-in amplifier

Another solution consists of using a second multiplier to create a quadrature lock-in amplifier (Section 3.7.3) (Figure 5.18 – Appendix J). Such lock-in amplifier can be used to retrieve the magnitude and the phase of the signal from the transimpedance

amplifier. The balancing of the DC bias from the voltage to current converter is still needed prior any measurements. The same zero crossing detection using a Schmitt trigger can be used to reduce the DC bias (Section 5.2.7.1).

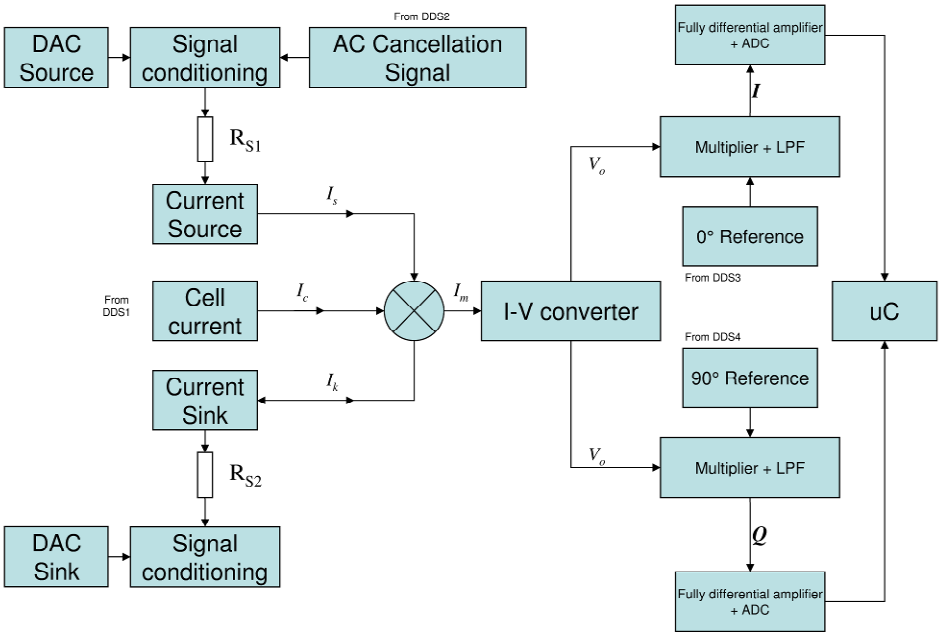

Figure 5.18: Implementation of the quadrature lock-in amplifier

After DC balancing, the phase from the cell (φ_1) can measured by retrieving the I (In-phase) and Q (Quadrature phase) values from the two multipliers without the cancelation signal. The phase can be measured using the following identities which correspond to a phase delay comparing to the reference signal $\varphi \in [0, \pi]$:

$$If\ I > 0\ and\ Q \geq 0 \Rightarrow \varphi = \tan^{-1}\left(\frac{Q}{I}\right) \tag{5.15}$$

$$If\ I < 0\ and\ Q \geq 0 \Rightarrow \varphi = \pi + \tan^{-1}\left(\frac{Q}{I}\right) \tag{5.16}$$

The following identities correspond to an advance in phase regarding the reference signal $\varphi \in [0, \pi]$:

$$If\ I < 0\ and\ Q \leq 0 \Rightarrow \varphi = \pi - \tan^{-1}\left(\frac{Q}{I}\right) \tag{5.17}$$

$$If\ I > 0\ and\ Q \leq 0 \Rightarrow \varphi = -\tan^{-1}\left(\frac{Q}{I}\right) \tag{5.18}$$

The phase of the cancellation signal (φ_2) also needs to be measured without the signal from the cell in order to account for inherent phase difference of the cancelation signal. Knowing the phase φ_1 and φ_2, DDS2's phase register can be set to the following phase for a matching cancelation phase:

$$\varphi_C = 180 - \varphi_1 + \varphi_2 \tag{5.19}$$

To fully cancel the signal from the cell, the amplitude of the cancellation signal (See Figure 5.9) needs to be set to match the magnitude of the signal from the transimpedance amplifier which can also be measured.

5.3. Conductivity detection in continuous flow

5.3.1. Contact mode

The baseline suppression was first tested in contact mode (Electrode in galvanic coupling) in continuous flow for different concentrations of Sodium Chloride (NaCl). The system was composed of an HPLC pump (Jasco 1580-PU) connected to an injector (Rheodyne 7125) followed by the cell, formed by a two way connector (Omnifit) with access hole for platinum wires. The frequency used was lower than for capacitive coupling (500 Hz) and the voltage was set to 20 Vpp with a 330 kΩ feedback resistor in the transimpedance amplifier. The supply rail of the amplifier was set to ±15 V, giving a maximum output voltage swing of 24 Vpp (8.48 V_{RMS}).
Figure 5.19 and Figure 5.20 show a comparison of successive injections of different NaCl concentrations (100 µM, 200 µM, 300 µM, 400 µM, 500 µM, 1 mM, 1.5 mM, 2 mM, 2.5 mM) without (Figure 5.19) and with (Figure 5.20) baseline current suppression.

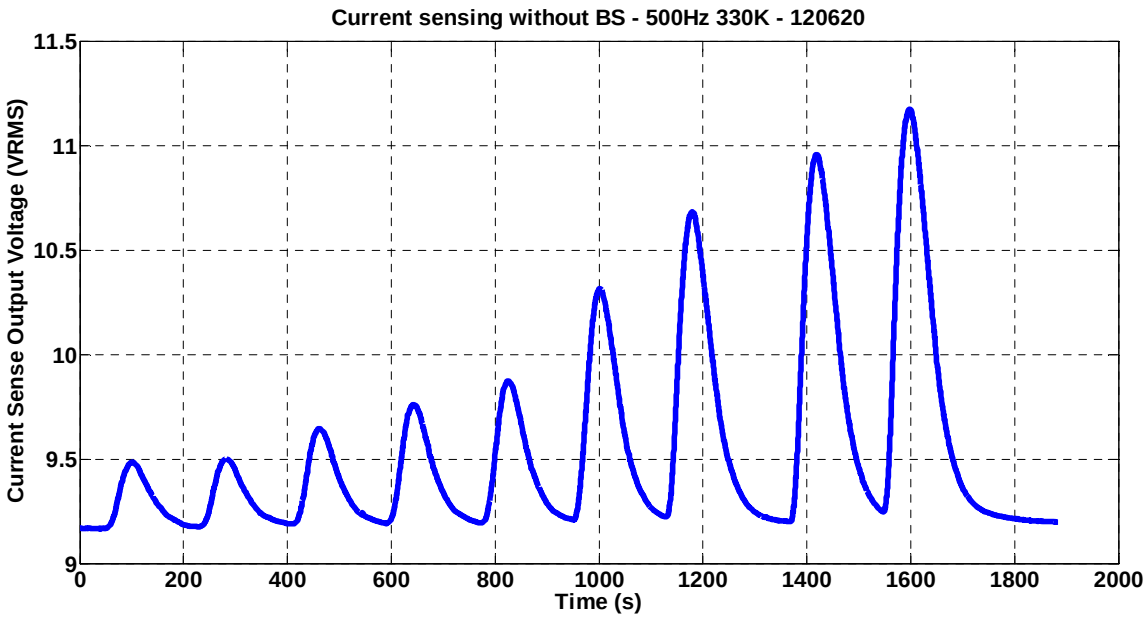

Figure 5.19: Output signal in contact mode without current baseline suppression

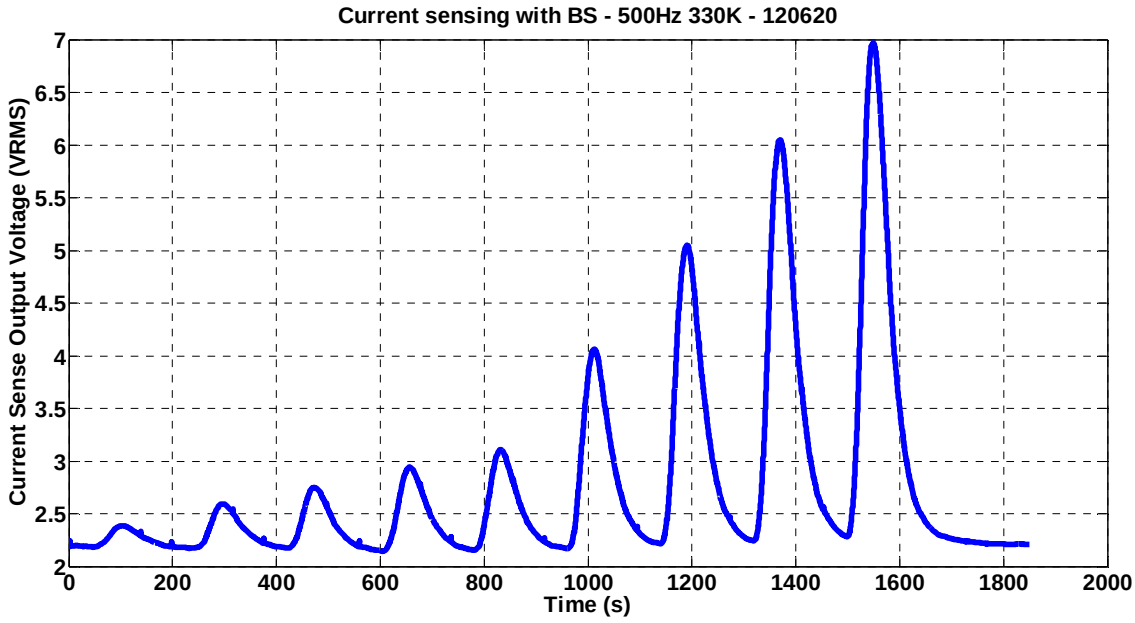

Figure 5.20: Output signal in contact mode with current baseline suppression

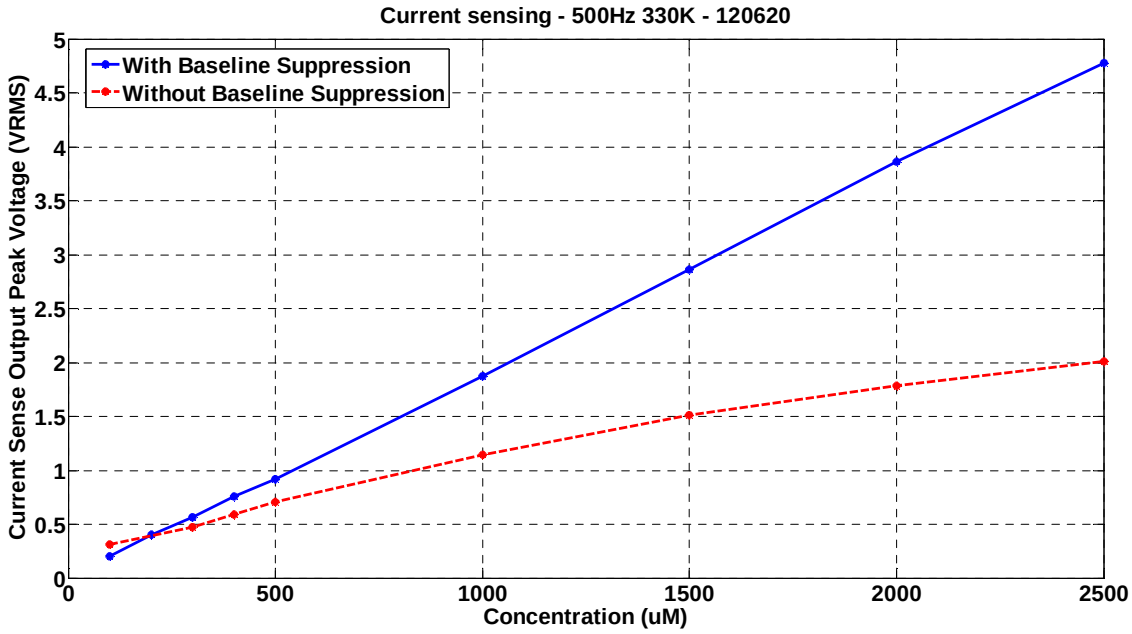

Figure 5.21: Calibration curve comparison without and with current baseline suppression

Figure 5.21 plots the peak values from Figure 5.19 and Figure 5.20, which are proportional to concentration. This demonstrates that without the baseline suppression, the response has a smaller slope (and thus sensitivity) than with the current baseline suppression, mainly due to saturation. Saturation is visible on the signal without baseline suppression as the curve tends to approach a finite value (When the sinusoidal signal is totally distorted into a square wave due to the output swing limitation of the transimpedance amplifier). Instead of a sharp clipping, a soft saturation is seen due to the RMS conversion of the output signal. In contact mode, with the baseline suppression, the dynamic range and the sensitivity are enhanced.

5.3.2. Contactless mode

The baseline suppression has then been tested in contactless mode using the PCB / PDMS cell described in Section 4.3.3.2 in continuous flow of pure water (MQW) from an HPLC pump for different concentrations of Sodium Chloride (NaCl) introduced by the means of an injector. The frequency was set at 250 kHz and the excitation voltage at 24 Vpp with a feedback resistor of 2 MΩ. Figure 5.22 and Figure 5.23 show different injections peaks (with replicates) without and with the baseline

suppression. As the signal baseline may vary during successive injections, both graphics have been referenced to zero for ease of comparison.

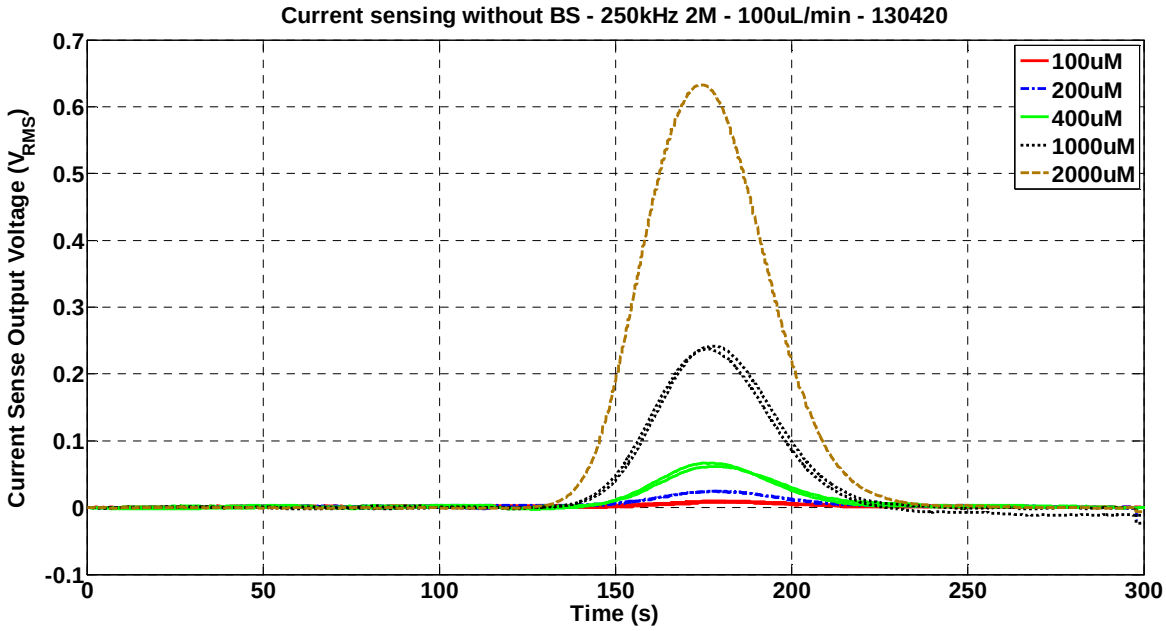

Figure 5.22: Output signal in contactless mode without current baseline suppression

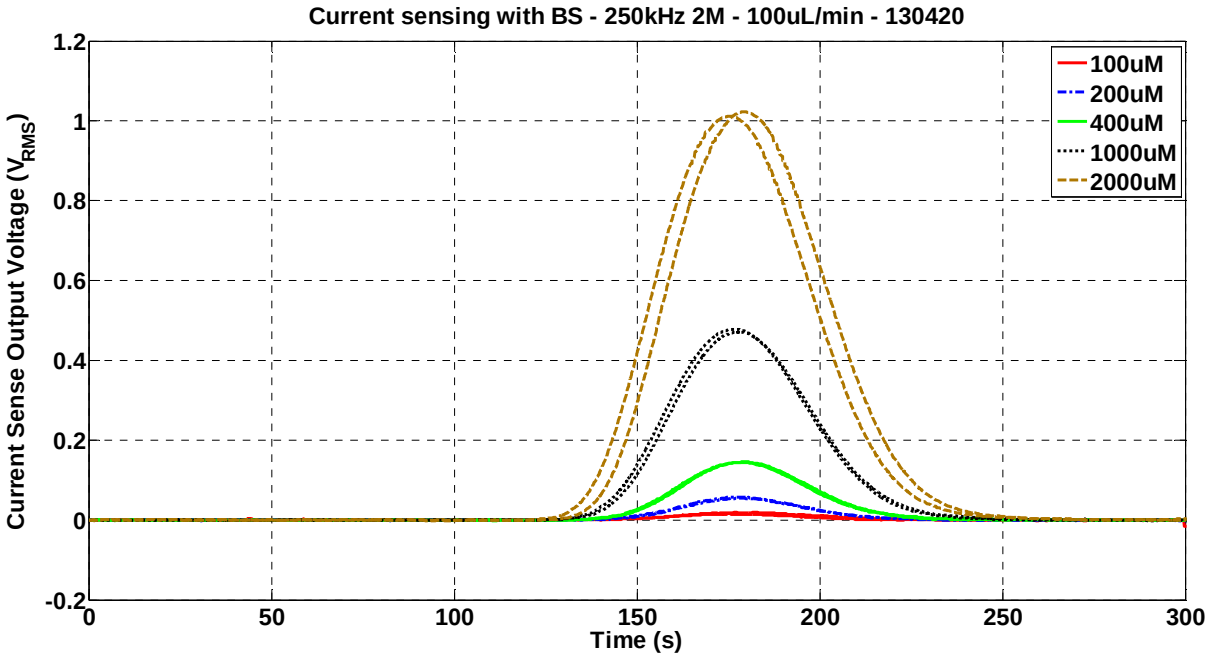

Figure 5.23: Output signal in contactless mode with current baseline suppression

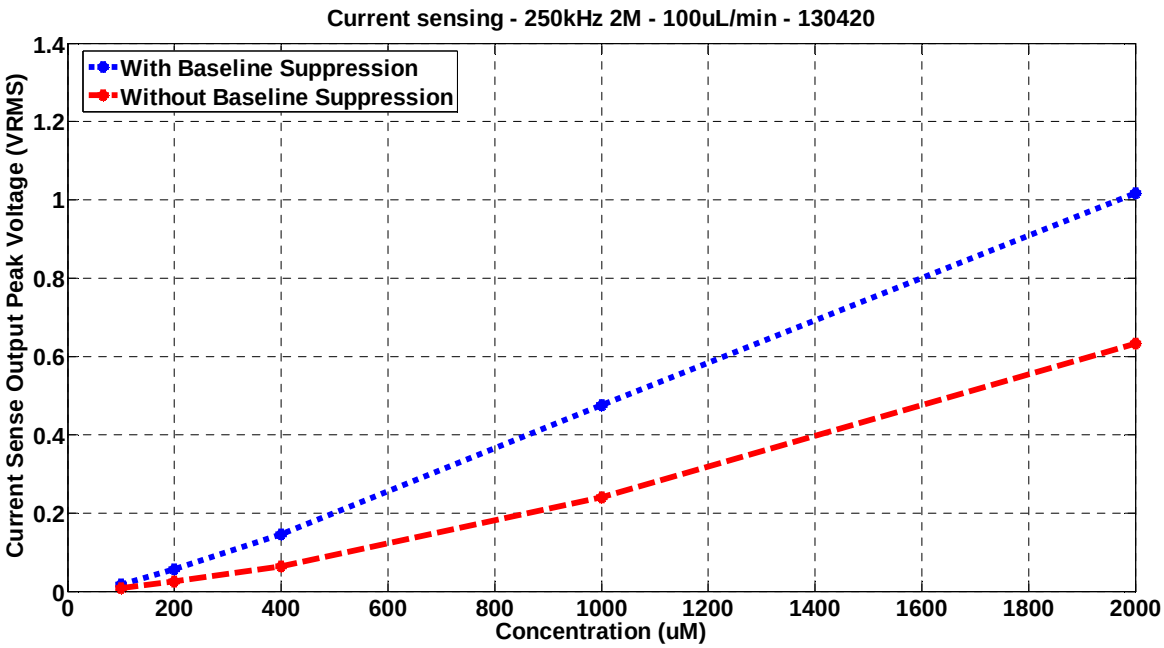

Figure 5.24: Calibration curve comparison without and with current baseline suppression

Figure 5.24 shows that the slope of the curve while using the baseline suppression is higher than without the baseline suppression. The signal is however not showing any saturation (Signal from the transimpedance amplifier not distorted) due to the higher total impedance of the cell created by the capacitive coupling. The associated sensitivity without and with the baseline suppression is respectively 331 µV/µM and 531 µV/µM. The R^2 values, which are an indicator of the quality of the linear curve fitting, are 0.9883 without suppression and 0.9992 with it. The LOD (3σ) for NaCl achieved with each system is 2.05 µM and 1.63 µM.

The feedback resistor of the transimpedance amplifier was varied from 1 MΩ to 4.7 MΩ in order to increase the sensitivity of the system. While a change of sensitivity was observed, the increase did not follow the ratio between the resistors. For example, between 1 MΩ and 2 MΩ, the increase in sensitivity was only 25% as for the noise too which is also increased. It has been decided to increase the excitation signal instead, following the work of Tanyanyiwa *et al.* [72, 75, 153] (Section 3.6.2).

The booster amplifiers used in these previous works were a Burr-Brown 3584 [153] and a PA94 [72, 75] from Apex Microtechnology Corporation. The 3584 is a high voltage, high speed operational amplifier with an output swing of ± 145 Vpp and a slew rate of 150 V/us. The PA94 is also a high voltage power operational amplifier capable of a full power (± 300 V) bandwidth of 300 kHz due to its high slew rate

(500 V/µs) [204]. For our application, the PA78 was used, which has a slew rate of 350 V/µs and an output voltage swing of ± 150 V. The achievable excitation signal voltage with this amplifier is 300 Vpp, which is sufficient for our application due to the fairly small insulating layer (Less risk of dielectric breakdown). Furthermore these chips retail price (£50) is five times less than the PA94 (£250), which is not negligible.

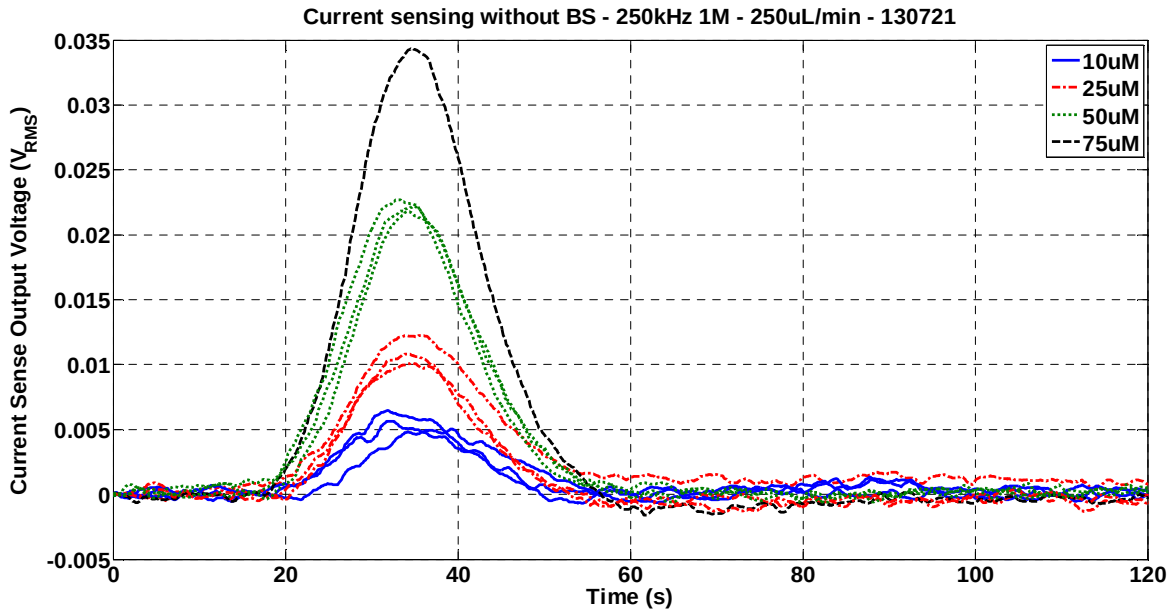

Figure 5.25: Output signal without current baseline suppression and moderate excitation voltage

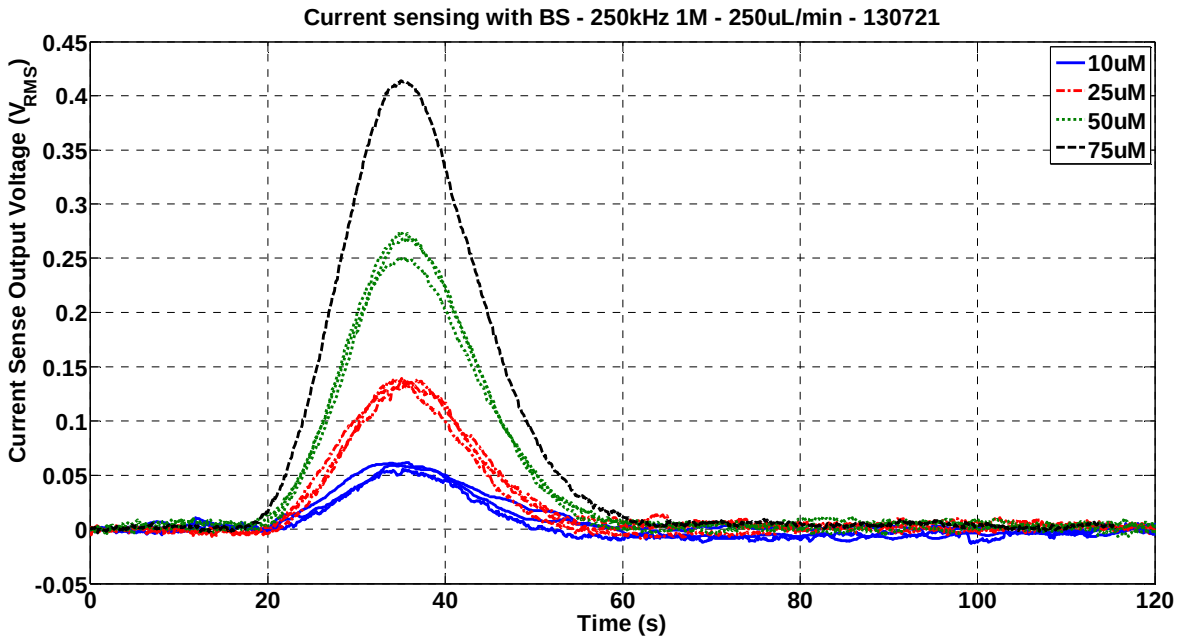

Figure 5.26: Output signal with current baseline suppression and high excitation voltage

Figure 5.25 and Figure 5.26 compare the signal from a capillary cell without the baseline current suppression and a moderate excitation voltage (21.4 Vpp) with the use of a high cell excitation voltage (100 Vpp) in conjunction with the baseline suppression. A capillary with ≈ 481 µm thick wall have been used as it permits the use of fairly high excitation voltage without the risk of causing breakdown (25 kV/mm). The excitation frequency is kept at 250 kHz and the feedback resistor of the transimpedance amplifier (THS4631) is 1 MΩ. The same experiment setup is used, an HPLC pump is used to flow MQW while different concentration of NaCl (10, 25, 50, 75 µM) is injected. The flow rate was increased from 100 µL/min to 250 µL/min compared to the previous setup which allow the sample plug to travel faster and thus to reduce the total experiment time. This increase in flow rate did not seem to affect the baseline noise if compared with lower flow rates.

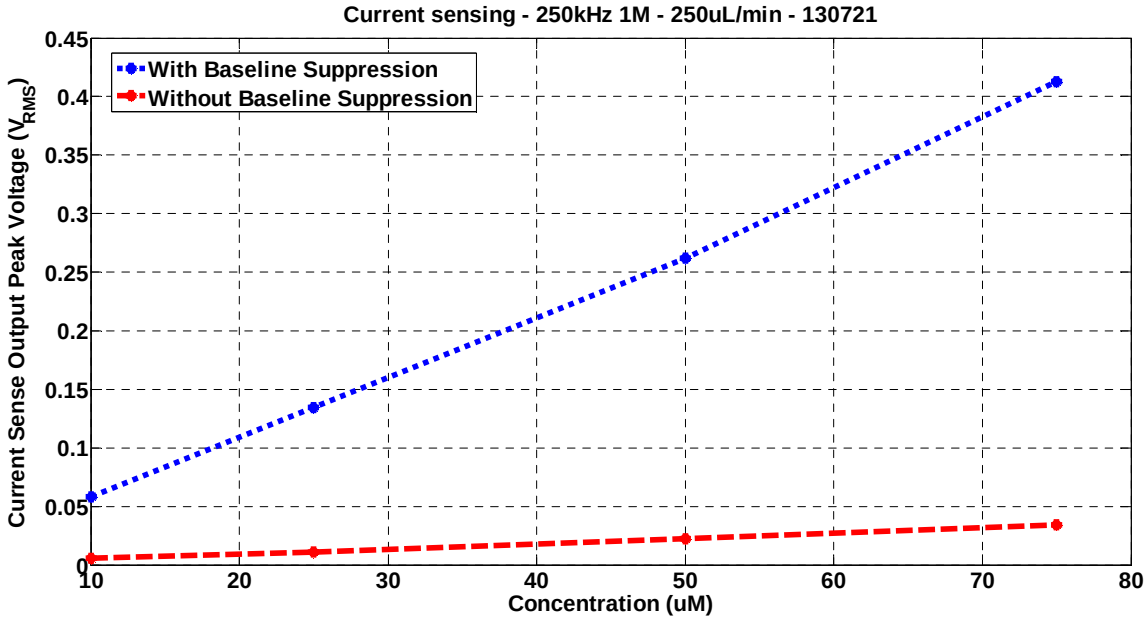

Figure 5.27: Calibration curve comparison

Figure 5.27 shows the calibration curve for the setup, the associated sensitivity without the baseline suppression and moderate excitation voltage is 442.9 µV/µM with a R^2 value of 0.9973. The sensitivity with the baseline suppression and the high voltage excitation signal is 5.43 mV/µM with a R^2 value of 0.9982. According to the R^2 values, the results show a really good linear fitting to the calibration curves. The LOD (3σ) for NaCl in this particular experiment is respectively 0.8653 µM and 0.0715 µM. It can clearly been seen that using a higher excitation voltage

significantly increased the sensitivity of the system. The baseline suppression is however useful to keep the baseline voltage low, which benefits the dynamic range of the system.

The observed increase in sensitivity can also be explained by the phase shift involved by the analyte plug. As shown in Figure 5.28, the plug travelling through the cell induces a change in phase to the output signal of the cell. This change in phase is translated as a change in amplitude due to the cancellation signal being set for the phase of the baseline. Indeed, the current of the cancellation signal of different phase will contribute to the output signal of the transimpedance amplifier. It can also be noted that the linearity of the system is not affected by this additional current from the baseline suppression signal as good R^2 are obtained.

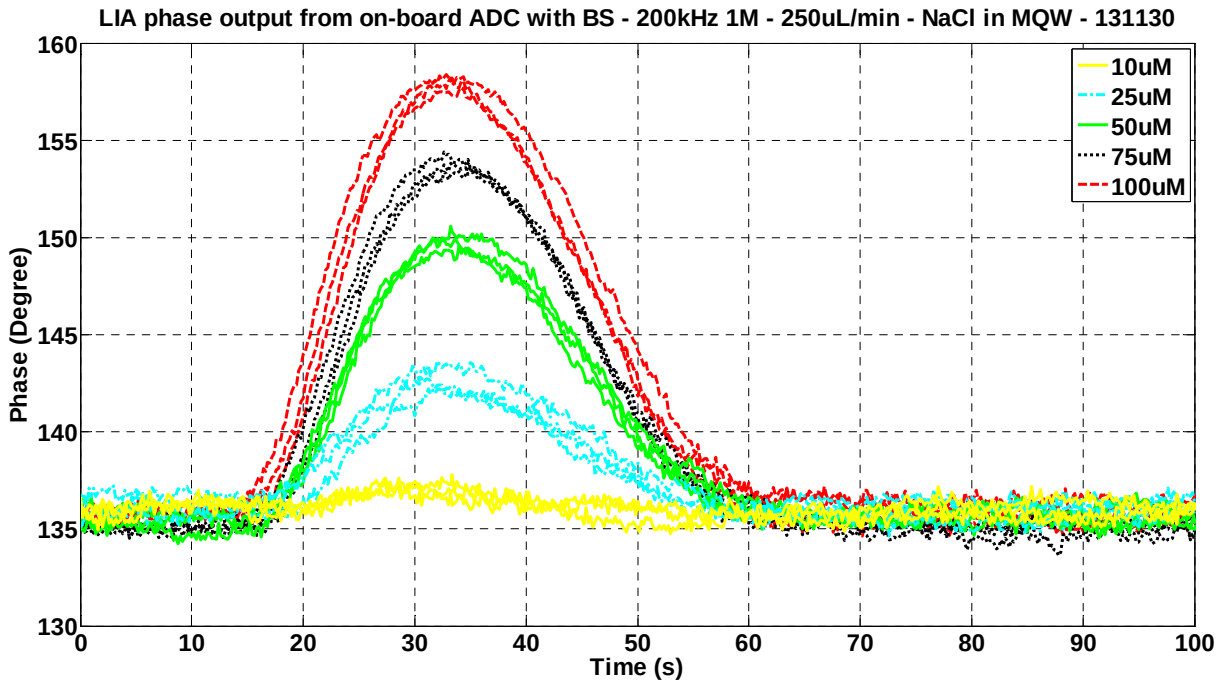

Figure 5.28: Phase output of the transimpedance amplifier during plug injection

5.4. Separation of inorganic ions with conductivity detection

5.4.1. Experimental setup

The purpose of this experiment is to separate inorganic ions by electrophoresis in a microfluidic chip and to detect them using contactless conductivity detection. Ideally the separation needs to be fast with a good resolution in order to be able to give an electropherogram with well defined peaks and high throughput. The background electrolyte, the injection process (injection technique, voltage, time, *etc.*) and the separation voltage needs to be optimised in order to achieve this goal. Preliminary work has been carried out with a simple C^4D system to evaluate the correct buffer composition for the separations of the analyte of interest of the project.

5.4.1.1. Reagents

The buffer and the different solutions containing the inorganic ions were prepared on the day from their chloride salt for the cations and potassium salt for the anions. The daughter solutions were diluted from the mother solution prepared with pure water. The samples were sonicated using an ultrasonic bath to degas and enhance the dilution of the salt. Solutions were stored near the system for 2 hours in order to be at the same temperature as the system. Before introduction into the system, the sample and buffer was filtered using filter paper with a pore size of 0.02 µm (Whatman Anotop).

5.4.1.2. Materials

The PMMA electrophoresis microchip (microfluidic ChipShop - Figure 3.4 - [78]) was a cross shape design with an injection channel length of 10 mm and a separation channel of 87 mm. Two microchip models were investigated, one with a channel cross section of 50 µm and an offset of 100 µm between the two injections branch, the other one with a cross section of 100 µm and no offset. The chip included four reservoirs, bonded to the chip for fluid storage and injection through Luer connectors. The chip also featured 100-150 nm thick gold electrodes for the contactless conductivity

detection which were deposited on the bottom lid (60 µm insulating layer) with a 10 nm titanium layer to help adhesion. In order to make contact between the deposited electrode and the detection circuit, a PCB with a track for each electrode was made and epoxy glued under the plastic microchip to be used as a support and as electrode extension for the through hole contact of the detection board to interconnect the electrode to the sensing board.

The high voltage necessary for the electrokinetic injection and the electrophoresis where provided by a home-made system built around small footprint high voltage module (Ultravolt D series). The system automation was done by a microcontroller (PIC32MX795F512L) coupled to a 16-bit DAC (AD5663R) for the control of voltage output of the high voltage module and 22-bit ADC (MCP3551) for a read back of the current and voltage supplied to the electrophoresis solution. Injection voltage and current was limited to a maximum of 2000 V and 500 µA for a total power of 1 W, separation voltage and current was limited to 6000 V and 670 µA for a total of 4 W.

Voltage switching of the electrode between the injection and the separation was done by four SPDT (Single pole double throw) relays, allowing the electrode to be either connected to the high voltage module or left floating. Injection and separation parameters (Duration, voltage) were sent to the system through a USB connection via a custom PC software application; the same program was use to set up others stage like the detection.

Risk due to the presence of high voltage was greatly reduced by the use of a wooden cabinet with a safety switch linked to the door, cutting off power to the high voltage module in case the door is opened during an experimental run.

5.4.1.3. Procedure

Prior to separation, the microchip was first flushed with the background electrolyte to wash off any residual elements. Then the buffer was introduced in the chip with the help of a plastic 1 mL syringe with male Luer connector (BD Plastipak) followed by the sample introduced in the reservoir via a micropipette. The microchip channel and reservoirs were then checked with a microscope for bubble or impurities (fibre, *etc.*) which may have been trapped inside the chip. After inspection, the PCB supporting the microchip was plugged into the detection board and the electrodes where placed according the type of separation (Cations or Anions).

The system was then isolated from the rest of the laboratory by closing the wooden door of the cabinet.

The parameters of the electrophoresis experiments (Duration, voltage, read back channel, *etc.*) were then entered into the PC software (UOHC4D) and transmitted to the autonomous system. The system will then stream the data to the PC outside the cabinet for real time display to the user and data logging.

After the experiment, the electrodes were removed and washed thoroughly with pure water. The PCB was then unplugged and the microchip was flushed with water and air prior to being stored in a sealed bag until the next experiment. Desiccant sachets can be introduced in the sealed bag in case liquid got spilled between the electrode and the PCB. See appendix O for the experimental method used for this experiment.

5.4.2. Preliminary electrophoresis results

Figure 5.29 and Figure 5.30 shows electropherograms of the separation of two mixtures of two different anions (Chloride, Sulphate and Phosphate). A mixture of respectively 2 mM of KCl^- and 3 mM of SO_4^{2-} in buffer (20 mM MES/HIS with 50 mM Acetic Acid) was used as a mixture of 3 mM KCl^- and 1 mM PO_4^{3-}, diluted in the same buffer. The procedure followed was a 5 s injection, the sample reservoir was grounded while the sample waste reservoir was set at 400 V with the buffer and waste reservoir being left floating. The injection was followed by the separation with the waste set at 3000 V with the buffer reservoir grounded and the sample and sample waste reservoir being left floating.

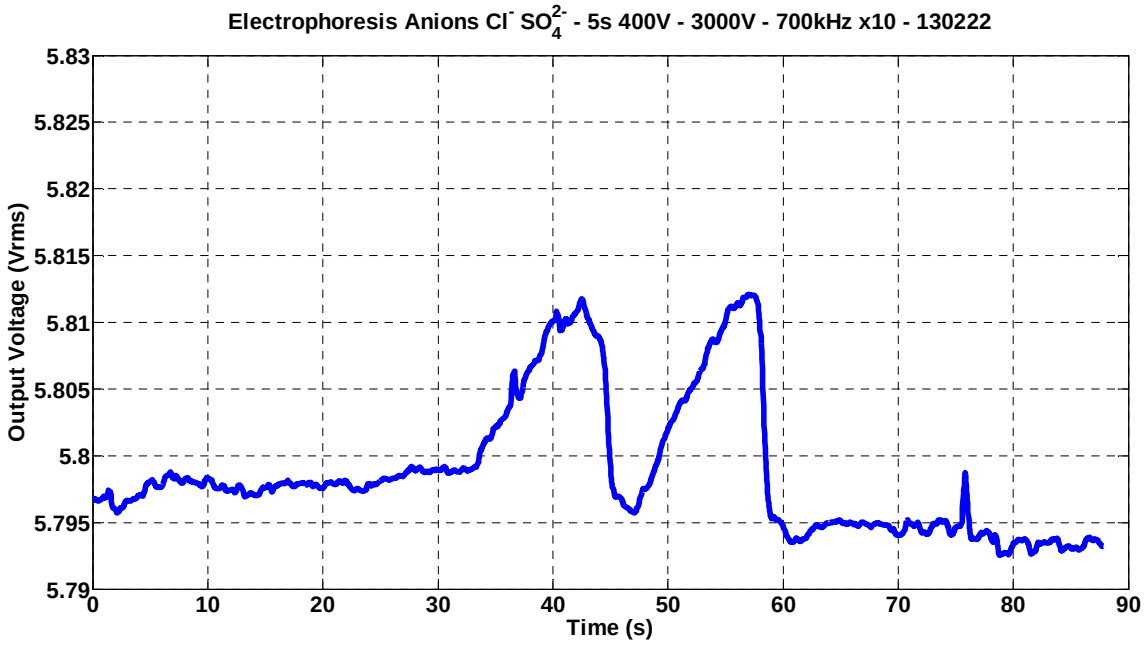

Figure 5.29: Electropherogram of two anions Cl^- and SO_4^{2-}

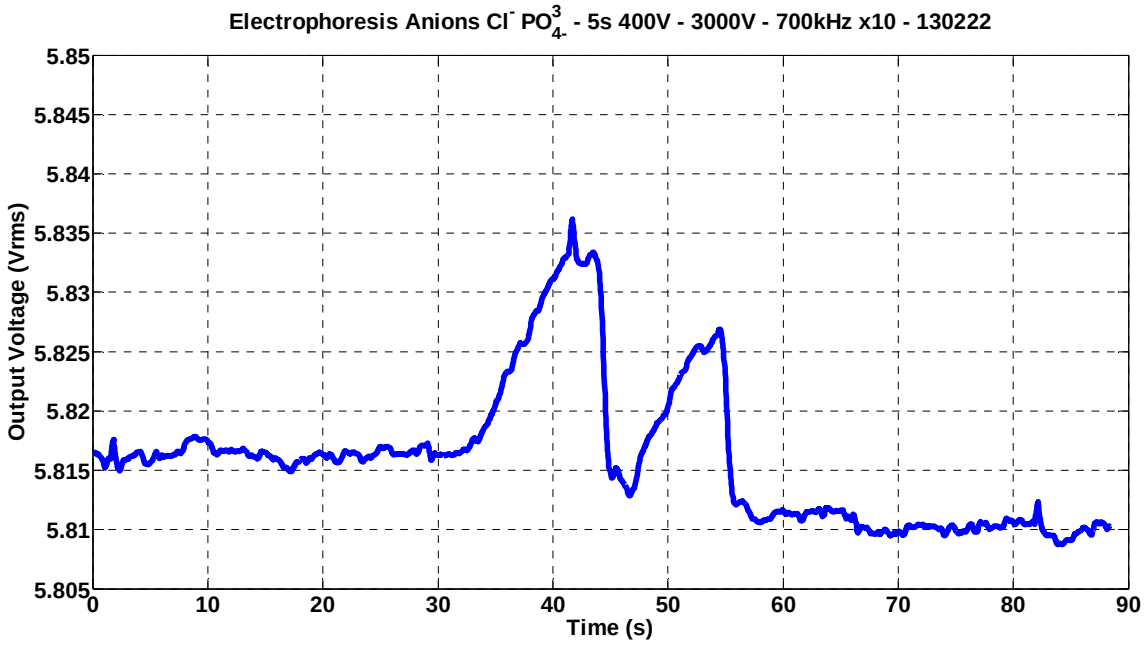

Figure 5.30: Electropherogram of two anions Cl^- and PO_4^{3-}

Theses electropherograms show the peaks corresponding to the two analytes present in the solution. The retention time for the first peak of chloride is around 33.3 s which is similar for the other separation. However the retention time for the sulphate and nitrate are the same which is an issue when doing a separation as peaks may overlap. More work on the buffer and electrophoresis voltage is needed. The detection system in this particular case is based on a simpler C^4D detection which do not implement

baseline suppression hence the signal being offset around 5.8 V. Baseline suppression can be used to reduce this offset but separation offering good efficiency and repeatability is needed before correct evaluation of the baseline suppression can be carried out, as peak shape relay directly to the system's limit of detection.

5.5. Summary of the chapter

This chapter mainly covered the electronics design involved in the creation of a more integrated C^4D system which features a baseline compensation technique. This baseline compensation helps with the offset current which can be caused by the background electrolyte or the stray capacitance of the cell, which effectively reduces the dynamic range of the conventional C^4D. Two possible approaches to automation of this baseline suppression have been presented, the first using one multiplier and the second using a quadrature lock-in amplifier (Two multipliers). The latter design also provides information about the amplitude and phase change of the conductivity signal. Using high excitation voltage (100 Vpp) in conjunction with baseline suppression, a LOD of 0.0715 µM was found for NaCl, which enhancing by an order of magnitude the LOD found when using a moderate excitation voltage (21.4 Vpp) without baseline suppression (0.8653 µM).

The chapter also demonstrates an electrophoresis run made from a homemade electrophoresis system using two high voltage modules. The system is able to run an electrophoresis run autonomously and stream the data from the C^4D detection to the user's computer.

Chapter 6 : Self-testing, fault detection and autonomous operation

6.1. Outline of the chapter

This chapter will be looking at the system self-testing capabilities and fault detection which can be applied while operating.

It is well known that all systems providing autonomous monitoring of water quality are subject to conditions and malfunctions which prevent collection of valid data (Freezing, biofouling, broken pipes, pump faults, sensor faults) [16]. This leads to lost data and suspect data, where, in the worst case, it may be difficult to differentiate between pollution events and sensor faults. Conventionally, environmental monitoring systems use limits and parameter correlations to detect sensor faults. Unfortunately with chemical sensors, limits are difficult to set and not particularly useful, due to the wide ranges of concentration values encountered. There are correlations between water quality measurements of different analytes at a site, mainly those less affected by biology. However, sub-daily water quality data is probably too complex to provide suitable fault models for correlation based fault detection. Therefore the proposed system in this thesis will include direct self testing of the fluid infrastructure, LOC, sensors and electronics, and provide a means to relate system health data with measurements, reducing the burden of manual decision making about data integrity which is present in current systems.

The faults include hard faults such as leaks and blockages in fluidic systems, transient conditions such as bubbles and large temperature fluctuations disrupting individual measurements and drift, for example caused by reagent degradation or gradual build up of fouling. Ideally the system needs to detect these faults and act to resolve them or take action to protect the system so no more damage can occur. This information needs to be recorded so that faults do not cause unexplained data anomalies during the data processing. Here we review typical fault conditions and potential detection mechanisms.

6.2. Self-testing

The first thing to do is to identify most of the faults which can occur in the system. The chip must be tested in the laboratory, but also in the field where other factors have to be taken in account due to the different environment and setup surrounding the system. It has been proven that using LOC for a long period of time in the field can cause failure like blockage due to biofouling [205].

Calibration is closely linked with self-test in environmental monitoring systems. Drift is a common problem in chemical sensors and often requires regular recalibration. Ideally some form of automatic recalibration may be possible. Ramanathan *et al.*[206] discussed a technique to improve the yield of a sensor network in the context of sensors in the soil – many of these issues are relevant to river water monitoring. Sensor and Hardware faults but also calibration is presented in this work. They presented a simple *in-situ* calibration method consisting of spiking regularly the sensor with a high concentration of analyte and compare the response of the sensor with the expected one. This technique could be applied to our system where a know concentration is injected into the system and measured. A drift in the system response could trigger an auto-calibration or a calibration alert asking the user to intervene.

6.3. Fault and methods of detection

The main focus of this chapter is on fault events such as bubbles and hardware failures (Pump failure, fluidic disconnect, *etc.*). We will look at different faults and analyse their effect on the system. We can then use this information to modify the system behaviour according to the data from the sensor in order to detect when this event occurs.

6.3.1. Bubble fault

The formation of bubbles in the system is a common problem in microfluidics and can originate from various causes. This unwanted gas can be due to improper solution degassing, improper fluid filing where a dead volume can cause air to be trapped

inside or due to a leak between the system and the surrounding environment. Electrochemical reactions can also engender the formation of gas at electrodes, which can group together to create a larger pocket.

These bubbles can have important consequences on the behaviour of the system. In an EOF pumping based system, electrolytically caused bubbles may cause the flow to cease if the channel gets clogged by bubbles due to the open circuit created between the two electrodes. Bubbles can also be a problem in separation system as they could create perturbation decreasing the separation efficiency, or overloading the detectors.

In the eventuality of bubble formation in the system, it is necessary to be able to detect them and be more careful when processing the results as they may have been compromised. Bubbles can be detected by various mean (Particle tracking, impedance spectroscopy, *etc.*). However in systems using conductivity detection these may be unnecessary as the bubbles are potentially detectable through signal processing of the conductivity signal. Bubbles will create a very rapid change of signal (Decrease in conductivity measurement) when they pass though the detection cell, which in general is different from the slower changing characteristics of typical IC or CE peaks, see Figure 6.1.

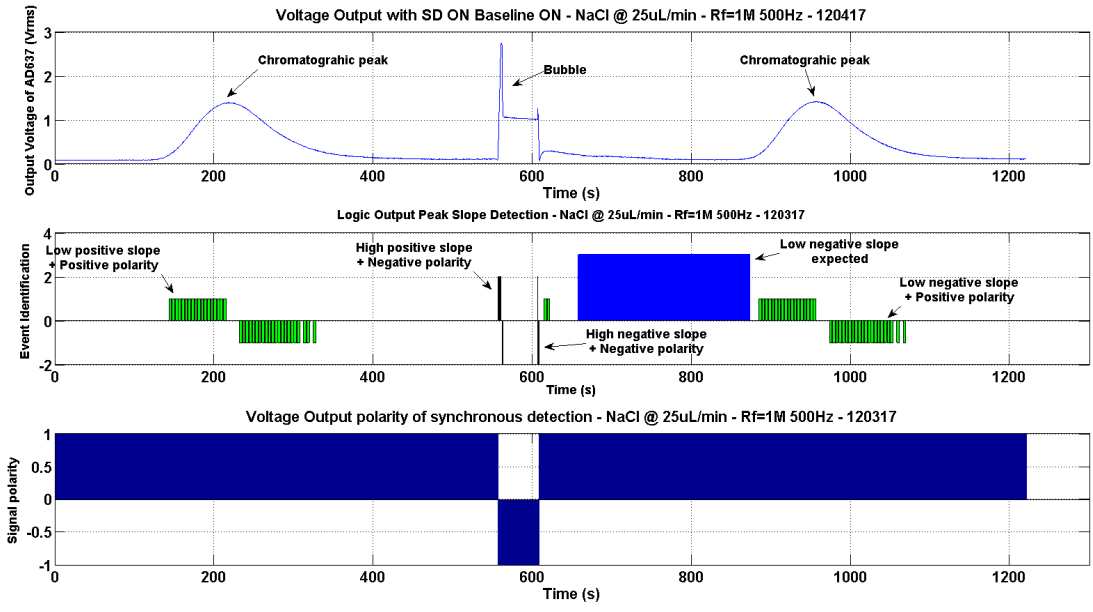

Figure 6.1: Detection of bubble injected in the system

The technique proposed here to detect bubbles is to analyze the signal at a fixed sample frequency of 5 Hz and compute the difference between two consecutive

points. The calculated slope is then compared to threshold values which has been set empirically. Very rapid slopes are indicative of bubbles. In addition to the slope value, the introduction of a bubble will create a radical change of phase in the sensed alternative current which will be translated to a negative output voltage by the synchronous detection system, see Figure 6.1. This phenomenon has been observed as typical of bubbles but does not occur with IC or CE peaks, which reduces the risk of false detection. The combination of these two indicators will trigger the bubble fault detection.

6.3.2. Electrophoresis current fault

During electrophoresis, the current and voltage can be monitored and stored for further processing. The applied voltage should be kept constant and the current should vary only slightly with the temperature and buffer conductivity change. However, erratic current readings can be a sign of a fault inside the channel. For example, generation of bubbles at the electrode or incomplete channel filling will generate erratic change on the current profile and thus the separation obtained will be likely to be corrupted. Figure 6.2 shows the difference between an abnormal separation current (Top) and a normal one (Bottom).

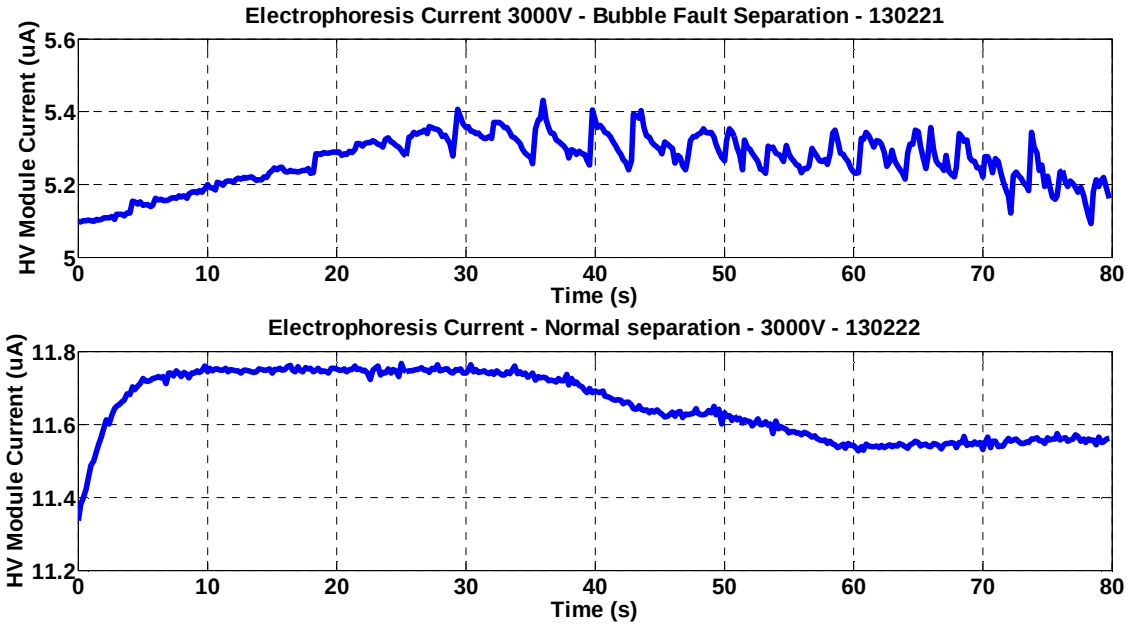

Figure 6.2: Comparison of normal and faulty current profile during separation

These rapid changes in the current readings can be detected by the system and the separations results may be marked as potentially inaccurate.

6.3.3. Pump fault

6.3.3.1. Pump noise

In systems using hydrodynamic pumping, it is typical to observe pump noise in the baseline as a periodic signal related to the pump speed. This effect is particularly prevalent with peristaltic pumps, which by their operating principal will create this fluctuation due to the change of pressure when the tubing is squeezed. This noise can be analyzed to extract fault information relating to the pump system and fluid connectivity between the pump and detector. By applying a fast Fourier transform on the baseline signal (Signal with only running buffer) (See appendix P for Matlab code), frequencies related to the pump operation can be observed, see Figure 6.3.

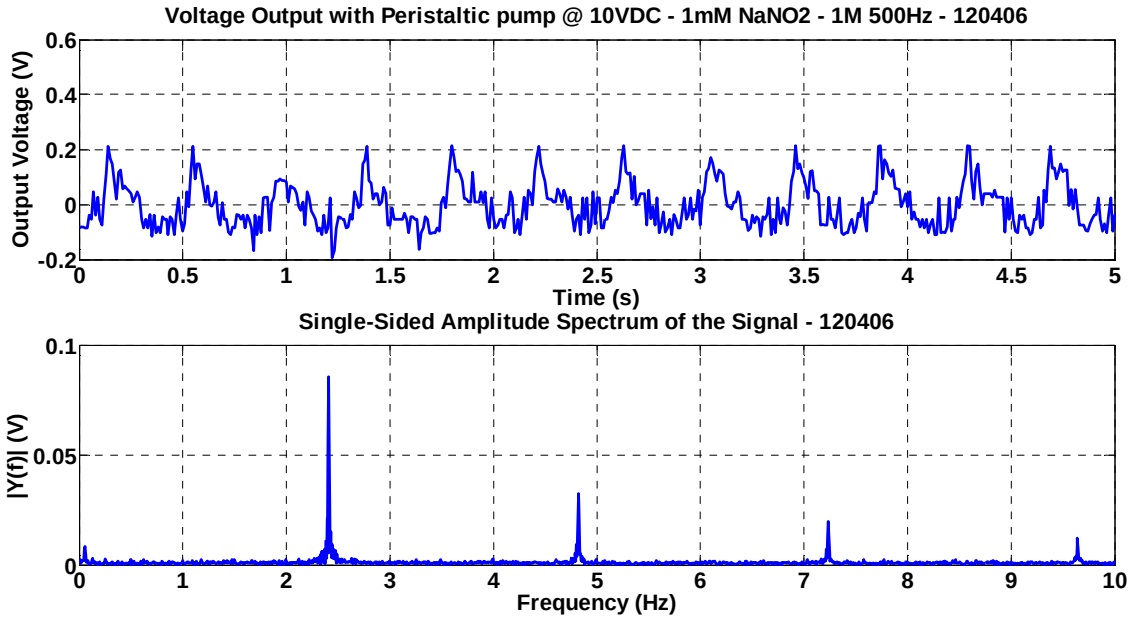

Figure 6.3: Baseline signal and associated spectrum

The extracted frequency is directly link to the pump rotation speed by a linear relation, see Figure 6.4.

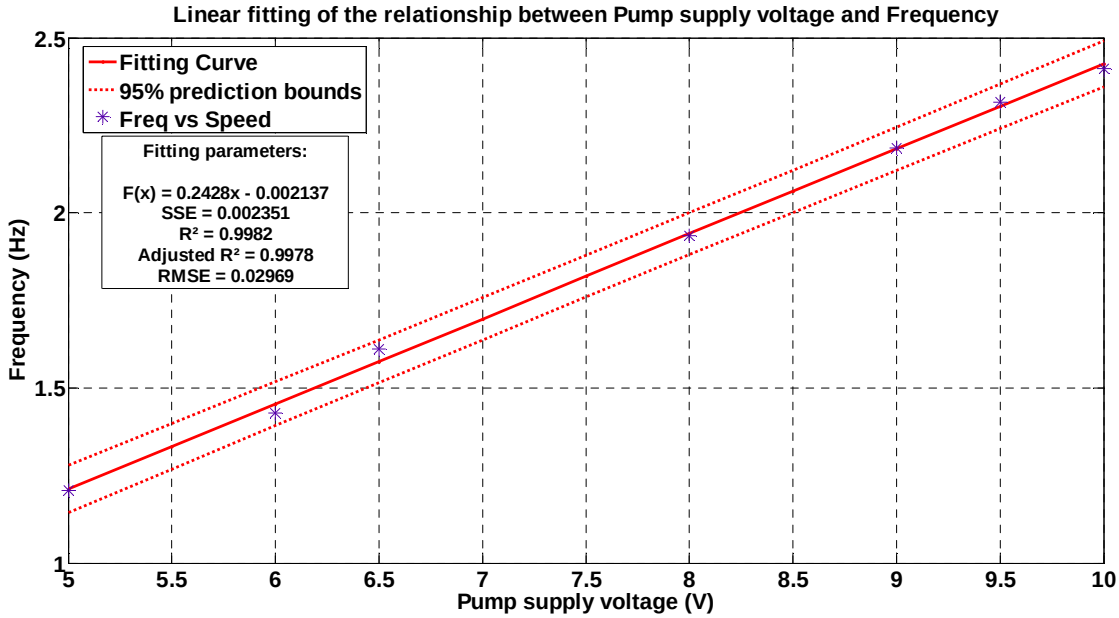

Figure 6.4: Linear fitting of the extracted pump noise frequency versus pump supply voltage

Disappearance of this signal, an unexpected shift of its frequency or an unexpected rise in amplitude may indicate a problem with the system. These frequency analyses may require more processing power than would be required for a basic data logging system. The use of a DSP specialised microcontroller is required to process such data and can potentially be integrated to a datalogging system.

6.3.3.2. Peak broadening due to pump fault

The slope of the chromatographic peaks (Peak produced by analytes passing through the detection window) can also be monitored to detect any deviation from their nominal value. Figure 6.5 shows a pump speed fault and its effect on the chromatographic peak from an injected analyte plug. By decreasing the flow rate from 25 µL/min to 10 µL/min in order to simulate a drop in flow rate, the peak gets broader and its slope is different than the faultless peaks. This difference in peak width may be coupled to the pump noise analysis for cross reference between the expected and the actual flow rate.

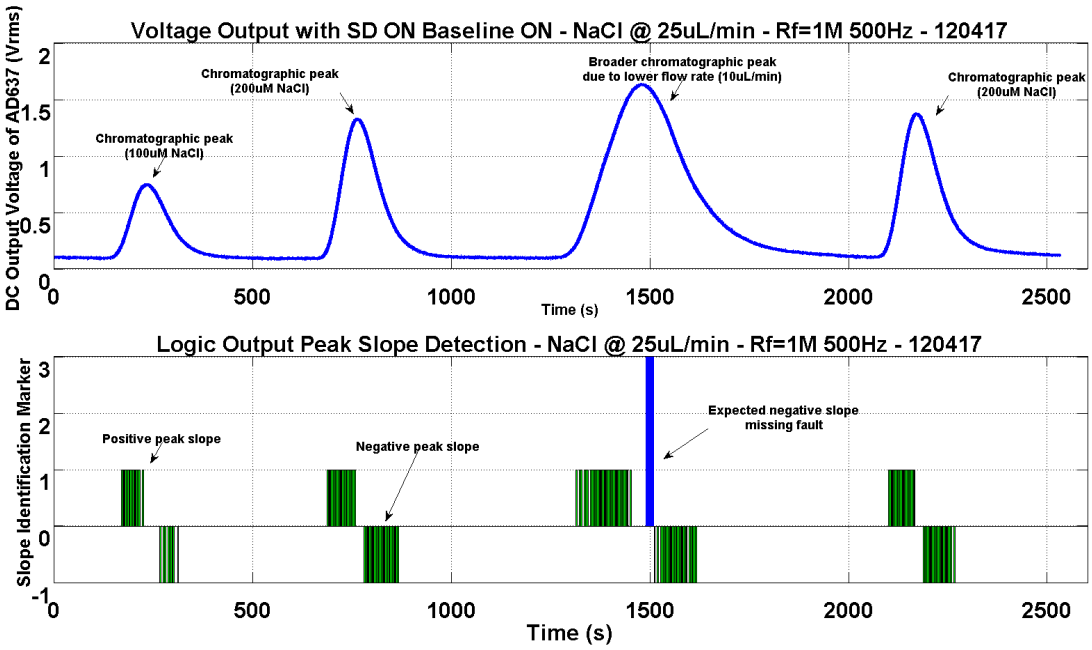

Figure 6.5: Detection of peak broadening due to pump failure

The positive slopes of the chromatographic peaks detected by the system are displayed by the positive green bars (Figure 6.5); the negative slopes are displayed with the negative green bars. When the time between a consecutive positive slope and a negative slope is longer than the set threshold, a broader peak fault can be triggered.

6.4. Field testing of LOC with real samples

As part of the evaluation of possible failure mechanism, river water samples have been passed through glass LOC devices for long periods. For example, a LOC device was located in the environmental monitoring station on the River Enborne near the village of Brimpton (Berkshire, UK), adjacent to the Environment Agency's flow gauging weir (See Appendix A). Water from the river was pumped continuously through it for over two and half months before failure occurred due to blockage, see Figure 6.6.

Figure 6.6: LOC channel showing blockage deposits from river water

This indicates both that a LOC-based measurement system is feasible in terms of the useable time *in-situ*, but also illustrates that failures are likely to occur at some point. In addition to the integration of fault detection, the system could also interact with the user to provide an alert. As an ideal scenario, the autonomous system could potentially detect the blockage and act to reduce the possible damage caused by it and trigger an alarm to the end-user. Doing so, it reduces the time it takes to put the system back into operation due to the minimum damage made to the existing system (Less part replacement) and the rapid communication with the end-user.

6.5. Summary of the chapter

In this chapter, system self-testing capabilities and fault detection has been discussed for common faults such bubbles or blockage encounter in microfluidics. Such faults can have different manifestations, such as the ones seen in continuous flow or electrophoresis. These different cases have been investigated for possible detection by the embedded system using real time processing (Section 6.3.1 and 6.3.3.2) as also post processing (Section 6.3.3.1). The fault detection is mainly based on signal derivation in order to extract the slope, after setting the parameters of the fault detection routine empirically, good detection with no false positive can be achieved by the embedded system. Field testing of a glass LOC has also been done in order to evaluate the robustness of microfluidic in conjunction with river water sample. The LOC was pumped continuously with water for two and a half month before failure,

demonstrating the feasibility of such system for remote operation and their extend lifetime. Nevertheless, the ability to be able to detect such fault is needed as blocking is likely to occur eventually when using channels in the micrometre and millimetre range.

Self test and chip robustness were investigated as these are important attributes of autonomous measurement system where both temporary disruption and eventual failure are to be expected due to the nature of the instrument and environment. Hydrologists expect to deal with some invalid data points from *in-situ* instruments and greater the confidence with which these can be attributed to specific system faults the better. Self test data handling is just part of the overall system design, which will be described in detail in the following chapter.

Chapter 7 : System integration

7.1. Outline of the chapter

This chapter will discuss the system integration proposed for the LIMPIDS project *in-situ* water quality monitoring instrument. The chapter will first give an overview of the system structure and introduce the role of the different users. The software architecture will then be described (Section 7.5), starting with a general overview, then a more in depth detail of its constituting blocks (Instrument Manager, GUI, and Communication). The hardware of the system is also presented.

7.2. Contributing developers

The software development was a collaborative effort between Ian Bell and Etienne Joly with major contributions as detailed below.

Ian Bell: PC software architecture, GUI for basic system features and *in-situ* configuration, data graphing, data packet structure, communications / packet handling on PC and embedded processor, command parser on embedded processor.

Etienne Joly: Embedded software architecture including timing / ADC sampling, PC GUI / command handling for C^4D, electrophoresis and baseline suppression system, PC data processing for raw ADC data, embedded software drivers for peripheral hardware (RTC, ADCs, DACs, EEPROM, SD card, *etc.*), control of C^4D measurement, control of electrophoresis measurement, automated baseline suppression algorithm.

7.3. Overview

The final system is intended for use by a hydrologist for autonomous *in-situ* monitoring of natural water systems. It is envisaged that it will be deployed close to the water (*e.g.* on a riverbank) in a suitable waterproof housing (Figure 7.1) or in a shed with the intake common with the other instruments. The system will be configured by the hydrologist prior to deployment using a PC / laptop based software (Figure 7.2). During deployment, the system will store data using a memory card, but could potentially also make use of any available telecommunication networks. Data recorded will relate to analytical measurements (As defined in the requirements for the LIMPIDS project), but will also include system self-monitoring and self test data which will linked to measurement data to improve data integrity as discussed in Chapter 6.

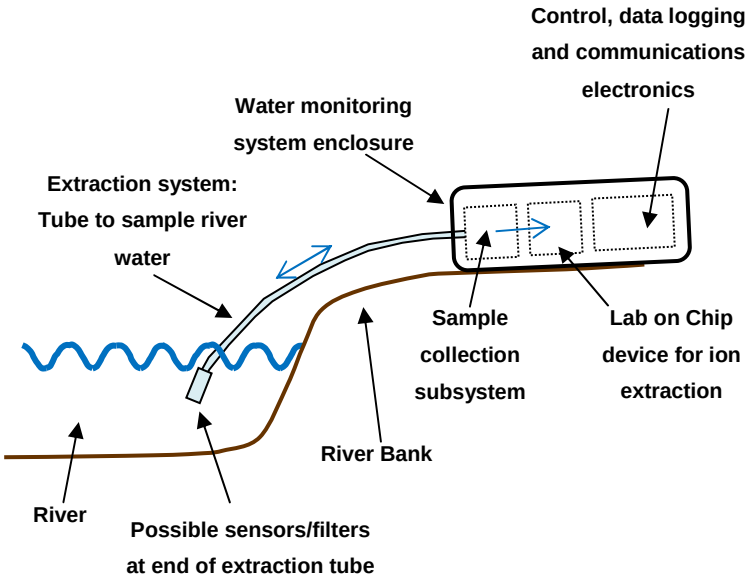

Figure 7.1: Possible system arrangement on a riverbank

It is expected that the system may also be of use as a lab instrument when it is not deployed in the field. Discussions with hydrologists indicated that this mode of operation may be worth developing. This mode will required a different physical sample interface and some additional software features; however, the majority of the required functionality will be present from the *in-situ* system. In fact the system has operated in a manner close to a lab Instrument mode during development, so this provision required little extra software development. It is also envisaged that the

system will required maintenance operations, including replacement of some fluidic components and calibration procedures. The activities related to different users / roles, which are discussed in more detail in Section 7.4.

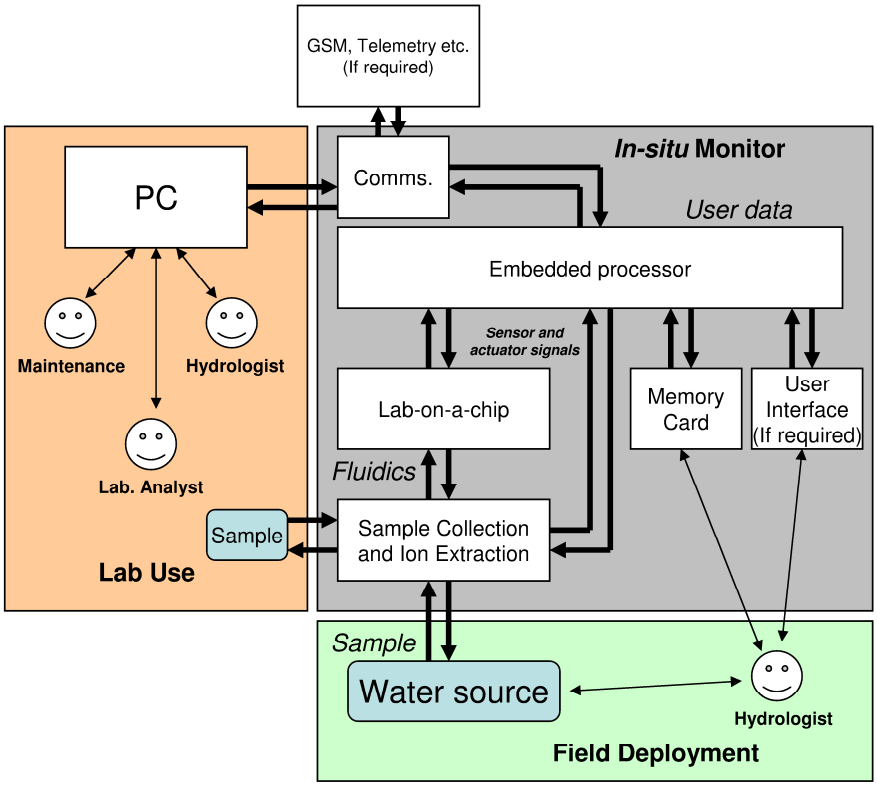

Figure 7.2: User roles and system structure

Figure 7.2 also shows basic system structure. The system is controlled by an embedded processor (PIC32MX7XX family, Microchip Technology Inc.) which is able to communicate with an external software application for system configuration and data retrieval. Data may also be retrieved by removing the data card from the system and using a card reader on any suitable computer. The embedded processor also manages the sample collection system and measurement process, including for example pumps for sample collection and sample introduction into the LOC device, high voltage power supplies for electrophoresis separation, baseline suppression and measurement of the C^4D detector signal. The embedded processor also collects and stores self monitoring and self-test information allowing data which may be suspect due to temporary system faults or extreme environmental conditions to be identified.

7.4. User roles

Potential user roles are identified below, together with the expected functionality associated with that role.

7.4.1. Hydrologist

This is the key operational mode where the instrument is used as an *in-situ* monitor of natural waters in the environment.

- Using PC / laptop, configures system for use in field (Parameters to measure, frequency, duration, start time, *etc.*).
- Deploys system in field (Possible control via Smartphone app or on-instrument LCD, *etc.*)
- Retrieves data from system (SD card swap, USB, telemetry) while *in-situ*. All analytical measurement data. Suspect data indicated by self test will be tagged as such.
- Retrieves deployed system from field (*in-situ* operation shutdown).

7.4.2. Lab Analyst

In this mode, the instrument is used in a laboratory like a typical analytical instrument. It can perform electrophoretic separation with C^4D detection of suitable samples. This may required a different chip-to world interface than that used for *in-situ* monitoring of natural waters. Potentially the core functionality could be deployed in other domains (See blood coagulation experiment in Section 8.5.2).

- Configures and runs experiments with system permanently connected to PC via USB.
- Data is streamed to PC, displayed live and stored on a hard drive.

7.4.3. Routine maintenance operative

This mode of use would typically occur between *in-situ* deployments and may well be formed by the same personnel. System is checked and prepared for next deployment, possibly including replacement of parts with finite usage life (*e.g.* Due to fouling).

- Run system checks, including calibration checks (Full access to self-test data).
- Replace user-replaceable parts when required.
- Able to activate high level system sub functions independently (*e.g.* Activate sampling pump) to confirm proper operation.

7.4.4. Repair and maintenance operative

If the system was developed as a product, this role would be similar to the routine maintenance with the difference that low level functions and diagnostic could also be accessed for deeper testing.

7.4.5. Developer mode

This is a not strictly an end user class, but at present the system is configured in a developer mode which exposes all features, plus additional functionality such as display of raw incoming serial data and use of built-in test functions. The test functions include a loopback transmitter which simulates instrument responses by trapping outgoing data packets, identifying certain key command strings and, if found, injecting received data packets into the incoming packet processor. There is also a test generator for “analogue” sensor data which is useful for testing data handling, processing and charting functions. These features facilitate PC software development without the need for an instrument to be constantly connected.

7.5. Software architecture

7.5.1. Overview

The PC software is written in C Sharp (CS or C#) using Microsoft's Visual Studio development environment and the .NET and Windows Forms libraries. The instrument is using a PIC32 processor with its software written in C using Microchip's MPLABX development environment and XC32 compiler. The current state of the software reflects the fact that the instrument is still under development and operations currently being performed are mainly experiments to verify specific aspects of functionality or performance. However, the software has been developed in a well structure way will facilitate rapid conversion to a deployable system once the experimental phase is complete.

Interaction between the instrument hardware and PC software is handled by a CS class called InstrumentManager (Which will be referred to as the Instrument Manager), see Figure 7.3. The user does not interact directly with the Instrument Manager; instead a separate Graphical User Interface (GUI) class (Derived from the Windows Form class) sends and receives information between the user and the InstrumentManager class. This separation of functions is a well known approach in software architectural patterns such as Model–View–Presenter (MVP).

We envisage the final system having multiple presentations via different GUIs which expose different subsets of functionally and mechanisms of system control to the user (See Figure 7.2, and Section 7.4 for user roles). During development work, another GUI has been used, which directly exposes low level interaction with the instrument hardware. However, this mode would not be appropriate for normal operation by an end user. Development of a GUI which is separated from the instrument interaction allows rapid development of a stable end-user GUI once the initial development cycle is complete. Stability is more likely because the end-user GUI only has to expose a sub-set of already developed functionality and no significant further development of the Instrument Manager will be required.

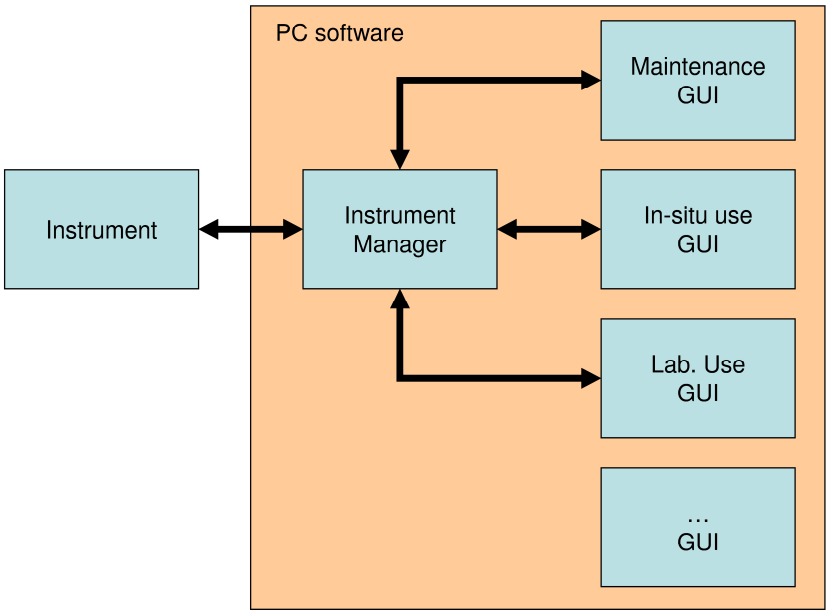

Figure 7.3: Block diagram of the Instrument manager

7.5.2. Instrument manager architecture

The architecture of the PC software is shown in Figure 7.4. The GUI and Instrument Manager interact through a variety of mechanisms which are described in more detail in Section 7.6. These allow the user to send commands to the instrument via the Instrument Manager and observe responses though updates. Sensor data from the instrument is held by the Instrument Manager and accessed by the GUI for display, analysis and storage.

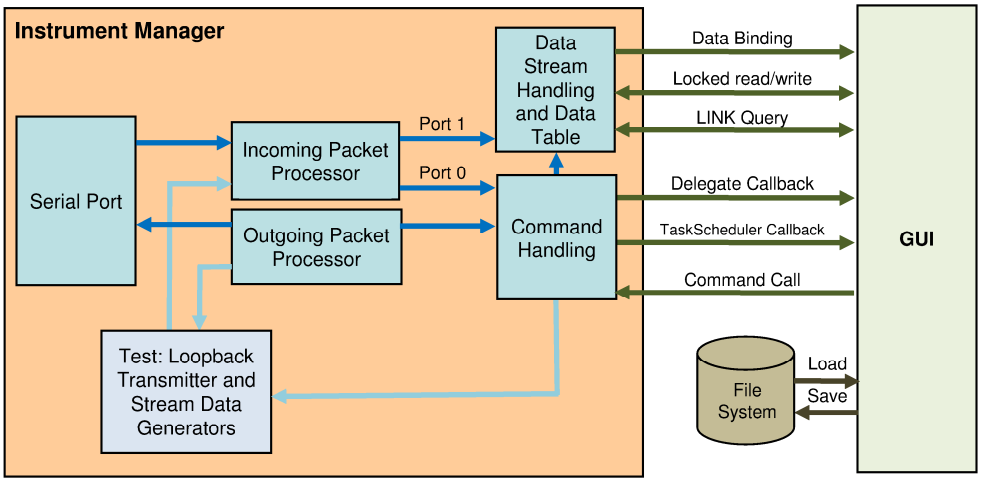

Figure 7.4: Architecture of the PC software

Commands for the instrument from the user / GUI are passed to the Instrument Manager Command Handler via a method call. The Instrument Manager does not parse the command text but simply passes it to the Outgoing Packet Processor which builds and sends a data packet to the instrument via the USB (Virtual serial communication port). A packet identification and associated data is lodged with the Command Handler so that instrument responses can be linked back to the outgoing command. Incoming packets from the serial port are decoded by the Incoming Packet Processor and passed on to the relevant handler (Identified by the port bits in the data packet, see Section 7.7.2). For basic command responses this is the Command Handler, which may pass responses back to the GUI via a callback mechanism (See Section 7.6).

For streamed sensor data, the response is passed to the Data Stream Handler which builds a data table from the incoming data. The GUI can read the data table, bind it to a suitable object such as a DataGrid, or submit a database-like query using a Language Integrated Query (LINQ) expression. In addition to containing raw numerical data from the sensors, the data table can contain flags (*e.g.* Related to data problems, instrument self-test issues, ADC overload, *etc.*).

The packet processing runs on a number of separate threads, which in effect form a processing pipeline. Thread management is handled using the mechanisms provided by the .NET Framework Task Parallel Library (TPL). Thread locking mechanisms provided by the .NET framework are used to prevent conflicts when the GUI and Instrument manager access shared resources (Particularly the data table).

7.5.3. Graphic User Interface (GUI) architecture

The current GUI of the LIMPIDS software is used at a developer level, thus all the features are exposed to the user. The interface includes different tabs which regroup different controls.

7.5.3.1. System Setup tab

The “System Setup” tab (Figure 7.5) regroups the configuration of the communication link (COM Port number, baud rate, protocol version, Loopback), the instrument (Soft) reset and the controls for the RTC (Read and set RTC time). The relevant COM port and baud rate must be selected manually, which is fine during development and is due to the use of the basic FTDI VCP driver. A commercial implementation would use a custom driver to make connection more straightforward (Using the PIC USB HID for example). There are some controls to manipulate the data protocol, which are intended for developer use only. The Loopback option is used for testing the PC software when an instrument is not present, as noted in Section 7.4.5. Auto-configuration sends a predefined sequence of commands to the instrument directly after a port connection is established.

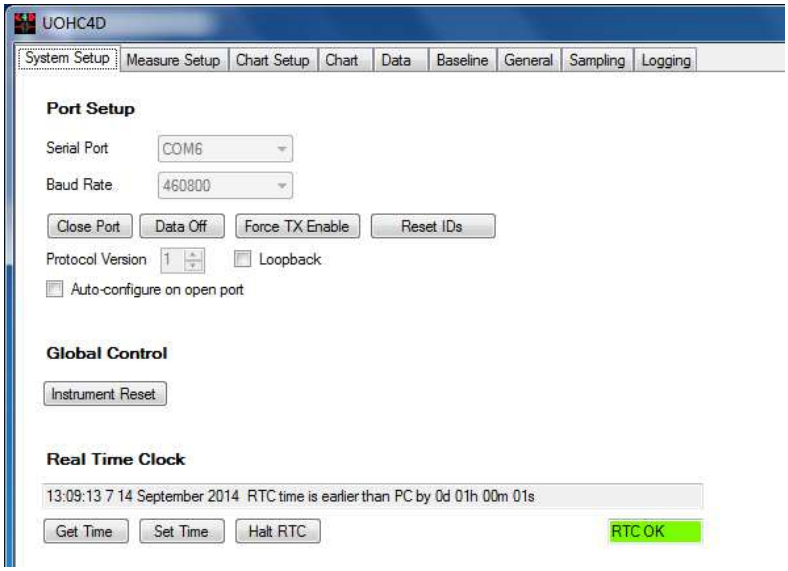

Figure 7.5: System Setup tab of the UOHC4D software GUI

7.5.3.2. Measure Setup tab

The second tab is called “Measure Setup” and is used to set up C^4D measurements (Frequency, amplitude) and the sequences for electrophoresis separations (Injection delay, Injection voltage, Separation delay, Separation voltage) (See Figure 7.19). It also displays a dynamic table which regroups all available measurement channels and their parameters (Channel name, Type of device, Activate, Sample rate, Scaling factor) (See Figure 7.6). This tab is initially more or less blank, but upon issue of the GETACHN command the instrument returns data which is used to build the GUI. There is also a test mode option on this panel, which is a developer function providing a set of virtual channels which can be linked to the “analogue” test generators and packet loopback test features.

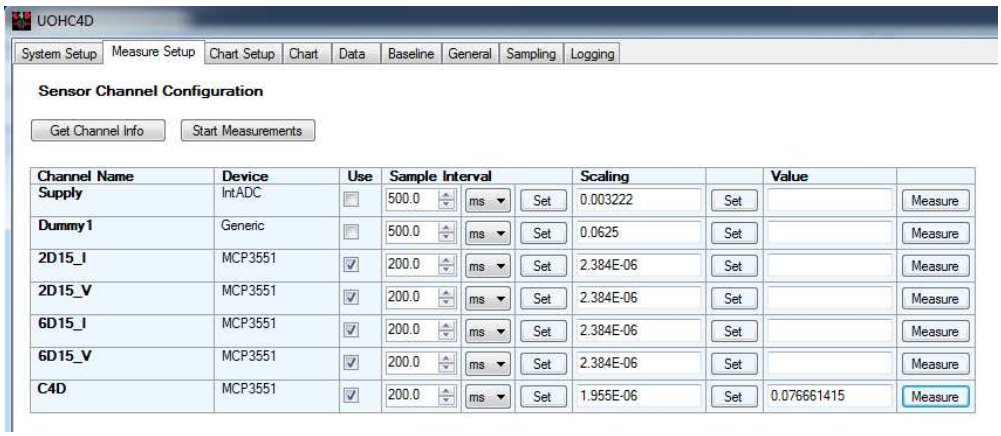

Figure 7.6: Customized section created by the GUI in function of the available data channels

7.5.3.3. Charting tabs

The next tabs (Third, fourth and fifth) are respectively related to the charting options, the chart (See Figure 7.7) and the DataTable. The chart displays real time measurements stored in the DataTable which could also be saved to a file for latter processing.

The “Chart setup” tab can be used to control settings such as the number of point between applications of autoscaling and the size of the “recent data” chart. There is also a set of controls for developer use which generates data to allow testing of charting and related functions to be tested without an instrument present.

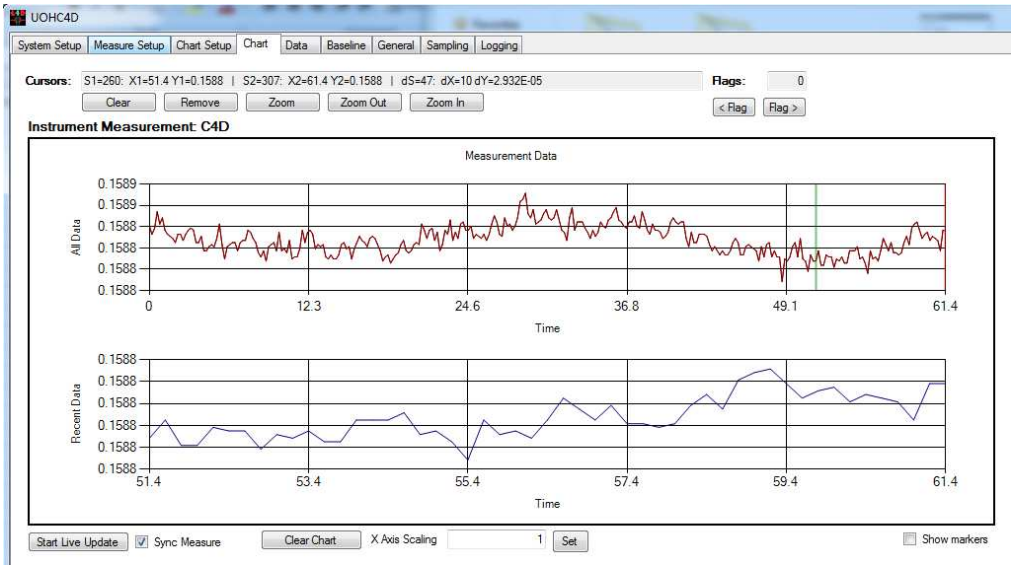

Figure 7.7: "Live" charting of the DataTable object

The "Chart" tab is used to display data collected by the instrument. It can provide a live updated display during data streaming. Any in-use channel can be displayed by right-clicking the chart and selecting the channel. Cursor and zoom functions are provided. The chart can also automatically find (Zoom to) flagged points in the data, which will typically occur where system self-test has indicated some issue such as an overload or other intermittent data-integrity problem. Live update can be switched on and off during streaming and live charting and start of measurements by the instrument can be synchronised if required (This is done by default).

The "Data" tab provides access to the main data table in the instrument (Analogue channel measurement data) and the tables used for display purposes. Data can be saved to a CSV file. A suitable CSV file can also be loaded and displayed on the chart. This tab also allows data to be deleted and measurement timing to be reset (For example to start a new experiment).

7.5.3.4. Baseline tab

The sixth tab is for the baseline suppression system (Figure 7.8); it contains the controls for the automated functions (Offset zeroing, phase synchronisation and amplitude matching) and the different components of the baseline suppression system (DDS, PGA, DAC). It can be used for fine tweaking of the baseline suppression and manual control of the baseline suppression.

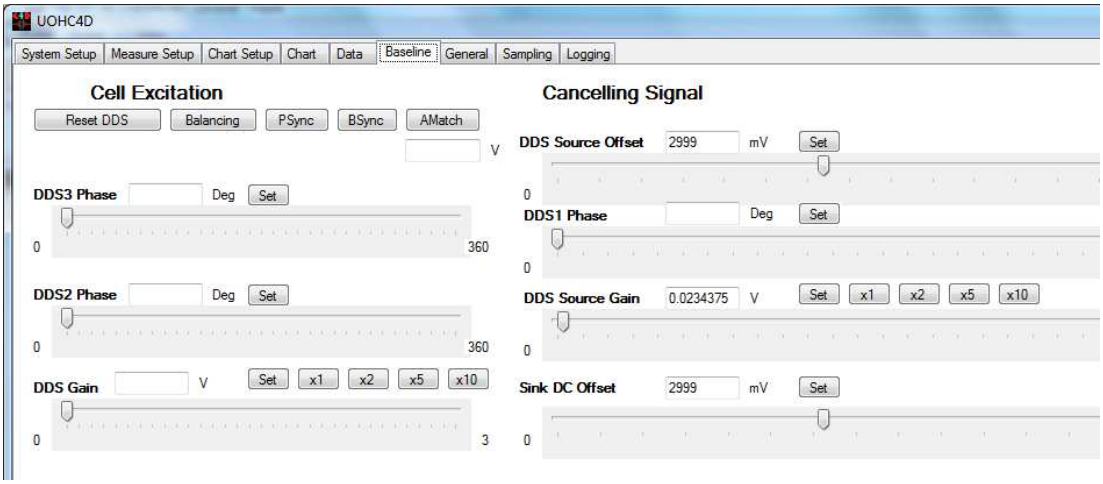

Figure 7.8: Baseline tab of the UOHC4D software GUI

7.5.3.5. Autonomous operation tabs

The last three tabs (Seventh, eighth, ninth) are related to the autonomous use of the overall system.

This "General" tab (Figure 7.9) is part of the configuration for an *in-situ* monitoring run. The tab is used to enter general details about the monitoring run, for example location, description and name of operator. Self-location (*e.g.* via GPS) can be used to set location data if the instrument or host (PC or other device running the software) has such capability. The instrument's capabilities are read by the PC software using the GETINST command during initial interaction between the PC and instrument and control the availabiltiy of settings options on this and the other monitoring run configuration tabs.

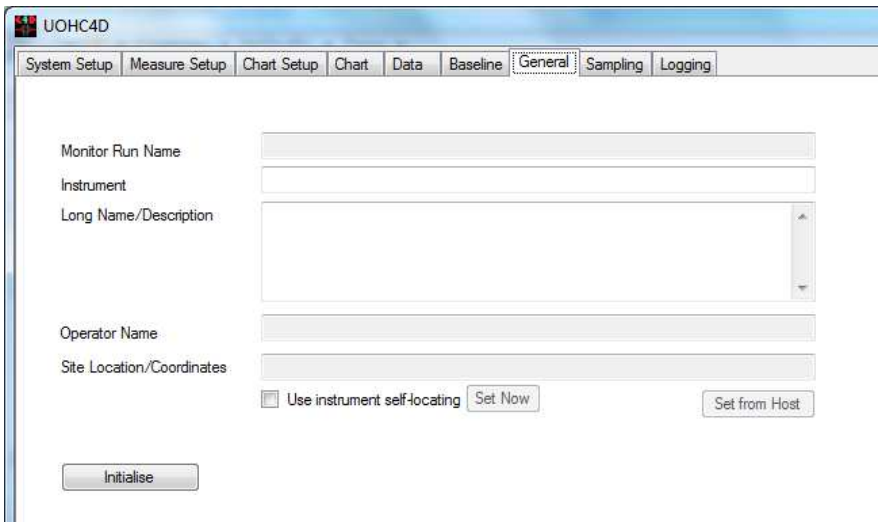

Figure 7.9: General tab of the UOHC4D software GUI

The “Sampling” tab (Figure 7.10) is used to control which parameters the instrument measures during an *in-situ* monitoring run and the sample rate and other settings for these parameters. The set-up is structured in terms of a set of sensors, each of which may measure multiple parameters. For example, an electrophoresis-based ion sensor may measure several ion concentration parameters and the input water temperature. Parameters belong to groups which have the same sampling attributes. For an electrophoresis sensor, ions concentration will all be measured in one operation, so it must occur together, but the temperature could be measured at other times (Even if this facility is unlikely to be used). In such a case, the ion concentration parameters would belong to a group and setting up any one would configure all the others in the same way.

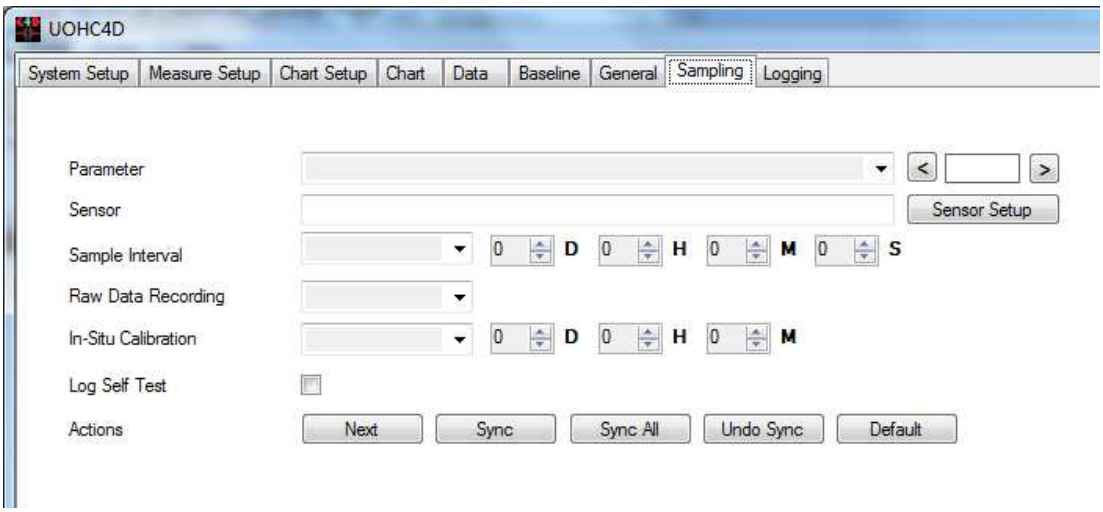

Figure 7.10: Sampling tab of the UOHC4D software GUI

Often parameters from different groups will use the same settings, so the sync button allows the previous set values to be applied to the current parameter (If feasible). The sync all sets all parameter’s setting to the last entered value (If feasible). Default settings can be selected and if the senor has any specific user-configurable settings (Other than those on the main screen), these can be accessed via the settings button.

Auto-calibration can be configured to run if this feature is supported by the senor. If supported, the user can select to store raw data (As directly measured by the sensor) as well as calculated parameter values. This facilitates problem diagnosis and potentially allows more sophisticated off lines analysis (*e.g.* of an electropherogram) that cannot be achieved with the computing power of the instrument. Self test data can be logged if this facility is available.

The PC software is not preloaded with information about the instruments sensors, parameters and capabilities. This information is obtained from the instrument using the GETSENS and GETSNPM commands, which are used to control the presentation settings available in this tab.

The “Logging” tab (Figure 7.11) is used to control the start and end of the data logging process for an *in-situ* monitoring run (*e.g.* Start time, action to take if data logging memory is full). The user can also obtain a brief or detailed summary of the configuration setup to confirm correctness before committing the instrument.

Figure 7.11: Logging tab of the UOHC4D software GUI

The bottom of the GUI also includes a console (Figure 7.12) which displays information for the user and the developer such as status, error or debug messages. Developers can also monitor received data bytes and packets when necessary. Text commands can also be sent from this console (See Section 7.7).

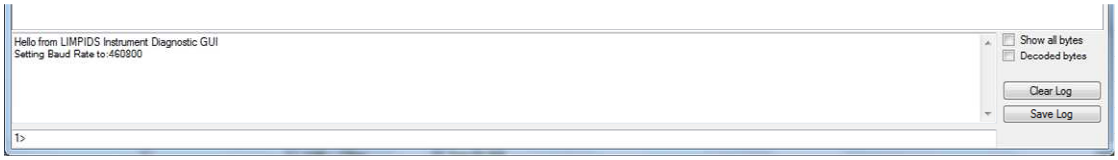

Figure 7.12: Built-in console of the UOHC4D software GUI

7.5.4. Embedded software architecture

The architecture of the embedded software is shown in Figure 7.13. The software interacts with the PC software via the UART module. Two UART modules are used in the embedded system which means there are two bidirectional channels that the software can access. One channel is used to communicate with the PC software while the additional channel can be used to send diagnostic message or could potentially be connect to a radio system such as the one using serial compatible GSM modem. More details will be given in Section 7.7.

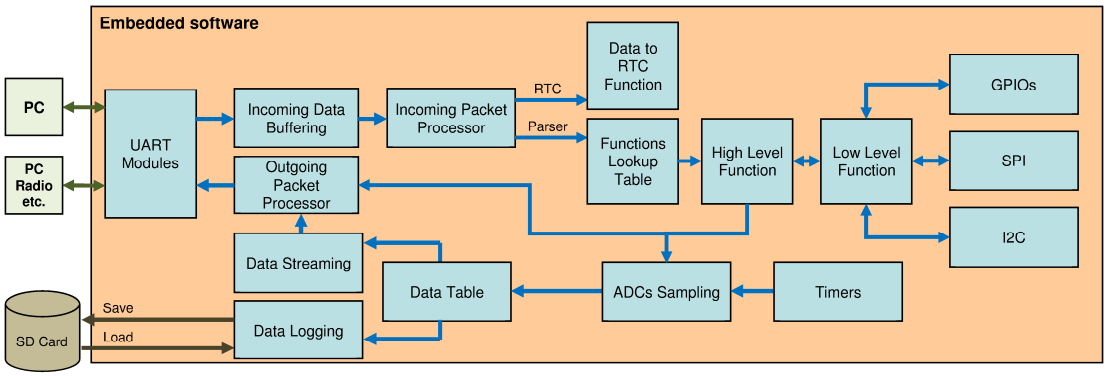

Figure 7.13: Overview of the embedded software architecture

The data sent by the PC software are first stored in a buffer (Incoming Data Buffer) before being sent to the Packet Processor. The Packet Processor checks the Data Packet structure (Section 7.7.2) and routes it to either the parser to execute the intended function or to the RTC for direct data loading. Other routing options could be developed in later version such as direct access to the SD card. The packet transmitted to the parser is decomposed to extract its content (Command and Arguments). The Command is then compared with a table containing the available functions (Functions Lookup Table) and the matching one is executed with the required Arguments (Section 7.7.1). The parser also informs the PC software of the outcome of the incoming command by sending back error messages where necessary for the user (*e.g.* Unexpected character, Command not recognised, *etc.*)

If requested by an incoming command, the data streaming (7.7.3) or logging can be triggered which enable the periodic sampling of the external ADCs which populate an

internal Data Table. The Data Table acts as short term buffer for data prior to streaming or logging.

7.6. Instrument manager to user interface interaction

The GUI holds an instance of the InstrumentManager class on which it can call methods to instigate actions from the Instrument. In event-driven situations, such as command responses, the Instrument Manager interacts with the GUI (Returns information to the user) using two callback mechanisms. For accessing the streamed sensor data the GUI reads from, or binds to (Using ADO.NET mechanisms) a data table in the Instrument Manager. Conflicts in data table access are prevented using thread locking.

The first callback mechanism is a standard delegate which the GUI registers on the InstrumentManager instance. This mechanism is used for actions not directly related to a response from the instrument. In such cases the Instrument Manager can immediately update the GUI via the delegate. The primary use of this mechanism is to update the command prompt and provide log / error messages to the GUI directly from the Instrument Manager.

The second callback mechanism is used when the GUI issues a command to the Instrument Manager which in turn will request a response from the instrument. In such cases the call-back will originate from the parallel processing thread handling the incoming data packets (Via the Command Handler). The specific action to be taken will depend on the out-going data packet / command, which will be associated with the response using the packet ID, as mentioned previously (Also see Section 7.7.2 for more details on packet structure). Thus the originating command identifies the GUI method which will handle the response data, but it is also necessary to know the thread synchronization context which will allow the work of that method to be scheduled on the GUI execution thread. To achieve this, when submitting the original command, the GUI passes an Action (Holding the callback method) and a TaskScheduler to the Instrument Manager. The TaskScheduler is obtained by calling TaskScheduler.FromCurrentSynchronizationContext() within the GUI.

The instrument can handle multiple sensor channels and / or multiple measurement parameters. These are not hard-wired into the Instrument Manager or GUI software.

Instead the Instrument Manager issues a command to the Instrument to discover the available data channels. This may be trigger automatically when the instrument connects, or be run manually via a command trigger from the GUI. The instrument's response is passed back to the GUI (Via the TaskScheduler mechanism) at which point the GUI builds a customized section of the user interface to reflect the available channels (See Figure 7.6 for an example).

Streamed data from instrument sensors is held in a DataTable object in the Instrument Manager. To display this data as a table, it bound to a DataGridView by the GUI. To display the data as a "live" chart, a background worker thread is used to periodically read the table using the locking mechanism provided by the .NET ReaderWriterLockSlim class to prevent conflicts with table updates from incoming data packets. Two charts are displayed by the GUI (See Figure 7.7). One of these (Lower chart) shows the most recent data in the selected channel (Typically 50 data points) and the other shows all data. The long term data chart is compressed if the number of data points exceeds the pixel count across the chart area.

7.7. PC to instrument interaction

Interaction between the PC software and instrument uses the System.IO.Ports.SerialPort Class from the .NET framework. The port can either be a legacy serial port or a virtual serial port using USB connectivity. The instrument uses an FTDI USB chip for serial communications, the driver of which provides a virtual COM port (VCP) on the PC. The instrument prototype also has a separate R232 serial port. This can be used to control external hardware, or as a means of sending diagnostic messages to a PC during software development.

The current system has one or two serial data links between a single instrument processor and a PC, with one of these carrying the interaction with the Instrument Manager. Diagnostics, when used, are displayed using a terminal emulation application such as RealTerm (realterm.sourceforge.net). However the system is designed to facilitate future development (See Figure 7.14), which would allow a single Instrument Manager to interact with multiple networked instruments (Typically

forming a sensor network) and / or multiple subsystem processors within a single instrument.

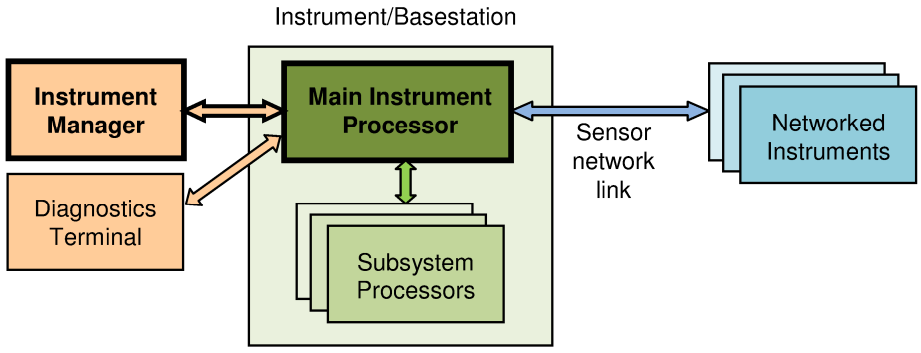

Figure 7.14: System communication overview

The instrument embedded software virtualizes its ports according to function (*e.g.* Command and Response, Diagnostics, Subsystem Control and Telemetry). The named ports (*e.g.* "Comms") are mapped to the processor's physical UARTs via a configuration table. This allows the software to be rapidly reconfigured if the hardware setup changes during development. The Comms port is used for interaction with the Instrument Manager.

The primary interaction between the Instrument and Instrument Manager is via text commands sent from the Instrument Manager to the instrument. The GUI provides a command prompt (Figure 7.12) at which the user may type commands to directly control the instrument. There is also potential for sequences of commands to be written as predefined scripts which perform more complex, but often repeated operations. Most typically however, a user will interact with the system via the GUI components such as buttons, text boxes and drop-down lists. These will configure command parameters and when appropriate (*e.g.* on a button click) will send the relevant command to the instrument. To do this, the GUI calls a method on the InstrumentManager class instance. Responses directly from the instrument manager or from the Instrument are passed to the GUI via the callback mechanisms described above (Section 7.5.2).

Data is transferred over the Instrument Manager to Instrument link using data packets. The structure of these packets is loosely based on those used in High speed Data Link Control (HDLC) and similar protocols, but no specific interoperability was designed into the system or packet definition.

Use of structured and identified data packets, rather than unframed serial commands and responses, facilitates asynchronous, multiple and simultaneous interactions between the Instrument and Instrument Manager. For example, commands to read and change operating parameters can be sent, and responses received, whilst streaming sensor data to the PC. Furthermore the Instrument manager does not have to wait for the instrument to respond before sending another command (Assuming the second command is not dependent on the response from the first). Reponses from commands do not necessarily have to be received from the instrument in the same order they were sent by the Instrument Manager. The ability to handle such out-of-order responses would be particularly important if the Instrument Manager was interacting with multiple networked instruments (See Figure 7.14).

7.7.1. Instrument commands

The instrument is controlled by text commands sent from the PC. These can be used to provide an immediate response (*e.g.* In lab instrument mode) or to configure parameters for autonomous *in-situ* operation. Commands are typically sent in response to button clicks, or other user interaction with the PC software GUI, but the user may type commands directly as text into the command area of the GUI (Figure 7.12) and the PC software may also send commands automatically (*e.g.* During initialisation).

The command text is sent, and responses are received, in framed data packets (See Section 7.7.2) so a simple terminal emulator cannot usually be used to send commands as pure text. However, it is possible to compile the instrument software with a flag set to use a simple text-only format. This was useful in initial development, but severely restricts functionality (in this mode, a text command cannot be sent until the instrument has finished processing the previous one, and commands which produce responses cannot be sent during data streaming).

The command format comprises the command name, a number of qualifiers and a number of parameters. It is based on the format of Unix csh and DOS prompt commands.

```
Name -qual1 -qual2 … -qualN param1 param2 … -paramM
```

The instrument software contains a table defining the commands which it understands. This table simply links the command name with a function pointer to the function which will execute that command. When a command packet is received by the instrument, the text is passed to a parser which identifies the command and collects qualifiers and parameters into an arguments array to pass to the execution function.

If a command is not identified by the parser, or syntax errors are present, a message is returned to the PC software (for display to the user) and no further action is taken by the instrument. The command execution code may also trigger error messages, for example if the number of parameters is incorrect. A function cPrintStdErrorMsg() is used to produce standard messages from a list, via an error number and with a severity level (Error, warning or information).

Commands requiring the Instrument Manager to perform processing prior to their issue, which alter the Instrument Manager's state, or which require special response processing are issued via method calls to instrument manager. It is also possible to use a generic SendCommand method to send any text command to the instrument, but the response is only processed as text.

Typically a button click, or other GUI action, will result in a method call to the instrument manager, passing information from other GUI controls (Numerical values *etc.*) where appropriate. The instrument manager will gather relevant information from its internal state, or perform other processing if required in order to formulate the command. This is then being sent as a data packet to the instrument and stored locally as described in Section 7.5.2. On receipt of the command response packet, the stored outgoing packet will be looked up and used to determine how the response is to be processed. This may both update the internal state of the Instrument Manager and instigate a callback to the GUI by the mechanisms detailed above.

The commands used by the instrument are defined in table in appendix Q.

7.7.2. Data Packet Structure

The packet structure is shown in Figure 7.15.

Figure 7.15: Packet structure

The packet starts with a Flag Byte (7E in hexadecimal). If the flag value occurs at any other point in the packet then a “byte stuffing” approach is used to prevent transmission of a premature end of packet. The flag byte is replaced by an escape byte (7D in hexadecimal) followed by the flag byte XORed with 04 hexadecimal. If the escape byte occurs in the packet it is treated in the same way. On receipt of an escape byte, the escape byte is removed from the byte stream and the following byte is XORed with 04 hexadecimal to recover the original byte (Either 7D or 7E).

The Flag is followed by the Address byte(s). The address comprises a 3-bit Instrument Manager response port (In the 3 LSBs) and an instrument / processor address. The instrument address is 4-bit by default, but can be expanded to any number of bits. A 1 in the MSB of an address byte indicates an extension to another byte. In most cases the Instrument Manger will act as a system master requesting a response from an addressed instrument. The instrument / processor uses its own address in a response packet. The current system does not make fully use of the address mechanism, with the address being fixed at 1. Currently two port values are used. Port 0 is used for “standard” command responses and port 1 is used for streamed sensor data (See Figure 7.4).

The Address is followed by a packet ID. The Instrument Manager sends packets IDs which are unique at the time of use. An ID will only be reused once a response packet has been received from the instrument which completes the transaction initiated by the original packet with that ID. The ID is one byte by default but may extend to any number of bytes if the number of IDs in use exceeds multiples of 128. A 1 in the MSB of an ID byte indicates an extension to another byte. The ID is used to match the instrument response to the original request / command, which in turn provides access to the callback mechanism required if a GUI update is required.

The ID is followed by the packet content, which may be empty if appropriate (*e.g.* If the packet is a command acknowledge that does not require return data).

The content is followed by a 2-byte checksum, which is not currently implemented.

The packet is terminated with a Flag Byte (7E in hexadecimal).

7.7.3. Data streaming

Before starting the data streaming between the instrument and the user's computer, the PC software needs to request ADC channel information, as described above (Using the GETACHN command). Using the generated GUI (See figure 7.6), the user can decide which channels need to be streamed and can configure its parameters such as scaling or sampling rate. Once the parameters are configured, the data streaming is started by sending the appropriate command (DATAON) to the instrument.

Periodically (Each milliseconds), the microcontroller will test if the sampling period previously set for each active channel is reached, at which point sampling activity is triggered. At sample time the microcontroller will initiated a conversion in the appropriate ADC and set that channel to trigger "sampling" again after the worse-case conversion time. The next channel action will be to read the value from the ADC and store it into data channel's table. The channel timing is reset to trigger the channel at the next sample point. The read function also sets an "InPacket" flag which is used to notify the SendPacket() function that new ADC data is ready to be send in that channel (After sending the data, the flag is reset). Data for all channels which currently have a sample pending is sent in a single packet during each system cycle.

The structure of the content section of the streamed data packet is shown in Figure 7.16. The first byte(s) contain flags which indicate which channels have data in the packet (One bit per channel). For each channel with data, that data follows in channel order. The number of bytes per channel is set by the ADC channel information and typically varies from one to three bytes where raw ADC data is sent. In some cases, where the instrument preprocesses data, a 4 byte floating point value is used.

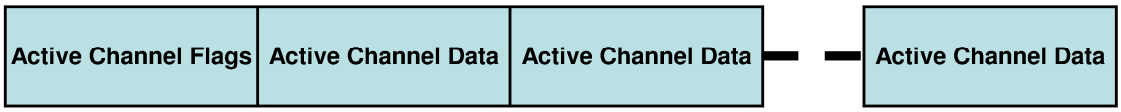

Figure 7.16: Packet structure for data streaming

The Instrument Manger in the PC software processes the incoming data stream packet from the instrument. Such packets received via port 1 (See Figure 7.4) and routed to the DataStreamPacketHandler. The role of the DataStreamPacketHandler is to

populate the internal data table of the PC software with the correct ADC and time values for recording and possible display on the GUI (See Figure 7.7).

The raw bytes corresponding to each channel must be converted to a single numerical value representing the value read for that channel at that sample point. Additional information such as ADC overflow flags may also be extracted and used (For example to warn the user of an overload). Thus the data in each channel must be processed in accordance with its individual format, which depends on the ADC device and any preprocessing performed by the instrument. To achieve this, each channel has an ADCDataDataProcessor delegate which holds a processing function used to convert the individual data bytes into a numerical value (and other information) for that channel. These delegates are configured using the device property of the ADC channel information upon receipt of channel information. The relevant delegate is called once for each active channel in each stream data packet by the DataStreamPacketHandler.

The user is able to add further custom processing of channel data. Typically this is just a scaling value, as shown in Figure 7.6, which is multiplied by the numerical value returned by the ADCDataDataProcessor delegate to give the actual voltage, or other parameter value, which the ADC is measuring. This is stored in the data table.

It is also possible to enter a mathematical formula written C Sharp in the “Scaling” box. If the first character is an equals sign (=) the entered string is assumed to be an expression in a variable X (Where X the numerical channel data value). For example, entering the string “=1/X” will cause the channel to record the reciprocal of the received value. The expression is compiled into an assembly and added to the application using the CSharpCodeProvider and Assembly classes. If present, the compiled object is called by DataStreamPacketHandler, passing it the numerical channel value returned by the ADCDataDataProcessor delegate. The subsequent returned value is entered in the data table.

7.8. Embedded hardware architecture

7.8.1. Overview

This part will give a description of the hardware involve in the LIMPIDS instrument. An overview of the embedded hardware is shown on Figure 7.17. The main element is a microcontroller (MCU) from Microchip, the PIC32MX795F512L running at 80 MHz. With its large program memory size (512 kB), future program updates to implement advance features are possible. This microcontroller has numerous general purpose input / output (GPIO) but also communication modules such as UART, SPI or I2C which their usage is described in Section 7.8.2 (See Appendix I for schematic).

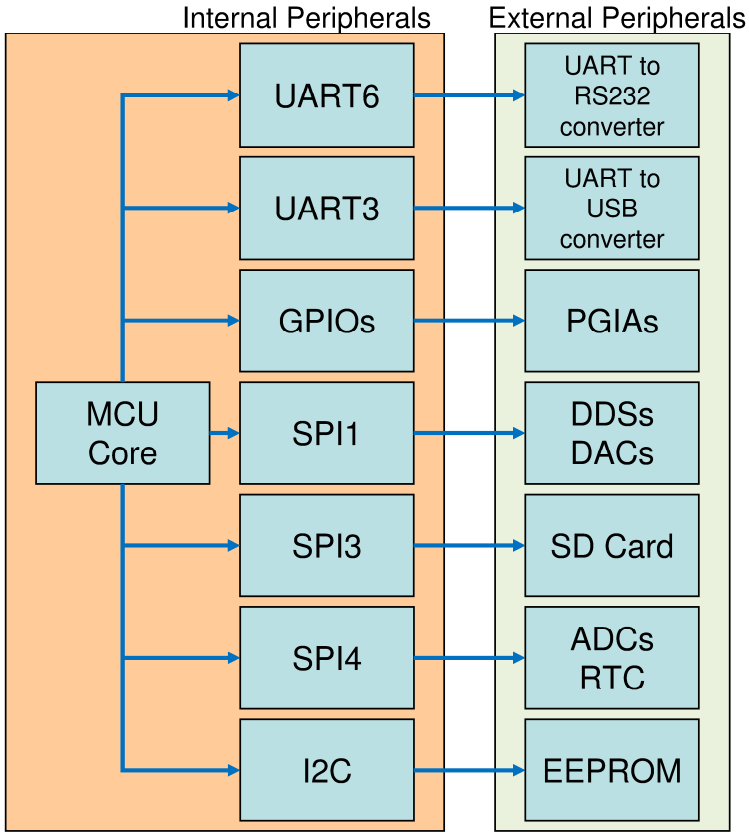

Figure 7.17: Block diagram of the embedded hardware

7.8.2. Embedded hardware description

An overview of the embedded hardware used for the LIMPIDS instrument is shown in Figure 7.17. Two different UART modules (3 and 6) are used to provide two communication channels, the main ones, which is connect to a FTDI FT232 chip to interface with a PC via USB using a VCP. This is the channel used to communicate with the PC software (Section 7.7). The second UART channel is connected to a MAX3232 (RS232 converter) and used mainly for diagnostic and debug purpose but could ultimately also be connected to a GSM module using serial as a communication protocol. This could be useful for remote operation when no physical link is present (*i.e.* Field operation).

Different SPI communication modules (1, 3 and 4) are used to communicate with various on-board components such as the Real Time Clock (RTC) for time consistency and the SD card, both useful for data logging. Data converters used to set reference voltage (DACs) and acquire voltage from the detection system (ADCs) are also controlled using this serial communication technique. Having different SPI channels is necessary when high SPI speed is necessary. Thus the channel could (In future developments) be used in conjunction of the Direct Access Memory (DMA) which does not require the CPU for write or read operations.

An I^2C communication module is used to allow the PIC MCU to retrieve system configuration parameters from the on-board Electrically Erasable Programmable Read-Only Memory (EEPROM). The I^2C bus could allow the possibility to use other I^2C enable components such as temperature sensor (*e.g.* LM73, ADT7420, TMP102, *etc.*), humidity sensor (HIH6130) or motor driver (DRV8830).

Two SPI (1 and 4) and 29 GPIOs are broken out to HE10 connectors and pin header to connect with expansion boards such as the one containing the C^4D system. The power for the embedded system is currently provided by TMR series DC/DC converter (Traco® Power). Use of more efficient DC/DC converter may be necessary for remote operation using battery as power source. If a battery is used, a charging circuitry may need to be implemented in the instrument. This would be useful in monitoring site such as the one at the river Kennet at Clatford [16] where a propane-fuelled generator is used. As such, it is susceptible to power outage but the operating

time of the battery will be extended by its ability to get charge when the generator is working.

7.8.3. Embedded hardware configuration

7.8.3.1. Initialisation

Prior to the MCU entering the main loop of the program forming the previously discussed architecture (Figure 7.13), the system initialisation is done, setting up numerous internal modules:

- Disabling unused MCU modules (JTAG, Ethernet, CAN)
- Configure Input and Output of the MCU
- Configure and Enable interrupts
- Set internal timers
- Set communication modules (SPI, I^2C, UART)
- Initialise external digital peripherals (RTC, DDSs, DACs)
- Load default configuration
- Initialise SD Card and file system

This hardware configuration allows, for example, the use of the microcontroller communication modules which are used to control most of the external digital components.

7.8.3.2. Interrupts

Interrupts are an important part of the embedded software and can be triggered outside the main MCU free running loop. In general microcontrollers have peripherals which can produce interrupts related to specific events. Once triggered, the interrupt is processed by the CPU. The interrupts can have different priority, and as such an "Interrupt priority controller" is used to order the interrupt events before being sent to the CPU. For example, priority can be given to the interrupt from the commands channel (CMD) over the diagnostic channel (DIAG). In our system, interrupt are

triggered upon the reception of a packet on both the CMD and DIAG channels. The relevant interrupt routine read the packet from the receive buffer of the peripheral and store it for future processing. Accurate tickers of different periods are also produced from the MCU's internal timers using interrupts (See Figure 7.18).

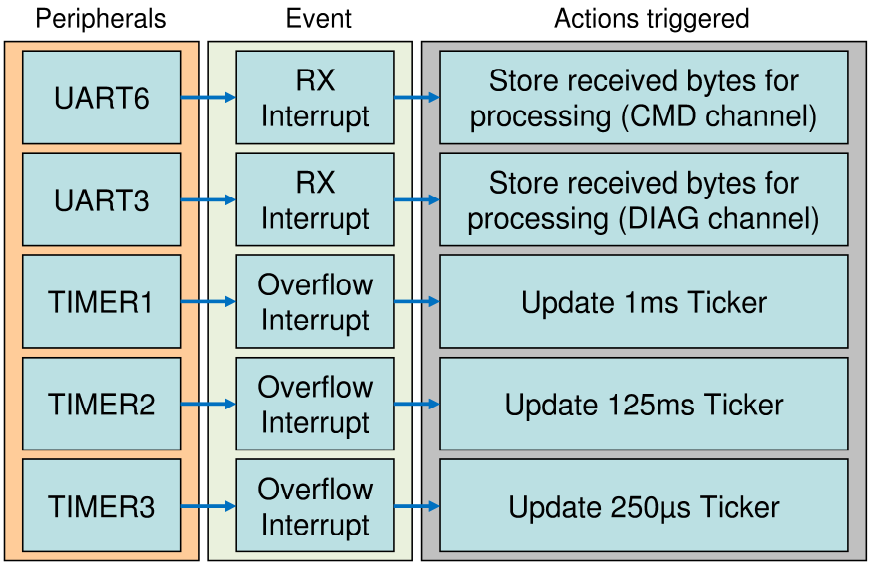

Figure 7.18: Embedded software interrupts

7.8.3.3. Main program routine

After the initialisation, which sequentially sets up the embedded system (See Section 7.8.3.1), the software enters into an infinite loop.

This loop currently contains three mains tasks, which once active, are triggered from interrupts:

- Management of the ADC sampling and data streaming, either to be sent to the master (PC) or to be logged into the SD Card.
- The triggering of the baseline suppression functions for automation of the process.
- The processing of the incoming commands from the Instrument manager (PC).
- Further processes such as periodic activation of sampling pumps or electrophoresis operations will be required in the final system

The interrupt from the MCU's Timer 1 is used for the data streaming. Periodically, each ADC channel is checked by the software to verify if they meet the criteria for streaming or logging. The ADC channel needs to be active (Selected by the user), have data available and the time must match the relevant sampling period.

The interrupts from the MCU's Timer 2 and 3 are used for the automation of the baseline suppression. Timer 3 is used for the current offset compensation, the microcontroller will send commands to change the current offset in the voltage to current converter periodically until it reaches a zero crossing point, which detected by a comparator (See Section 5.2.7). Timer 2, which has a longer period (125ms), is used for the phase synchronisation and the amplitude matching of the signal from the cell and the current to voltage converter. The longer period is used for the ADC sampling and the on-board floating point math computation.

The main loop also checks if any bytes received by the MCU's UARTS have been buffered during a recent serial receive interrupt. If so, these are routed to the relevant destination (Usually the command parser). Initially the data router decodes the packet framing (ID and address) and then passes further bytes to the command parser until an end-of-packet flag is received (Other routing destinations for packet content can be used). The parser is a state machine which changes state as necessary when new bytes arrive and retains its state; it does not have to be passed a complete command line at one time. Once the parser has found a complete and valid command line the relevant function is called to execute the command. The list of available commands can be found in appendix Q.

7.8.4. Electrophoresis operation

7.8.4.1. Setting up the electrophoresis sequence

The system provides the capability to run electrophoresis experiments, which can be setup using a dedicated panel in the instrument GUI (Electrophoresis Instrument Control). This panel (See Figure 7.19) is used to set the parameters needed for a simple electrophoresis separation with electrokinetic injection (See Appendix O for electrophoresis protocol). After pressing the SET button, the parameters are passed to

the instrument using the commands “SETEXP” which takes the voltage and duration needed for the injection and the separation. Upon the reception of the “STAREXP” command, the DACs controlling the high voltage modules are initialised and the voltage is applied to the electrophoresis chip. Each steps have a finite duration which is the one passed to the instrument from the GUI. This duration is compared with the internal timers of the instrument, once the duration of the current step is achieved, the next step is activated, if no further steps exist, the electrophoresis system is switched off (DACs at zero, high voltage module inhibited, relay open).

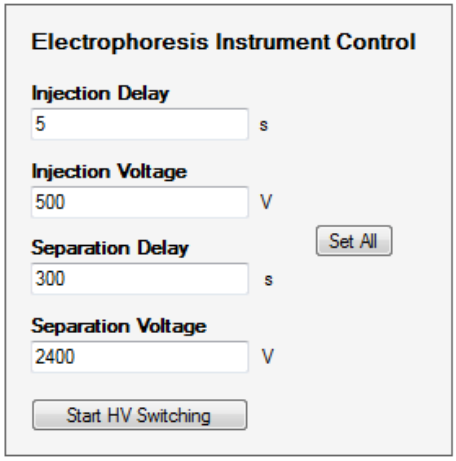

Figure 7.19: GUI for the control of the electrophoresis experiment

7.8.5. Data converters control for C^{4}D measurement

The system is controlled by, and measures, a number of analogue signals therefore data converters are needed to interface the digital electronics to these analogue subsystems. A C^{4}D measurement involves the generation of a sinusoidal signal with a certain frequency and amplitude which will be picked-up by the detection circuitry (See Section 3.7). As previously seen (See Section 5.2), this signal can be created using digitally controlled devices such as DDS, DAC and PGA. The DAC and the PGA will be used to set the amplitude of the signal generated by the DDS. These components can be accessed individually by the user from the GUI when operating in developer mode which exposes most of the features to the user.

The DACs used (AD5663R) have a resolution of 16-bit with a built-in reference of either +3 V (DDS amplitude) or +5 V (Voltage bias of voltage to current converter

circuit). These DACs can be individually accessed by the PC software using the command “DAC” which take two arguments (DAC ID number and the 16-bit value). After the command has been processed by the parser, the correct high level function is called and the arguments are passed to it so that low level SPI functions can be used to set the DAC to the correct output voltage.

The PGAs used have a 2-bit parallel connexion which gives the user the choice between four different gains. The PGAs can be accessed via the “GAIN” command which take two arguments (PGA ID number and the 2-bit value).

The DDSs (AD9834) can be seen as a form of data converter, the DDS can be accessed the same way as the DACs, using a command and two arguments. The DDSs however have three different functions, the “DDSRST” function which is used to switch on (0) or off (1) a DDS and thus can also be used to synchronise all the DDS together. The “FREQ” function is used to set the frequency of the output sine wave. A frequency of 0 Hz turn the DDS into a 10-bit DAC where its output voltage is a function of the phase word (See device datasheet [207] for full details). The phase is controlled by the command “PHI” which set the phase of the addressed DDS, and synchronises it with the rest of the DDSs.

7.8.6. Baseline suppression automation

The baseline suppression routine with the quadrature lock-in circuit is described in Section 5.2.7.2 but further details on the automation will be given in this section.

The first step is to cancel the current offset which can be seen at the output of the transimpedance circuit. This current can be due to errors in the voltage to current converter stage, and if too high will affect the dynamic range of the sensing circuit. In order to automate the process, the system uses a low pass filter followed by a comparator to know whether the signal average is positive or negative. The current is then changed (Decreased or increased depending of the comparator) by modifying the output of the DAC responsible of the current bias in the voltage to current converter. The system periodically checks if the value of the comparator has changed, if it did not, a new output value is sent to the DAC. When the signal average changes polarity, the comparator changes state and the DAC value stays at its current value. This value corresponds to an output signal from the transimpedance amplifier centred on zero.

The second stage is synchronisation of the cancellation current with the current from the cell. The first step is to know the phase difference between the DDS creating the excitation signal passing through the cell and the output of the transimpedance amplifier. To measure this phase, only the DDS for the cell excitation is activated, the DDS for the cancellation current is turned off. The value of the phase can then be calculated using the I and Q value from the quadrature lock-in amplifier measured by the ADC. The value of the phase is calculated by the embedded system, with these values and stored for future use.

The second step is to know the phase difference between the DDS generating the cancellation current and the output of the transimpedance amplifier. The same method is used for this second step, only the DDS used for the cancellation current is turned on and the phase is measured. Knowing the phase measured in the first step and the second step, the two sinusoidal signals can be synchronised using the equation 5.19 from Section 5.2.7.2.

The next and last stage is to increase the cancellation current in order to suppress the baseline signal from the cell when only buffer solution is present. The output amplitude of the signal from the transimpedance amplifier is measured (Either by computing I and Q from the quadrature lock-in or by using a TRMS converter chip coupled to an ADC) and the current is increased until the amplitude threshold set by the user is reached. Once the threshold is reached, the baseline automation routine is stopped and the system is ready for the experiment.

7.9. Summary of the chapter

In this chapter, an overview of the system integration has been given (System deployment, system users) which highlights the different usage of the system (*in-situ* monitoring or laboratory use). An extensive description of the software used to communicate and control the instrument was given in Section 7.5. This section described the three mains architectures which constitute the system software (Instrument Manager, GUI and Embedded software). Information was given on the construction of the different software parts and how they operate. Section 7.6 and 7.7 respectively described the interaction of the Instrument Manager and the GUI and the interaction of user's computer and the instrument. This latter section is focused on the

communication protocol used; the instrument commands are sent via data packets with a particular structure. Data streaming is also an important part of the communication process between the user computer and the instrument, especially if used in its laboratory mode. The embedded hardware architecture used in conjunction with the software described earlier is presented in Section 7.8. The main functions executed by the microcontroller are detailed (Initialisation, Main loop, Interrupt routines). Particular operations (Electrophoresis, Data converters and baseline suppression) are also described from an hardware point of view in this section.

Although a completed monitoring system was no deployed during this project, the work presented here means that the electronic hardware and software is very close to being ready for use in a deployable system. The software and hardware developed is fully functional for use of the system in laboratory instrument mode.

Chapter 8 : Conclusion

This thesis discussed the separation and detection of organic ions for applications in water quality monitoring, especially in rivers. The final aim of the LIMPIDS project is the development of an autonomous system which can be used for *in-situ* monitoring. This monitoring system will help provide high frequency data in order to refine pollutant transport models for catchments.

The objectives of this project and their respective advancement will be discussed in the following sections. Section 8.1 is dedicated to the creation of a LOC device and electrode structure for C^4D detection (Objectives 1 and 2 in Section 1.2). The main criteria for such device are low cost manufacturing and robustness for field deployment. Section 8.2 addresses the development and evaluation of a detection system for a LOC based separation system. Efforts have been made toward integration while having an improved limit of detection when using the detector in conjunction with its baseline suppression capability (Objectives 1, 3 and 4 in Section 1.2). Section 8.3 is related to the self-test capabilities of the system which is an important point when dealing with autonomous system for field deployment (Objective 5 in Section 1.2). Section 8.4 is about the system integration and depicts the software and embedded hardware developed for the project in order to provide the user with a reliable and easy to use instrument (Objective 4 in Section 1.2).

8.1. Development of a Lab-on-chip for IC

As part of the project objectives, the development of a microfluidic platform suitable for electrophoresis separation, using electrodes for capacitively coupled contactless conductivity detection (C^4D), which can be manufactured easily, has been investigated. Solutions including cylindrical electrodes, plug and planar electrodes have been tested. Cylindrical electrodes using capillaries are a good solution for electrophoresis experiments, the surface chemistry is well understood and they can deal with high voltages. The electrode fabrication is however difficult to repeat. Furthermore this design cannot be implemented into a microfluidic chip which goes

against the objective of having a miniature cell constituting a LOC device. The use of plugs containing electrodes, while providing good sensitivity, was prone to leakage and may require expensive manufacturing processes to be made repeatable. This design is however a step closer to a LOC device as the channel is created in the microfluidic chip. The use of a printed circuit as a base for the microfluidic chip solves the problem of cheap and repeatable manufacture of the electrodes. The insulation layer made from spin coating is also easily controllable by the viscosity of the solution and the spin parameters. Possible future work on his latest design will be discussed in Section 8.5.1. Good sensitivity has been achieved for flow experiments and application to medical sample has also been proved using the electrodes coupled to a conductivity detector (see Section 8.5.2).

8.2. Design of a conductivity detector with baseline suppression

During the development of the detection / signal processing system for miniature / LOC separation based chemical analysis, the design of the capacitively coupled contactless conductivity detector (C^4D) circuit used for the experiment has been modified to implement a novel baseline suppression system. The cancellation current generated by the suppression stage helps to use the full dynamic range of the transimpedance amplifier by lowering the offset formed by the background electrolyte and the parasitic coupling. It enhances the sensitivity by allowing the use of higher excitation voltage (*e.g.* 100 Vpp) which in conjunction with the baseline suppression improved the LOD to 0.0715 µM for NaCl. This is an enhancement by an order of magnitude compared to the LOD found when using a moderate excitation voltage (21.4 Vpp) without baseline suppression for NaCl (0.8653 µM). The phase change induced by the plug of analyte travelling through the cell produces a change in the recorded output signal of the detector. This phase change has the effect of increasing the sensitivity of the system when using the baseline suppression system. The automation of the baseline suppression system has been investigated using one multiplier with a quadrature reference signal, or two multipliers with an in-phase and a quadrature reference signal. The use of two multipliers simplified automation of the

baseline suppression as it provides information about both the amplitude and phase of the signal, allowing a faster matching of the suppression current.

One of the objectives is the development of a self-contained system for field deployment with integrated control and signal processing. The system developed has integrated all the necessary components which are often provided by benchtop equipment in existing detector designs (*e.g.* signal generator, acquisition front end, logging, *etc.*). Being built around embedded electronics, the control software has been developed with the aim of providing the user with an autonomous system which can be used as standalone equipment in the laboratory or in the field. More details of the different software architectures were discussed in Chapter 7. Such hardware and software design is a step forward toward more integrated measurement equipment which is needed for the fulfilment of this project's objectives.

8.3. Self-testing, fault detection and autonomous operation

An autonomous system for *in-situ* monitoring can be subject to temporary extreme conditions which can influence the operating life of the system by causing (temporary or permanent) dysfunction. Thus the system should provide self-test capabilities to facilitate identification of rogue data, improve overall data robustness, and alert users of actual or pending failures. Investigation of fault detection using the results collected during flow experiments and electrophoresis runs has been carried out to address this issue. Autonomous detection of bubble induced peaks by the on-board microcontroller from typical chromatographic peaks has been successfully proven and can help identify system failure (*e.g.* leaks, valve failure). Pump speed has also been extracted afterward from datalogged results using an FFT, which related the noise pattern to the speed of the peristaltic pump. It has also been highlighted that current reading from the power supplies used for electrophoresis can provide useful information about the nature of the content of the current path (*i.e.* channels). Bubbles or changes in the buffer concentration may be detected by analysing the current profile during the separation process.

Field testing of a flow cell has been carried out at a monitoring station to investigate its robustness. Blockage occurred after a period of over two and a half months,

proving that failure is likely to occur and early detection of system failure is necessary.

8.4. System integration

Development of an easy to use integrated measurement system is one of the objectives required for the LIMPIDS project. This involves embedded electronics and software development to control it. Efforts have been made toward the creation of high level software capable of giving easy control of the instrument to the user (*e.g.* Hydrologist). In that aspect, simple, user specific, GUI interfaces have been developed in parallel to provide robust and flexible interaction with the Instrument Manager which interfaces with the physical system. This GUI will permit any user to access the functions of interest for their intended usage. The communication between the PC software and the embedded software benefits from a reliable packet structure (Packet ID, Checksum) which has been tested for data streaming of continuous flow and electrophoresis experiments (See Appendix O for measurement protocol).
Embedded hardware has also been developed to control the measurement electronics developed for the project. The main board is composed of a microcontroller which can communicate with the user through the LIMPIDS software and the rest of the system. It can thus provide automation for the baseline suppression, the electrophoresis injection, electrophoresis separation and datalogging. The current embedded hardware architecture is described, and possible future extensions are listed (Wireless communication, *etc.*), in Section 7.8.

8.5. Further work

This work has made significant progress towards the development and deployment of an *in-situ* water quality monitoring system. The whole project requires some further development of the chemistry part (Objective 6 and 7 in Section 1.2), particularly in the areas of sample extraction, ion preconcentration, separation and LOC device / microfluidic integration, which have not been addressed in detail in this thesis. Work in this area is ongoing at the time of writing. The developed system is

operational as a lab instrument and provides the bulk of the functionality required to perform autonomous *in-situ* measurement and data logging; however there is room for improvement in terms of both performance and functionality. These issues will be discussed in the first part of this section. The C^4D detection system has wider applications than water quality monitoring; indeed the system developed here was used in another project and this will also be briefly described to highlight the wider application of this work.

8.5.1. Future development

During the course of the project, one of the objectives has been the development of a LOC device for separation-based chemical analysis (*e.g.* electrophoresis and ion chromatography). Cell (Electrode and channel) geometry, manufacturing processes and performance have been investigated. However, there are opportunities for further progress towards the objective of creating a novel, high-resolution, multiparameter water quality measuring system using an innovative miniaturised chemical sensing device.

First, the current cell design can be optimised. For example, the insulation layer can be tuned toward higher sensitivity by the use of thinner coating and the possible doping of the PDMS. The introduction of high dielectric particles such as Barium-strontium titanate ($BaSrTiO_3$) or Titanium dioxide (TiO_2) has been proven to increase the dielectric constant of the PDMS mixture and thus increase the capacitive coupling between the electrode and the channel through it [178]. The second point is related to the introduction of the separation process which was developed by the Chemistry Department at the University of Hull.

The detection technique has been proven on a commercial LOC device (microfluidic ChipShop) during the ongoing development and optimisation of the separation technique (Section 5.4). Despite the fact that the detection cell was developed with the objective to include both the sample introduction and separation method currently in development, these module have not been implemented together yet. This is still being developed by the Chemistry Department (Chemistry part of the objective from Section 1.2). Thus extra work will be needed to implement the sample introduction and separation technique and optimise the existing detection cell for this system. The

sample introduction being based on Electrodialysis, additional electrodes may need to be created on the PCB substrate. The structure of the LOC device will also need the creation of additional channels

Further work could also be done on the detection and control electronics. For example, the performance of the analogue front end and the data converters could be improved by using different hardware architecture and / or integrated circuits. The use of ADC with faster sampling rate will help increase the speed at which the baseline suppression automation process is done. The current ADC was chosen for high precision (22-bit) and low power (600 µW). Fortunately, numerous models of ADC exist, which make it possible to find a component with equivalent (or higher) precision and higher sampling rate, while consuming a small amount of current.

The quiescent current for each integrated circuit could also be investigated if power consumption is a problem. However when dealing with microfluidics, solenoid valves and pumps are required for the fluid handling. They may represent most of the power consumption of the system compared to the control and acquisition electronics, even if only active for a short period of time. Power consumption is an important factor when dealing with autonomous, portable system like the one developed for the LIMPIDS project. However, the instrument developed has been mainly tested in a controlled environment when mains power was available. As a consequence, very little development time have been used to investigated the power source (Battery type, capacity, integration) and power management circuitry needed to confer the instrument with an optimised battery life. The integration of reliable, efficient, low noise power supply into the system is part of the future developments needed for the system to perform during field deployment.

Additional miniaturisation of the electronics is possible by reducing the footprint of the components, which requires better printed circuit board manufacturing process thus allowing design rules with smaller features. Use of individual integrated circuits with identical function could be replaced by regrouping multiple functions in the same package. In the case of the DDS, the 4 individual integrated circuits could be replaced by a 4-channel DDS, such as the AD9959. When multiple digital components are needed, a field-Programmable Gate Array (FPGA) can be an interesting choice for the designer. The usage of such programmable device permits the creation of digital block with user specified characteristics. In the case of DDS, the block diagram seen in Section 5.2.3 can be reproduced in a FPGA with a more accurate phase accumulator

(Allow smaller frequency and higher phase resolution). FPGA based system may however suffers from larger component cost, extra development time and major hardware redesign. FPGA are only justified if high speed processing unsuitable for a MCU or a DSP is needed.

The control software and associated GUI has been thoroughly tested by the developers during the course of the project. However, the main users will be the hydrologists in charge of the *in-situ* monitoring. This may cause some additional work on the GUI to modify it to the liking of the final user (Even if hydrologists were consulted during the initial GUI development). It is also possible that software bugs still exist and thus may require the intervention of the developers to correct them.
The baseline-suppressed C^4D detection system developed during the course of the LIMPIDS project can potentially be used for other applications than inorganic ions sensing. This system can be used for the sensing of any charged species. It can be adapted for other experiment, for example, in biosensors.

8.5.2. Monitoring of clotting process using conductivity detection

The C^4D system (Hardware and software) developed for the LIMPIDS project was also used for a biomedical application involving the measurement of blood clotting time.

8.5.2.1. Background

The applications of conductivity detection have recently became broader, being used in the field of chemistry still [163] but also fluid mechanics [138] and biology [197] (Section 3.9). The following case is about the study of blood clotting using conductivity detection for characterization of this physiological process.
Such study could lead to the development of a point of care device capable of monitoring the blood coagulation process. For example, patients with certain cancers (*e.g.* Ovarian, pancreas and lung), have an elevated risk of venous thromboembolism (VTE). This is most likely due to circulating tumour derived microparticles (MP)

which have tissue factor (TF) expressed on the membrane surface making them highly procoagulant. Currently, the standard technique used to measure the coagulation process is the activated partial thromboplastin time (APTT) [208].

APTT involves the separation of the plasma from the whole blood by centrifugation, followed by the mixing of the plasma with phospholipids, calcium and activator of the blood coagulation pathway (Silica, kaolin, *etc.*). Once the blood clotting process is triggered, the clotting time is recorded. Being a labour intensive process (Blood sample collection, plasma separation, *etc.*) with the possibility of delay between the time the sample is taken and processed (which can affect the result), a faster diagnostic method is preferable. Rapid monitoring of the blood coagulation at the patient bedside could help proactively dispense anticoagulant to the patient in order to avoid VTE. During clotting, the plasma changes from a conductive liquid form to an insulating sol-gel form. This variation in electrical properties can be detected using a conductivity detector such as the one previously presented and help to move toward small footprint medical test equipment.

8.5.2.2. Materials and procedure

The experimental setup is composed of a microfluidic chip with a fabrication process similar from the PCB / PDMS design from Chapter 4. However, prior to the coating of the PCB substrate with PDMS, dielectric particles ($BaSrTiO_3$) prepared from [209, 210] were blended into the polymer. Such dielectric particles are used for the doping of the insulation layer to increase its dielectric constant, and thus its sensitivity, by enhancing the coupling of the electrode to the liquid solution [178]. As the current system is not using a high separation or excitation voltage, thinner layer (µm range) can be achieved without the risk of electrical breakdown of the insulation layer.

The gap of the electrode was set to 4 mm for greater sensitivity (To the detriment of the special resolution not needed in that case), with an excitation frequency of 100 kHz and an excitation voltage of 5.5 Vpp. The background electrolyte has a concentration of 0.4 mM.

8.5.2.3. Preliminary results

Figure 8.1 shows the change in impedance measured for the blood sample (Red) and the blank cell culture media (Black). The clotting was induced by adding 25 mM $CaCl_2$ to the same volume of fresh human blood containing EDTA. The mixture for the blank media contained 25 mM $CaCl_2$ and RPMI 1640-fetal bovine serum-antibiotics, kept at 37 °C.

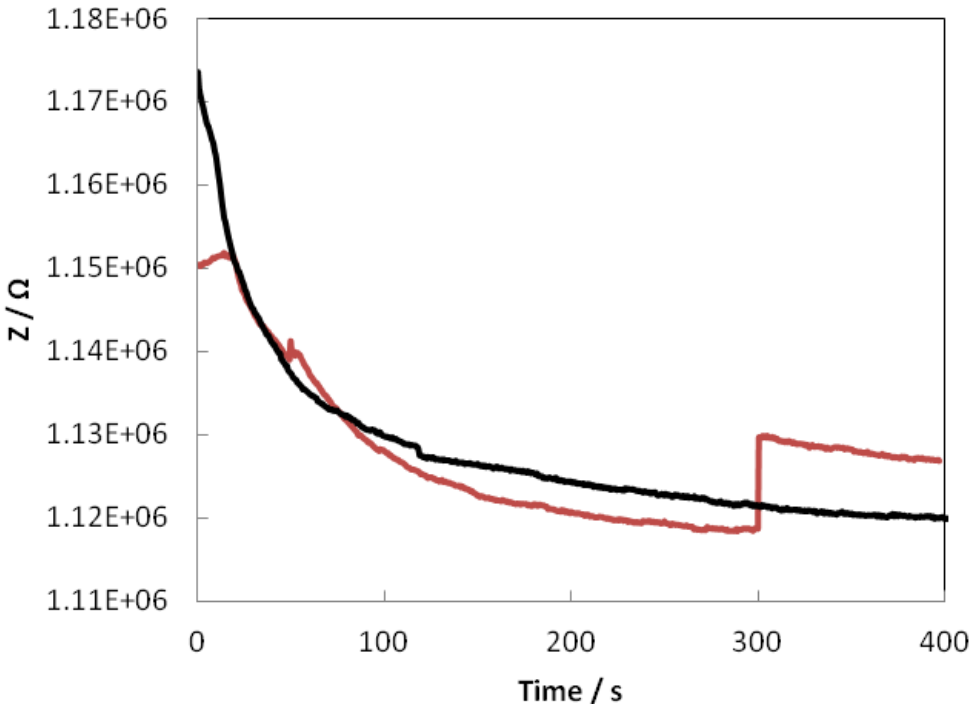

Figure 8.1: Evolution of the impedance of the coagulating blood and blank cell culture media

It is clear that there is a sharp increase in impedance at 300 s with the blood sample, 323 s if adding the preparation step (Time after mixing and before injection). This result is consistent with the blood coagulation time (370 s) tested by a Coagulometer (Thrombotrack, Technoclone Ltd.). It can be noted that no increase in impedance is observed for the blank media.

[Data provided courtesy of Dr Yuehua Dou and Professor John Greenman]

Bibliography

1. Beven, K. and A. Binley, *The Future of Distributed Models - Model Calibration and Uncertainty Prediction.* Hydrological Processes, 1992. **6**(3): p. 279-298.
2. Kirchner, J.W., *Getting the right answers for the right reasons: Linking measurements, analyses, and models to advance the science of hydrology.* Water Resources Research, 2006. **42**(3).
3. Neal, C., et al., *Lowland river water quality: a new UK data resource for process and environmental management analysis.* Hydrological Processes, 2012. **26**(6): p. 949-960.
4. Kirchner, J.W., et al., *The fine structure of water-quality dynamics: the (high-frequency) wave of the future.* Hydrological Processes, 2004. **18**(7): p. 1353-1359.
5. Robson, A.J., et al., *Linking variations in short- and medium-term stream chemistry to rainfall inputs — some observations at Plynlimon, Mid-Wales.* Journal of Hydrology, 1993. **144**(1–4): p. 291-310.
6. Jang, A., et al., *State-of-the-art lab chip sensors for environmental water monitoring.* Measurement Science & Technology, 2011. **22**(3).
7. Halliday, S.J., et al., *An analysis of long-term trends, seasonality and short-term dynamics in water quality data from Plynlimon, Wales.* Sci Total Environ, 2012.
8. Neal, C., et al., *High-frequency water quality time series in precipitation and streamflow: from fragmentary signals to scientific challenge.* Sci Total Environ, 2012. **434**: p. 3-12.
9. Kuban, P., et al., *On-site simultaneous determination of anions and cations in drainage water using a flow injection-capillary electrophoresis system with contactless conductivity detection.* Journal of Environmental Monitoring, 2004. **6**(3): p. 169-174.
10. Marle, L. and G.M. Greenway, *Microfluidic devices for environmental monitoring.* Trac-Trends in Analytical Chemistry, 2005. **24**(9): p. 795-802.
11. Li, H.F. and J.M. Lin, *Applications of microfluidic systems in environmental analysis.* Analytical and Bioanalytical Chemistry, 2009. **393**(2): p. 555-567.
12. Jokerst, J.C., J.M. Emory, and C.S. Henry, *Advances in microfluidics for environmental analysis.* Analyst, 2012. **137**(1): p. 24-34.
13. Palmer-Felgate, E.J., et al., *Phosphorus dynamics and productivity in a sewage-impacted lowland chalk stream.* Journal of Hydrology, 2008. **351**(1-2): p. 87-97.
14. Jordan, P., et al., *High-resolution phosphorus transfers at the catchment scale: the hidden importance of non-storm transfers.* Hydrology and Earth System Sciences, 2005. **9**(6): p. 685-691.
15. Soulsby, C., et al., *Seasonal and Inter-Annual Variability in Hyporheic Water Quality Revealed by Continuous Monitoring in a Salmon Spawning Stream.* River Research and Applications, 2009. **25**(10): p. 1304-1319.
16. Wade, A.J., et al., *From existing in situ, high-resolution measurement technologies to lab-on-a-chip – the future of water quality monitoring?* Hydrology and Earth System Sciences Discussions, 2012. **9**: p. 6457-6506.

17. SBRI. *Innovative Environmental Sensors*. 2012 [cited 2012 26 June]; Available from: http://www.innovateuk.org/content/competition/sbri/innovative-environmental-sensors.ashx.
18. Manz, A., N. Graber, and H.M. Widmer, *Miniaturized Total Chemical-Analysis Systems - a Novel Concept for Chemical Sensing.* Sensors and Actuators B-Chemical, 1990. **1**(1-6): p. 244-248.
19. Dertinger, S.K.W., et al., *Generation of gradients having complex shapes using microfluidic networks.* Analytical Chemistry, 2001. **73**(6): p. 1240-1246.
20. Mao, H.B., et al., *Reusable platforms for high-throughput on-chip temperature gradient assays.* Analytical Chemistry, 2002. **74**(19): p. 5071-5075.
21. Kenis, P.J.A., R.F. Ismagilov, and G.M. Whitesides, *Microfabrication inside capillaries using multiphase laminar flow patterning.* Science, 1999. **285**(5424): p. 83-85.
22. Hessel, V., H. Lowe, and F. Schonfeld, *Micromixers - a review on passive and active mixing principles.* Chemical Engineering Science, 2005. **60**(8-9): p. 2479-2501.
23. Auroux, P.A., et al., *Micro total analysis systems. 2. Analytical standard operations and applications.* Analytical Chemistry, 2002. **74**(12): p. 2637-2652.
24. Reyes, D.R., et al., *Micro total analysis systems. 1. Introduction, theory, and technology.* Analytical Chemistry, 2002. **74**(12): p. 2623-2636.
25. Duffy, D.C., et al., *Rapid prototyping of microfluidic systems in poly(dimethylsiloxane).* Analytical Chemistry, 1998. **70**(23): p. 4974-4984.
26. Koch, M., et al., *A Novel Micromachined Pump Based On Thick-Film Piezoelectric Actuation*, in *Solid State Sensors and Actuators*1997: Chicago. p. 353-356.
27. Lillehoj, P.B., et al., *Rapid electrochemical detection on a mobile phone.* Lab-on-a-Chip, 2013. **13**(15): p. 2950-5.
28. Mai, T.D., et al., *Automated capillary electrophoresis with on-line preconcentration by solid phase extraction using a sequential injection manifold and contactless conductivity detection.* Anal Chim Acta, 2012. **727**: p. 1-7.
29. Unger, M.A., et al., *Monolithic microfabricated valves and pumps by multilayer soft lithography.* Science, 2000. **288**(5463): p. 113-6.
30. Beebe, D.J., et al., *Functional hydrogel structures for autonomous flow control inside microfluidic channels.* Nature, 2000. **404**(6778): p. 588-90.
31. Oosterbroek, R.E. and A. van den Berg, eds. *Lab-on-a-Chip*. 2003, Elsevier: Amsterdam. 394.
32. Hwang, H., et al., *Lab-on-a-disc for simultaneous determination of nutrients in water.* Anal Chem, 2013. **85**(5): p. 2954-60.
33. Pamme, N., *Continuous flow separations in microfluidic devices.* Lab-on-a-Chip, 2007. **7**(12): p. 1644-59.
34. Karlinsey, J.M., *Sample introduction techniques for microchip electrophoresis: a review.* Anal Chim Acta, 2012. **725**: p. 1-13.
35. Bessoth, F.G., A.J. deMello, and A. Manz, *Microstructure for efficient continuous flow mixing.* Analytical Communications, 1999. **36**(6): p. 213-215.
36. Schonfeld, F., V. Hessel, and C. Hofmann, *An optimised split-and-recombine micro-mixer with uniform 'chaotic' mixing.* Lab-on-a-Chip, 2004. **4**(1): p. 65-69.

37. Liu, R.H., et al., *Passive mixing in a three-dimensional serpentine microchannel.* Journal of Microelectromechanical Systems, 2000. **9**(2): p. 190-197.
38. Stroock, A.D., et al., *Chaotic mixer for microchannels.* Science, 2002. **295**(5555): p. 647-651.
39. Chang, C.C. and R.J. Yang, *Computational analysis of electrokinetically driven flow mixing in microchannels with patterned blocks.* Journal of Micromechanics and Microengineering, 2004. **14**(4): p. 550-558.
40. Liu, R.H., et al., *Bubble-induced acoustic micromixing.* Lab-on-a-Chip, 2002. **2**(3): p. 151-7.
41. Ahmed, D., et al., *A fast microfluidic mixer based on acoustically driven sidewall-trapped microbubbles.* Microfluidics and Nanofluidics, 2009. **7**(5): p. 727-731.
42. Oddy, M.H., J.G. Santiago, and J.C. Mikkelsen, *Electrokinetic instability micromixing.* Anal Chem, 2001. **73**(24): p. 5822-32.
43. El Moctar, A.O., N. Aubry, and J. Batton, *Electro-hydrodynamic micro-fluidic mixer.* Lab-on-a-Chip, 2003. **3**(4): p. 273-80.
44. Effenhauser, C.S., et al., *Integrated capillary electrophoresis on flexible silicone microdevices: analysis of DNA restriction fragments and detection of single DNA molecules on microchips.* Anal Chem, 1997. **69**(17): p. 3451-7.
45. Dittrich, P.S. and P. Schwille, *An integrated microfluidic system for reaction, high-sensitivity detection, and sorting of fluorescent cells and particles.* Analytical Chemistry, 2003. **75**(21): p. 5767-5774.
46. Zhang, C.X. and A. Manz, *Narrow sample channel injectors for capillary electrophoresis on microchips.* Anal Chem, 2001. **73**(11): p. 2656-62.
47. Desai, S.P., D.M. Freeman, and J. Voldman, *Plastic masters-rigid templates for soft lithography.* Lab-on-a-Chip, 2009. **9**(11): p. 1631-1637.
48. Bartolo, D., et al., *Microfluidic stickers.* Lab-on-a-Chip, 2008. **8**(2): p. 274-9.
49. Carlborg, C.F., et al., *Beyond PDMS: off-stoichiometry thiol-ene (OSTE) based soft lithography for rapid prototyping of microfluidic devices.* Lab-on-a-Chip, 2011. **11**(18): p. 3136-47.
50. Saharil, F., et al., *Dry Transfer Bonding of Porous Silicon Membranes to Oste(+) Polymer Microfluidic Devices.* 2012 Ieee 25th International Conference on Micro Electro Mechanical Systems (Mems), 2012.
51. Becker, H. and C. Gartner, *Polymer microfabrication methods for microfluidic analytical applications.* Electrophoresis, 2000. **21**(1): p. 12-26.
52. Chien, R.D., *Hot embossing of microfluidic platform.* International Communications in Heat and Mass Transfer, 2006. **33**(5): p. 645-653.
53. Chou, S.Y., P.R. Krauss, and P.J. Renstrom, *Imprint lithography with 25-nanometer resolution.* Science, 1996. **272**(5258): p. 85-87.
54. Attia, U.M., S. Marson, and J.R. Alcock, *Micro-injection molding of polymer microfluidic devices.* Microfluidics and Nanofluidics, 2009. **7**(1): p. 1-28.
55. McCormick, R.M., et al., *Microchannel electrophoretic separations of DNA in injection-molded plastic substrates.* Analytical Chemistry, 1997. **69**(14): p. 2626-2630.
56. Griebel, A., et al., *Integrated polymer chip for two-dimensional capillary gel electrophoresis.* Lab-on-a-Chip, 2004. **4**(1): p. 18-23.
57. Ogilvie, I.R.G., et al., *Reduction of surface roughness for optical quality microfluidic devices in PMMA and COC.* Journal of Micromechanics and Microengineering, 2010. **20**(6).

58. Becker, H. and L.E. Locascio, *Polymer microfluidic devices.* Talanta, 2002. **56**(2): p. 267-87.
59. Klank, H., J.P. Kutter, and O. Geschke, *CO2-laser micromachining and back-end processing for rapid production of PMMA-based microfluidic systems.* Lab-on-a-Chip, 2002. **2**(4): p. 242-246.
60. Coltro, W.K.T., J.A.F. da Silva, and E. Carrilho, *Rapid prototyping of polymeric electrophoresis microchips with integrated copper electrodes for contactless conductivity detection.* Analytical Methods, 2011. **3**(1): p. 168-172.
61. Guijt, R.M., et al., *Microfluidic chips for capillary electrophoresis with integrated electrodes for capacitively coupled conductivity detection based on printed circuit board technology.* Sensors and Actuators B-Chemical, 2011. **159**(1): p. 307-313.
62. Han, J., et al. *UV adhesive bonding techniques at room temperature for plastic lab-on-a-chip*. in *7th International Conference of Miniaturized Chemical and Biochemical Analysis Systems, October 5-9, 2003, Squaw Valley, California, USA*. 2003.
63. Roy, S., et al., *Thermal bonding of microfluidic devices: Factors that affect interfacial strength of similar and dissimilar cyclic olefin copolymers.* Sensors and Actuators B-Chemical, 2012. **161**(1): p. 1067-1073.
64. Tsao, C.W., et al., *Low temperature bonding of PMMA and COC microfluidic substrates using UV/ozone surface treatment.* Lab-on-a-Chip, 2007. **7**(4): p. 499-505.
65. Cortese, B., M.C. Mowlem, and H. Morgan, *Characterisation of an irreversible bonding process for COC-COC and COC-PDMS-COC sandwich structures and application to microvalves.* Sensors and Actuators B-Chemical, 2011. **160**(1): p. 1473-1480.
66. Zhang, Z., et al., *Thermal assisted ultrasonic bonding method for poly(methyl methacrylate) (PMMA) microfluidic devices.* Talanta, 2010. **81**(4-5): p. 1331-8.
67. Zhang, Z., et al., *Thermal assisted ultrasonic bonding of multilayer polymer microfluidic devices.* Journal of Micromechanics and Microengineering, 2010. **20**(1).
68. Mahabadi, K.A., et al., *Restrictive dual capacitively coupled contactless conductivity detection for microchip electrophoresis.* Proceedings of the Eurosensors Xxiii Conference, 2009. **1**(1): p. 1351-1354.
69. Mahabadi, K.A., et al., *Capacitively coupled contactless conductivity detection with dual top-bottom cell configuration for microchip electrophoresis.* Electrophoresis, 2010. **31**(6): p. 1063-1070.
70. Pumera, M., et al., *Contactless conductivity detector for microchip capillary electrophoresis.* Analytical Chemistry, 2002. **74**(9): p. 1968-1971.
71. Wang, J., et al., *Measurements of chemical warfare agent degradation products using an electrophoresis microchip with contactless conductivity.* Analytical Chemistry, 2002. **74**(23): p. 6121-6125.
72. Tanyanyiwa, J., et al., *High-voltage contactless conductivity-detection for lab-on-chip devices using external electrodes on the holder.* Analyst, 2003. **128**(8): p. 1019-1022.
73. Kuban, P. and P.C. Hauser, *Effects of the cell geometry and operating parameters on the performance of an external contactless conductivity detector for microchip electrophoresis.* Lab-on-a-Chip, 2005. **5**(4): p. 407-415.

74. Chen, Z.G., et al., *A thin cover glass chip for contactless conductivity detection in microchip capillary electrophoresis.* Talanta, 2007. **71**(5): p. 1944-1950.
75. Tanyanyiwa, J. and P.C. Hauser, *High-voltage capacitively coupled contactless conductivity detection for microchip capillary electrophoresis.* Analytical Chemistry, 2002. **74**(24): p. 6378-6382.
76. Zhao, J., et al., *A novel microchip based on indium tin oxide coated glass for contactless conductivity detection.* Talanta, 2011. **85**(5): p. 2614-9.
77. Liu, B., et al., *Determination of heavy metal ions by microchip capillary electrophoresis coupled with contactless conductivity detection.* Electrophoresis, 2012. **33**(8): p. 1247–1250.
78. Becker, H., et al., *Portable CE-system with contactless conductivity detection in an injection molded polymer chip for on-site food analysis.* Microfluidics, Biomems, and Medical Microsystems Vi, 2008. **6886**: p. C8860-C8860.
79. Fercher, G., et al., *End-to-End Differential Contact less Conductivity Sensor for Microchip Capillary Electrophoresis.* Analytical Chemistry, 2010. **82**(8): p. 3270-3275.
80. Fercher, G., W. Smetana, and M.J. Vellekoop, *Microchip electrophoresis in low-temperature co-fired ceramics technology with contactless conductivity measurement.* Electrophoresis, 2009. **30**(14): p. 2516-2522.
81. Wong, I. and C.M. Ho, *Surface molecular property modifications for poly(dimethylsiloxane) (PDMS) based microfluidic devices.* Microfluid Nanofluidics, 2009. **7**(3): p. 291-306.
82. Nikcevic, I., et al., *Characterization and performance of injection molded poly(methylmethacrylate) microchips for capillary electrophoresis.* J Chromatogr A, 2007. **1154**(1-2): p. 444-53.
83. Hupert, M., et al., *Evaluation of micromilled metal mold masters for the replication of microchip electrophoresis devices.* Microfluidics and Nanofluidics, 2007. **3**(1): p. 1-11.
84. Tsao, C.W. and D.L. DeVoe, *Bonding of thermoplastic polymer microfluidics.* Microfluidics and Nanofluidics, 2009. **6**(1): p. 1-16.
85. Liu, J., et al., *A polydimethylsiloxane electrophoresis microchip with a thickness controllable insulating layer for capacitatively coupled contactless conductivity detection.* Electrochemistry Communications, 2012. **25**(0): p. 147-150.
86. Beaton, A.D., et al., *An automated microfluidic colourimetric sensor applied in situ to determine nitrite concentration.* Sensors and Actuators B: Chemical, 2011. **156**(2): p. 1009-1014.
87. Sieben, V.J., et al., *Microfluidic colourimetric chemical analysis system: Application to nitrite detection.* Analytical Methods, 2010. **2**(5): p. 484-491.
88. Floquet, C.F., et al., *Nanomolar detection with high sensitivity microfluidic absorption cells manufactured in tinted PMMA for chemical analysis.* Talanta, 2011. **84**(1): p. 235-9.
89. Beaton, A.D., et al., *Lab-on-chip measurement of nitrate and nitrite for in situ analysis of natural waters.* Environ Sci Technol, 2012. **46**(17): p. 9548-56.
90. Nakanishi, K., *Pore Structure Control of Silica Gels Based on Phase Separation.* Journal of Porous Materials, 1997. **4**(2): p. 67-112.
91. Zakaria, P., et al., *Latex-coated polymeric monolithic ion-exchange stationary phases. 2. Micro-ion chromatography.* Anal Chem, 2005. **77**(2): p. 417-23.

92. Pelletier, S. and C.A. Lucy, *Achieving rapid low-pressure ion chromatography separations on short silica-based monolithic columns.* Journal of Chromatography A, 2006. **1118**(1): p. 12-18.
93. Riordain, C.O., et al., *Double gradient ion chromatography using short monolithic columns modified with a long chained zwitterionic carboxybetaine surfactant.* J Chromatogr A, 2006. **1109**(1): p. 111-9.
94. Sugrue, E., P.N. Nesterenko, and B. Paull, *Fast ion chromatography of inorganic anions and cations on a lysine bonded porous silica monolith.* J Chromatogr A, 2005. **1075**(1-2): p. 167-75.
95. Siouffi, A.M., *Silica gel-based monoliths prepared by the sol-gel method: facts and figures.* J Chromatogr A, 2003. **1000**(1-2): p. 801-18.
96. Stulik, K., et al., *Monolithic organic polymeric columns for capillary liquid chromatography and electrochromatography.* J Chromatogr B Analyt Technol Biomed Life Sci, 2006. **841**(1-2): p. 79-87.
97. Mangelings, D., et al., *Evaluation of polymeric methacrylate-based monoliths in capillary electrochromatography for their potential to separate pharmaceutical compounds.* J Chromatogr Sci, 2007. **45**(9): p. 578-86.
98. Xu, Q., et al., *Dodecylsulfate-coated monolithic octadecyl-bonded silica stationary phase for high-speed separation of hydrogen, magnesium and calcium in rainwater.* J Chromatogr A, 2004. **1026**(1-2): p. 191-4.
99. Tanaka, N. and K.K. Unger, *The Basic Idea and the Drivers*, in *Monolithic Silicas in Separation Science*2011, Wiley-VCH Verlag GmbH & Co. KGaA. p. 1-7.
100. Wu, R., et al., *Recent development of monolithic stationary phases with emphasis on microscale chromatographic separation.* J Chromatogr A, 2008. **1184**(1-2): p. 369-92.
101. Fletcher, P.D.I., et al., *Permeability of silica monoliths containing micro- and nano-pores.* Journal of Porous Materials, 2011. **18**(4): p. 501-508.
102. Svec, F. and J.J. Frechet, *Temperature, a Simple and Efficient Tool for the Control of Pore Size Distribution in Macroporous Polymers.* Macromolecules, 1995. **28**(22): p. 7580-7582.
103. Stachowiak, T.B., et al., *Fabrication of porous polymer monoliths covalently attached to the walls of channels in plastic microdevices.* Electrophoresis, 2003. **24**(21): p. 3689-93.
104. Ladner, Y., et al., *New "one-step" method for the simultaneous synthesis and anchoring of organic monolith inside COC microchip channels.* Lab-on-a-Chip, 2012. **12**(9): p. 1680-1685.
105. Faure, K., et al., *Electrochromatography in poly(dimethyl)siloxane microchips using organic monolithic stationary phases.* Electrophoresis, 2007. **28**(11): p. 1668-1673.
106. Schaller, D., E.F. Hilder, and P.R. Haddad, *Monolithic stationary phases for fast ion chromatography and capillary electrochromatography of inorganic ions.* J Sep Sci, 2006. **29**(12): p. 1705-19.
107. Mair, D.A., et al., *Injection molded microfluidic chips featuring integrated interconnects.* Lab-on-a-Chip, 2006. **6**(10): p. 1346-54.
108. Evenhuis, C.J., et al., *Determination of inorganic ions using microfluidic devices.* Electrophoresis, 2004. **25**(21-22): p. 3602-24.
109. Bartle, K.D. and P. Myers, eds. *Capillary Electrochromatography*. ed. R.S. Smith2001, Royal Society of Chemistry: Cambridge. 157.

110. Kuhn, R. and S. Hoffstetter-Kuhn, *Capillary Electrophoresis: Principles and Practive*, 1993, Berlin: Springer-Verlag. 375.
111. Landers, J.P., ed. *Handbook of Capillary and Microchip Electrophoresis and Associated Microtechniques*. 2008, Taylor & Francis Group: Boca Raton.
112. Swinney, K. and D.J. Bornhop, *Detection in capillary electrophoresis.* Electrophoresis, 2000. **21**(7): p. 1239-1250.
113. Francisco, K.J.M. and C.L. do Lago, *A compact and high-resolution version of a capacitively coupled contactless conductivity detector.* Electrophoresis, 2009. **30**(19): p. 3458-3464.
114. Hutchinson, J.P., et al., *Identification of inorganic ions in post-blast explosive residues using portable CE instrumentation and capacitively coupled contactless conductivity detection.* Electrophoresis, 2008. **29**(22): p. 4593-4602.
115. Kuban, P., et al., *New fully portable instrument for the versatile determination of cations and anions by capillary electrophoresis with contactless conductivity detection.* Electroanalysis, 2007. **19**(19-20): p. 2059-2065.
116. Kuban, P., M.A. Muri, and P.C. Hauser, *Application of a contactless conductivity detector to the determination of inorganic ions in ion chromatography.* Analyst, 2004. **129**(1): p. 82-86.
117. Kuban, P. and P.C. Hauser, *A review of the recent achievements in capacitively coupled contactless conductivity detection.* Analytica Chimica Acta, 2008. **607**(1): p. 15-29.
118. Kuban, P. and P.C. Hauser, *Ten years of axial capacitively coupled contactless conductivity detection for CZE - a review.* Electrophoresis, 2009. **30**(1): p. 176-188.
119. Pumera, M., *Contactless conductivity detection for microfluidics: Designs and applications.* Talanta, 2007. **74**(3): p. 358-364.
120. Zemann, A.J., *Capacitively coupled contactless conductivity detection in capillary electrophoresis.* Electrophoresis, 2003. **24**(12-13): p. 2125-2137.
121. Johns, C., et al., *Recent significant developments in detection and method development for the determination of inorganic ions by CE.* Electrophoresis, 2009. **30**: p. S53-S67.
122. Kuban, P. and P.C. Hauser, *Contactless conductivity detection in capillary electrophoresis: A review.* Electroanalysis, 2004. **16**(24): p. 2009-2021.
123. Gas, B., M. Demjanenko, and J. Vacik, *High-Frequency Contactless Conductivity Detection in Isotachophoresis.* Journal of Chromatography, 1980. **192**(2): p. 253-257.
124. da Silva, J.A.F. and C.L. do Lago, *An oscillometric detector for capillary electrophoresis.* Analytical Chemistry, 1998. **70**(20): p. 4339-4343.
125. Zemann, A.J., et al., *Contactless conductivity detection for capillary electrophoresis.* Analytical Chemistry, 1998. **70**(3): p. 563-567.
126. Johnston, S.E., et al., *Expanded electrical model of a contactless conductivity detector: Development and verification.* Journal of Chromatography A, 2005. **1094**(1-2): p. 148-157.
127. Gas, B., et al., *Optimization of the high-frequency contactless conductivity detector for capillary electrophoresis.* Electrophoresis, 2002. **23**(20): p. 3520-3527.
128. Liu, J., et al., *Modeling of capacitively coupled contactless conductivity detection on microfluidic chips.* Microsystem Technologies, 2013. **19**(12): p. 1991-1996.

129. Zhang, H.F., et al., *Effect of the Detector Parameters on the Sensitivity of Contactless Conductivity Detector for Micrchip electrophoresis.* 7th International Conference on System Simulation and Scientific Computing Asia Simulation Conference 2008, Vols 1-3, 2008: p. 355-358.
130. Huang, Z.Y., et al., *A new method of capacitively coupled contactless conductivity detection based on series resonance.* Sensors and Actuators B-Chemical, 2009. **143**(1): p. 239-245.
131. Brito-Neto, J.G.A., et al., *Understanding capacitively coupled contactless conductivity detection in capillary and microchip electrophoresis. Part 2. Peak shape, stray capacitance, noise, and actual electronics.* Electroanalysis, 2005. **17**(13): p. 1207-1214.
132. Opekar, F., P. Tuma, and K. Stulik, *Contactless impedance sensors and their application to flow measurements.* Sensors (Basel), 2013. **13**(3): p. 2786-801.
133. Kang, Q., et al., *Reduction of the impedance of a contactless conductivity detector for microchip capillary electrophoresis: Compensation of the electrode impedance by addition of a series inductance from a piezoelectric quartz crystal.* Analytical Chemistry, 2008. **80**(20): p. 7826-7832.
134. Shih, C.Y., et al., *A resonance-induced sensitivity enhancement method for conductivity sensors.* 2006 Ieee Sensors, Vols 1-3, 2006: p. 271-274.
135. Shen, D.Z., et al., *Application of a low impedance contactless conductometric detector for the determination of inorganic cations in capillary monolithic column chromatography.* Talanta, 2011. **84**(1): p. 42-48.
136. Huang, Z.Y., et al., *Design of capacitively coupled contactless conductivity detection sensor.* Flow Measurement and Instrumentation, 2012. **27**: p. 67-70.
137. Gillespie, E., et al., *Development of a contactless conductivity detector cell for 1.6 mm OD (1/16th inch) HPLC tubing and micro-bore columns with on-column detection.* Analyst, 2008. **133**(8): p. 1104-1110.
138. Wang, L., et al., *Flow Pattern Identification of Gas-Liquid Two-Phase Flow Based on Capacitively Coupled Contactless Conductivity Detection.* Ieee Transactions on Instrumentation and Measurement, 2012. **61**(5): p. 1466-1475.
139. Tuma, P., F. Opekar, and I. Jelinek, *A contactless conductometric detector with easily exchangeable capillary for capillary electrophoresis.* Electroanalysis, 2001. **13**(12): p. 989-992.
140. Tuma, P., F. Opekar, and K. Stulik, *A contactless conductivity detector for capillary electrophoresis: Effects of the detection cell geometry on the detector performance.* Electrophoresis, 2002. **23**(21): p. 3718-3724.
141. Guijt, R.M., et al., *New approaches for fabrication of microfluidic capillary electrophoresis devices with on-chip conductivity detection.* Electrophoresis, 2001. **22**(2): p. 235-241.
142. Lichtenberg, J., N.F. de Rooij, and E. Verpoorte, *A microchip electrophoresis system with integrated in-plane electrodes for contactless conductivity detection.* Electrophoresis, 2002. **23**(21): p. 3769-3780.
143. Macka, M., et al., *Miniaturized movable contactless conductivity detection cell for capillary electrophoresis.* Electrophoresis, 2003. **24**(12-13): p. 2144-2149.
144. Mayrhofer, K., et al., *Capillary electrophoresis and contactless conductivity detection of ions in narrow inner diameter capillaries.* Analytical Chemistry, 1999. **71**(17): p. 3828-3833.
145. da Silva, J.A.F., N. Guzman, and C.L. do Lago, *Contactless conductivity detection for capillary electrophoresis - Hardware improvements and*

optimization of the input-signal amplitude and frequency. Journal of Chromatography A, 2002. **942**(1-2): p. 249-258.
146. Vuorinen, P.S., et al., *Integration of a contactless conductivity detector into a commercial capillary cassette - Detection of inorganic cations and catecholamines.* Journal of Chromatography A, 2003. **990**(1-2): p. 45-52.
147. Novotny, M., F.E. Opekar, and K. Stulik, *The effects of the electrode system geometry on the properties of contactless conductivity detectors for capillary electrophoresis.* Electroanalysis, 2005. **17**(13): p. 1181-1186.
148. Novotny, M., et al., *Improved dual photometric-contactless conductometric detector for capillary electrophoresis.* Analytica Chimica Acta, 2004. **525**(1): p. 17-21.
149. Kuban, P. and P.C. Hauser, *Fundamental aspects of contactless conductivity detection for capillary electrophoresis. Part I: Frequency behavior and cell geometry.* Electrophoresis, 2004. **25**(20): p. 3387-3397.
150. Kuban, P. and P.C. Hauser, *Fundamental aspects of contactless conductivity detection for capillary electrophoresis. Part II: Signal-to-noise ratio and stray capacitance.* Electrophoresis, 2004. **25**(20): p. 3398-3405.
151. Brito-Neto, J.G.A., et al., *Understanding capacitively coupled contactless conductivity detection in capillary and microchip electrophoresis. Part 1. Fundamentals.* Electroanalysis, 2005. **17**(13): p. 1198-1206.
152. Chen, C.G., et al., *AC impedance characteristics of capacitively coupled contactless conductivity detector cell in capillary electrophoresis.* Electrochimica Acta, 2009. **54**(27): p. 6959-6962.
153. Tanyanyiwa, J., et al., *Improved capacitively coupled conductivity detector for capillary electrophoresis.* Analyst, 2002. **127**(2): p. 214-218.
154. Chvojka, T., et al., *Dual photometric-contactless conductometric detector for capillary electrophoresis.* Analytica Chimica Acta, 2001. **433**(1): p. 13-21.
155. Hilder, E.F., et al., *Anion-exchange capillary electrochromatography with indirect UV and direct contactless conductivity detection.* Electrophoresis, 2001. **22**(7): p. 1273-1281.
156. *TraceDec® Contactless Conductivity Detector*. Available from: http://www.istech.at/product.htm.
157. Kuban, P., et al., *Application of a contactless conductometric detector for the simultaneous determination of small anions and cations by capillary electrophoresis with dual-opposite end injection.* Journal of Chromatography A, 2002. **964**(1-2): p. 227-241.
158. Unterholzner, V., et al., *Simultaneous separation of inorganic anions and cations using capillary electrophoresis with a movable contactless conductivity detector.* Analyst, 2002. **127**(6): p. 715-718.
159. Segato, T.P., et al., *Microfab-less Microfluidic Capillary Electrophoresis Devices.* Anal Methods, 2013. **5**(7): p. 1652-1657.
160. Kuban, P., et al., *Comparison of different contactless conductivity detectors for the determination of small inorganic ions by capillary electrophoresis.* Electroanalysis, 2006. **18**(13-14): p. 1289-1296.
161. Muhlberger, H., et al., *Polymer Lab-on-a-Chip system with electrical detection.* Ieee Sensors Journal, 2008. **8**(5-6): p. 572-579.
162. Wang, J., G. Chen, and A. Muck, *Movable contact less-conductivity detector for microchip capillary electrophoresis.* Analytical Chemistry, 2003. **75**(17): p. 4475-4479.

163. Walsh, Z., et al., *The use of scanning contactless conductivity detection for the characterisation of stationary phases in micro-fluidic chips.* Lab-on-a-Chip, 2010. **10**(14): p. 1777-1780.
164. Zhang, H.F., et al., *Design of Movable Contactless Conductivity Detector for Microchip Capillary Electrophoresis.* 2009 4th Ieee International Conference on Nano/Micro Engineered and Molecular Systems, Vols 1 and 2, 2009: p. 190-193.
165. Paull, B., et al., *Non-invasive characterization of stationary phases in capillary flow systems using scanning capacitively coupled contactless conductivity detection (sC(4)D).* Trac-Trends in Analytical Chemistry, 2010. **29**(8): p. 870-884.
166. Gillespie, E., et al., *Accurate non-invasive determination of pK(a) of surface functionalised ion exchange monoliths using capacitively coupled contactless conductivity detection.* Analyst, 2008. **133**(7): p. 874-876.
167. Shang, T., et al., *Contactless conductivity detection of small ions in a surface micro-machined CE chip.* Electrophoresis, 2010. **31**(15): p. 2596-2601.
168. Xu, Y., et al., *Characterization of a capacitance-coupled contactless conductivity detection system with sidewall electrodes on a low-voltage-driven electrophoresis microchip.* Analytical and Bioanalytical Chemistry, 2010. **397**(4): p. 1583-1593.
169. Thredgold, L.D., et al., *On-chip capacitively coupled contactless conductivity detection using "injected" metal electrodes.* Analyst, 2013. **138**(15): p. 4275-9.
170. Gaudry, A.J., M.C. Breadmore, and R.M. Guijt, *In-plane alloy electrodes for capacitively coupled contactless conductivity detection in poly(methylmethacrylate) electrophoretic chips.* Electrophoresis, 2013.
171. Guijt, R.M., et al., *Capillary electrophoresis with on-chip four-electrode capacitively coupled conductivity detection for application in bioanalysis.* Electrophoresis, 2001. **22**(12): p. 2537-2541.
172. Laugere, F., et al., *On-chip contactless four-electrode conductivity detection for capillary electrophoresis devices.* Analytical Chemistry, 2003. **75**(2): p. 306-312.
173. Laugere, F., et al., *Design of an electronic interface for capacitively coupled four-electrode conductivity detection in capillary electrophoresis microchip.* Sensors and Actuators B-Chemical, 2002. **83**(1-3): p. 104-108.
174. Liao, H.H., et al., *Modeling and simulation of in-plane four-electrode contactless conductivity detector of electrophoresis microchip in VHDL-AMS.* Icic 2009: Second International Conference on Information and Computing Science, Vol 4, Proceedings, 2009: p. 42-45.
175. Liu, J.S., et al., *A three-layer PMMA electrophoresis microchip with Pt microelectrodes insulated by a thin film for contactless conductivity detection.* Lab-on-a-Chip, 2011. **11**(5): p. 969-973.
176. Jin, Q.H., et al., *A simple poly(dimethylsiloxane) electrophoresis microchip with an integrated contactless conductivity detector.* Microchimica Acta, 2011. **172**(1): p. 193-198.
177. Jin, Q.H., et al., *A simplified poly(dimethylsiloxane) capillary electrophoresis microchip integrated with a low-noise contactless conductivity detector.* Electrophoresis, 2011. **32**(6-7): p. 699-704.
178. Lima, R.S., et al., *Doping of a dielectric layer as a new alternative for increasing sensitivity of the contactless conductivity detection in microchips.* Lab-on-a-Chip, 2011. **11**(24): p. 4148-4151.

179. Opekar, F., K. Stulik, and K. Fenclova, *A simple Contactless Conductivity Detector Employing a Medium Wave Radio Integrated Circuit for the Signal Treatment.* Electroanalysis, 2009. **22**(2): p. 161-167.
180. Jung, W., *Op Amp Applications Handbook*, 2005: Newnes.
181. Liao, H.H., et al., *A control and acquisition system design of low-voltage electrophoresis microchip based on SOPC and DDS.* Proceedings of the International Conference on Embedded Software and Systems, 2008: p. 251-257.
182. Baltussen, E., et al., *Considerations on contactless conductivity detection in capillary electrophoresis.* Electrophoresis, 2002. **23**(17): p. 2888-2893.
183. Liao, H.H., et al., *Study of orthogonal vector lock-in amplifier in contactless conductivity detector of electrophoresis microchip*, in *International Conference on Computer Application and System Modeling*2010. p. 203-207.
184. Small, H., T.S. Steven, and W.C. Bauman, *Novel ion exchange chromatographic method using conductimetric detection.* Analytical Chemistry, 1975. **47**(11): p. 1801-1809.
185. Timmer, B., et al., *Optimization of an electrolyte conductivity detector for measuring low ion concentrations.* Lab-on-a-Chip, 2002. **2**(2): p. 121-124.
186. Gong, X.Y., et al., *Separation of enantiomers in capillary electrophoresis with contactless conductivity detection.* Journal of Chromatography A, 2005. **1082**(2): p. 230-234.
187. *EH Systems, Capillary Electrophoresis, CEP-5100*. Available from: http://www.ehsystems.com/en_US/products/cep/CEP-5100/.
188. Mai, T.D., et al., *Portable capillary electrophoresis instrument with automated injector and contactless conductivity detection.* Anal Chem, 2013. **85**(4): p. 2333-9.
189. da Costa, E.T., et al., *Unmanned platform for long-range remote analysis of volatile compounds in air samples.* Electrophoresis, 2012. **33**(17): p. 2650-9.
190. Rong, L., et al., *Simultaneous determination of inorganic cations by capillary ion chromatography with a non-suppressed contactless conductivity detector.* Anal Sci, 2012. **28**(4): p. 367-71.
191. Thi, K.O.D., et al., *Analysis of inorganic cations in biological samples by the combination of micro-electrodialysis and capillary electrophoresis with capacitively coupled contactless conductivity detection.* Electrophoresis, 2011. **32**(3-4): p. 464-471.
192. Elbashir, A.A. and H.Y. Aboul-Enein, *Applications of capillary electrophoresis with capacitively coupled contactless conductivity detection (CE-C4D) in pharmaceutical and biological analysis.* Biomed Chromatogr, 2010. **24**(10): p. 1038-44.
193. Nogueira, T. and C.L. do Lago, *Determination of Ca, K, Mg, Na, sulfate, phosphate, formate, acetate, propionate, and glycerol in biodiesel by capillary electrophoresis with capacitively coupled contactless conductivity detection.* Microchemical Journal, 2011. **99**(2): p. 267-272.
194. Kuban, P., et al., *Analysis of inorganic cations in biological samples by the combination of micro-electrodialysis and capillary electrophoresis with capacitively coupled contactless conductivity detection.* Electrophoresis, 2011. **32**(3-4): p. 464-471.
195. Kuban, P. and P.C. Hauser, *Capacitively coupled contactless conductivity detection for microseparation techniques - recent developments.* Electrophoresis, 2011. **32**(1): p. 30-42.

196. Kuban, P. and P.C. Hauser, *Contactless conductivity detection for analytical techniques: developments from 2010 to 2012.* Electrophoresis, 2013. **34**(1): p. 55-69.
197. Lima, R.S., et al., *Contactless conductivity biosensor in microchip containing folic acid as bioreceptor.* Lab-on-a-Chip, 2012. **12**(11): p. 1963-6.
198. Loock, H.-P. and P.D. Wentzell, *Detection limits of chemical sensors: Applications and misapplications.* Sensors and Actuators B: Chemical, 2012. **173**(0): p. 157-163.
199. Carrilho, E., W.K.T. Coltro, and J.A.F. da Silva, *Fabrication and integration of planar electrodes for contactless conductivity detection on polyester-toner electrophoresis microchips.* Electrophoresis, 2008. **29**(11): p. 2260-2265.
200. *ET120 C4D Headstage for Capillary Electrophoresis*. Available from: http://www.edaq.com/ET120.
201. Devices, A. *A Technical Tutorial on Digital Signal Synthesis*. 1999.
202. Buchanan, D. *AN-237: Chossing DACs for Direct Digital Synthesis*. 1992.
203. Devices, A. *MT-085: Fundamentals of Direct Digital Synthesis (DDS)*. 2008.
204. Microtechnology, A., *PA94 Datasheet - High Voltage Power Operational Amplifiers*.
205. Joly, E., et al. *Design and Test Issues for Lab-on-Chip Ion Separation for In-Situ Water Quality Monitoring*. in *Mixed-Signals, Sensors and Systems Test Workshop (IMS3TW), 2012 18th International*. 2012.
206. Ramanathan, N., et al., *The Final Frontier: Embedding Networked Sensors in the Soil*, 2006.
207. Devices, A., *AD9834 Datasheet*.
208. Lei, K.F., et al., *Real-Time Electrical Impedimetric Monitoring of Blood Coagulation Process under Temperature and Hematocrit Variations Conducted in a Microfluidic Chip.* PLoS One, 2013. **8**(10): p. e76243.
209. Yang, X., X. Yao, and L. Zhang, *The dielectrical properties of (B,Si) doped (Ba,Sr)TiO3 thin films fabricated by sol–gel technique.* Ceramics International, 2004. **30**(7): p. 1763-1765.
210. Fang, X., O.K. Tan, and M.S. Tse, *Metal Oxide Barium Strontium Titanate Thin Films for Electrical Immunosensing Applications.* Sci. Adv. Mater., 2011. **3**(5): p. 763-786.

Appendix

Monitoring Site Description

A – River Enborne at Brimpton

Catchment description

The River Enborne flows in an easterly direction from its source near the village of West Woodhay, past the town of Newbury, and enters the River Kennet downstream of the village of Woolhampton. The catchment land use is predominantly agricultural (grassland and arable) and broad-leaved woodland. Urban and semi-urban land use make up 6.5 % of the catchment area. The river receives wastewater effluent from several small sewage treatment works at Washwater, Bishop's Green and Kingsclere. There are chalk outcrops in the headwaters, but the rest of the catchment is mainly covered in impervious Tertiary clays. The mean flow at the study site at Brimpton is *ca.* 1.3 m^3 s^{-1}.

Monitoring equipment

Water quality monitoring equipment has been installed near the village of Brimpton, adjacent to the Environment Agency's flow gauging weir. Total reactive phosphorus and nitrite concentrations are being monitored at hourly sampling interval, using a Micromac C nutrient auto-analyser (Systea Analytical Technologies, Anagni, Italy). The instrument transmits data via a Meteorburst telemetry system.

Water quality data

Average water quality data for the River Enbourne at Brimpton (November 2009 to November 2010)

pH		7.7
Suspended Solids	mg/L	9.4
Soluble reactive P	µg/L-P	150
Total dissolved P	µg/L-P	178
Total P	µg/L-P	225
Ammonia	mg/L-NH_4	0.072
Dissolved Silicon	mg/L-Si	7.01
Nitrite	mg/L-NO_2	0.055
Nitrate	mg/L-NO_3	17.8

[Information provided by CEH]

B – River The Cut at Bray

Catchment description

The Cut rises in North Ascot, Berkshire, on the outskirts of the town of Bracknell, and flows north to join the River Thames near Maidenhead. The catchment land cover consists of arable (24%), grassland (28%), with major urban / semi-urban development (24%). The river receives significant sewage effluent inputs from the large towns of Bracknell, Ascot and Maidenhead. The catchment is underlain by impervious London Clay. The course of The Cut has been altered greatly over time, and much of the river's course is now within artificial concrete channels. The mean flow at Binfield (upper catchment, downstream of Bracknell) is 0.38 $m^3 s^{-1}$.

Monitoring equipment

Water quality monitoring equipment has been installed at Bray, near The Cut's confluence with the River Thames. Total phosphorus and total reactive phosphorus concentrations are being monitored at hourly sampling interval, using a Hach Lange Phosphax Sigma analyser.

The instrument transmits data via a Meteorburst telemetry system.


Water quality data

Average water quality data for the The Cut at Paley Street (February 2009 to November 2010)

pH		7.6
Suspended Solids	mg/L	8.5
Soluble reactive P	µg/L-P	525
Total dissolved P	µg/L-P	602
Total P	µg/L-P	689
Ammonia	mg/L-NH_4	0.29
Dissolved Silicon	mg/L-Si	5.9
Nitrite	mg/L-NO_2	0.43
Nitrate	mg/L-NO_3	91

[Information provided by CEH]

COMSOL

C - Simulation of the electrode stray capacitance for various gap with a fussed silica capillary (ID 500 µm / OD 1000 µm)

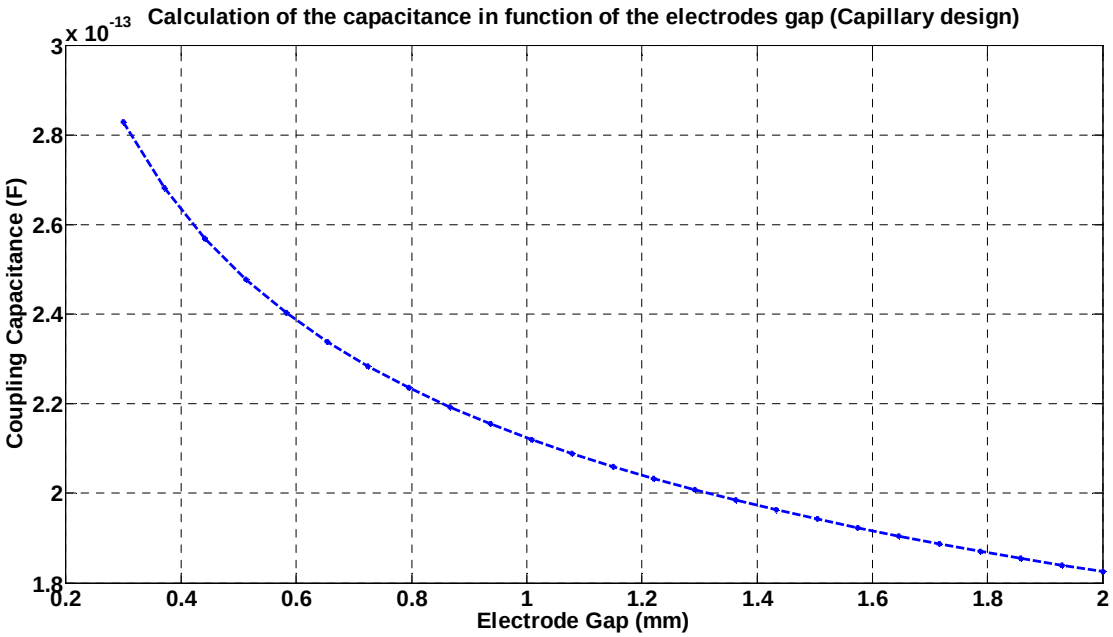

D – 3D model used

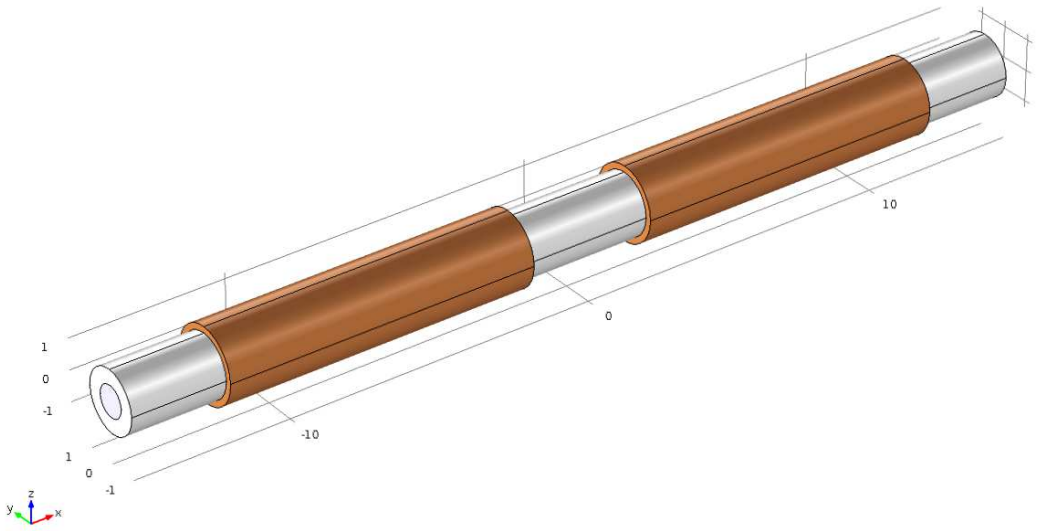

Numerical method

E – Calculation of the limit of detection (LOD)

From [198]:

We first require repeated measurements of a blank sample, *i.e.* one that does not contain analyte. The sensor response is repeatedly measured. The American Chemical Society recommends k = 10 of such measurements, but many agencies only require 7 measurements of the blank's response.

We then prepare samples that contain analyte at a concentration about 1–5 times higher than the expected LOD and again perform *k* measurements at this concentration. The mean value and the standard deviation of the measurement, s_y, can be determined. Ideally the samples should be prepared independently from each other and using different stock solutions.

$$y_{LOD} = \bar{y}_{blank} + t_{\alpha,k-1}.s_y \quad (1)$$

Here $\bar{y}_{blank}$ is the average signal of the k measurements of the blank samples and $t_{\alpha,k-1}$ is the α-quantile of Student's *t*-function with *k-1* degrees of freedom where (1-α) designates the required confidence level. For example, if it is required that the measurement at the LOD has a 99% probability of being larger than the blank, then α= 0.02, or (1-α) = 0.98, owing to the two-sided nature of the *t*-distribution. When 10 samples are analyzed (k = 10) one obtains $t_{0.02,9}$ = 2.821, whereas $t_{0.02,7}$ = 2.998 for *k* = 8.

The concentration at the detection limit can then be calculated from the sensitivity, *r*, *i.e.* the slope of the calibration curve. For convenience the value of the student t-function is frequently assumed to be t = 3, but this implies that a minimum of about 16 samples (8 blanks and 8 low-concentration samples) have been analyzed. Assuming a linear calibration curve near the LOD, we calculate the minimum detectable concentration as:

$$LOD = \frac{t.s_y}{r} \quad (2)$$

PCB CAD

F - Schematic of the amplitude control

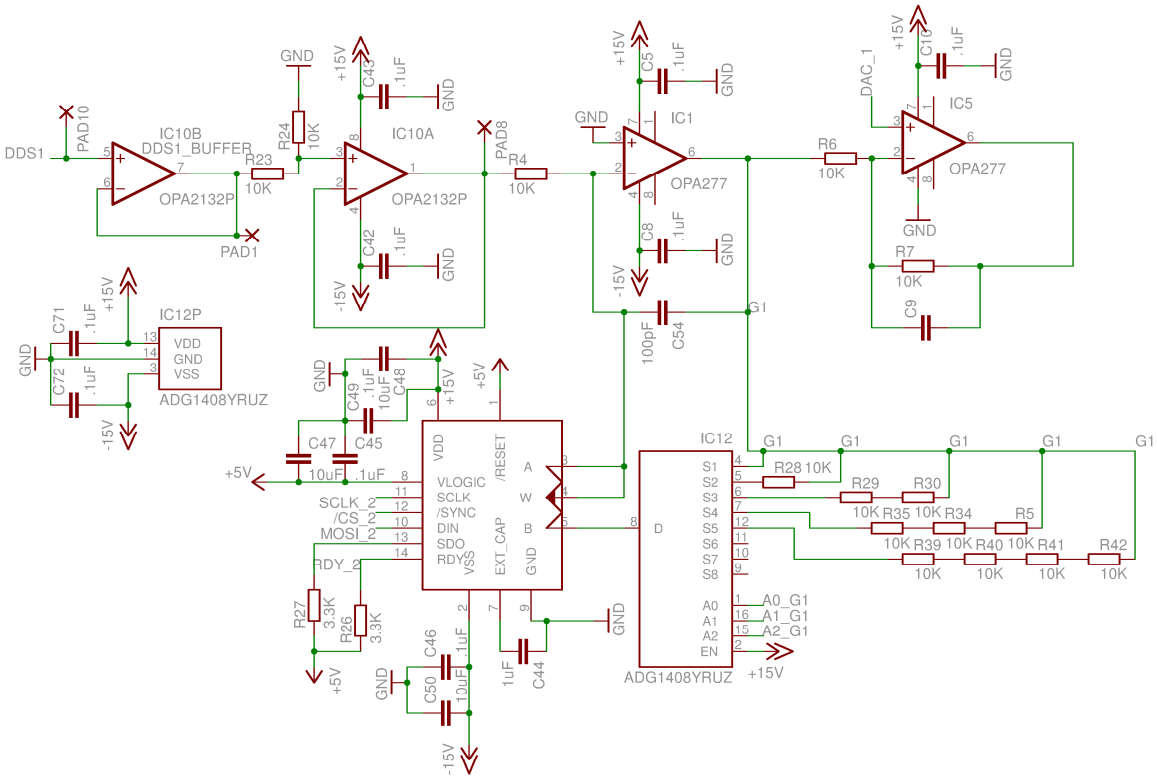

G - Schematic of the voltage to current conversion

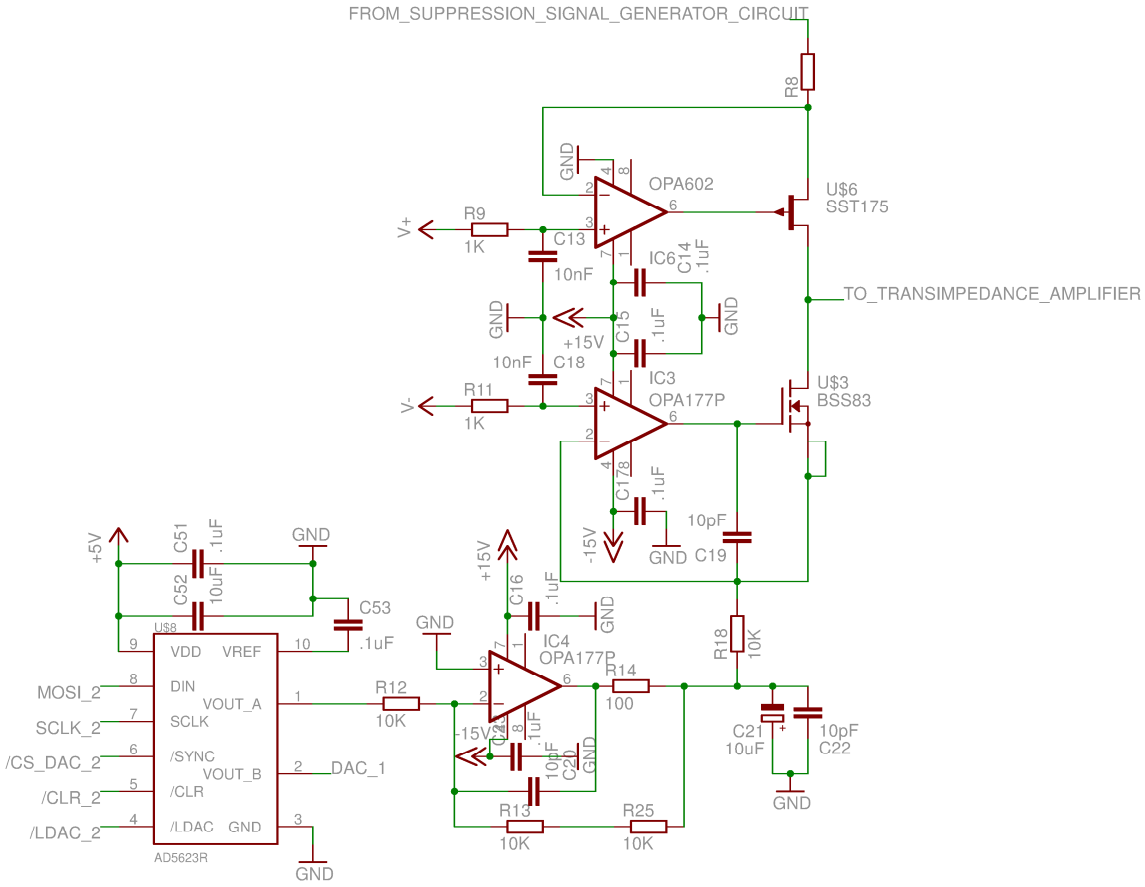

H - Schematic of the digitally controlled suppression voltage generator

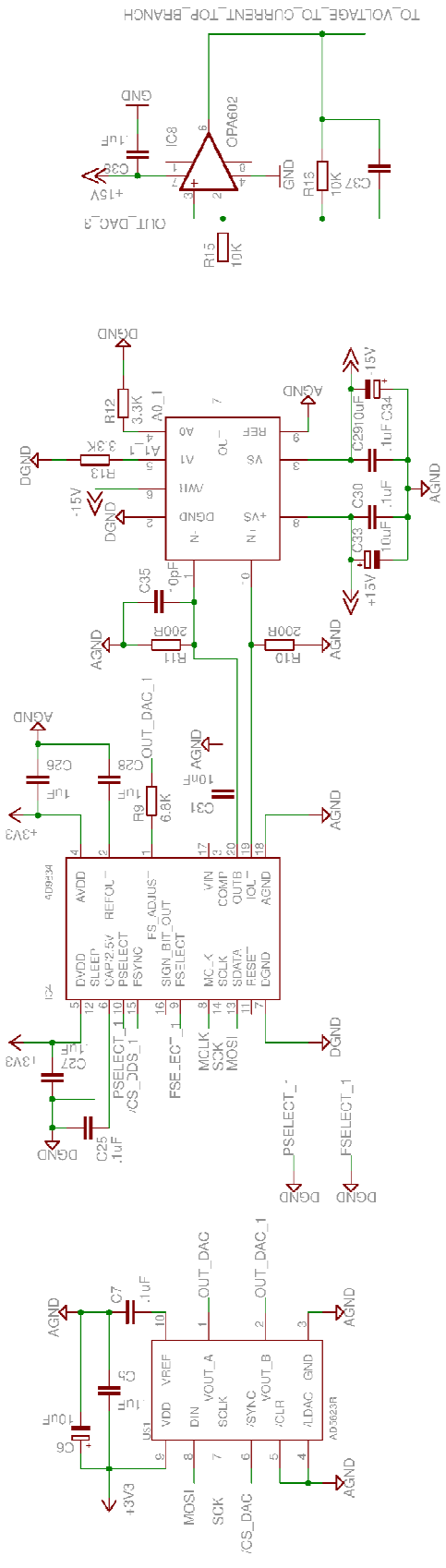

I - Schematic of the control circuit for baseline suppression and datalogging

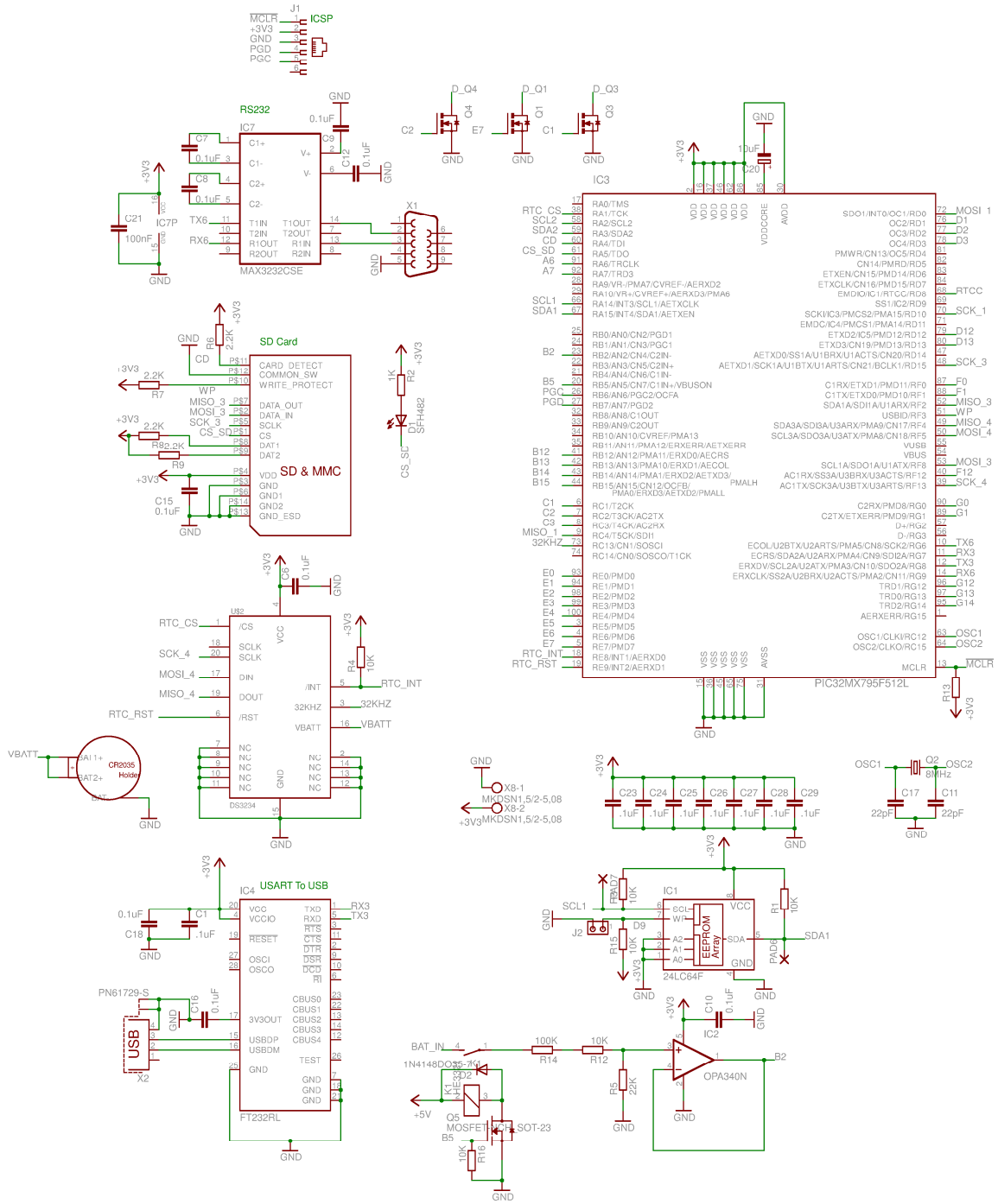

J - Schematic of the baseline suppression with quadrature lock-in amplifier

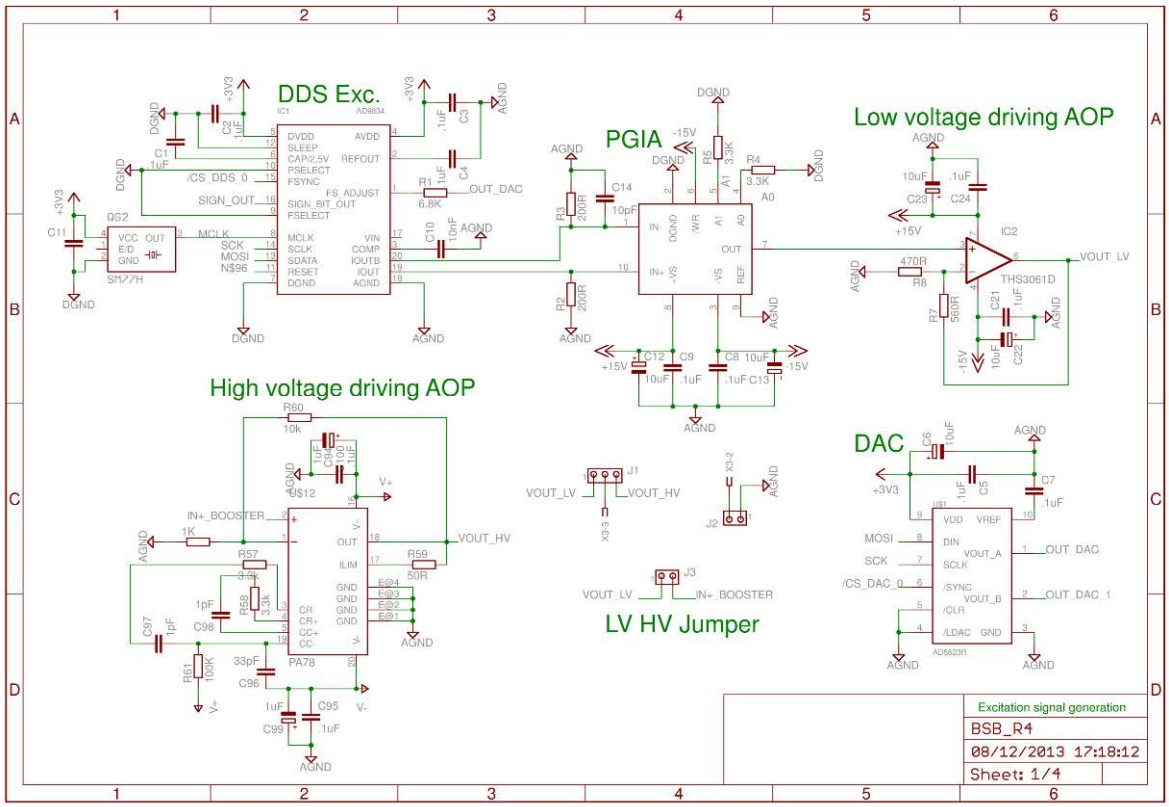

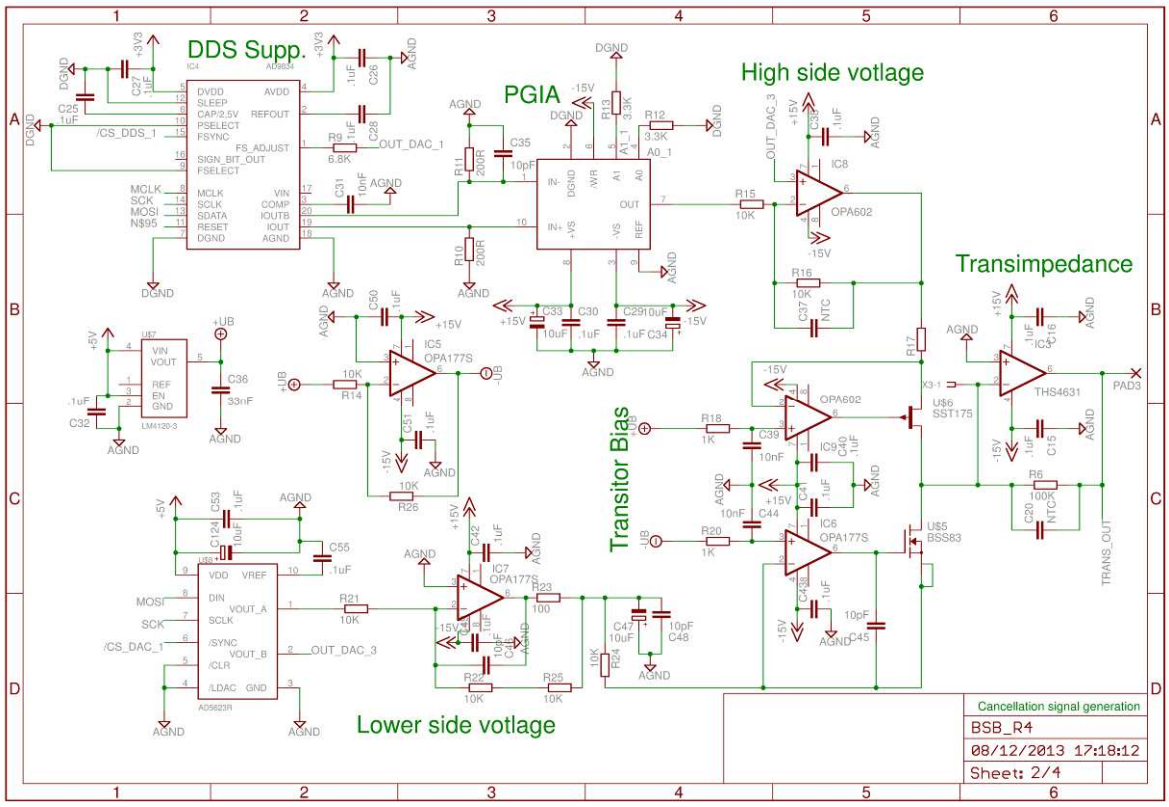

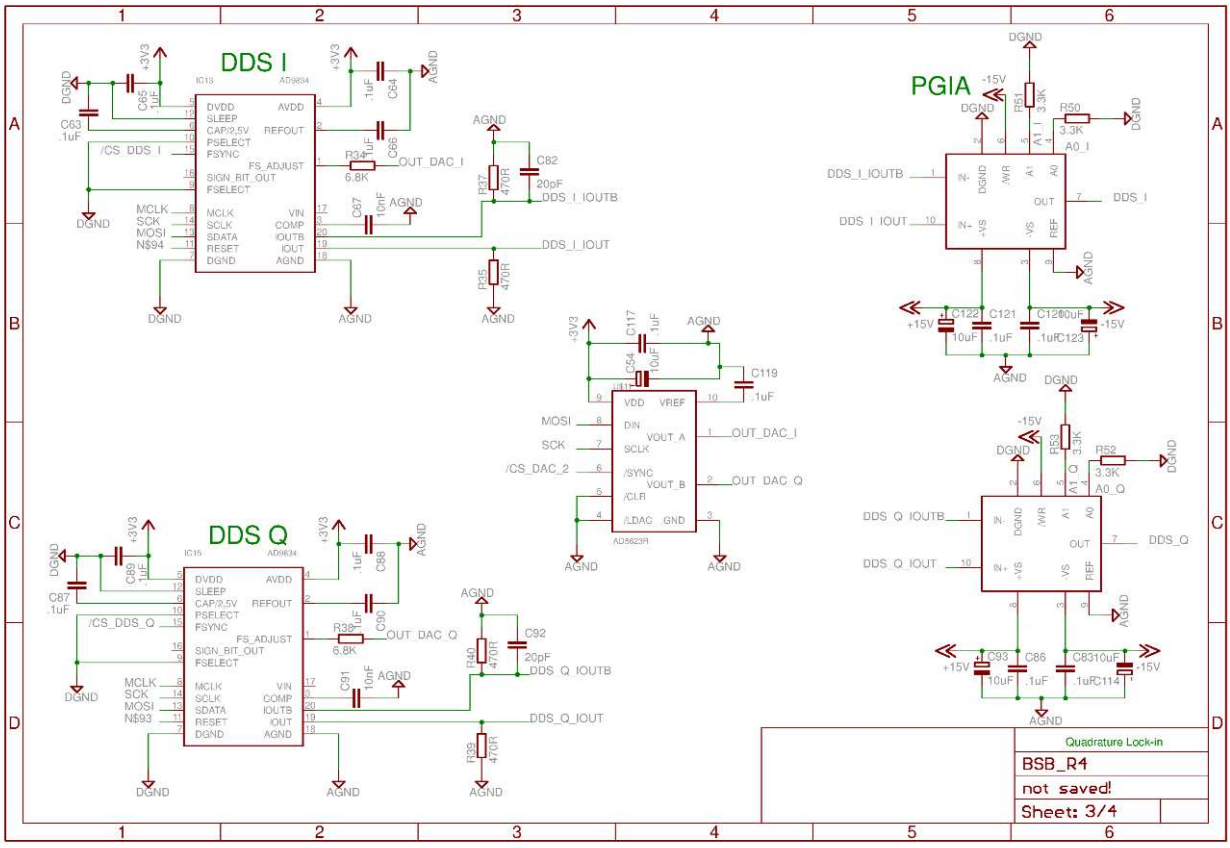
DDS I
DDS Q
PGIA
AD9834
AD5623R
DVDD
AVDD
SLEEP
CAP/2.5V
REFOUT
PSELECT
FSYNC
FS_ADJUST
SIGN_BIT_OUT
FSELECT
MCLK
SCK
MOSI
N$94
N$93
SCLK
SDATA
RESET
DGND
VIN
COMP
IOUTB
IOUT
AGND
/CS_DDS_I
/CS_DDS_Q
OUT_DAC_I
OUT_DAC_Q
DDS_I_IOUTB
DDS_I_IOUT
DDS_Q_IOUTB
DDS_Q_IOUT
+3V3
6.8K
20pF
10nF
470R
VDD
VREF
DIN
VOUT_A
VOUT_B
/SYNC
/CLR
/LDAC
GND
/CS_DAC_2
MOSI
SCK
AD8253
DDS_I_IOUTB
DDS_I_IOUT
DDS_I
DDS_Q_IOUTB
DDS_Q_IOUT
DDS_Q
A0_I
A0_Q
A1_I
A1_Q
/WR
OUT
REF
-VS
+VS
+15V
-15V
10uF
.1uF
Quadrature Lock-in
BSB_R4
not saved!
Sheet: 3/4

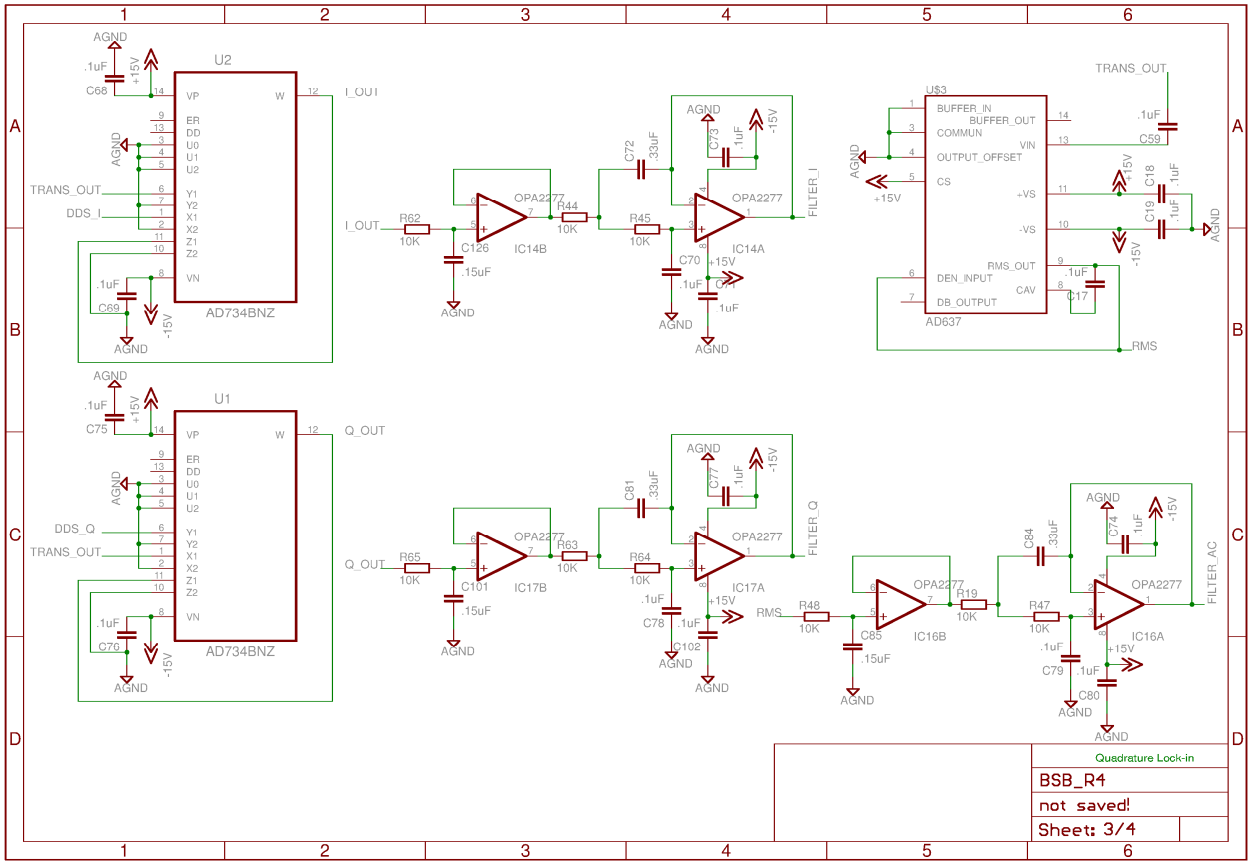
U2
U1
AD734BNZ
VP
VN
W
ER
DD
U0
U1
U2
Y1
Y2
X1
X2
Z1
Z2
I_OUT
Q_OUT
TRANS_OUT
DDS_I
DDS_Q
OPA2277
IC14B
IC14A
IC17B
IC17A
IC16B
IC16A
FILTER_I
FILTER_Q
FILTER_AC
U$3
AD637
BUFFER_IN
BUFFER_OUT
COMMUN
VIN
OUTPUT_OFFSET
CS
+VS
-VS
RMS_OUT
DEN_INPUT
CAV
DB_OUTPUT
RMS
AGND
+15V
-15V
10K
15uF
.33uF
.15uF
.1uF
Quadrature Lock-in
BSB_R4
not saved!
Sheet: 3/4

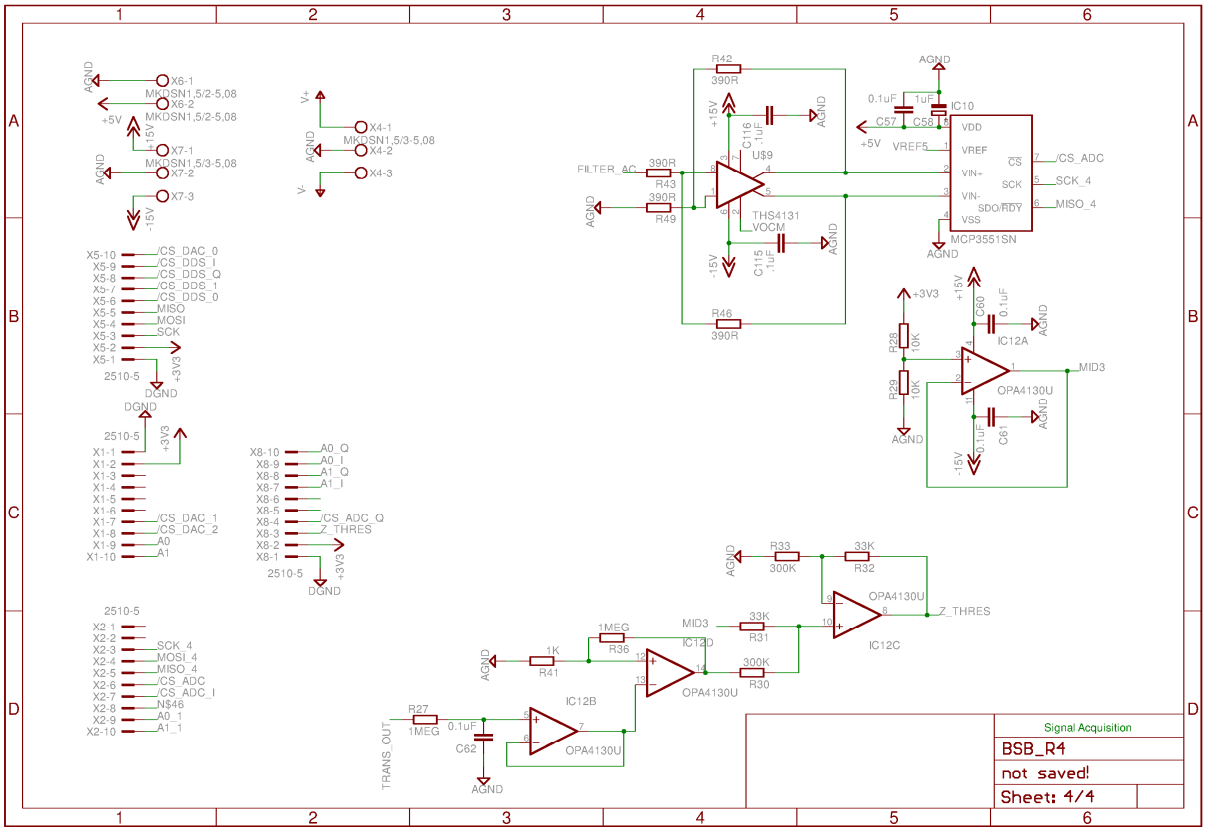
Signal Acquisition
BSB_R4
not saved!
Sheet: 4/4

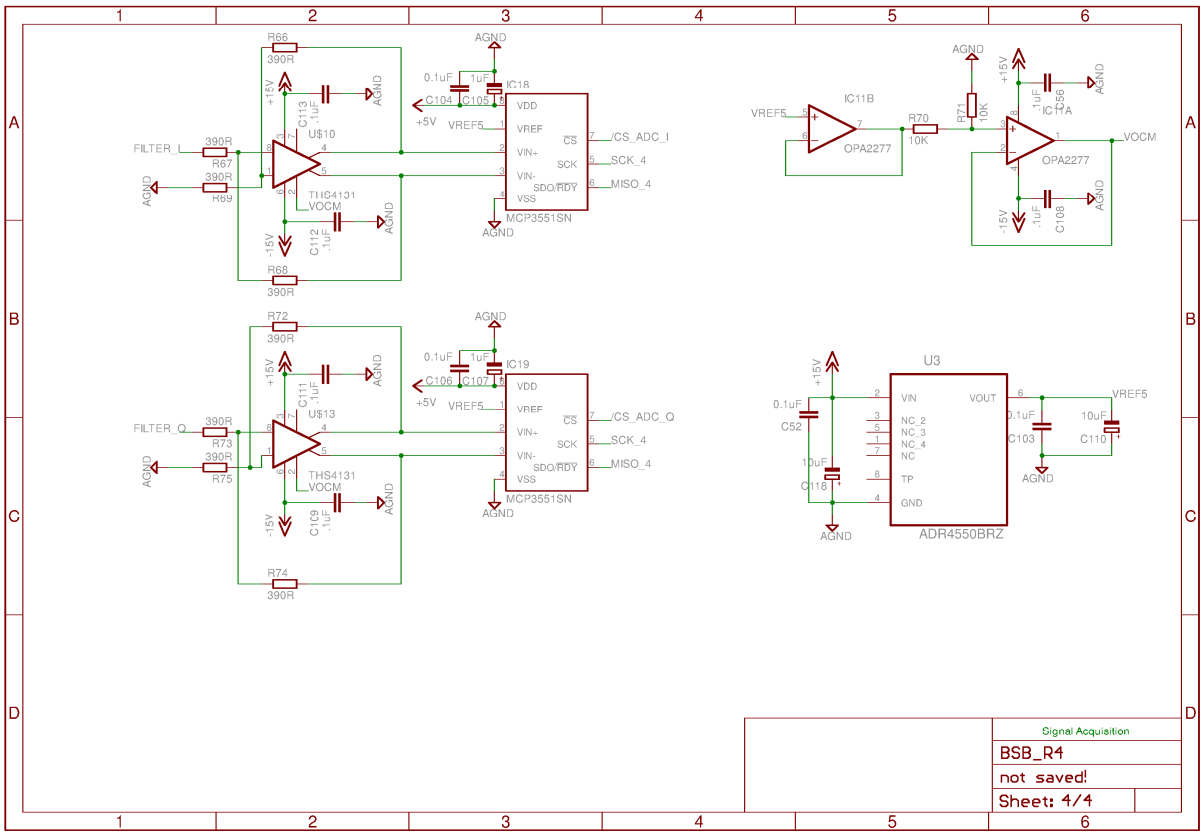
Signal Acquisition
BSB_R4
not saved!
Sheet: 4/4

LT Spice

K - Schematic of the simulation of the AC coupling of DDS3

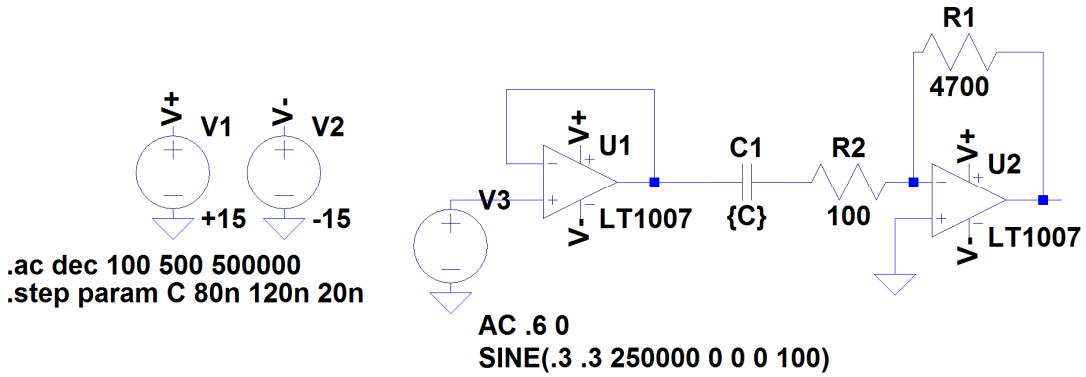

Pictures

L - Electronics setup for electrophoresis experiments

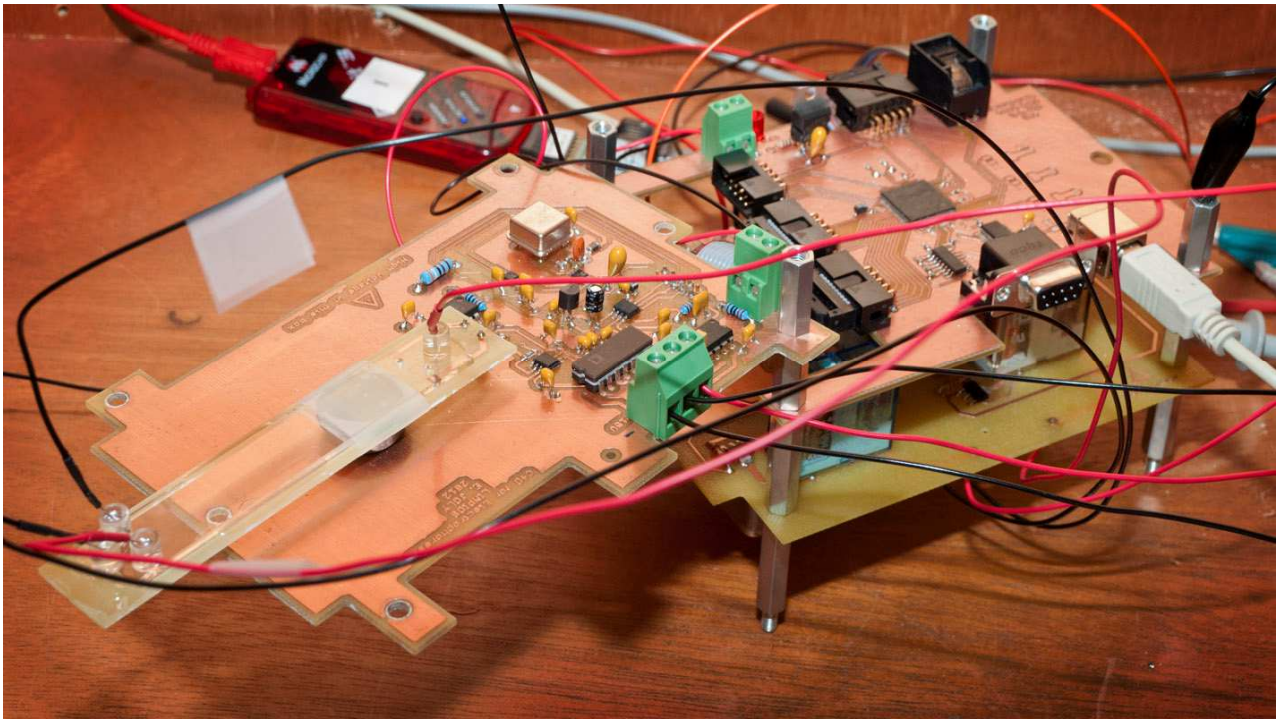

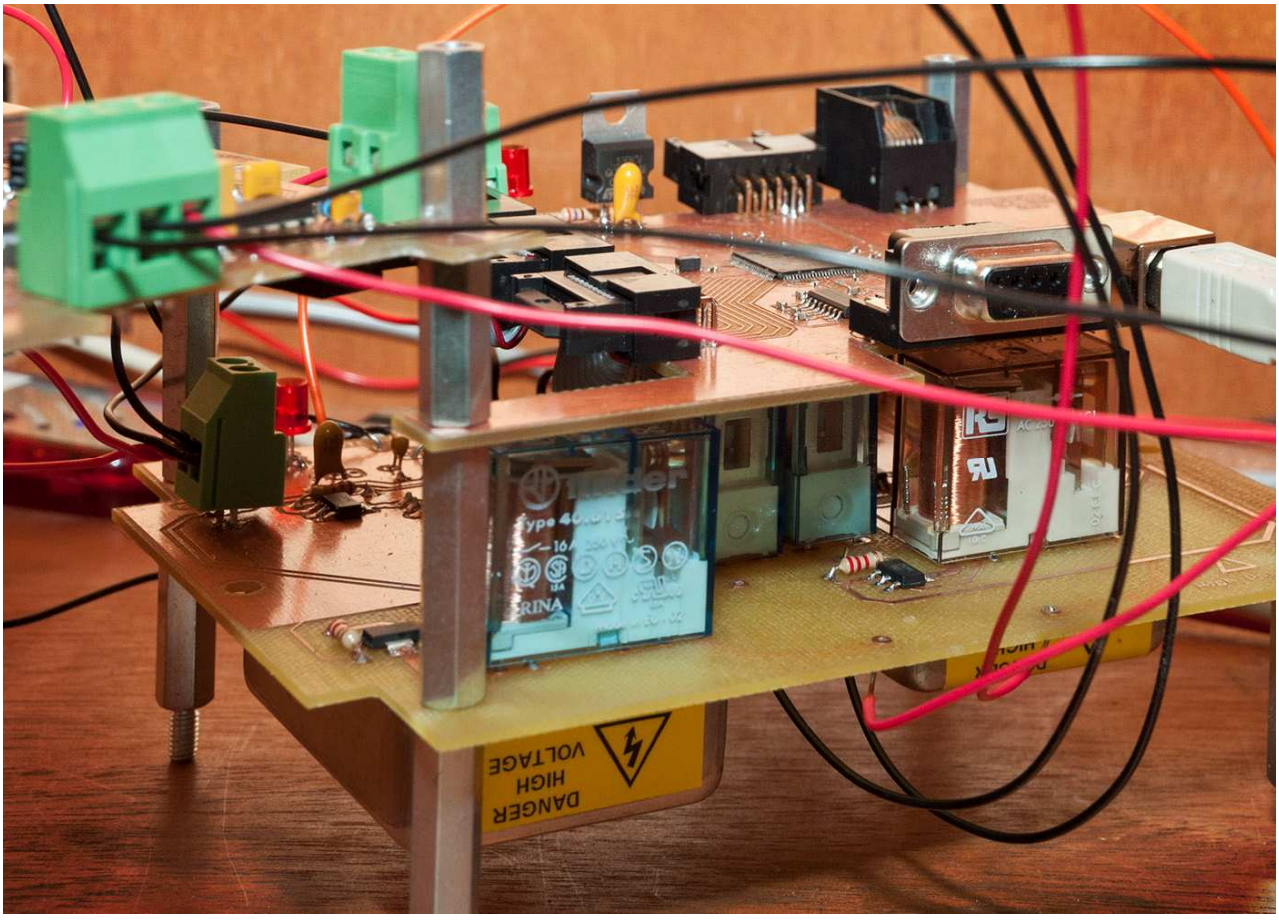

M – Baseline suppression board with two multipliers

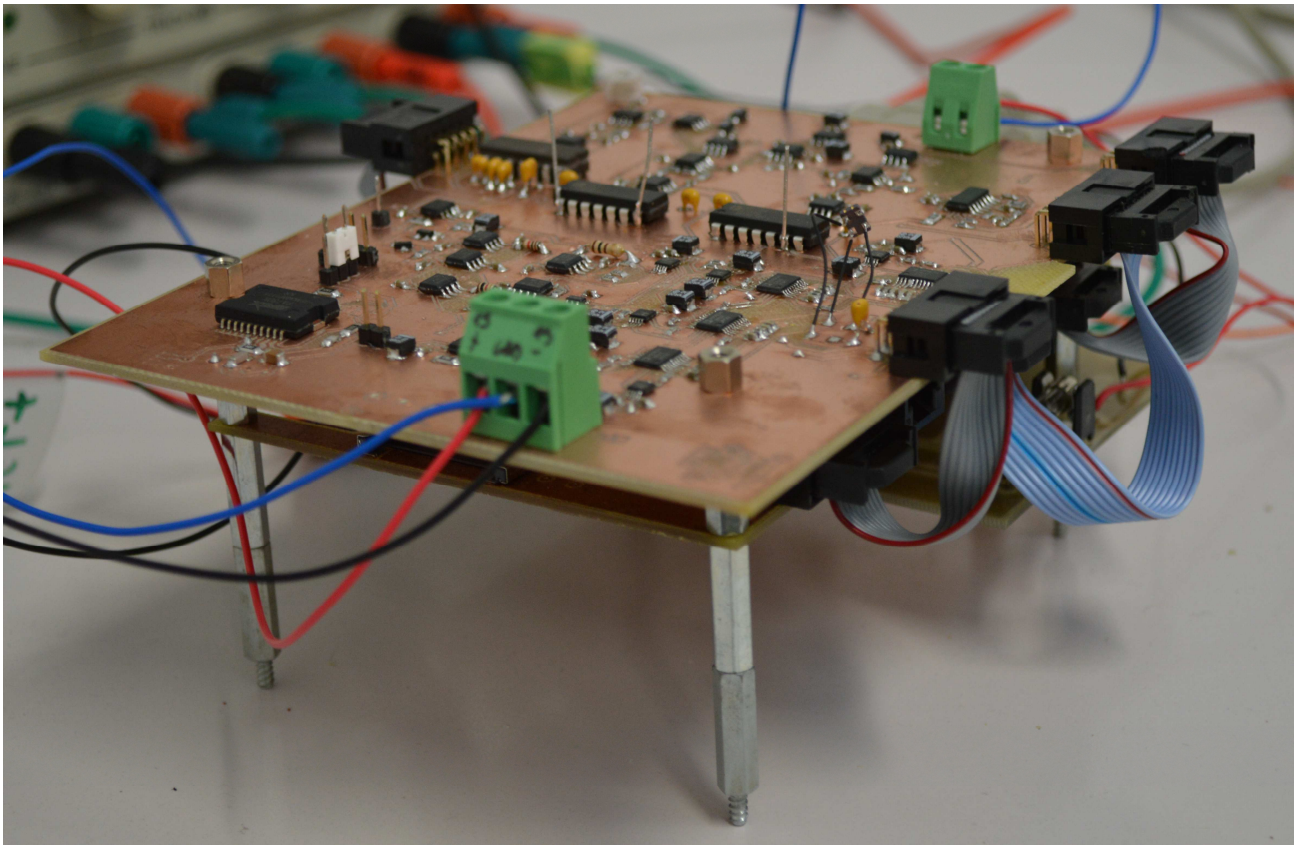

N - Box housed electronics for autonomous datalogging of conductivity measurements

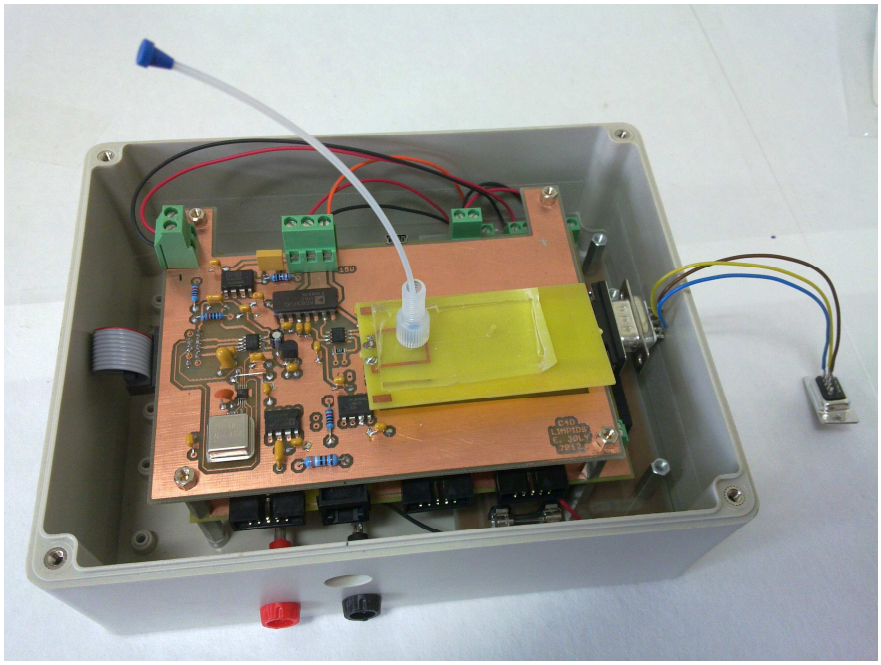

Experimental method

O – Control and measurement software (UOHC4D)

Start the UOHC4D software by clicking the icon:

The UOHC4D software should run, presenting the “System Setup” tab from its user interface

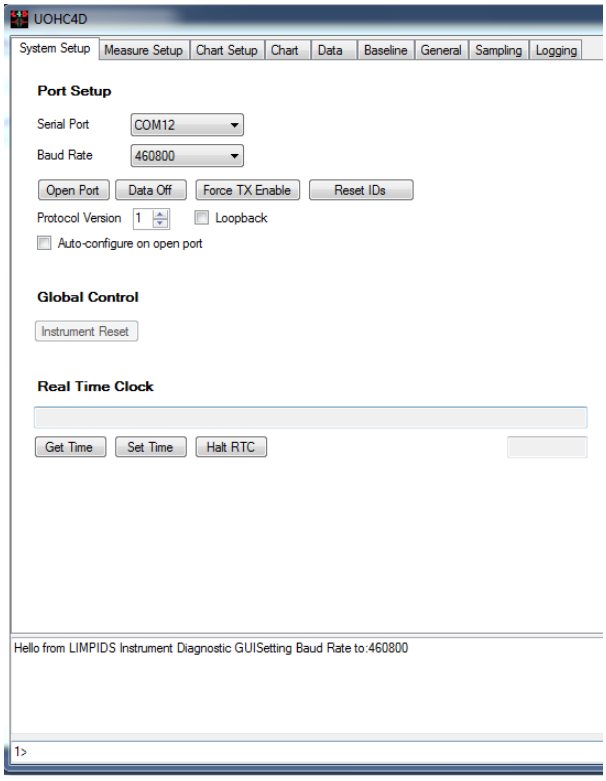

Check that the correct serial port and baud rate (460800) is selected on the dropdown list. On the current setup the correct port is COM12, but it may change.

When the correct COM port is selected, click “Open Port” to establish a connection between the PC and processor in the C4D measurement system. The UOHC4D software should respond with a message like “Opened Port COM12 at 460800 baud”. Click the “Instrument Reset” button. A message like “LIMPIDS in-situ monitor. Compiled *date time*”, which is sent from the instrument should be displayed by the UOHC4D software. This confirms that the instrument processor is operational and communicating with the PC software.

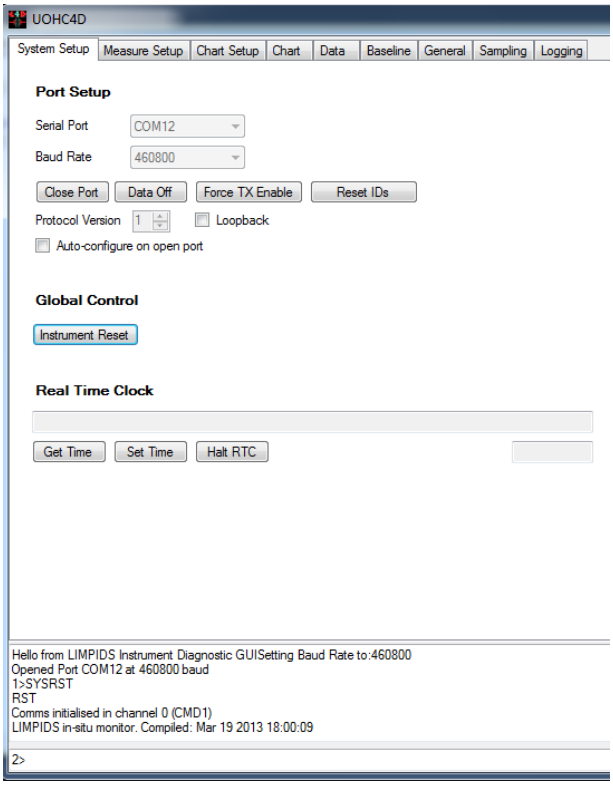

Click on the "Measure Setup" tab and then on the "Get Channel Info" button. This will list the available measurement channels from the instrument.

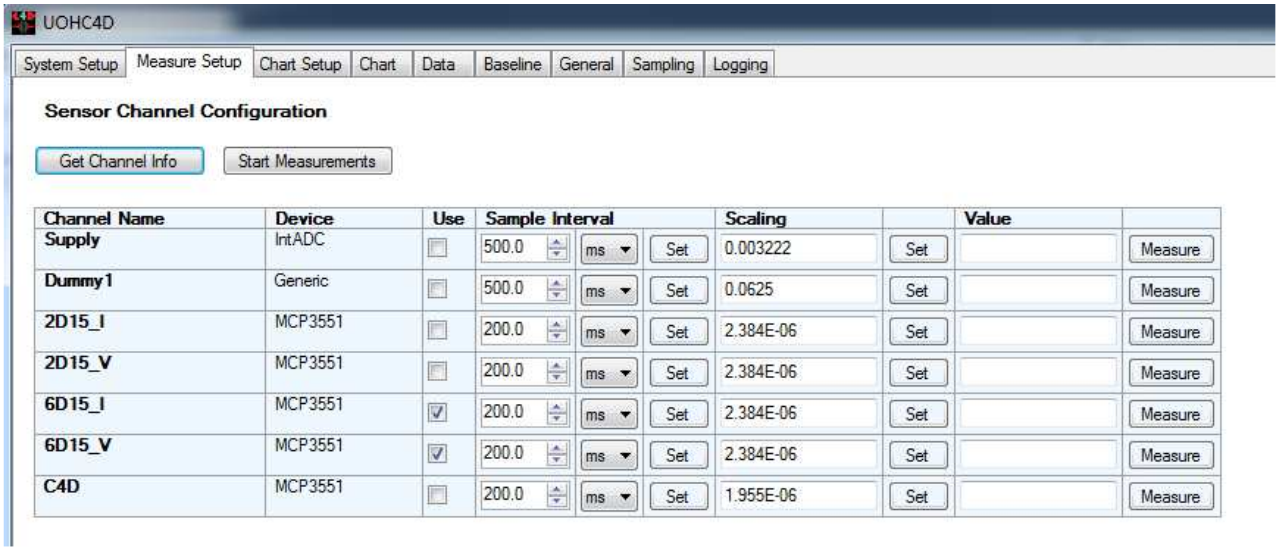

The channels are:

Supply – System Supply Voltage. Not implemented, do not use

Dummy – Fixed data sequence, for testing purposes, do not use.

2D15_I – Injection voltage supply, current monitor. Use of this can help diagnostics.

2D15_V – Injection voltage supply, voltage monitor. Use of this can help diagnostics.

6D15_I – Separation voltage supply, current monitor. Use of this can help diagnostics.

6D15_V – Separation voltage supply, voltage monitor. Use of this can help diagnostics.
C4D- The conductivity measurement. You need to use this.

Check the "Use" checkbox for each channel you want to record data for and uncheck any that you do not need. You can read the current value for any channel by clicking its "Measure" button

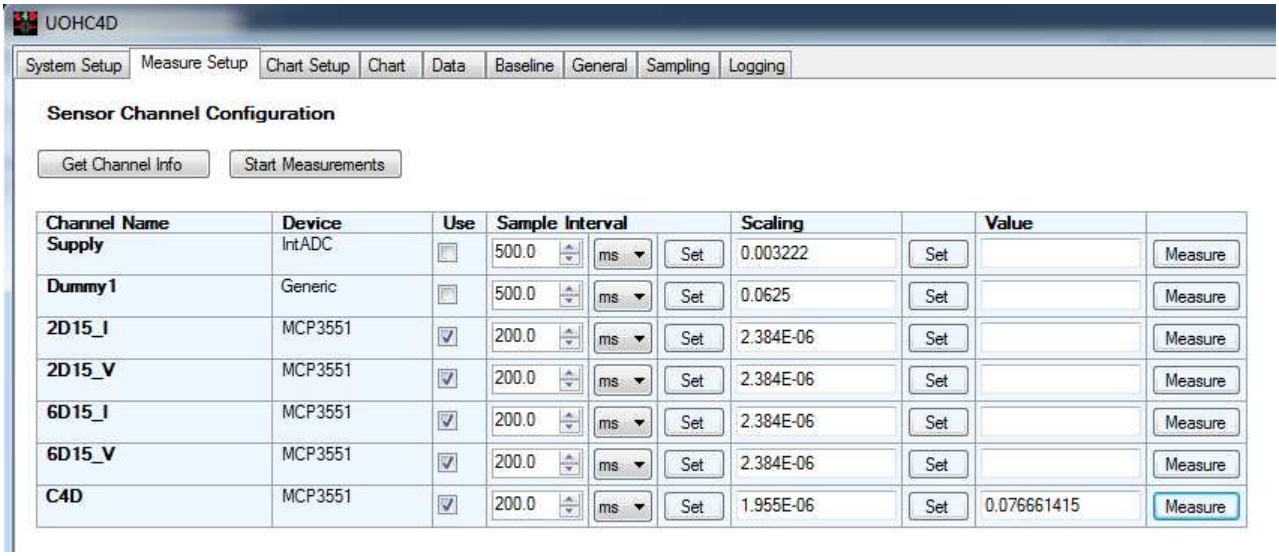

In the "C4D Instrument Control" panel enter the required DDS frequency. This should be in the range 200000 to 700000 (for 200 to 700 kHz). Click the "Set" button next to the frequency value.

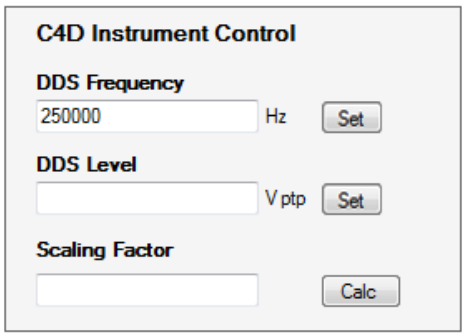

In the "Electrophoresis Instrument Control" panel set up the times and voltages required for the current experiment, then click "Set All". If you get the values wrong just change them and click "Set All" again. **Do not** click "Start HV switching" yet.

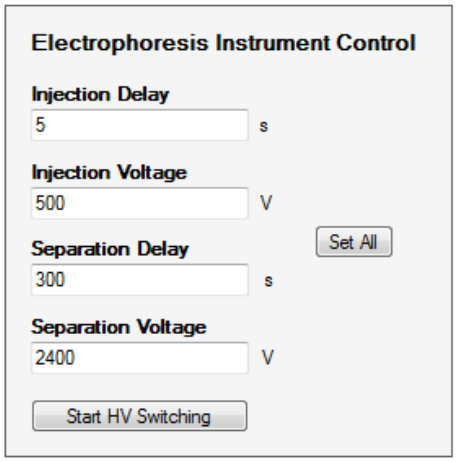

Typical values are

Injection delay	5s
Injection voltage	500V
Separation Delay	300s
Separation voltage	2400V

Make sure that the door of the HV isolation box is closed because the HV supplies will not be active when it is open. There is an LED on the bottom board which tells when voltage is being applied to the HV modules.
Return to the "Measure Setup" tab and click the "Measure" button for the C4D channel. The value should be between 2V and 3V. (The voltage shown here is not correct because the chip was not in place for this screenshot.)

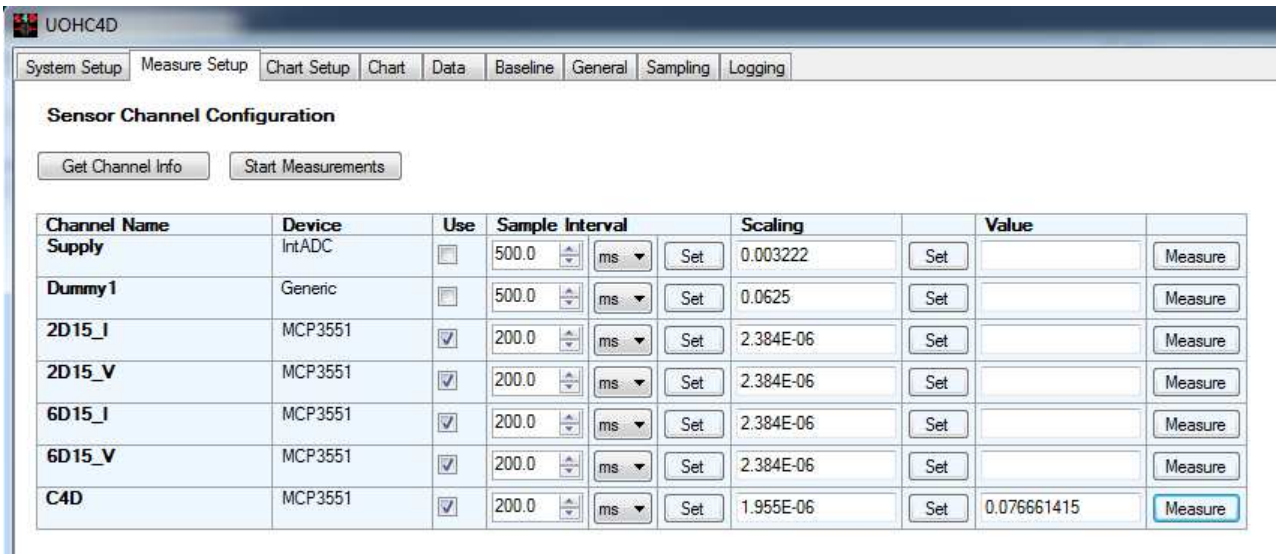

If the voltage is not in the correct range move to the "Baseline" tab and "Cell Excitation" panel and adjust the cell excitation by changing the DDS gain. Click the x1, x2 buttons as appropriate and move back to the "Measure Setup" tab to check the voltage. (Note: the x5 or x10 options will probably not be needed in the current setup.)

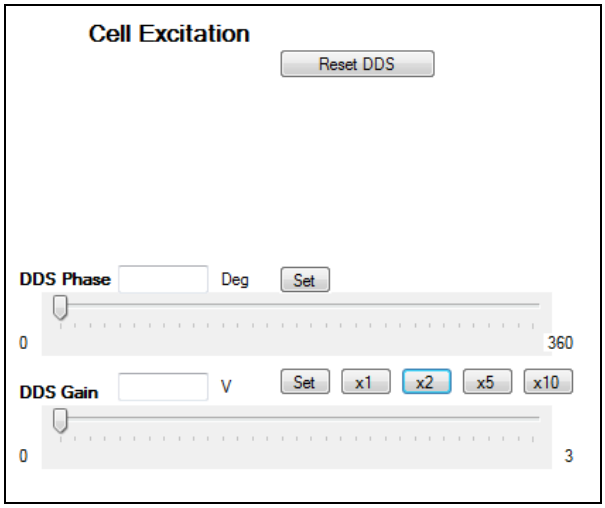

Move to the “Chart” tab and right click on the “Measurement Data” area to select the channel to display. Select C4D. This will appear in the title above the “Measurement Data” area.
Check the “Sync Measure” checkbox.

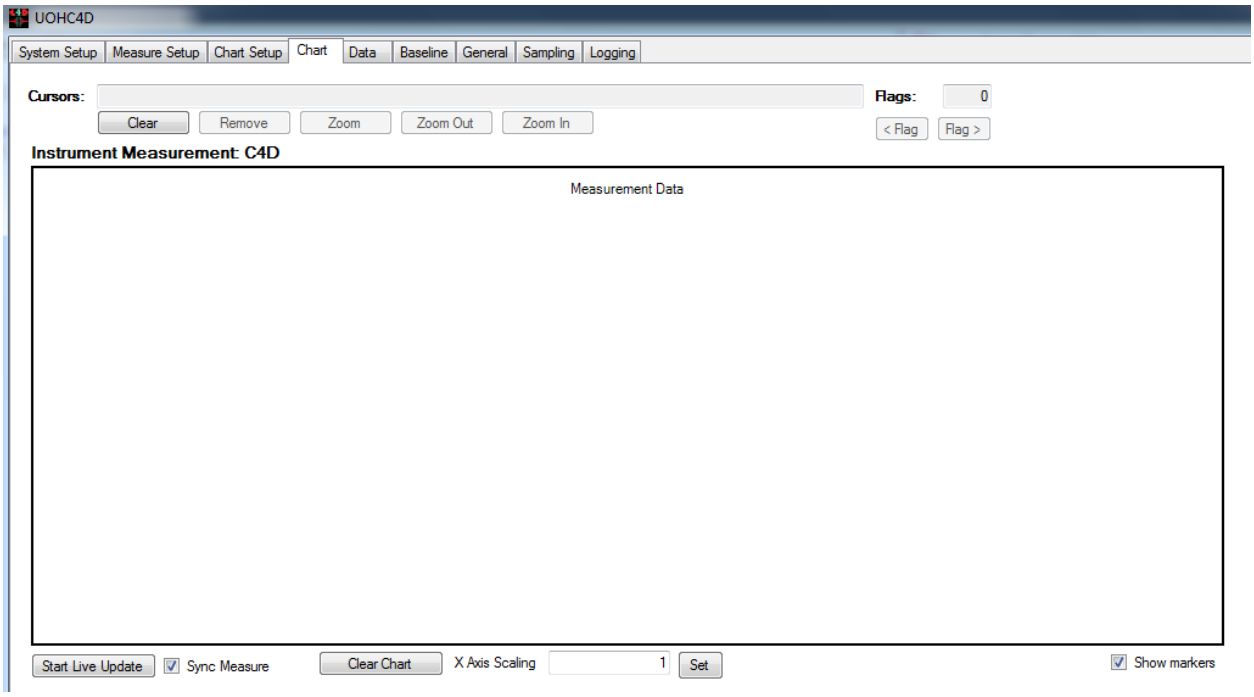

When you are ready to run the experiment click the “Start Live Update” button, then move quickly to the “System Setup” tab and click the “Start HV switching” button in the “Electrophoresis Instrument Control” panel. You should here the relays click as the measurement process starts.
Move back to the “Chart” tab to observe the progress of the experiment. You can switch between active measurement channels by right clicking on the chart. All data in used channel is saved irrespective of what channel you are observing in the live monitoring. The data shown here is not representative of a real experiment as no chip was connected at the time.

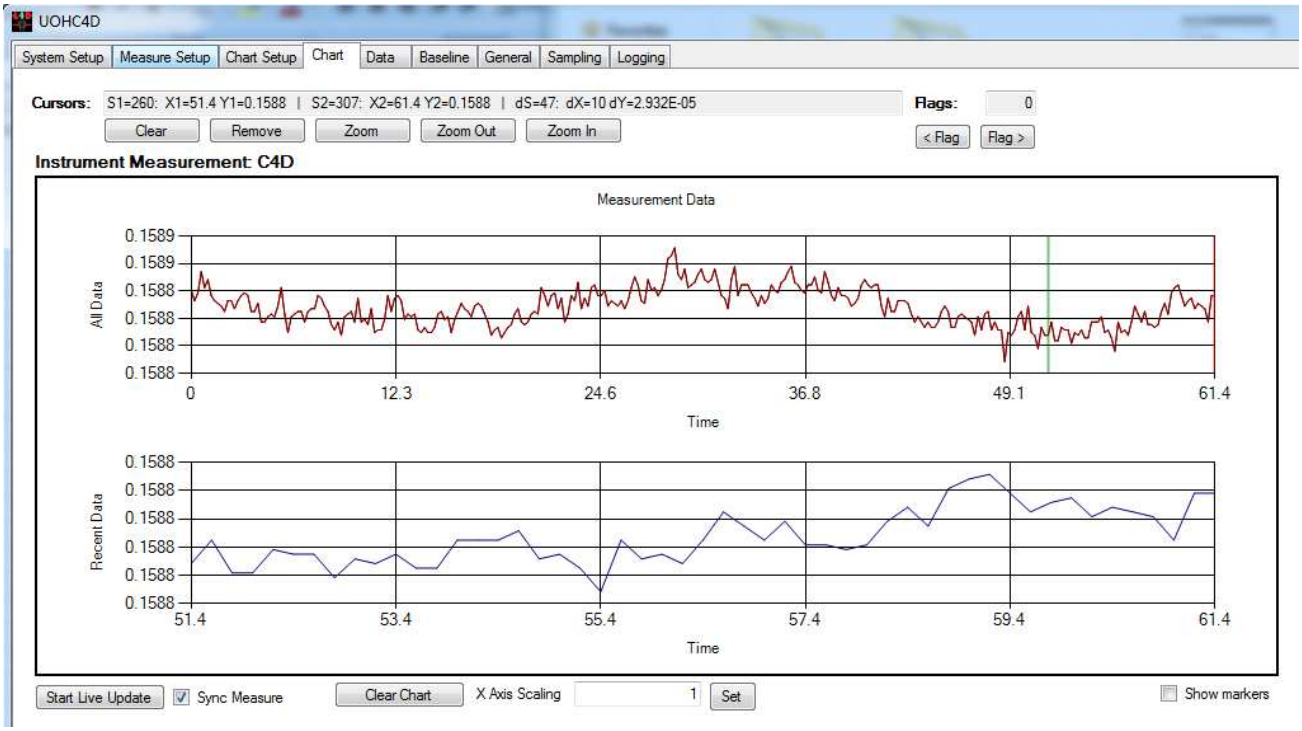

When the experiment has finished click the “Stop Live Update” button in the chart tab to stop data recording. To save your data go to the “Data” tab , make sure “Measurements” is selected in the “Table “ drop-down box and click the “Show/Update” button to display the data. Click “Save to File” to save the data.

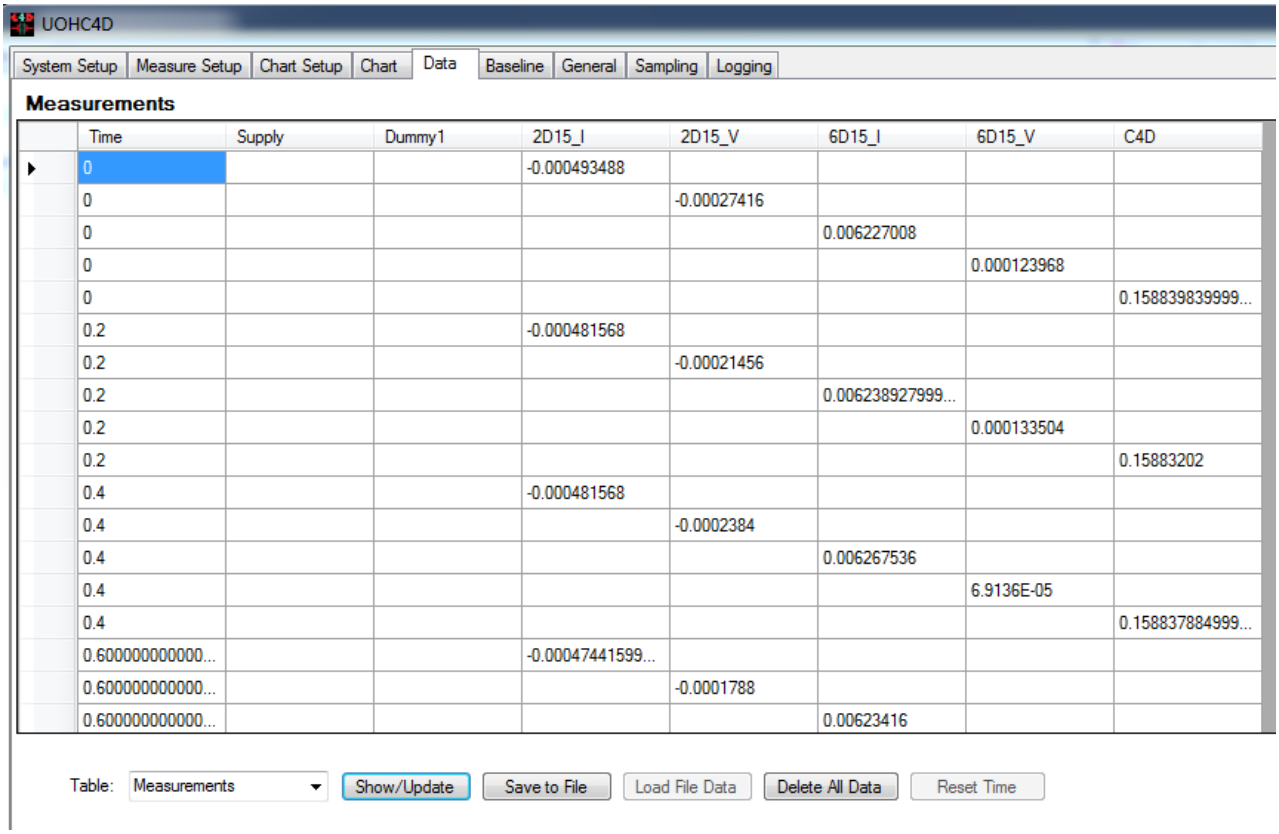

Time	Supply	Dummy1	2D15_I	2D15_V	6D15_I	6D15_V	C4D
0			-0.000493488				
0				-0.00027416			
0					0.006227008		
0						0.000123968	
0							0.158839839999...
0.2			-0.000481568				
0.2				-0.00021456			
0.2					0.006238927999...		
0.2						0.000133504	
0.2							0.15883202
0.4			-0.000481568				
0.4				-0.0002384			
0.4					0.006267536		
0.4						6.9136E-05	
0.4							0.158837884999...
0.600000000000...			-0.00047441599...				
0.600000000000...				-0.0001788			
0.600000000000...					0.00623416		

The data is saved in .csv (comma separated variable) format and can be opened by Microsoft Excel and other applications.

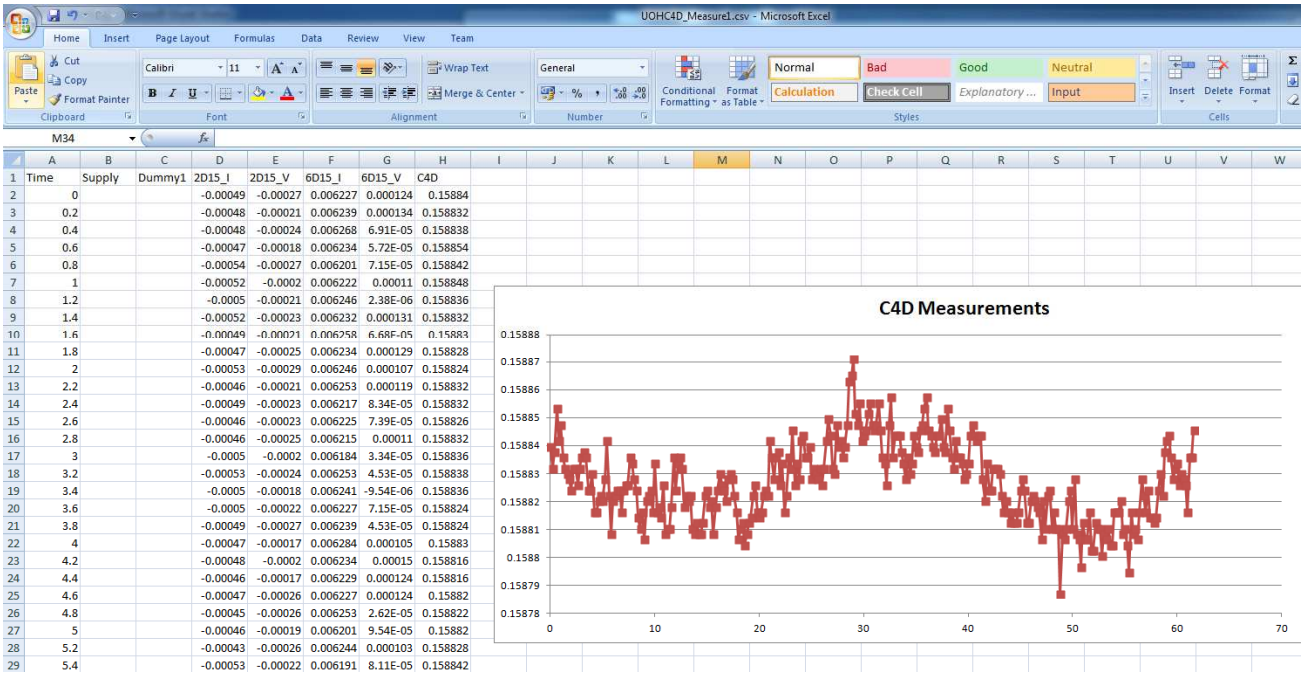

	A	B	C	D	E	F	G	H
1	Time	Supply	Dummy1	2D15_I	2D15_V	6D15_I	6D15_V	C4D
2	0			-0.00049	-0.00027	0.006227	0.000124	0.15884
3	0.2			-0.00048	-0.00021	0.006239	0.000134	0.158832
4	0.4			-0.00048	-0.00024	0.006268	6.91E-05	0.158838
5	0.6			-0.00047	-0.00018	0.006234	5.72E-05	0.158854
6	0.8			-0.00054	-0.00027	0.006201	7.15E-05	0.158842
7	1			-0.00052	-0.0002	0.006222	0.00011	0.158848
8	1.2			-0.0005	-0.00021	0.006246	2.38E-06	0.158836
9	1.4			-0.00052	-0.00023	0.006232	0.000131	0.158832
10	1.6			-0.00049	-0.00021	0.006258	6.68E-05	0.15883
11	1.8			-0.00047	-0.00025	0.006234	0.000129	0.158828
12	2			-0.00053	-0.00029	0.006246	0.000107	0.158824
13	2.2			-0.00046	-0.00021	0.006253	0.000119	0.158832
14	2.4			-0.00049	-0.00023	0.006217	8.34E-05	0.158832
15	2.6			-0.00046	-0.00023	0.006225	7.39E-05	0.158826
16	2.8			-0.00046	-0.00025	0.006215	0.00011	0.158832
17	3			-0.0005	-0.0002	0.006184	3.34E-05	0.158836
18	3.2			-0.00053	-0.00024	0.006253	4.53E-05	0.158838
19	3.4			-0.0005	-0.00018	0.006241	-9.54E-06	0.158836
20	3.6			-0.0005	-0.00022	0.006227	7.15E-05	0.158824
21	3.8			-0.00049	-0.00027	0.006239	4.53E-05	0.158824
22	4			-0.00047	-0.00017	0.006284	0.000105	0.15883
23	4.2			-0.00048	-0.0002	0.006234	0.00015	0.158816
24	4.4			-0.00046	-0.00017	0.006229	0.000124	0.158816
25	4.6			-0.00047	-0.00026	0.006227	0.000124	0.15882
26	4.8			-0.00045	-0.00026	0.006253	2.62E-05	0.158822
27	5			-0.00046	-0.00019	0.006201	9.54E-05	0.15882
28	5.2			-0.00043	-0.00026	0.006244	0.000103	0.158828
29	5.4			-0.00053	-0.00022	0.006191	8.11E-05	0.158842

Running another Experiment

If you want to run another separation, you need to clear the former data. If not, the new data will continue after the former data.

Make sure live data is not being recorded (e.g. click the “Stop Live Update” button in the “Chart” tab).

Go to the “Data” tab and click the "Delete All Data" button. Make sure you save the current data first if required.

Click the “Reset Time” button

Go to the “Chart” tab and click the "Clear Chart" button.

The system is now ready to start a new experimental run. You need to click “Set All” in the “C4D Instrument Control” panel even if you are using the same values again before clicking “Start HV switching” to start the new experiment.

After the Experiment

Close the UOHC4D software by clicking the X at the top right of its window. Click “Yes” to the “Do you want to close” message.

Close Microsoft Visual Studio 2010. There is no need to save anything from Visual Studio.

Switch off the measurement electronics power supply (currently bottom PSU in stack), positive rail first.

Switch off the digital and high voltage power supply (currently top PSU in stack).

Open the HV isolation box.

Carefully remove the electrode holder from above the chip and place it out of the way.

Unplug the electrophoresis chip board and place it on the lab bench.

Clean the electrode with MilliQ water to avoid any crystal formation.

Close the HV isolation box so that the door is not protruding.

Drain the chip, flush with MilliQ water and inject air into to it to remove as much liquid as possible. Place they chip in the desiccant bag.

MATLAB

P – *.m file for the calculation of the peristaltic pump spectrum

```
close all; clear all;

data_0=load ('1mM_NaNO2_65_7.csv');
RAW_0=(data_0*12/2^15);
RAW_0=RAW_0-mean(RAW_0);
L_0=length(data_0);
X_0=linspace(0,L_0*0.01,L_0);

Fs=100;

% figure();
% subplot(2,1,1);
% plot(X_0,RAW_0);
% xlabel('Time (s)');
% ylabel('DC Output Voltage with Peristaltic pump @ 6.5VDC');
% title('Voltage Output - 1mM NaNO2 - 1M 500Hz - 120406');
% grid;

NFFT_0 = 2^nextpow2(L_0);
Y_0 = fft(RAW_0,NFFT_0)/L_0;
f_0 = Fs/2*linspace(0,1,NFFT_0/2+1);
% Plot single-sided amplitude spectrum.
% subplot(2,1,2);
% plot(f_0,2*abs(Y_0(1:NFFT_0/2+1)))
% title('Single-Sided Amplitude Spectrum of the Signal - 120406')
% xlabel('Frequency (Hz)')
% ylabel('|Y(f)|')
% grid;
% xlim([0 10]);

Index_0=find(2*abs(Y_0(1:NFFT_0/2+1))==max(2*abs(Y_0(1:NFFT_0/2+1))));

data_1=load ('1mM_NaNO2_5_8.csv');
RAW_1=(data_1*12/2^15);
RAW_1=RAW_1-mean(RAW_1);
L_1=length(data_1);
X_1=linspace(0,L_1*0.01,L_1);

% figure();
% subplot(2,1,1);
% plot(X_1,RAW_1);
% xlabel('Time (s)');
% ylabel('DC Output Voltage with Peristaltic pump @ 5VDC');
% title('Voltage Output - 1mM NaNO2 - 1M 500Hz - 120406');
% grid;

NFFT_1 = 2^nextpow2(L_1);
Y_1 = fft(RAW_1,NFFT_1)/L_1;
f_1 = Fs/2*linspace(0,1,NFFT_1/2+1);
% Plot single-sided amplitude spectrum.
% subplot(2,1,2);
% plot(f_1,2*abs(Y_1(1:NFFT_1/2+1)))
% title('Single-Sided Amplitude Spectrum of the Signal - 120406')
% xlabel('Frequency (Hz)')
% ylabel('|Y(f)|')
% grid;
% xlim([0 10]);

Index_1=find(2*abs(Y_1(1:NFFT_1/2+1))==max(2*abs(Y_1(1:NFFT_1/2+1))));

data_2=load ('1mM_NaNO2_8_9.csv');
RAW_2=(data_2*12/2^15);
RAW_2=RAW_2-mean(RAW_2);
L_2=length(data_2);
X_2=linspace(0,L_2*0.01,L_2);

Fs=100;

% figure();
% subplot(2,1,1);
% plot(X_2,RAW_2);
% xlabel('Time (s)');
% ylabel('DC Output Voltage with Peristaltic pump @ 8VDC');
% title('Voltage Output - 1mM NaNO2 - 1M 500Hz - 120406');
% grid;

NFFT_2 = 2^nextpow2(L_2);
Y_2 = fft(RAW_2,NFFT_2)/L_2;
f_2 = Fs/2*linspace(0,1,NFFT_2/2+1);
% Plot single-sided amplitude spectrum.
% subplot(2,1,2);
% plot(f_2,2*abs(Y_2(1:NFFT_2/2+1)))
% title('Single-Sided Amplitude Spectrum of the Signal - 120406')
% xlabel('Frequency (Hz)')
% ylabel('|Y(f)|')
% grid;
% xlim([0 10]);

Index_2=find(2*abs(Y_2(1:NFFT_2/2+1))==max(2*abs(Y_2(1:NFFT_2/2+1))));

data_3=load ('1mM_NaNO2_10_10.csv');
RAW_3=(data_3*12/2^15);
RAW_3=RAW_3-mean(RAW_3);
L_3=length(data_3);
X_3=linspace(0,L_3*0.01,L_3);

figure();
subplot(2,1,1);
plot(X_3,RAW_3);
xlabel('Time (s)');
ylabel('DC Output Voltage with Peristaltic pump @ 10VDC');
title('Voltage Output - 1mM NaNO2 - 1M 500Hz - 120406');
grid;

NFFT_3 = 2^nextpow2(L_3);
Y_3 = fft(RAW_3,NFFT_3)/L_3;
f_3 = Fs/2*linspace(0,1,NFFT_3/2+1);
% Plot single-sided amplitude spectrum.
subplot(2,1,2);
% figure();
plot(f_3,2*abs(Y_3(1:NFFT_3/2+1)))
title('Single-Sided Amplitude Spectrum of the Signal - 120406')
xlabel('Frequency (Hz)')
ylabel('|Y(f)|')
grid;
xlim([0 10]);
```

```
Index_3=find(2*abs(Y_3(1:NFFT_3/2+1))==max(2*abs(Y_3(1:NFFT_3/2+1))));


data_4=load ('1mM_NaNO2_6_12.csv');
RAW_4=(data_4*12/2^15);
RAW_4=RAW_4-mean(RAW_4);
L_4=length(data_4);
X_4=linspace(0,L_4*0.01,L_4);

% figure();



data_4=load ('1mM_NaNO2_6_12.csv');
RAW_4=(data_4*12/2^15);
RAW_4=RAW_4-mean(RAW_4);
L_4=length(data_4);
X_4=linspace(0,L_4*0.01,L_4);

% figure();
% subplot(2,1,1);
% plot(X_4,RAW_4);
% xlabel('Time (s)');
% ylabel('DC Output Voltage with Peristaltic pump @ 6VDC');
% title('Voltage Output - 1mM NaNO2 - 1M 500Hz - 120406');
% grid;

NFFT_4 = 2^nextpow2(L_4);
Y_4 = fft(RAW_4,NFFT_4)/L_4;
f_4 = Fs/2*linspace(0,1,NFFT_4/2+1);
% % Plot single-sided amplitude spectrum.
% subplot(2,1,2);
% plot(f_4,2*abs(Y_4(1:NFFT_4/2+1)))
% title('Single-Sided Amplitude Spectrum of the Signal - 120406')
% xlabel('Frequency (Hz)')
% ylabel('|Y(f)|')
% grid;
% xlim([0 10]);

Index_4=find(2*abs(Y_4(1:NFFT_4/2+1))==max(2*abs(Y_4(1:NFFT_4/2+1))));

data_5=load ('1mM_NaNO2_9_11.csv');
RAW_5=(data_5*12/2^15);
RAW_5=RAW_5-mean(RAW_5);
L_5=length(data_5);
X_5=linspace(0,L_5*0.01,L_5);

% figure();
% subplot(2,1,1);
% plot(X_5,RAW_5);
% xlabel('Time (s)');
% ylabel('DC Output Voltage with Peristaltic pump @ 9VDC');
% title('Voltage Output - 1mM NaNO2 - 1M 500Hz - 120406');
% grid;

NFFT_5 = 2^nextpow2(L_5);
Y_5 = fft(RAW_5,NFFT_5)/L_5;
f_5 = Fs/2*linspace(0,1,NFFT_5/2+1);
% % Plot single-sided amplitude spectrum.
% subplot(2,1,2);
% plot(f_5,2*abs(Y_5(1:NFFT_5/2+1)))
% title('Single-Sided Amplitude Spectrum of the Signal - 120406')
% xlabel('Frequency (Hz)')
% ylabel('|Y(f)|')
% grid;
% xlim([0 10]);

Index_5=find(2*abs(Y_5(1:NFFT_5/2+1))==max(2*abs(Y_5(1:NFFT_5/2+1))));

data_6=load ('1mM_NaNO2_95_13.csv');
RAW_6=(data_6*12/2^15);
RAW_6=RAW_6-mean(RAW_6);
L_6=length(data_6);
X_6=linspace(0,L_6*0.01,L_6);

% figure();
% subplot(2,1,1);
% plot(X_6,RAW_6);
% xlabel('Time (s)');
% ylabel('DC Output Voltage with Peristaltic pump @ 9VDC');
% title('Voltage Output - 1mM NaNO2 - 1M 500Hz - 120406');
% grid;

NFFT_6 = 2^nextpow2(L_6);
Y_6 = fft(RAW_6,NFFT_6)/L_6;
f_6 = Fs/2*linspace(0,1,NFFT_6/2+1);
% % Plot single-sided amplitude spectrum.
% subplot(2,1,2);
% plot(f_6,2*abs(Y_6(1:NFFT_6/2+1)))
% title('Single-Sided Amplitude Spectrum of the Signal - 120406')
% xlabel('Frequency (Hz)')
% ylabel('|Y(f)|')
% grid;
% xlim([0 10]);

Index_6=find(2*abs(Y_6(1:NFFT_6/2+1))==max(2*abs(Y_6(1:NFFT_6/2+1))));

figure();
V=[5 6 6.5 8 9 9.5 10];
F_Speed=[f_1(Index_1) f_4(Index_4) f_0(Index_0) f_2(Index_2) f_5(Index_5)
f_6(Index_6) f_3(Index_3)];
plot(V,F_Speed,'*');
xlabel('Applied Pump Voltage (V)')
ylabel('Frequency (Hz)')
title('Baseline spectrum maximum peak vs Pump supply voltage - 1mM NaNO2 -
1M 500Hz - 120406');
grid;
```

Q – List of the available instrument commands

Command	Description
VER	Print software version/compile date
DATAON	Switch data stream on
DATAOFF	Switch data stream off
STREAM adcchannel status	Add/remove ADC channel adcchannel from data stream. Status is 0 for do not stream this channel and is 1 if streaming is required.
SETSP adcchannel timer period	Set sample period for ADC channel adcchannel. Timer is 1 for ms ticks and 2 for seconds ticks. Period is number of ticks of set timer for sampling interval.
SYSRST	Execute soft reset of microcontroller
FREQ ddschannel frequency	Set DDS Frequency for C4D measurement system. ddschannel is ignored in current implementation, but must be set. frequency is the DDS output frequency in Hz.
GETACHN	Get details of analogue channels.
READADC adcchannel	Read the ADC (single reading) in channel adcchannel.
GETINST	Get Instrument Information. Returns the following system parameter information: Name, SerialNumber, Version.Major, Version.Minor, Version.Build, Version.Revision, ProductID, HasGPS, HasStartTrigger, HasRemoteCommand, SensorCount.
GETSENS SensorNumber	Get Sensor Information. Returns the following information for sensor subsystem SensorNumber: Name, SerialNumber, Version.Major, Version.Minor, Version.Build, Version.Revision, NoOfParameters.
GETSNPM SensorNumber ParamNumber	Get Sensor Parameter Information. Returns the following information for parameter ParamNumber measured by sensor subsystem SensorNumber: Name, Group, GroupName,

	HasValue, HasRaw, HasRawAnom, HasAutoCal, HasCalRate, HasSelfTest, MaxRate.Days, MaxRate.Hours, MaxRate.Minutes, MaxRate.Seconds, MaxRate.Milliseconds, MaxRate.Microseconds, RateStep.Days, RateStep.Hours, RateStep.Minutes, RateStep.Seconds, RateStep.Milliseconds, RateStep.Microseconds, MaxCalRate.Days, MaxCalRate.Hours, MaxCalRate.Minutes, MaxCalRate.Seconds, MaxCalRate.Milliseconds, MaxCalRate.Microseconds, CalRateStep.Days, CalRateStep.Hours, CalRateStep.Minutes, CalRateStep.Seconds, CalRateStep.Milliseconds, CalRateStep.Microseconds
BALANCE	Correct the current offset from the current to voltage converter
PSYNC	Synchronise the signal from the cell and the signal from the current to voltage converter
AMATCH amplitude	Increase the amplitude of the signal from the current to voltage converter to suppress the signal from the cell until the signal reach amplitude
GETRTC [-b]	Get Time and Date from RTC. If the –b qualifier is used the data is sent in binary format (bytes directly from RTC device) otherwise an ascii text time/date string is send.
SETRTC year month date day hour minute second **SETRC –b binarydata**	Set RTC Time and Date on instrument from current time on PC. Without the –b qualifier seven text parameters are required as shown. With the –b qualifier the binary data is send directly to the RTC device.